

Computational tailoring of multifunctional oxide materials

# Dissertation

zur Erlangung des Doktorgrades der Naturwissenschaften  
(Dr. rer. nat.)

der

Naturwissenschaftlichen Fakultät II  
Chemie, Physik und Mathematik

der Martin-Luther-Universität  
Halle-Wittenberg

vorgelegt von

Herrn Hichem Ben Hamed  
geb. am 2. September 1985 in Zarzis



## Gutachter:

- Prof. Dr. Wolfram Hergert
- Prof. Dr. Jamal Berakdar
- Prof. Dr. Andreas Ney

Datum der öffentlichen Verteidigung: 02.12.2020





## Abstract

The recent advances in computing power has enormously boosted the investigations of material properties. Among these materials, which are attracting an increasing interest in nowadays nanotechnologies, are functional oxide materials. Therefore, it is the scope of this thesis to use computational methods in order to reproduce experimental results and to propose methods to tailor oxide properties. Three main structural modifications are investigated, namely defects, strain and by formation of solid solutions. The main framework of the computational methods is the density functional theory. Two approaches are exploited, namely pseudopotential plane-wave methods but also a Green's function Korringa-Kohn-Rostoker method. The insertion of defects was shown to induce magnetism in the non-magnetic pristine  $\text{TiO}_2$ . By means of defects or applied strain it is possible to stabilize the hexagonal phase of  $\text{BaTiO}_3$ . In addition, the magnetic properties of  $\text{GdMnO}_3$  were shown to be altered by biaxial strain or in dependence on the concentration in the solid solution with  $\text{Gd}_{1-x}\text{Ca}_x\text{MnO}_3$ .

**Keywords:** Density functional theory, magnetism,  $d^0$ -magnetism, defect formation energy, perovskites, rare earth manganites, Heisenberg model, functional oxides

## Zusammenfassung

Die neuesten Fortschritte in der Rechenleistung der Computer hat die Untersuchung von Materialeigenschaften enorm verstärkt. Unter diesen Materialien, welche wachsendes Interesse in den heutigen Nanotechnologien hervorrufen, sind funktionelle oxidische Materialien. Es ist deshalb ein Schwerpunkt dieser Arbeit experimentelle Ergebnisse zu reproduzieren und Methoden vorzuschlagen um Oxideigenschaften zu verändern. Drei hauptsächliche strukturelle Modifikationen werden untersucht, Defekte, mechanische Spannungen und die Bildung von Mischkristallen. Die Computermethoden basieren auf der Dichtefunktionaltheorie. Neben der Pseudopotentialmethode wird auch eine auf Greenschen Funktionen basierende Korringa-Kohn-Rostoker Methode verwendet. Die Einbringung von Defekten erzeugt Magnetismus im ansonsten nichtmagnetischen  $\text{TiO}_2$ . Mit der Einbringung von Defekten oder der Anwendung mechanischer Spannung ist es möglich die hexagonale Phase von  $\text{BaTiO}_3$  zu stabilisieren. Außerdem wurde gezeigt, dass die magnetischen Eigenschaften von  $\text{GdMnO}_3$  durch biaxiale mechanische Spannung oder im Mischkristall  $\text{Gd}_{1-x}\text{Ca}_x\text{MnO}_3$  in Abhängigkeit von der Konzentration geändert werden können.

**Stichworte:** Dichtefunktionaltheorie, Magnetismus,  $d^0$ -Magnetismus, Defektbildungsenergie, Perovskite, Seltenerd-Manganite, Heisenberg-Modell, funktionelle Oxide



# Contents

<b>1</b>	<b>Introduction</b>	<b>1</b>
<b>2</b>	<b>Density functional theory</b>	<b>5</b>
2.1	Many-body problem . . . . .	5
2.2	Hohenberg-Kohn approach . . . . .	8
2.3	Kohn-Sham equations . . . . .	9
2.4	Exchange-correlation approximation . . . . .	11
<b>3</b>	<b>Methods</b>	<b>15</b>
3.1	Plane-wave formulation . . . . .	15
3.2	Green's function method . . . . .	20
3.3	Disorder in crystal structures . . . . .	26
3.4	Magnetic exchange interactions . . . . .	33
3.5	Monte Carlo simulations . . . . .	35
3.6	Defect formation energies . . . . .	37
<b>4</b>	<b>Defect induced magnetism: TiO<sub>2</sub> as an example</b>	<b>41</b>
4.1	Theoretical background . . . . .	43
4.2	Vacancies . . . . .	44
4.3	Interstitials . . . . .	51
4.4	Defects complexes . . . . .	52
4.5	Formation energies . . . . .	56
4.6	Magnetocrystalline anisotropy . . . . .	59
<b>5</b>	<b>Strain and doping induced structural stability in BaTiO<sub>3</sub></b>	<b>63</b>
5.1	Crystal structure . . . . .	64
5.2	Structural stability with Fe-doping . . . . .	65
5.3	Structural stability with biaxial strain . . . . .	67
<b>6</b>	<b>Doping induced magnetic phase transitions in GdMnO<sub>3</sub></b>	<b>77</b>
6.1	Structural, electronic and magnetic properties . . . . .	79
6.2	Solid solutions with Ca doping . . . . .	84
6.3	Hole doping region . . . . .	86
6.4	Half doping region . . . . .	88
6.5	Electron doping region . . . . .	90
6.6	Transition temperatures of GCMO series . . . . .	92
<b>7</b>	<b>Strain induced magnetic phase transitions in GdMnO<sub>3</sub></b>	<b>95</b>
7.1	Extend of magnetic exchange interactions . . . . .	96
7.2	Lattice distortions effect on the magnetic interactions . . . . .	99

## Contents

---

7.3	Uniaxial strain . . . . .	102
7.4	Biaxial strain . . . . .	103
<b>8</b>	<b>Summary</b>	<b>107</b>
	<b>Bibliography</b>	<b>109</b>
	<b>List of Publications</b>	<b>129</b>

# 1 Introduction

Oxide materials are of particular interest in nowadays nanotechnologies and are increasingly the focus of much attention in theoretical and experimental investigations. In particular metal oxides, those containing at least one transition element, constitute one of the most investigated material classes due to their versatile applications. The scope of applicability covers nearly all technological fields like batteries [1–3], thermoelectric energy conversion [4–6], gas sensors [7–9] and electronic devices for future alternatives of silicon ones [10, 11]. The extend of such outstanding applicability is demonstrated by the multiple and interesting features of metal oxides. The coexistence of more than two features in the same oxide material defines it as a multifunctional oxide material. Such property is not very common in nature because most of the materials exhibit only few functionalities, hence are exploited for these target properties. For instance,  $\text{TiO}_2$  is a well known oxide for photocatalysis applications [12] but does not demonstrate any magnetic response which is crucial for spintronics applications. Similarly, the usage of other oxides might be limited to certain fields.

To trigger the multifunctionality of oxides many routes have been proposed in literature. One of the successful ways is the fabrication of oxide heterostructures from components exhibiting ferroelectric, magnetic, semiconducting, and insulating properties. Thus the features of each component will be combined in the designed heterostructure material. This scheme was the aim of the Collaborative Research Center "Functionality of Oxide Interfaces"(SFB 762) [13]. Apart the fabrication of heterostructures, the design of multifunctional oxides could be made as well through the variation of different factors such as composition (doping), temperature, pressure, strain, external fields, defects and film orientations.

An experimental realization of crystalline structure modifications through the aforementioned factors is widely used in literature and was also applied in the framework of the SFB 762. Biaxial strain for example could be applied whether in a compressive or a tensile form. It is acquired by an epitaxial growth of the oxide material on another crystalline substrate [14]. Thence the strain is induced from the lattice mismatch between the oxide and the substrate. Based on neutron-diffraction and resonant soft x-ray scattering measurements, epitaxial strain in  $\text{GdMnO}_3$  grown on  $\text{YAlO}_3$  substrate was demonstrated to alter the spin ordering of  $\text{GdMnO}_3$  [15]. Crystal defects, in particular point defects, are on the other hand mostly unavoidable in the fabrication and growth of oxide crystals. The formation for example of oxygen vacancies is typical in oxide materials. Such formation is controlled by the oxygen partial pressure which fixes the oxide stoichiometry when the total pressure and temperature are kept constant. An increase (decrease) of the oxygen chemical pressure leads to a higher oxygen interstitials (vacancies) concentration. Hence the stability of different phases of the oxide is obtained. As an example and on the grounds of electron paramagnetic resonance investigations, the presence of oxygen vacancies was shown to stabilize the ferromagnetic order in hexagonal phase of  $\text{BaTiO}_3$  in the presence of Fe impurities [16]. Another modification of the crystal structure, which will be checked in this thesis, is the

chemical doping. This modification is produced by implementing immobile impurities at certain lattice sites. Therein, a transition or rare earth element is substituted by another one which could have the same or different valency as the initial element. This method is known to be the most efficient and established way to modify structural, electronic and magnetic properties of materials. For instance, calcium doping of  $\text{GdMnO}_3$  induces a completely new phenomena which was not present in the pristine system. Apart the new spin ordering in the doped  $\text{GdMnO}_3$ , charge and orbital ordering were also detected based on magnetoresistive measurements [17]. The coupling between these orderings induces, at a certain concentration of calcium, the appearance of colossal magnetoresistance [18, 19]. This latter is of tremendous technological importance in the design of new devices such as in magnetic sensors [20] or read heads and non-volatile memories [21].

In order to emulate the already demonstrated functionalities of oxides or to predict theoretically new ones, a multicode approach is adopted here in this thesis. The involved approach is purely *ab initio*, i. e. does not require in principle any experimental inputs. It combines two distinct implementations of the density functional theory (DFT). The first one aims to resolve the DFT equations in a basis set fashion, namely plane waves. Whereas the second method stems from the multiple scattering theory. The first principles codes which are used for the plane waves method are VASP [22, 23] and QUANTUM ESPRESSO [24]. The multiple scattering theory on the other hand is in the framework of the Korringa-Kohn-Rostoker approach (KKR) [25, 26] which is implemented in HUTSEPOT [H1]. Each of the two methods has its own advantages and disadvantages depending on the kind of the involved crystalline structure modification. For example, the modeling of point defects and doped materials with basis-set methods needs a considerable enlargement of the considered cells which is not the case with the multiple scattering theory. With this latter, already well founded theories such as the coherent potential approximation (CPA) [27, 28] exist and are used to deal with doped systems particularly. Another interesting feature of doped materials is the structural disorder. This property can be directly described with the CPA method but not with the plane waves method. For this purpose, special structures [29] are constructed by means of a stochastic Monte-Carlo approach as implemented in ATAT toolkit [30]. Therein, the distribution of the alloy elements are controlled by correlation functions which have to mimic as much as possible those of a random alloy. The resulting structures are used thereafter in plane waves calculations to obtain the electronic structure of the target oxide material. It follows that magnetic properties as well can be determined. In this thesis, magnetism is essentially described with the exchange interaction constants between the magnetic sites regardless of the studied material, i. e. whether doped or undoped material.

As two methods are used to get the electronic structure of oxides in this thesis, magnetic exchange interactions are as well determined from two methods. The first one is mapping the total energies of different magnetic structures onto a Heisenberg Hamiltonian. It is well suited for the plane waves method and does not require any additional theoretical consideration but rather involves more computational resources. It might be necessary to construct large supercells in order to account for all considered exchange interactions, hence more computational time. On the other hand, only the unit cell is needed within the KKR method as long as the magnetic force theorem [31] is applied. Subsequently, the obtained exchange interactions are used in Monte Carlo simulations [H1] to obtain the magnetic transition temperatures.

---

This manuscript is organized into eight chapters including the actual introduction and a summary at the end. The relevant general theoretical background is given in [Chap. 2](#). In this chapter, the basic formulations of the density functional theory are presented. To deal with real oxide materials, computational details which are necessary to apply the DFT, are summarized in [Chap. 3](#). As mentioned earlier, two different approaches are proposed, namely the plane waves and the KKR method. More straightforward applications are also given, like disorder treatment, magnetic exchange interactions determination, Monte Carlo method and defect formation energies. All these notions provide a clear, solid picture for discussing the different scenarios for understanding and tuning oxide material multifunctionalities. The results of inducing magnetic order in  $\text{TiO}_2$  without any magnetic element are discussed in [Chap. 4](#). The presence of magnetic elements is shown on the other hand in [Chap. 5](#) to stabilize together with oxygen vacancies the complicated structure of hexagonal  $\text{BaTiO}_3$ . This requirement is demonstrated as well to not be the only scheme for the phase stability of hexagonal  $\text{BaTiO}_3$  in the second part of [Chap. 5](#). By means of zone center phonon modes analysis, the application of a biaxial compressive strain larger than 2% is demonstrated to accomplish the structural stability. Increasing further the structural complexity is discussed in [Chap. 6](#). Therein,  $\text{GdMnO}_3$ , a material which display a large Jahn-Teller effect and a  $\text{GdFeO}_3$ -type lattice distortion, is considered. In this chapter, deep insights into the physics underlying the rich magnetic phase diagram of the disordered  $\text{GdMnO}_3$ , in the presence of calcium doping, is gained. A spin model is considered to explain the different experimentally observed magnetic phase transitions. Such spin model is further extended in [Chap. 7](#) to explain the stability of new magnetic orders in  $\text{GdMnO}_3$  under different kinds of strain. The results presented in this thesis could be understood as a demonstration for a theoretical tuning and understanding of the functionalities of oxides in general.





## 2 Density functional theory

The description of materials has evolved with the development of quantum-mechanic theories. One of the fundamental roots is based on the de Broglie hypothesis, which asserts that an electron as well as any other particle may be regarded simultaneously as a particle and a wave. Therewith any particle could be represented by a wavefunction. Nevertheless oxide materials, subject of nowadays technological interest contain thousands of electrons and ions. A straightforward description of these materials with the exact many particles wavefunction is therefore impossible. Despite the exponential evolution of computing power, an exact determination of physical and chemical properties of materials remains unachievable. The reasons behind this complexity will be discussed in the following.

In this chapter, the key ideas of the considered theoretical framework of this thesis will be illustrated. All of the results are obtained with the density functional theory (DFT). The aim of using this method is to describe precisely oxide materials properties with the simple quantity of the electronic density. This latter depends only on three variables instead of the many body wavefunction which depends on the number of particles in the considered material. This method establishes the most known tool in first-principles methods, also referred to as *ab initio*, owing to its independence from any external parameter. In this context, an in-depth introduction of the necessary approximations which permit a practical resolution of the many-body problem is discussed.

### 2.1 Many-body problem

Solid state materials are constituted by an arrangement of a large number of interacting electrons and ions. This arrangement is unique for every material and can be described by the many-body wavefunction  $\Psi$ . It follows that any property could be accessed through the solution of the time-independent Schrödinger equation (SE), which reads:

$$\hat{\mathcal{H}}\Psi = E\Psi. \quad (2.1)$$

The Hamiltonian  $\hat{\mathcal{H}}$  describes the system of  $N$  interacting electrons feeling the field of  $M$  ions. Its expression is given by:

$$\hat{\mathcal{H}} = - \underbrace{\frac{\hbar^2}{2m_e} \sum_{i=1}^N \nabla_i^2}_{\hat{T}_e} - \underbrace{\frac{\hbar^2}{2} \sum_{I=1}^M \frac{1}{M_I} \nabla_I^2}_{\hat{T}_N} + \underbrace{\frac{1}{2} \sum_{i \neq j}^N \frac{e^2}{4\pi\epsilon_0 |\mathbf{r}_i - \mathbf{r}_j|}}_{\hat{V}_{e-e}} - \underbrace{\sum_{i=1}^N \sum_{I=1}^M \frac{Z_I e^2}{4\pi\epsilon_0 |\mathbf{r}_i - \mathbf{R}_I|}}_{\hat{V}_{e-N}} + \underbrace{\frac{1}{2} \sum_{I \neq J}^M \frac{Z_I Z_J e^2}{4\pi\epsilon_0 |\mathbf{R}_I - \mathbf{R}_J|}}_{\hat{V}_{N-N}}. \quad (2.2)$$

The indices  $i$  and  $j$  in Eq. (2.2) run over electrons whereas  $I$  and  $J$  run over nuclei.  $m_e$  and  $M_I$  are the mass of one electron and one nucleus respectively. The quantity  $e$  denotes an elementary electrical charge while  $\epsilon_0$  refers to the permittivity of the vacuum. The terms  $T_e$  and  $T_N$  are the kinetic energy of electrons and ions, respectively. On the other hand,  $V_{e-e}$  and  $V_{e-N}$  are the Coulomb potentials, which describe the electron-electron and electron-ion interactions, respectively. The last term,  $V_{N-N}$ , corresponds to the ion-ion interactions.

As a consequence, the complexity of the SE grows exponentially with the number of electrons and nuclei. Therefore, an analytical solution cannot be acquired for a system with more than two particles. Thus, one needs to consider several approximations in order to solve the SE.

### 2.1.1 Born-Oppenheimer approximation

One of the required approximations to solve the many-body problem is the adiabatic approximation, also known as the Born-Oppenheimer approximation (BOA) [32]. It relies on the ratio of the nuclear mass to the electronic one, i.e., the nuclear mass is three orders of magnitude larger than the electronic mass. This gives rise to a large difference in motion between the light electrons and the heavy nuclei. Consequently, when an electron is rapidly moving, the nuclei are assuming to remain in their instantaneous configurations. Owing to their large mass, the nuclei can not follow the motion of every surrounding electron but feel their averaged field. Contrarily, an electron can follow any changes in the nuclei positions and relax rapidly to the instantaneous ground state of the nuclei. To this end, the electronic problem could be decoupled from the nuclear one. The electronic wavefunction is then determined by the instantaneous position of the nuclei. Therefore the total wavefunction can be written as the product of ionic and electronic wavefunctions:

$$\Psi(\mathbf{r}, \mathbf{R}) = \chi(\mathbf{R}) \psi(\mathbf{r}, \mathbf{R}), \quad (2.3)$$

here  $\psi$  stands for the electronic wavefunction and  $\chi$  for the nuclear wavefunction. The set of all electronic and nuclear coordinates are represented by  $\mathbf{r}$  and  $\mathbf{R}$ , respectively. It follows that Eq. (2.2) is decomposed into an electronic and nuclei parts. Owing to the slow nuclear motion, the nuclear kinetic energy,  $T_N$ , in Eq. (2.2) could be neglected. Consequently, the system could be described only with electronic degrees of freedom. Hence Eq. (2.2) is simplified, after adopting here and throughout the whole manuscript the atomic units ( $\hbar = e^2 = m_e = 4\pi\epsilon_0 = 1$ ), into:

$$\hat{\mathcal{H}} = -\frac{1}{2} \sum_{i=1}^N \nabla_i^2 + \frac{1}{2} \sum_{i \neq j}^N \frac{1}{|\mathbf{r}_i - \mathbf{r}_j|} + \hat{V}_{\text{ext}}(\mathbf{r}). \quad (2.4)$$

The electron-nuclei interactions are denoted here by the external potential  $V_{\text{ext}}(\mathbf{r})$ . It is worth mentioning here that the BOA could fail in systems where large electron-lattice interactions occur [33, 34]. In fact, the simplification brought by the BOA in the resolution of the many-body problem is still not enough to easily and accurately handle the SE.

### 2.1.2 Wavefunctions methods

Many attempts were made to solve the still complicated SE in Eq. (2.1) using Eq. (2.4). One of the earliest approximations was due to Hartree [35]. This approximation assumes that the many particles wave function could be written as the product of the single particle functions.

$$\psi(\mathbf{r}_1, \mathbf{r}_2 \cdots \mathbf{r}_N) = \varphi_1(\mathbf{r}_1) \varphi_2(\mathbf{r}_2) \cdots \varphi_N(\mathbf{r}_N). \quad (2.5)$$

Each of the functions  $\varphi_i(\mathbf{r}_i)$  satisfies the one-electron SE with a potential term arising from the average field of other electrons, but the violation of the Pauli principle in this approximation demonstrates its biggest drawback. Later, Fock [36] and Slater [37] incorporated the Fermi statistics in the Hartree decomposition of the many-electrons wavefunction by replacing the product of the single-particle wavefunction by the Slater determinant, which is known as the Hartree-Fock approximation. The wavefunction is then written as

$$\psi(\mathbf{x}_1, \mathbf{x}_2 \cdots \mathbf{x}_N) = \frac{1}{\sqrt{N!}} \begin{vmatrix} \varphi_1(\mathbf{x}_1) & \varphi_2(\mathbf{x}_1) & \cdots & \varphi_N(\mathbf{x}_1) \\ \varphi_1(\mathbf{x}_2) & \varphi_2(\mathbf{x}_2) & \cdots & \varphi_N(\mathbf{x}_2) \\ \vdots & \vdots & \ddots & \vdots \\ \varphi_1(\mathbf{x}_N) & \varphi_2(\mathbf{x}_N) & \cdots & \varphi_N(\mathbf{x}_N) \end{vmatrix}, \quad (2.6)$$

where the combined variable  $\mathbf{x}_i = (\mathbf{r}_i, \sigma_i)$  refers to the spatial  $\mathbf{r}_i$  and spin  $\sigma$  degrees of freedom of the  $i$ th electron. The inclusion of the Fermi statistics in this picture leads to a new non-local potential term in the SE, called the exchange potential. This approximation was widely used in molecular physics in the early age of microscopic simulations. However this single configuration with the Slater determinant leads to overestimation of band gaps and underestimation of the binding energies due to neglect of the correlation effects. In this approximation, electron-electron interactions in the system are described within their average locations instead of their real ones. A linear combination of Slater determinants was shown to improve significantly all material properties. It is the spirit of the configuration interaction method [38]. The method aims to mix many single-configurations in order to reach the chemical accuracy. In view of the enormous increase in the number of configurations with increasing the number of electrons, this method is still limited to systems with relatively small number of electrons.

## 2.2 Hohenberg-Kohn approach

A complete different path from the previous described methods to solve the SE was proposed by Thomas [39] and Fermi [40]. They suggested for the first time the electronic density as basic quantity instead of the complicated  $N$ -electron wavefunctions to solve the SE. This electronic density is defined as

$$\rho(\mathbf{r}) = N \int d\mathbf{r}_1 \cdots \int d\mathbf{r}_N \psi^*(\mathbf{r}, \mathbf{r}_1, \dots, \mathbf{r}_N) \psi(\mathbf{r}, \mathbf{r}_1, \dots, \mathbf{r}_N), \quad (2.7)$$

where the spin coordinates  $\sigma_i$  are omitted hereafter for sake of simplicity and will be only explicitly written whenever needed. The proposed scheme by Thomas and Fermi assumes that the motion of electrons are uncorrelated and the kinetic energy of the electronic system could be approximated to an explicit functional of the density of electrons in an homogeneous electron gas (HEG). In this model the electronic density varies very slowly in space, therefore considered fixed in the entire space. The local approximation of the kinetic energy is then given by

$$T[\rho] = \frac{3}{10} (3\pi^2)^{2/3} \int d\mathbf{r} \rho(\mathbf{r})^{5/3}. \quad (2.8)$$

Like previous methods, the Thomas Fermi (TF) model does not take into account all the physics of the system. One of the most important effects, electronic exchange-correlations are neglected within this model. This leads to wrong total energies and the divergence of the density. This latter becomes infinite, close to the nucleus and fails to produce the shell structure of atoms [41] or the binding of molecules[42].

The crude definition of the kinetic energy functional made by TF was later improved in the work of Weizsäcker [43]. Therein a correction term is added to account for the spatial variation of the density. As well an exchange correction was added later by Dirac [44]. Nevertheless, the TF model with these two corrections is still far from being exact.

It was due to Hohenberg and Kohn [45] (HK) that the TF model was reformulated to an exact theory for many-body systems. They developed and proved two theorems which could be applied to any system of interacting particles.

**Theorem I:** For any system of interacting particles exposed to an external potential  $V_{\text{ext}}$ , this potential is solely determined by the ground state electronic density.

**Theorem II:** For any external potential,  $V_{\text{ext}}$ , it exists an universal energy functional  $E[\rho]$ . The minimization of this functional with respect to the electronic density leads to the exact ground state of the system.

According to Theorem I, the Hamiltonian and consequently all physical properties (many-body wavefunction,  $\dots$ ) are fully accessed via the ground state density. This implies that the ground state total energy of the system can be written as:

$$E[\rho] = V_{\text{ext}}[\rho] + F_{\text{HK}}[\rho]. \quad (2.9)$$

The new term  $F_{\text{HK}} = T + V_{\text{e-e}}$ , is called the HK density functional. It includes the classical and non-classical effects and is independent of the external potential. It depends only on the ground state wavefunction and hence on the ground state density. A concrete physical interpretation of this functional was given by Levy[46] and Lieb [47] (LL). They showed how  $F_{\text{HK}}[\rho]$  could be determined even in the case of a degenerate ground state (a condition not satisfied by the first theorem).

The main simplification of the many-body problem, made by HK and LL, is the reference to the ground state density instead of the many-body wavefunction in the resolution of the many-body problem. The external energy, associated with  $V_{\text{ext}}$ , can be easily expressed in terms of the electronic density. Similarly the electron-electron interaction can be also expressed in terms of the electronic density with the help of the two-particle density because two electrons are involved here. The dependence of the electron-electron energy on only the one particle electronic density is recovered by employing the Coulomb hole function [48, 49]. However, expressing the kinetic energy operator in terms of the electronic density is not possible, at least at this stage, because of the derivative term in its expression:

$$T = -\frac{1}{2} \sum_{i=1}^N \int d\mathbf{r} \psi^* (\mathbf{r}_1, \mathbf{r}_2, \dots, \mathbf{r}_N) \nabla_i^2 \psi (\mathbf{r}_1, \mathbf{r}_2, \dots, \mathbf{r}_N). \quad (2.10)$$

## 2.3 Kohn-Sham equations

Although the great simplification of the many-body problem with the HK approach, it is still far away from being directly applied. The reasons are on one hand, the difficulty to express the kinetic energy in terms of the electronic density ( Eq. (2.10)). On the other hand, HK do not provide a practical guide to construct the unknown functional  $F_{\text{HK}}$  despite its formulation in terms of the electronic density.

An efficient and simple approach was introduced by Kohn and Sham (KS) [50]. It is considered as one of the break-through developments in modern solid state theories [51]. The main achievement of this approach is mapping the interacting system of electrons, in the external potential  $V_{\text{ext}}$  into a fictitious system of non-interacting KS particles, in an effective potential  $V_{\text{KS}}$ . The fictitious system has the same ground state density  $\rho(\mathbf{r})$  as the original interacting system. The KS Hamiltonian is then given by

$$\hat{\mathcal{H}}_{\text{KS}} = -\frac{1}{2} \nabla^2 + \hat{V}_{\text{KS}}(\mathbf{r}), \quad (2.11)$$

where the effective KS potential is constituted by

$$\hat{V}_{\text{KS}}(\mathbf{r}) = \hat{V}_{\text{H}}(\mathbf{r}) + \hat{V}_{\text{ext}}(\mathbf{r}) + \hat{V}_{\text{XC}}(\mathbf{r}). \quad (2.12)$$

Therefore, the many-body problem is solved with the so-called Kohn-Sham equations:

$$\hat{\mathcal{H}}_{\text{KS}} \phi_i(\mathbf{r}) = \epsilon_i \phi_i(\mathbf{r}), \quad (2.13)$$

where  $\epsilon_i$  are the KS eigenvalues. The electronic density of the non interacting system is expressed in terms of the single particle orbitals  $\phi_i$ , called KS orbitals:

$$\rho(\mathbf{r}) = \sum_{i=1}^N |\phi_i(\mathbf{r})|^2. \quad (2.14)$$

The independent particle kinetic energy is given by

$$T_s = -\frac{1}{2} \sum_{i=1}^N \langle \phi_i | \nabla_i^2 | \phi_i \rangle. \quad (2.15)$$

The KS kinetic energy functional  $T_s$  is just a particular case of the HK functional (Eq. (2.9)) when electron-electron interactions are neglected. But it is now an unique functional of the density. Using the second theorem of HK, the energy functional of the interacting many-body system can be rewritten as:

$$E_{\text{KS}}[\rho] = T_s[\rho] + E_{\text{H}}[\rho] + E_{\text{XC}}[\rho] + \int d\mathbf{r} V_{\text{ext}}(\mathbf{r}) \rho(\mathbf{r}). \quad (2.16)$$

The new term  $E_{\text{XC}}$  in Eq. (2.16) incorporates all exchange and correlation interactions. It has no exact description and should be approximated. In consequence, the ambiguity in the construction of the HK functional is migrated with KS approach to the exchange correlation energy. It is formally defined as the difference between the HK functional and the sum of the Hartree and kinetic energies

$$E_{\text{XC}}[\rho] = F_{\text{HK}}[\rho] - (T_s[\rho] + E_{\text{H}}[\rho]) = \left[ \langle \langle T \rangle \rangle - T_s[\rho] + \widehat{V}_{\text{e-e}} - \widehat{V}_{\text{H}} \right]. \quad (2.17)$$

This equation is only valid by considering the central assertion of the KS approach: the ground state density of the effective system has to be the same as for the interacting system, otherwise,  $F_{\text{HK}}$  and  $T_s$  are defined for the two different systems of interacting and non interacting particles. Since no exact expression of this energy is known, it will be approximated as will be shown later.

The solution of the KS equations in Eq. (2.13) requires the knowledge of the electronic density which is still in turn unknown. The HK variational principle, given in the second HK theorem, provides the necessary background to solve the KS equation. Therein, the ground state density minimizes the total energy functional:

$$\frac{\delta E[\rho]}{\delta \rho(\mathbf{r})} = \mu. \quad (2.18)$$

The Lagrange multiplier  $\mu$  is inserted here to ensure that the number of particles is conserved. It defines as well the minimization condition. Afterwards, a self-consistent loop is required to solve the KS problem in Eqs. (2.11) and (2.12) and obtain the ground state electronic density which is used as constraint. An initial guess has to be done. A good starting point could be based on the atomic orbitals. Then,  $\rho(\mathbf{r})$  enters Eq. (2.18) and start to be iterated. The exact electronic density is taken after convergence of the self consistent loop.

## 2.4 Exchange-correlation approximation

The main advantage of the KS scheme is mapping the problem from finding a good approximation of  $F_{\text{HK}}$  (Hohenberg-Kohn functional) to finding a good approximation of the exchange correlation energy  $E_{\text{XC}}$ , which is smallest among other energies in Eq. (2.16). The derived potential reads:

$$V_{\text{XC}}(\mathbf{r}) = \frac{\delta E_{\text{XC}}[\rho(\mathbf{r})]}{\delta \rho(\mathbf{r})}. \quad (2.19)$$

### 2.4.1 Local density approximation

The first and most used approximation of the exchange correlation functional is the local density approximation (LDA). This functional was initially proposed with the homogeneous electron gas (HEG) condition in the original paper of Kohn [45]. In that condition, the density varies very slowly in the space. Therefore, it is considered as locally homogeneous. The local approximation of the exchange correlation gives :

$$E_{\text{XC}}^{\text{LDA}}[\rho] = \int d\mathbf{r} \rho(\mathbf{r}) \tilde{\epsilon}_{\text{XC}}(\rho(\mathbf{r})), \quad (2.20)$$

where  $\tilde{\epsilon}_{\text{XC}}(\rho(\mathbf{r}))$  is the exchange correlation energy per particle of the HEG with density  $\rho(\mathbf{r})$ . The exchange correlation energy in the local approximation depends only on the spherical average of the exchange correlation hole. To simplify its evaluation, the exchange and correlation energy per electron  $\tilde{\epsilon}_{xc}$  can be divided into two distinct contributions (exchange + correlation) :

$$\tilde{\epsilon}_{\text{XC}} = \tilde{\epsilon}_{\text{X}} + \tilde{\epsilon}_{\text{C}}. \quad (2.21)$$

The exchange part can be evaluated analytically [52] while the correlation part can be calculated using quantum Monte Carlo simulations [53–56]. Despite its simplicity, the local density approximation was demonstrated to give good qualitative results even for systems beyond the uniform electron gas limit. However it might lead to wrong results for strongly correlated electron systems where localized  $d$  or  $f$  states are involved. As examples, the calculated structural parameters (cell's volume, bond lengths), electronic properties (band gap) and magnetic moments with LDA are mostly underestimated. Cohesive energies of solids are on the other hand overestimated with LDA [57].

### 2.4.2 Generalized gradient approximation

A more elaborated approximation of the exchange correlation is the Generalized Gradient Approximation (GGA). It includes the spatial variation of the density by taking into account higher order derivatives of the density:

$$E_{\text{XC}}^{\text{GGA}}[\rho] = \int d\mathbf{r} \tilde{\epsilon}_{\text{XC}}(\rho(\mathbf{r})) \rho(\mathbf{r}) f_{\text{XC}}[\rho(\mathbf{r}), \nabla \rho(\mathbf{r}), \nabla^2 \rho(\mathbf{r}) \dots]. \quad (2.22)$$

The new term in the expression of the exchange correlation energy compared to that of LDA is a function designed to enhance the qualitative description of the non homogeneity by taking into account the density variation at the vicinity of the electronic position  $\mathbf{r}$ . Gradient corrections should

be carried out very carefully to retain all the relevant contributions from higher order by means of the introduced function  $f_{xc}$ . This function offers a great flexibility to describe real materials. A large number of modified gradient expansions were proposed in literature [58–60]. Most of the modern GGA approximations differ from the original gradient expansion approximation proposed in the original paper of Kohn, where only the gradient of the density was taken into account. However, GGA derived functionals were shown to perform only a little better than LDA as will be shown below for ZnO electronic properties.

### 2.4.3 Strong interactions beyond DFT

An extensive development of exchange correlation functionals was made in the recent years and about hundreds of functionals are stored and adapted for the available DFT codes, e. g. in the LIBXC library [61]. Nevertheless, a unique and universal functional which can be used for any material is still not available. This follows from the functional derivative discontinuities of the related exchange correlation energies when adding or extracting one electron from the system [62, 63]. Another drawback of the current DFT approximations is the presence of the self interaction in the electron-electron interactions, more accurately in the Hartree term. It is mainly due to non physical interaction of one electron with itself. Perdew and Zunger [54] suggested two methods to remove this error. The first one consists of adding an orbital dependent single particle potential. The second method manifests in a local potential correction to the KS potential. Both methods were demonstrated to improve significantly the LDA and GGA results but at the cost of computationally expensive calculations [64].

An alternative approach was developed by Liechtenstein *et al.* [65], it was demonstrated to give accurate results for transition metal oxides and also Mott-Hubbard insulators where the bare DFT band gap is underestimated by roughly 60 %. The method is inspired from the Hubbard model [66] where an on-site Coulomb interaction  $U$  is added to the Hamiltonian together with the Hund's exchange energy  $J$ . The  $U$  term reduces the hopping of  $d$  or  $f$  electrons while  $J$  reduces the spin inter-atomic exchange. Therefore, the Mott-Hubbard system is described as an insulator and not a metal or semi-metal. In addition, for distorted lattices, orbital polarization might play an important role in the ground state stabilization. Therefore, it is included in this method through the Hartree-Fock energy  $E^{\text{HF}}$ , where only orbitals of the correlated states are included in the calculation:

$$E^{\text{DFT+U}} = E^{\text{DFT}} + E^{\text{HF}} - E^{\text{DC}}. \quad (2.23)$$

The term  $E^{\text{DC}}$  is included to take out the double counting of state contributions in  $E^{\text{DFT}}$  and  $E^{\text{HF}}$ . It reads:

$$E^{\text{DC}} = \frac{U}{2} \tilde{N}(\tilde{N} - 1) - \frac{J}{2} \left[ \tilde{N}^{\uparrow}(\tilde{N}^{\uparrow} - 1) + \tilde{N}^{\downarrow}(\tilde{N}^{\downarrow} - 1) \right], \quad (2.24)$$

where  $\tilde{N}$  is total number of  $d$  or  $f$  electrons, i. e.  $\tilde{N}^{\uparrow} + \tilde{N}^{\downarrow}$ . A simpler approach was proposed by Dudarev *et al.* [67] where only an effective  $U_{\text{eff}}$  value ( $U - J$ ) enters Eq. (2.24). The method is widely used because of its easier control compared to Liechtenstein approach, i. e. one instead of two parameters to fit in order to produce the experimental results. Hence, it will be adapted in the following discussions.



TABLE 2.1: The effect of different exchange correlation treatments on the electronic properties of ZnO, namely the position of Zn  $3d$  states in the band structure of ZnO  $E(d_{\text{Zn}})$ , the electronic band gap of ZnO  $E_{\text{Gap}}$  and the deformation potential  $D_{\text{pot}}$ .  $D_{\text{pot}}$  is defined as the change of the band gap with an applied strain. The reported theoretical values by Adeagbo *et al.* [77] are used here for the comparison with the experimental results.

XC	$E(d_{\text{Zn}})$ (eV)	$E_{\text{Gap}}$ (eV)	$D_{\text{pot}}$ (eV)
LDA	-5.59	0.67	-2.26
GGA	-5.57	0.73	-2.18
GGA+U	-7.41	1.45	-2.91
HSE06	-7.24	3.28	-2.90
GW	-7.05	3.20	-4.02
Expt.	-7.4 to -8.6 [73–75]	3.43 [71]	-2.04 [72]

While the DFT method is an exact theory, its accuracy is mainly based on the best approximation of the exchange correlation potential in Eq. (2.19). In the following, the semiconductor prototype ZnO is used to demonstrate the effect of such potential approximation on the band structure. The electronic structure of ZnO is commonly considered as a good criteria to check the accuracy of the exchange correlation approximations, particularly for the problematic Zn  $d$ -states position in the band structure. In this direction, three parameters are checked here for ZnO and compared to experiment. They are the position of the Zn  $d$ -states, the electronic band gap and the deformation potential which is associated with the strain effect on the electronic structure. Each of the three parameters is calculated with different treatments of the exchange correlation potential: the simplest LDA, GGA with PBE functional [59], an added  $U$  correction to the PBE functional (PBE+U), the hybrid functionals with HSE06 method [68] and finally the many-body perturbation theory with the GW approximation [69, 70]. As can be clearly seen from Tab. 2.1, the LDA gives the lowest value of the band gap which is far from the experimental value of 3.43 eV [71] but gives at the same time one of the closest values of the deformation potential compared to the experiment [72]. Nevertheless, the position of the Zn  $3d$  states is still far away from its experimental values [73–75], i. e.  $\approx 2.5$  eV higher. Applying the GGA does not change much the three calculated properties. However, by adapting the computationally expensive methods like hybrid functionals or GW approximation, only the band gap and the position of  $d$  states are enhanced while the deformation potential is highly overestimated, about two times the experimentally measured value with GW approximation. The best compromise between the three properties is found for the computationally cheap method of GGA+U. Note that the values presented in Tab. 2.1 could be even brought into a perfect agreement with experiment because the values in Tab. 2.1 are obtained with  $U_d = 6.5$  eV. For instance, Ma *et al.* [76] showed that applying  $U$  corrections on both Zn  $3d$  ( $U_d = 10$  eV) and O  $2p$  orbitals ( $U_p = 7$  eV) accurately reproduces not only the band gap but most of the structural and electronic properties of ZnO. Since this thesis is focused on complex materials with structural and chemical modifications, meaning the requirement of additional computational resources, and the already demonstrated success of GGA+U for the prototype material of ZnO, the GGA+U method will be adapted as exchange correlation treatment for all the calculated material properties in this thesis.



## 3 Methods

This chapter is devoted to introduce the computational methods used in this thesis. The theoretical background is already described in the previous chapter. The necessary equations are recast here to describe infinite periodic systems of ordered and disordered structures. Two frameworks are considered to solve the Kohn-Sham equations, namely the plane-wave pseudopotential method and the Korringa-Kohn-Rostoker Green's function method. The first one is a basis set method, while the second is based on multiple scattering theory. The main purpose of using these two methods, and also other electronic structure methods, is to solve the single-particle Kohn-Sham equations for extended systems. Afterwards any quantity of interest can be accessed, e.g, total energies, density of states, forces, response functions.

### 3.1 Plane-wave formulation

To deal with any physical property in the basis set methods, one has to expand the single-particle eigenstates of the Kohn–Sham equation (Eq. (2.11)) into a set of orthogonal basis functions. Thus, one needs to solve the secular equation:

$$\sum_i \left( \langle \phi_i | \hat{H}_{KS} | \phi_j \rangle - \delta_{i,j} \epsilon \right) c_i = 0. \quad (3.1)$$

The most widely used basis set in solid state physics within DFT are plane waves. Apart their easy implementation of the DFT equations, plane waves have interesting features, like the basis orthonormality and its energy-independence, compared to other methods. A further advantage is the potential independence on the atomic radius where the entire space is treated on the same footing. Besides the Hellmann-Feynman theorem can be directly applied in order to get the atomic forces without any restriction. All these features make the use of plane-wave basis set as the method of choice for most modern DFT calculations, particularly for periodic crystals.

In a periodic crystal, Bloch's theorem states that the electronic wavefunction can be written as a periodic function  $u_{n,\mathbf{k}}$  modulated by a plane wave:

$$\phi_{n,\mathbf{k}}(\mathbf{r}) = u_{n,\mathbf{k}}(\mathbf{r}) e^{i\mathbf{k}\mathbf{r}}, \quad (3.2)$$

where  $n$  is the band index,  $\mathbf{k}$  is a wave vector. The function  $u_{n,\mathbf{k}}$  incorporates the lattice periodicity, i. e.  $u_{n,\mathbf{k}}(\mathbf{r}) = u_{n,\mathbf{k}}(\mathbf{r} + \mathbf{R})$ , where  $\mathbf{R}$  is a lattice vector. The periodic function  $u_{n,\mathbf{k}}$  can be as well expressed as a discrete sum over the reciprocal lattice vectors  $\mathbf{G}$ . It follows that the electronic wavefunction is given by

$$\phi_{n,\mathbf{k}}(\mathbf{r}) = \sum_{\mathbf{G}} \tilde{u}_{n,\mathbf{k}}(\mathbf{G}) e^{i(\mathbf{k}+\mathbf{G})\mathbf{r}}. \quad (3.3)$$

Equation. (3.3) involves a summation over an infinite number of  $\mathbf{G}$  vectors. This summation can be practically truncated up to a certain  $\mathbf{G}_{\max}$  owing to the fact that the Fourier coefficients  $\tilde{u}_{n,\mathbf{k}}(\mathbf{G})$  decrease with increasing  $\mathbf{G}$ . The upper limit  $\mathbf{G}_{\max}$  defines the so-called cut-off energy, which is a crucial parameter for controlling the calculation quality. Convergence tests have to be done carefully for each studied system.

Another considerable simplification is possible, if the symmetry group of SE can be used [78], either in real space ( $\mathbf{r}$ ) or reciprocal space ( $\mathbf{k}$ ). A system is called symmetric under the transformation  $\hat{S}$ , when  $\hat{S}|\psi\rangle$  is a solution of the SE which has initially  $|\psi\rangle$  as solution. The operator  $\hat{S}$  presents all possible transformations, i.e, the identity, an inversion, a reflection, rotation, translation or a combination of these transformations. In matrix representation,  $\hat{S}$  is described by  $3 \times 3$  matrices.

By using the symmetries of the SE group, the number of  $\mathbf{k}$  vectors can be as well reduced to those inside the irreducible part of the Brillouin zone. Based on the slow variation of the electronic wavefunction between two adjacent  $\mathbf{k}$ -points, only discrete values over a chosen  $\mathbf{k}$ -points set can be used. It is the spirit of Monkhorst and Pack method [79] (MP), which extended the early works of Baldereschi [80] and Chadi and Cohen [81]. The MP method takes advantage of the reciprocal space symmetries to give an accurate interpolation of the periodic functions between certain special points. It is valid for bulk crystals and also for slab systems. The error induced by this scheme can be systematically reduced by increasing the density of the  $\mathbf{k}$ -mesh. In insulating materials, few number of  $\mathbf{k}$ -points,  $\sim 10$ , turn out to give good converged results. For metallic systems and also accurate density of states, a tetrahedron method [82, 83] was shown to perform better than the MP method [82–84]. The tetrahedron method divides the space between the grid points into tetrahedra and interpolates quadratically the energy inside each tetrahedron from its four corners. This scheme is employed in all density of state calculations in this thesis.

### 3.1.1 Pseudopotential method

By virtue of defining a cutoff energy, the infinite summation over the  $\mathbf{G}$  vectors is truncated to take into account a defined number of vectors. Although a huge number has still to be considered in order to accurately describe the strong oscillations of the electronic wavefunction close to the nucleus. The pseudo-potential (PP) concept [85], which originates from the orthogonalized plane wave approach [86], offers a great simplification of this problem.

The idea consists of replacing the strong Coulomb potential of the nucleus  $V_{\text{ext}}$  in Eq. (2.12) by an effective ionic PP, which acts only on limited number of electrons, more precisely those which are valence ones. The reason lies on the fact that chemical bonds and atomic interactions in materials are essentially ascribed to the valence electrons. Moreover, the electronic wavefunction oscillations diminish beyond a certain distance to the nucleus. Therefore a real space cutoff radius  $r_c$  can be chosen to distinguish between the valence and core regions where the electrons in the core region are considered as frozen. Consequently the pseudo wavefunction  $\tilde{\phi}$  is strictly constructed from the valence electrons but with a crucial condition: The pseudo wavefunction has to exactly match the real wavefunction  $\phi$  beyond  $r_c$ . This apply as well to the corresponding Coulomb potentials as illustrated in Fig. 3.1

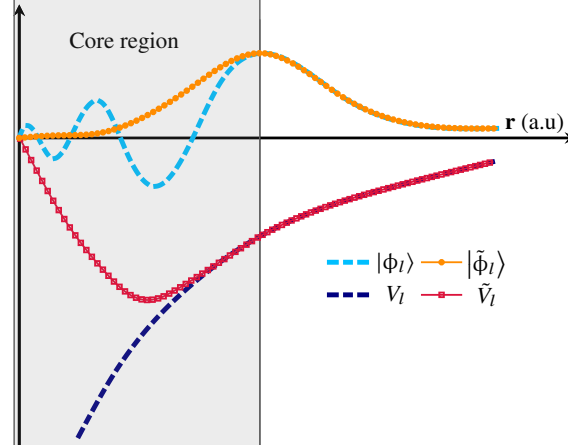


FIGURE 3.1: Schematic representation of the real space separation into a core region (gray color) and valence region (white color). The idea of pseudopotential is demonstrated by the relationship between the all-electron wavefunction  $|\phi_l\rangle$  and the pseudo-wavefunction  $|\tilde{\phi}_l\rangle$  on one hand and the all-electron potential  $V_l$  and the pseudopotential  $\tilde{V}_l$  on the other hand.

Following Philips and Kleinman [85], the core electron wavefunctions  $\phi_c$ , although not explicitly considered, must be orthogonal to the valence wavefunctions  $\phi_v$ :

$$|\tilde{\phi}\rangle = |\phi_v\rangle + \sum_c |\phi_c\rangle \langle \phi_c | \tilde{\phi} \rangle, \quad (3.4)$$

here the sum runs over all core states  $c$ . This form shows that away from the core region  $|\tilde{\phi}\rangle = |\phi_v\rangle$ . If the valence wavefunction in Eq. (3.4) is normalized to unity, the norm of the pseudo-wavefunction is just approximately one:

$$\langle \tilde{\phi} | \tilde{\phi} \rangle = 1 + \sum_c |\langle \phi_c | \tilde{\phi} \rangle|^2. \quad (3.5)$$

The last term is typically in the order of 0.1. Despite its small value, it could cause an incorrect charge distribution between the valence and core region in the self-consistent calculations. This problem can be overcome with the introduction of the norm conserving pseudo-potential by Hamann *et al.* [87].

In fact not only norm conservation fostered the use of PP in modern theory of electronic structure but mostly their *ab initio* construction. In this direction, Bachelet *et al.* [88] constructed a set of PP for most of the periodic-table elements. The construction of PP was done self-consistently for isolated atoms through the solution of the radial part of the KS system:

$$\left( -\frac{1}{2} \frac{d^2}{dr^2} + \frac{l(l+1)}{2r^2} + V_{\text{KS}}(r) - \epsilon_l \right) \phi_l = 0. \quad (3.6)$$

In order to produce accurate and norm-conserving PPs, five criteria have to be fulfilled [87]: the equality of the true and pseudo eigenvalues, i. e.  $\tilde{\epsilon}_l = \epsilon_l$ , the coincidence of true and pseudo wavefunctions beyond the defined cut-off radius  $r_c(l)$ . This radius defines the extension of the core region for each angular momentum  $l$ . The third condition ensures the equality of charge densities within the defined core region. Such condition is very crucial for DFT results accuracy, since the

charge density is the main ingredient of the theory. Moreover the logarithmic derivatives and also their first energy derivatives of the true and pseudo-wavefunction must be the same outside the core region ( $r \geq r_c$ ). This last criterion is mandatory in order to ensure the PP transferability. That means the same generated PP is valid and can be used in different chemical environments. For example, the same oxygen PP could be used to calculate the electronic structure of the water molecule and also of the perovskite oxides. After involving the five mentioned conditions, the pseudo-wavefunction and also the PP can be obtained. Afterwards, an unscreening procedure is applied to obtain the ionic PP from the isolated atom PP.

Actually, the best PP does not exist for any element in the sense that it is unique and gathers all the necessary features. For a defined exchange correlation functional, the PP depends only on the cutoff radius  $r_c$ . There is a large arbitrariness in the choice of  $r_c$ , since no exact value could be provided. Only a good compromise between two factors is sought: The first factor is the already explained transferability. It is accomplished by choosing a small cut-off radius  $r_c$  to prevent a possible overlap between core regions of neighboring atoms. This in turn gives an accurate description, which comes at the cost of large needed number of plane waves to describe the wavefunction. The second factor on the other hand is the smoothness of the PP, which can be obtained with a large cut-off radius  $r_c$ . Thus the PP becomes soft and the wavefunction can be described with few plane waves. The smoothness of pseudo-potentials was and still is the objective of active works [89–91]. The purpose is to find a computationally efficient pseudo-potential scheme, which reproduces the all-electron behavior outside the core region and accurately describes the ionic potential close to the nuclei with a minimal basis set. Such objective is accomplished by the successful method of projector augmented waves [92].

### 3.1.2 Projector augmented wave method

The idea of the projected augmented waves method (PAW) is similar to what was shown previously by the mapping of the real system into a KS effective system. The mapping here concerns the transformation of the nodal wavefunction  $\psi_i$  to a numerically convenient auxiliary wavefunction  $\tilde{\psi}_i$ . The mapping is insured by the linear transformation  $\hat{T}$ , which transforms the auxiliary wavefunction  $\tilde{\psi}_i$  to the real wavefunction  $\psi_i$ , i. e.

$$|\psi_i\rangle = \hat{T} |\tilde{\psi}_i\rangle. \quad (3.7)$$

The index  $i = (n, \mathbf{k}, \sigma)$  contains the band index, the wave vector  $\mathbf{k}$  and the spin index  $\sigma$ . An explicit definition of the operator  $\hat{T}$  is still nevertheless unknown at this stage. Since the real wave function is already smooth beyond a certain  $r$  distance to the nucleus (as already discussed in Sec. 3.1.1), the operator  $\hat{T}$  should act only on the region close to the nucleus. Therefore, it can be expressed as the sum of an identity operator and the sum of local atom-centered contributions:

$$\hat{T} = \hat{1} + \sum_I \hat{T}_I, \quad (3.8)$$

where  $I$  is the atom index and  $\hat{T}_I$  acts only within a defined augmentation region  $\Omega_I$  close to the nucleus. Inside  $\Omega_I$ , the pseudo-wavefunction is expanded into pseudo-partial waves:

$$|\tilde{\Psi}\rangle = \sum_i |\tilde{\phi}_i\rangle c_i. \quad (3.9)$$

On the same footing, the real wave function in Eq. (3.7) can be expanded into partial waves as:

$$|\psi\rangle = \hat{T} |\tilde{\psi}\rangle = \sum_i c_i |\phi_i\rangle . \quad (3.10)$$

As the required  $\hat{T}$  transformation has to be linear, the expansion coefficients  $c_i$  should be linear functionals of  $|\tilde{\psi}\rangle$ . Thus,  $c_i$  are the scalar products of the partial waves with the projector functions  $\tilde{p}_i$ :

$$c_i = \langle \tilde{p}_i | \tilde{\psi} \rangle . \quad (3.11)$$

Since the augmentation regions around each atom do not overlap, the one-center expansion of the partial wave function inside the augmentation region  $\Omega_I$  is identical to the partial wave function itself. This implies the condition:

$$\langle \tilde{p}_i | \tilde{\phi}_j \rangle = \delta_{i,j} . \quad (3.12)$$

The projector functions are in turn localized within  $\Omega_I$ . Therefore, the linear transformation  $\hat{T}$  can be simplified as:

$$\hat{T} = 1 + \sum_i (|\phi_i\rangle - |\tilde{\phi}_i\rangle) \langle \tilde{p}_i| . \quad (3.13)$$

It follows that the real wave function is obtained by:

$$|\psi\rangle = |\tilde{\psi}\rangle + \sum_i (|\phi_i\rangle - |\tilde{\phi}_i\rangle) \langle \tilde{p}_i | \tilde{\psi} \rangle . \quad (3.14)$$

Accordingly, three quantities are involved in the determination of  $\hat{T}$ : the real partial waves  $|\phi_i\rangle$ , the auxiliary partial wave  $|\tilde{\phi}_i\rangle$  and the projector function  $|\tilde{p}_i\rangle$ . The real partial waves are the solutions of the radial SE for the isolated atom. The pseudo partial waves can be expanded into any basis set where Blöchl [92] used in his original paper the plane-waves basis set. The projector functions are also calculated firstly as radial functions multiplied by spherical harmonics then expanded into the same basis set as the pseudo-wavefunctions.

In fact, norm conserving and PAW potentials are pseudized and the accuracy of the DFT results within these two basis sets might depend on the chosen core states while the choice is not unique. Therefore, pseudopotential methods are usually benchmarked against all-electron DFT approaches which are considered to be a standard for DFT calculations [93]. Table 3.1 shows the accuracy of norm conserving (PAW) pseudo-potentials in two available libraries, against four public all-electron codes (FLEUR, WIEN2K, ELK and EXCITING). The produced errors with the PP method of FHI98pp/ABINIT is larger than 13 meV which could induce a large deviation for all calculated properties. However, the error is reduced to  $\approx 1.3$  meV with the new QUANTUM ESPRESSO (QE) interfaced library of NC, ONCVSP(SG12)1/QE. Even though, this error is still large compared to PAW potentials, it is minimized to 0.3 meV with the VASP library. Therefore, the VASP library of pseudo-potentials is used in all total energy calculations in this thesis. Owing to the simplicity of implementing the density functional perturbation theory with norm-conserving pseudopotentials, especially for vibrational spectroscopy calculations, the NC library, ONCVSP(SG12)1/QE, will be only used for the Infra-red calculations of BaTiO<sub>3</sub> in Chap. 5.

TABLE 3.1: Comparison between the accuracy of norm-conserving pseudopotential (NC) and Projector augmented wave methods (PAW) with all-electron method as implemented in four all-electron DFT codes, namely Fleur, Wien2k, Elk and Exciting. Two different libraries are used for each pseudopotential method: For NC PP, the FHI98pp/ABINIT and ONCVSP(SG12)1/QE are shown. The JTH02/ABINIT and VASPGW2015/VASP are shown for PAW potentials. The errors presented in the table are calculated for 71 elemental crystals and present the root-mean-square difference between the equilibrium lattice parameters and the bulk modulus calculated with all-electron and pseudopotential methods. The errors are in meV per atom. The table is adapted from [93]

	FLEUR [94]	WIEN2K [95]	ELK [96]	EXCITING [97]
NC (ABINIT)	13.2	13.4	13.5	13.4
NC (QE)	1.3	1.3	1.4	1.3
PAW (ABINIT)	0.6	0.5	0.6	0.6
PAW (VASP)	0.6	0.3	0.4	0.4

### 3.2 Green's function method

A very successful all-electron approach was initially introduced by Korringa [25] and further developed by Kohn and Rostoker [26]. It becomes known since then as the Korringa-Kohn-Rostoker (KKR) method. Extensive studies were made after the publication of the Kohn-Rostoker paper to generalize the method to treat also finite clusters and periodic solids [98–101]. The success of the KKR method arises from its foundation on the versatile and powerful theory of multiple scattering. This latter uses the Green's function (GF) as key quantity [102, 103]. Within the GF, the eigenvalue problem in Eq. (3.1) to solve the KS equation is replaced by solving a differential equation with an energy dependent GF as:

$$(z - \hat{H})\mathcal{G}(z) = \mathbb{1}, \quad (3.15)$$

where the  $\mathbb{1}$  is the identity operator and  $z$  are the complex energies with the form  $z = E + i\eta$ . The positive infinitesimal number  $\eta$  is introduced here for mathematical and numerical purposes. Equation (3.15) hints that the poles of  $\mathcal{G}(z)$  are the eigenvalues of  $\hat{H}$ . Therefore determining the poles of  $\mathcal{G}(z)$  gives the solutions of  $H$ .

Since the operator  $\hat{H}$  is Hermitian, all of its eigenvalues are real. This implies that Eq. (3.15) is not well defined on the real axis but is satisfied only for  $z$  values away from real axis [104]. This means that  $\mathcal{G}(z)$  is an analytic function in the complex plane and can be evaluated by a complex energy contour integration. In fact the GF representation is also related to the electronic density, which is the key quantity of DFT as discussed in Chap. 2. The connection between the two quantities is established by

$$\rho(\mathbf{r}) = -\frac{1}{\pi} \int dE \Im \mathcal{G}(\mathbf{r}, \mathbf{r}, E), \quad (3.16)$$

where  $\Im \mathcal{G}$  describes the imaginary part of the GF. Once the electronic density is obtained, all related formulations, which are shown in Chap. 2 can be rewritten in terms of the GF. The importance of using the GF approach becomes more clear in cases where the wavefunctions are not very helpful, like in disordered systems or if a huge number of atoms has to be considered as in defective systems as will be shown later.



### 3.2.1 Dyson equation

Despite the great usefulness of the GF method, its direct evaluation is still complicated because of the still unknown  $\mathcal{G}$ . A practical way to solve Eq. (3.15) relies on finding a proper relation of the unknown  $\mathcal{G}$  to an already known and easy to calculate GF. Based on the fact that any Hamiltonian can be decomposed into:

$$\hat{H} = \hat{H}_0 + \Delta V, \quad (3.17)$$

where  $\hat{H}_0$  is the free-particle Hamiltonian ( $\hat{H}_0 = -\nabla^2$ ) taken as the kinetic energy operator.  $\Delta V$  is a perturbation added to the initial free-particle Hamiltonian. Therefore the GF of the unperturbed system is given by

$$\mathcal{G}_0(z)^{-1} = (z - \hat{H}_0). \quad (3.18)$$

It is also called the free particle propagator. The perturbed GF is defined as well as

$$\mathcal{G}(z)^{-1} = (z - (\hat{H}_0 + \Delta V)). \quad (3.19)$$

Inverting Eq. (3.19) and multiplying by  $\mathcal{G}_0$  leads to:

$$\mathcal{G}(z) = \mathcal{G}_0(z) + \mathcal{G}_0(z)\Delta V\mathcal{G}(z). \quad (3.20)$$

Eq. (3.20) is the so-called Dyson equation for  $\mathcal{G}$  [105]. It can be solved by replacing  $\mathcal{G}(z)$  in the right hand side of Eq. (3.20) and make successive iterations:

$$\begin{aligned} \mathcal{G}(z) &= \mathcal{G}_0(z) + \mathcal{G}_0(z)\Delta V [\mathcal{G}_0(z) + \mathcal{G}_0(z)\Delta V\mathcal{G}(z)] \\ &= \mathcal{G}_0(z) + \mathcal{G}_0(z)\Delta V [\mathcal{G}_0(z) + \mathcal{G}_0(z)\Delta V(\mathcal{G}_0(z) + \mathcal{G}_0(z)\Delta V(\dots))] . \end{aligned} \quad (3.21)$$

This infinite series, called also Born series, of GFs expansion can be interpreted as a series of scattering events. The first term in the right-hand side of Eq. (3.21) represents the contribution of the free particle, the second term shows the contribution of a single scattering process. The third term shows as well the contribution of a two-fold scattering process and so on and so forth. The expression of Dyson equation becomes more compact by defining the series of scattering events as scattering matrix operator  $\hat{T}$ . Thus Eq. (3.21) transforms into

$$\mathcal{G}(z) = \mathcal{G}_0(z) + \mathcal{G}_0(z)\hat{T}\mathcal{G}_0(z). \quad (3.22)$$

Similarly to Eq. (3.22), the wavefunctions of the perturbed and unperturbed system can be related by means of the so-called Lippmann-Schwinger equation [106]:

$$\phi = \phi_0 + \mathcal{G}_0(z)\hat{V}\phi. \quad (3.23)$$

This equation is an efficient way to determine the wavefunction  $\phi$  for any potential  $\hat{V}$  only from the wavefunction  $\phi_0$  of the free particle system.

### 3.2.2 Single-site scattering

As already shown in Eq. (3.22), the GF can be obtained once a reference system GF is known. Thus, the single-site GF (defined with a single scattering) will be related in the following to the one of free space. Assuming now a spherical atomic potential embedded in free space implies that the reference system is the GF for one electron in free space, which reads:

$$\mathcal{G}_0(\mathbf{r}, \mathbf{r}', E) = -\frac{1}{4\pi} \frac{\exp(-i\sqrt{E}|\mathbf{r} - \mathbf{r}'|)}{|\mathbf{r} - \mathbf{r}'|}, \quad (3.24)$$

with  $\sqrt{E} = k$ . In order to deal with the GF in Eq. (3.24), an expansion of its constituting terms has to be made in an appropriate representation. One of the most useful expansions of the GF in the framework of scattering is the angular momentum representation. With this expansion, the plane wave,  $\exp(i\mathbf{k}\mathbf{r})$ , is expanded in spherical harmonics:

$$\exp(i\mathbf{k}\mathbf{r}) = 4\pi \sum_L (i)^l j_l(\sqrt{E}r) Y_L(\hat{\mathbf{r}}) Y_L(\hat{\mathbf{k}}). \quad (3.25)$$

The sum here runs over all possible values of  $L$ , where the combined index  $L$  carry the orbital quantum number  $l$  and the magnetic quantum number  $m$ .  $j_l$  is the spherical Bessel function,  $Y_L$  are the spherical harmonics. By means of the expansion in Eq. (3.25), the GF in Eq. (3.24) transforms into

$$\mathcal{G}_0(\mathbf{r}, \mathbf{r}', E) = \sum_L Y_L(\hat{\mathbf{r}}) g_l(r, r', E) Y_L^*(\hat{\mathbf{r}}'), \quad (3.26)$$

where  $g_l$  are the expansion coefficients. They are given by

$$g_l(r, r', E) = -i\sqrt{E} j_l(\sqrt{E}r_<) h_l(\sqrt{E}r_>), \text{ where } \begin{cases} r_< = \min(r, r') \\ r_> = \max(r, r') \end{cases}. \quad (3.27)$$

The new function  $h_l$  is the spherical Hankel function defined by  $h_l = j_l + in_l$ , where  $n_l$  is the spherical Neumann function. The radius  $r_<$  ( $r_>$ ) is the smallest (largest) value of  $r$  and  $r'$ . This distinction is made because Hankel and also Neumann functions diverge as  $r \rightarrow 0$ .

The GF in Eq. (3.26) corresponds to the free system where the Hamiltonian is defined only by the kinetic energy. However, the potential in the KKR method is divided into distinct scattering regions. The simplest construction of these regions was done with the Muffin-tin approximation (MTA) [107]. In this approximation, the system is divided into non overlapping spheres (see Fig. 3.2). The basic idea consists of considering the potential as spherically symmetric inside the spheres and constant in the interstitial regions between the spheres. This method was found very successful for metallic close-packed systems. Another and a more efficient way is called the atomic sphere approximation (ASA) [108]. It stems from blowing up the atomic (Muffin-tin) spheres to fill up the entire crystal volume. This approximation is used successfully in the linear muffin-tin orbital method. It might be necessary with some crystal structures to add some empty spheres with an atomic charge  $Z = 0$  to have the volumes of the spheres match the cell volume. It might be also possible to have a minimum overlap between the spheres contrarily to the Muffin-tin approximation. The main idea behind this space separation into distinct regions (single sites) is to have a local and separate GF for each region. Each of these GFs can be solved independently and its solutions can be connected later to others.

Consider now, for sake of simplicity, a spherical potential  $V(\mathbf{r})$  inside the region  $n$  defined by the radius  $r_{\text{MT}}$ , beyond that region the potential vanishes:

$$V(\mathbf{r}) = \begin{cases} V(r) & \text{if } r \leq r_{\text{MT}} \\ 0 & \text{if } r > r_{\text{MT}} \end{cases}. \quad (3.28)$$

The eigenfunctions are therefore determined by

$$\left[ E - \hat{H}_0 - V(\mathbf{r}) \right] \phi(\mathbf{r}) = 0. \quad (3.29)$$

Because of the spherical symmetry of the potential, the wavefunction can be separated into an angular and a radial contribution, i. e.  $\phi(\mathbf{r}, E) = Y_L(\hat{\mathbf{r}})R_l(\mathbf{r}, E)$ , where the  $R_l$  are the radial wavefunctions which satisfy the radial SE. This latter leads to two linearly independent solutions: a regular one which converges at  $r \rightarrow 0$  and an irregular solution which diverges at  $r \rightarrow 0$ .

For  $r > r_{\text{MT}}$ , the regular solution can be obtained by using the asymptotic behavior of the Bessel functions (at  $r \rightarrow \infty$ ) and the Lippmann-Schwinger equation (Eq. (3.23)) [109]:

$$R_l(r, E) = j_l(\sqrt{E}r) - i\sqrt{E}h_l(\sqrt{E}r)t_l(E), \quad (3.30)$$

where the single-scattering  $t$ -matrix is given by [109] :

$$t_l(E) = \int_0^{r_{\text{MT}}} dr r^2 j_l(\sqrt{E}r)V(r)R_l(r, E), \quad (3.31)$$

it represents the scattering strength on a single-site potential  $V(r)$  and ensures the matching of the radial KS equation solutions at the boundary  $r = r_{\text{MT}}$  [110]. The  $t$ -matrix is as well related to the phase shift for an incoming wave which is scattered by the potential. They are related by:  $t_l(E) = -\sin(\delta_l(E)) / \sqrt{E} \exp(i\delta_l(E))$ .

On the other hand, an outward numerical integration of the radial SE in the region from 0 to  $r_{\text{MT}}$  gives  $R_l(r, E)$  where the boundary condition at  $r_{\text{MT}}$  is ensured by the  $t$ -matrix. As well, an inward integration of the radial KS from  $r_{\text{MT}}$  to 0 yields to the divergence of the irregular solution  $H_l$  which fixes the second boundary condition for  $r > r_{\text{MT}}$  [111]:

$$H_l(r, E) = h_l(\sqrt{E}r). \quad (3.32)$$

The corresponding single site GF  $\mathcal{G}^S$  can be then written, in analogy with the free-electron GF in Eq. (3.26) [110], as the product of the two solutions [112]:

$$\mathcal{G}^S(\mathbf{r}, \mathbf{r}', E) = \sum_L Y_L(\hat{\mathbf{r}})g_l^S(r, r', E)Y_L(\hat{\mathbf{r}}'), \quad (3.33)$$

$$= \sum_L Y_L(\hat{\mathbf{r}}) \left[ -i\sqrt{E} R_L(r_<, E)H_L(r_>, E) \right] Y_L(\hat{\mathbf{r}}'). \quad (3.34)$$

### 3.2.3 Multiple scattering theory

The single scattering event discussed so far describes only the scattering of one particle in an empty space by a single potential. Such situation does not occur in solids where more than one scattering potential exist. The best framework to extend the previous development is the multiple scattering theory. This latter is the method of choice when dealing with disordered alloys, impurities in crystals or even with surfaces without requiring any construction of supercells.

For a proper description of the multiple scattering theory and the related equations, it is more convenient to divide the space into connected cells as shown in figure 3.2. Each of the cells is identified by an index  $n$  and its center is connected to the universal origin by a vector  $\mathbf{R}_n$ . Any point inside the cell is denoted by the relative and absolute vectors  $\mathbf{r}_n$  and  $\mathbf{r}_n^a$ , respectively. Therefore the absolute vector  $\mathbf{r}_n^a$  is given by  $\mathbf{r}_n^a = \mathbf{R}_n + \mathbf{r}_n$ . Since the two points  $\mathbf{r}_n$  and  $\mathbf{r}_m$  belong to two

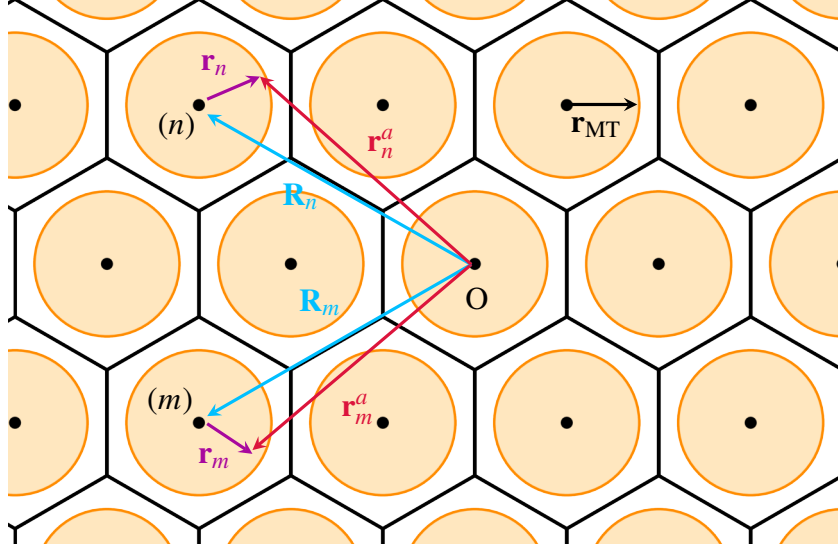


FIGURE 3.2: Illustration of the space division into adjacent cells arranged in a periodic lattice. The spheres inside each cell denote the muffin tin spheres within the Muffin-tin approximation (assuming here a mono-atomic system for the sake of simplicity). The absolute origin of the space coordinates is denoted by  $O$ . The relative vectors inside the cells or scatterers  $n$  and  $m$  are  $\mathbf{r}_n$  and  $\mathbf{r}_m$ , respectively. The lattice vectors to the cells  $n$  ( $m$ ) are expressed as  $\mathbf{R}_n$  ( $\mathbf{R}_m$ ). The absolute vectors are then defined as  $\mathbf{r}_n^a = \mathbf{R}_n + \mathbf{r}_n$  and  $\mathbf{r}_m^a = \mathbf{R}_m + \mathbf{r}_m$ .

different cells, as shown in Fig. 3.2, the free-electron GF has to be rewritten in such a way that the Bessel functions are centered around the two different sites,  $\mathbf{r}_n$  and  $\mathbf{r}_m$ . Furthermore, the Hankel functions are expanded as well by using the addition theorem [113]. This leads to:

$$\mathcal{G}_0(\mathbf{r}_n^a, \mathbf{r}_m^a, E) = \sum_{LL'} J_L(\mathbf{r}_n, E) g_{LL'}^{nm}(E) J_{L'}(\mathbf{r}_m, E), \quad (3.35)$$

where  $J_L(\mathbf{r}, E) = j_l(\sqrt{E}r)Y_L(\hat{\mathbf{r}})$ . The coefficients  $g_{LL'}^{nm}(E)$  are the free-electron structural constants, which only depend on the lattice structure. They are given by

$$g_{LL'}^{nm}(E) = 4\pi\sqrt{E}(\delta_{nm} - 1) \sum_{L''} i^{l-l'-l''} C_{LL'L''} H_{L''}(\mathbf{R}_m - \mathbf{R}_n, E), \quad (3.36)$$

where  $C_{LL'L''}$  are the Gaunt coefficients defined by an integral over the product of three real spherical harmonics. The delta function in the last equation is very important because it decouples the single scattering GF, manifested by  $n = m$ , from the multiple scattering properties. This establishes one of the main advantages of using the KKR method [109]. Similarly, the free-electron GF in Eq. (3.35) can be as well decomposed into a single-site GF and multiple scattering contributions:

$$\mathcal{G}_0(\mathbf{r}_n^a, \mathbf{r}_m^a, E) = \delta_{nm} \mathcal{G}_S(\mathbf{r}_n, \mathbf{r}_m, E) + \sum_{LL'} J_L(\mathbf{r}_n, E) g_{LL'}^{nm}(E) J_{L'}(\mathbf{r}_m, E). \quad (3.37)$$

Consider now that the system's potential is coming from all the scattering centers, defined so far within the cells  $n$ . The total potential  $V$  is then the linear superposition of all individual cell potentials [114]:

$$V = \sum_n V^n \quad (3.38)$$

The corresponding GF can be obtained with analogy to Eq. (3.37) as [115]:

$$\mathcal{G}(\mathbf{r}_n^a, \mathbf{r}_m^a, E) = \delta_{nm} \mathcal{G}_S(\mathbf{r}_n, \mathbf{r}_m, E) + \sum_{LL'} R_L^n(\mathbf{r}_n, E) G_{LL'}^{mm}(E) R_{L'}^m(\mathbf{r}_m, E), \quad (3.39)$$

where  $G_{LL'}^{mm}$  are the structural GF in the presence of finite potential. They can be calculated using the so-called structural Dyson equation [116]:

$$G_{LL'}^{mm}(E) = g_{LL'}^{nm}(E) + \sum_{pL''L'''} g_{LL''}^{np}(E) t_{LL''}^p G_{L''L'''}^{pm}(E). \quad (3.40)$$

This equation is of a great importance and remains valid with little improvements for crystal impurities treatment as will be show later with the coherent potential approximation. Note that the summation in the GF and the structural GF expressions are over an infinite number of angular momenta. Based on the fact that the GF vanishes with large  $L$  values, the summation can be cut up to a cut-off momentum  $\approx (2l_{\max} + 1)^2$ . Such value is still rather small even for  $f$  systems [109, 115].

Besides the GF, a full description of the scattering properties of the system can be obtained with the so-called scattering path operator [117, 118]. It can be as well decomposed in terms that describe all possible scattering events which can occur for an electron propagating from the cell  $n$  to the cell  $m$  [117, 118]:

$$\hat{T}(E) = \sum_{nm} \tau^{nm}(E), \quad (3.41)$$

where  $\hat{T}$  is the scattering matrix operator shown in Eq. (3.22).  $\tau^{nm}$  is the scattering path operator accounting for all possible scattering events, which may take place in between the two sites  $n$  and  $m$ . Like other operators,  $\tau^{nm}$  satisfies the Dyson equation:

$$\tau^{nm}(E) = t^n(E) \delta_{nm} + t^m(E) \sum_{p \neq n} \tau^{np}(E) \mathcal{G}_0(\mathbf{r}_n^a, \mathbf{r}_p^a, E). \quad (3.42)$$

**Equation. (3.42)** demonstrates the main essence of the KKR method: the decoupling of the crystal geometry (structural GF) and chemical species ( associated with the scattering events). The crystal geometry is stored in  $\mathcal{G}_0(\mathbf{r}_n^a, \mathbf{r}_p^a, E)$  Eq. (3.39) while the single and multiple scattering are described by  $t^n(E)$  and  $\tau^{np}(E)$ , respectively. In addition, Eq. (3.42) establishes a practical way to calculate the properties of alloyed systems in framework of coherent potential approximation as will be shown later. The main advantage is that only the calculation of the scattering path operator is needed while the structural GF and consequently the GF are taken from the parent system GF as the crystal structure is assumed to be the same as the parent crystal structure.

Besides the simple MT approximation of the potential, there are also other approximations as already discussed. Fig. 3.3 shows the calculated density of states of MgO with three different treatments of the potential within the KKR method. They are the muffin-tin approximation, the atomic sphere approximation and the full potential approximation. This latter assumes an arbitrarily shaped potential defined by a shape function [119]. The results are also compared to the experimental valence band photoemission spectra [120]. In overall, a good agreement is found for the three considered potential approximations with the experimental spectra.

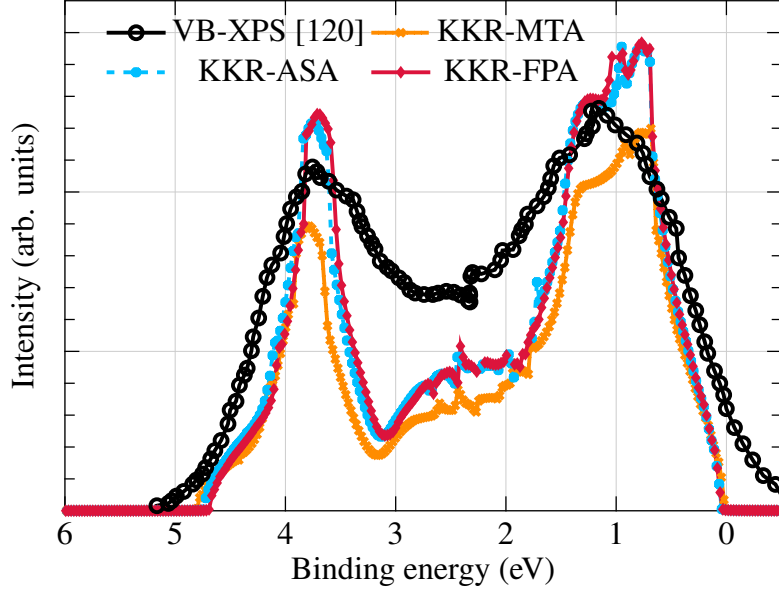


FIGURE 3.3: A comparison between the calculated density of states of MgO with the experimental valence band photoemission spectra [120] (black line with open circles). Three different treatments of the potential within the KKR method are considered here, namely the ASA approximation (dashed blue line), MTA approximation (orange line) and full potential approximation (red line).

### 3.3 Disorder in crystal structures

The simplest method to deal with disordered systems is the virtual crystal approximation [121]. This approximation could be used in both plane-wave and KKR-GF methods. It is mostly used in substitutional alloy studies. The method is based on concentration-weighted average of all the potentials forming the alloy and restricting the calculation to the unit cell. Therefore a virtual atom is produced with a potential constructed from the potentials of all species  $i$  in the alloy:

$$V_{vca} = \sum_i c_i V_i, \quad \text{where } 0 \leq c_i \leq 1. \quad (3.43)$$

Here  $c_i$  presents the concentration of each species in the substitutional alloy system. This method yields quite reasonable results for alloys with similar potentials [122], but breaks down in averaging completely different potentials like substituting a transition metal or rare earth element by  $s,p$ -elements due to their different electronic localization.

#### 3.3.1 Coherent potential approximation

The KKR-GF method presents one of the most promising methods to describe all kinds of crystal imperfections including doping and point defects. The first attempt to describe disorder in the KKR framework was due to the average  $t$ -matrix approximation (ATA) [123, 124], which has the previously described method of VCA as roots. The Dyson equation of the configurational average of the GF is given by

$$\langle \mathcal{G} \rangle = \mathcal{G}_0 + \mathcal{G}_0 \langle T \rangle \mathcal{G}_0. \quad (3.44)$$

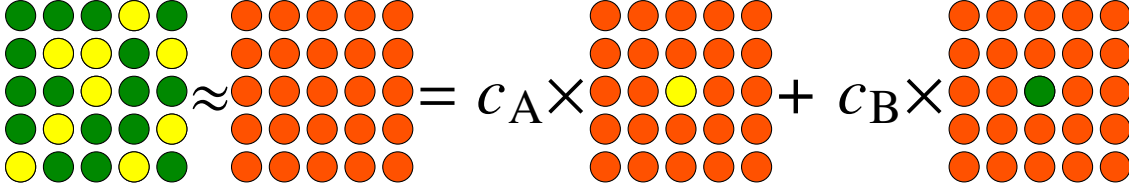


FIGURE 3.4: Schematic illustration of the coherent potential approximation condition for a binary alloy  $A_{1-c}B_c$ . The disordered system in the left panel is approximated as ordered set of effective scatterers placed at each of the crystal lattice sites. A coherent potential function is then used for each of the scatterers.

By considering the system potential as the sum of all individual site contributions, the configurational average of the  $t$ -matrix presented in Eq. (3.44) can be obtained as

$$\langle T_{ij} \rangle = \langle t_i \rangle \delta_{ij} + \langle t_i \rangle \sum_{k \neq i} \mathcal{G}_0^{ik} \langle T_{kj} \rangle, \quad (3.45)$$

where the average of the site  $t$ -matrix is the configurational average of the  $t$ -matrices of the pure materials:

$$\langle t_i \rangle = \sum_i c_i t_i. \quad (3.46)$$

This method provides good results at low concentrations which is the case for example for point defects. At higher concentrations, the correlation effects between different sites become more important and so does the inter-site scattering. This leads to unreliable results with the ATA [114].

Another mean field theory method is the coherent potential approximation (CPA) [27, 28]. It is also based on the multiple scattering theory and follows up the formulation of ATA method. The CPA method is considered by far as one of the best available mean field theories to tackle the electronic structure of random substitutional alloys. The idea is to suppose that the entire system is an auxiliary medium as illustrated in Fig. 3.4 and characterized by the single  $t$ -matrix  $t_c$ . The construction of this effective medium is made in such a way that the additional scattering coming from the real individual potential of  $\alpha$  (A or B in Fig. 3.4) should vanish on the average, i. e.  $\langle t_\alpha \rangle = 0$ . The situation is at some extent similar to the concept of a single impurity embedded in a perfect host lattice discussed earlier in the works of Lifshitz [125] and further developed in [116, 126–128]. Irrespective of the universality of the CPA method for multi-component alloys, the focus will be in the following on binary alloys for the reason of simplicity. Afterwards the concept could be easily generalized.

Consider for instance the simplest example; a real space lattice containing only one atom per unit cell (like fcc and bcc lattices). This atom could be either an element A or B in the binary substitutional alloy of the formula  $A_{1-c}B_c$ , see Fig. 3.4. All possible configurations of this alloy

have to be implicitly taken into account in the CPA medium. This can be realized by calculating the average of the total scattering [129] :

$$\begin{aligned}
 \langle T(E) \rangle &= \sum_n \langle T^n(E) \rangle \\
 &= \sum_n \langle t^n(E) \rangle \left[ 1 + \mathcal{G}_0(E) \sum_{m \neq n} \langle T^m(E) \rangle \right] \\
 &\quad + \left\langle [t^n(E) - \langle t^n(E) \rangle] \mathcal{G}_0(E) \sum_{m \neq n} [T^m(E) - \langle T^m(E) \rangle] \right\rangle.
 \end{aligned} \tag{3.47}$$

The first term in Eq. (3.47) consists only of single-site terms, which is not the case for the second term. The later describes any sort of fluctuation or correlation resulting for example from the short-range order effects [130]. It is also a complicated term to evaluate. Neglecting it and restricting Eq. (3.47) only to the first term is the reason behind referring the method as the single-site approximation of CPA.

By adapting the single-site approximation of the CPA ( $n = m$ ) and using the origin cell (noted here as 0, i. e.  $\mathbf{r}_n = \mathbf{r}_0$ ), the indices ( $n, m$ ) in all previous equations transform simply into (0, 0). The scattering path operator in Eq. (3.42) is therefore simplified by using the translational symmetry and lattice Fourier transformations of the GF [130] at the unit cell origin as:

$$\tau_c^{00} = \Omega_{\text{BZ}}^{-1} \int_{\text{BZ}} d\mathbf{k} [(t_c(E))^{-1} - \mathcal{G}_0(\mathbf{k}, E)]^{-1}. \tag{3.48}$$

Employing now the restricted ensemble averages, which is described in [114] leads to:

$$\langle \tau_c^{00}(E) \rangle_{0=\alpha} \equiv \tau_\alpha^{00}(E), \tag{3.49}$$

where the right-hand side is given by

$$\tau_\alpha^{00}(E) = [1 + \tau_c^{00}(E)(t_\alpha^{-1}(E) - t_c^{-1}(E))]^{-1} \tau_c^{00}(E). \tag{3.50}$$

Then the CPA condition, or KKR-CPA equation, in the binary alloy within the single-site approximation reads:

$$\tau_c^{00}(E) = c\tau_A^{00}(E) + (1 - c)\tau_B^{00}(E). \tag{3.51}$$

Since the  $t_c$ -matrix is unknown, an initial guess has to be made for its self consistent determination through Eq. (3.51). A good initial value could be of course the ATA  $t$ -matrix. For the generalization of the KKR-CPA equation for complex lattices (more than one sub-lattices, e. g. ABO<sub>3</sub> perovskite oxides), it is more convenient to adapt the super-matrix notation. Therewith sub-lattices are expressed in terms of rows and columns. As example, the CPA single site  $t$ -matrix has the form:

$$t_c^{-1}(E) = \begin{pmatrix} (t_c^n(E))^{-1} & 0 & 0 \\ 0 & (t_B^m(E))^{-1} & 0 \\ 0 & 0 & (t_O^p(E))^{-1} \end{pmatrix}, \tag{3.52}$$

where the site A is disordered like in the alloy system Gd<sub>1-c</sub>Ca<sub>c</sub>MnO<sub>3</sub> (see Chap. 6). B and O are ordered sub-lattices.



### 3.3.2 Special quasi-random structures

Another approach to model disordered systems was pioneered by Zunger *et al.* [29] and called the special quasi-random structure (SQS) approach. It is a way to mimic as much as possible the disorder in crystal structure with a moderate size of supercell. Besides, the correlations between different sites have to converge towards those of a completely random distribution. Thus it is called a quasi-random structure. Actually, getting a perfectly disordered system needs the employment of large computational resources and becomes in some cases unfeasible. Therefore the terminology of the best SQS candidate is used here for the determined SQS structures. To get more insight into the theory, one needs to discuss briefly the generalized cluster expansion Method (CE) for multi-component systems [131, 132] where the SQS derives its roots. This CE method was designed for a rigorous consideration of binary, ternary and multi-component alloy systems in the plane-wave framework.

Consider a  $M$ -component alloy with  $N$  different sites. Each site  $i$  is characterized after the Ising lattice model [133] by an occupation number  $\sigma_i$ , where  $\sigma_i = (\pm m, \pm(m-1), \dots, \pm 1)$  and  $M = 2m$ . For example in the binary alloy  $A_{1-c}B_c$ ,  $M = 2$  (two species) and  $m$  can be either  $+1$  or  $-1$ . This means a site  $i$  can be either occupied by A ( $\sigma = +1$ ) or B ( $\sigma = -1$ ). The overall arrangement of ions on the crystalline system is called configuration, see Fig. 3.5, and is denoted by the  $N$ -dimensional vector  $\sigma$ :

$$\sigma = (\sigma_1, \sigma_2, \dots, \sigma_N). \quad (3.53)$$

This vector stores the occupation of each of the  $N$  sites. Undoubtedly, the discussion of cluster expansion method cannot be made without defining its main ingredient. A cluster  $\alpha$  is a set of sites within a configuration. It can be a single site (ignored here) or formed by two sites, called pair cluster. It can be also a triplet (with 3 sites), quadruplet (connecting 4 sites) and even larger. An illustration of the most common clusters are given in Fig. 3.5. Each of them can connect nearest-neighbor sites and also neighbors from distant shells. In addition, each cluster can be described by a cluster function  $\gamma_\alpha$ , which corresponds to the product of all occupation numbers  $\sigma_i$  presented in the cluster:

$$\gamma_\alpha(\sigma) = \prod_{i \in \alpha} \sigma_i(\sigma). \quad (3.54)$$

Owing to the enormous number of different kinds and sizes of clusters, which can be present in real systems, a direct description of the disordered lattice with single clusters transforms to a cumbersome task. To ease the handling and the understanding of the following equations, it is more convenient to discretize each alloy configuration, denoted previously by  $\sigma$ , into its components, called "figures". A figure  $f = (k, m)$  is defined by the number  $k$  of atoms located on the cluster vertices and the order  $m$  of neighboring shells separating the atoms on the vertices. As example, the figure  $f = (3, 2)$  corresponds to a triplet cluster built from an atom and its two second-nearest neighbors. In addition, the location and the orientation of each figure in the lattice is specified by the vector  $l$ . It is also obvious that all sites contribute to more than one equivalent figure, i. e. same cluster type and same neighboring shell. This multiplicity is denoted by  $D_f$ . Similarly to clusters (Eq. (3.54)), a figure function  $\gamma_f(l, \sigma)$  can be also assigned to each figure. Within all these definitions, a lattice average over all possible locations  $l$  of a figure  $f$  in the lattice can be written as

$$\bar{\Gamma}_f(\sigma) = \frac{1}{ND_f} \sum_l \gamma_f(l, \sigma). \quad (3.55)$$

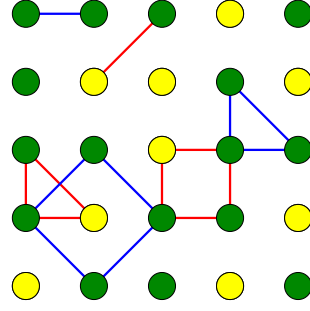


FIGURE 3.5: Different kinds of clusters in a binary disordered alloy: Pair clusters linking two sites, triplet connecting three sites and quadruplet connecting 4 sites. The corresponding clusters functions are displayed by the red lines for ( $\gamma = -1$ ) and blue lines for ( $\gamma = +1$ ).

Consequently, any measurable physical property  $\mathcal{P}$  can be expanded into:

$$\mathcal{P}(\sigma) = N \sum_f D_f \bar{T}_f(\sigma) p_f, \quad (3.56)$$

where  $p_f$  denotes the contribution of the figure  $f$  to the physical property  $\mathcal{P}$ . This equation shows the cluster expansion of the property  $\mathcal{P}$  into figure contributions and the expansion coefficients  $p_f$  are generally referred to as the effective cluster interactions. These coefficients have the space group symmetry of the crystal and are independent of  $l$ . Accordingly, the ensemble average of  $\mathcal{P}$  is given by:

$$\langle \mathcal{P} \rangle = \sum_f D_f \langle \bar{T}_f \rangle p_f. \quad (3.57)$$

The averaged  $\langle \bar{T}_f \rangle$  functions are the correlation functions, which are already known in a perfectly random alloy ( $R$ ), e. g. for the binary alloy  $A_{1-c}B_c$ ,  $\langle \bar{T}_f \rangle_R = (2c - 1)^k$ . Hence  $\langle \bar{T}_f \rangle_R$  vanishes with  $c = 1/2$  for each figure having  $k \neq 0$ .

The standard approach for evaluating Eq. (3.57) for a binary alloy is to assume that each lattice site is individually and randomly occupied by A or B. By statistical sampling, a representative structure is chosen in a way that its correlation functions approach those of a random distribution. This might need an averaging over a large number of supercells and configurations. The standard deviation from randomness is measured through calculating  $\eta_f(N) = |\langle \bar{T}_f^2 \rangle|^{1/2}$ . It might be also possible that even getting  $\eta_f(N) = 0$  is not enough for a complete randomness because the variance on the average is not necessarily zero. This means that the selected structure at random from the averaged ensemble might contain errors shown by the variance deviation.

The method proposed by Zunger *et al.* consists of designing only one single special periodic structure  $S$ . The correlation functions for  $S$  must match as much as possible those of a random alloy  $R$  in a way that:

$$\langle \mathcal{P} \rangle_R - \mathcal{P}_S = \sum_{k>1,m} D_{k,m} \left[ (2c - 1)^k - \bar{T}_{k,m}(S) \right] p_{k,m}. \quad (3.58)$$

Indeed, any physical property  $\mathcal{P}$  of disordered systems depends mainly on the local environment. Beyond that region, the contributions  $p_{k,m}$  are expected to vanish exponentially. Therefore, Eq. (3.58) can be truncated to take into account a limited number of figures. It is obvious that figures involving first and second neighboring sites are the most important ones. Therefore Eq. (3.58) is minimized hierarchically following Zunger's idea. The most important correlation functions have to match firstly those of the random alloy. Thereafter the best match for the remaining functions with their random counterparts is sought. Many investigations of disordered systems by means of the SQS method have considered only pair correlation functions, i. e. only  $\bar{T}_{2,m}(S)$  are calculated. Those pair correlations were proven [29, 134], with a rather small supercell containing 8 atoms, to be more than enough to describe binary semiconductor alloys. However this size might lead to wrong results for other lattice types and larger cells have to be used. This limits the error of the SQS method to only the extend of the considered correlation functions and the size ( $N$ ) of the supercell. These two criteria can be easily checked with first principles calculations. But nevertheless some physical properties would require at the same time both large supercell and number of correlation functions. Thus the task turns into a computationally intractable problem. Based on the quotient group, a group theoretical concept, associated with each derivative superstructure from the parent lattice, Hart *et al.* [135] developed an efficient algorithm to enumerate all possible unique derived structures. This was promoted later by involving a stochastic Monte-Carlo approach by Van de Walle *et al.* [30]. The lookup for the best SQS supercell in its original idea, as previously shown, is based on the perfect match between SQS candidate and random correlation functions for a set of pre-specified functions. This criterion was moderately adjusted in Van de Walle's idea for computational purposes. The best desired SQS candidate is then the one, which has the maximum match between the correlation functions. Also, a single parameter to estimate the deviation from randomness is introduced for a quick check of the SQS quality instead of checking deviations of each individual correlation function. This was achieved by introducing the objective function as:

$$Q = -\omega L + \sum_{f \in A} |\Delta \bar{T}_f|, \quad (3.59)$$

where the importance of pair correlations is stressed out by specifying the distance  $L$ . Inside  $L$ , all pair correlation functions must match those of a random alloy.  $\omega$  is a weight function. Moreover, the summation over figures is truncated to consider only the pre-defined set  $A$ . The individual deviations of correlation functions are measured by  $\Delta \bar{T}_f$ .

The objective function in Eq. (3.59) is then calculated for all enumerated supercells with a pre-defined size. Each of the supercells has a distinct configuration. Afterwards, only that with best (more negative value) objective function is identified and kept for the next sampling. Subsequently, this objective function is used in a Monte-Carlo simulated annealing loop with a probability proportional to  $e^{-Q/T}$  for each configuration. The temperature  $T$  is only fictitious here. The new objective function is checked after each loop with its predecessor and only the best corresponding structure is kept. The best SQS is accordingly decided.

As example of application, the SQS method is used here for the solid solution of  $\text{Mg}_x\text{Zn}_{1-x}\text{O}$  and compared to the results of the CPA method. A concentration of  $x = 0.75$  was chosen with the equilibrium volume of the rock-salt phase [136]. Thus, the SQS structure is constructed with a supercell of 64 atoms (32 times larger than the unit cell) as shown in Fig. 3.6. In order to sufficiently mimic the correlation functions of a random distribution of Mg and Zn inside the supercell, three kinds of clusters are considered, i. e. pair, triplet and quadruplet clusters. Those clusters characterize

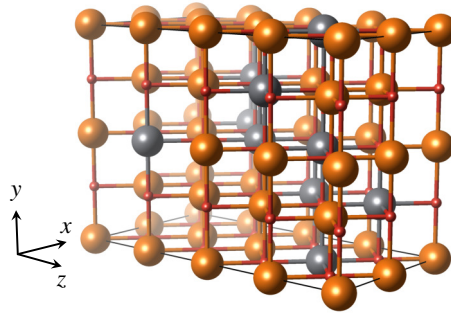


FIGURE 3.6: The best SQS candidate to model the solid solution of  $\text{Mg}_{0.75}\text{Zn}_{0.25}\text{O}$  in the rock-salt phase. The SQS distribution is shown by the arrangement of Zn atoms (gray balls) and Mg atoms (orange balls). The oxygen atoms are presented with the red balls.

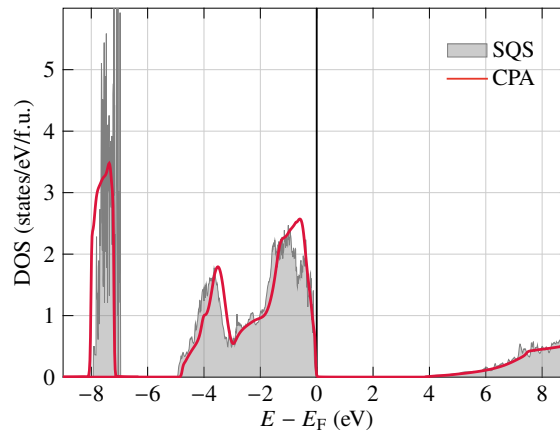


FIGURE 3.7: Comparison of the density of states of the solid solution of  $\text{Mg}_{0.75}\text{Zn}_{0.25}\text{O}$ , calculated with SQS method (filled gray areas) and with the CPA (red line). The zero energy corresponds to the Fermi energy.

the interactions between two, three and four sites (Mg, Zn) respectively. The pair clusters are taken into account up to the seventh nearest neighbors, while the triplet and quadruplet clusters are only considered up to the third and first nearest neighbors, respectively. In both compared methods, SQS and CPA, the same method of  $\text{LDA}+U$  was used for correlation corrections [67]. Note that the  $U$  values should not be necessarily the same in both methods because of its different implementations inside the DFT codes. It is quite common that the best  $U$  value, which fits the experimental data is smaller within the KKR method than VASP. The effective  $U$  values of 8 eV and 4 eV are used here for the VASP-SQS and KKR-CPA calculations, respectively. Figure 3.7 compares the density of states of the two methods where a good agreement of both calculations was obtained. This explains one more the strength of each method. On one hand, the CPA method does not require more than a unit cell but takes advantages of the GF at the cost of neglecting the structural relaxations. On the other hand the SQS method takes into account the structural relaxations but at the cost of using a large supercell. However, when the concentration is low, like in this case, both methods lead to similar results.

### 3.4 Magnetic exchange interactions

As magnetic properties of oxide materials triggered much of the efforts in development of devices and applications, these properties will be demonstrated in the following with a connection to the previous discussions. Actually, the establishment of modern theory of magnetism goes back to the concept of local magnetic moments [137–139]. These magnetic moments result from not fully occupied  $d$ - or  $f$ -shells. The understanding was initially based only on the classical point of view with the Langevin-Weiss theory [137, 138]. Wherewith, essential properties of ferromagnets were explained with molecular field interactions between atomic magnetic moments. This theory suffers from the underestimation of the magnetic dipole-dipole interactions by almost three orders of magnitude. This problem was cured later in the framework of quantum mechanics [140]. It is due to Heisenberg [141] that Langevin-Weiss theory is generalized with quantum mechanical consideration. The energy levels of the localized spins are expressed by first-order exchange coupling integrals  $J$  between each spin and its nearest neighbors. Besides the exchange couplings, a total "spin"  $S$  of the ion was defined. It depends mainly on the internal structure of the ion (oxidation state). This determines the number of participating (unpaired) electrons  $s_e$  and is expressed in half integer values multiplied by  $s_e$ , i. e.  $S = 1/2, 1, 3/2, 2, 5/2, 3, 7/2$ . While the lowest value corresponds to one  $t_{2g}$  electron in an octahedral environment and the largest to  $f$ -electrons in rare-earths. Therefore, a spin Hamiltonian is defined as:

$$\mathcal{H}_{\text{spin}} = -\frac{1}{2} \sum_{i \neq j} J_{ij} \mathbf{S}_i \cdot \mathbf{S}_j, \quad (3.60)$$

where  $(i, j)$  are pairs of magnetic sites.  $J_{ij}$  are the inter-site magnetic exchange interactions. A positive value of  $J_{ij}$  means that the two magnetic sites  $(i, j)$  are ferromagnetically coupled and a negative value signifies an antiferromagnetic coupling between the two sites.  $\mathbf{S}_i = S_i \mathbf{e}_i$ , where  $\mathbf{e}_i$  are the unit vectors pointing in the direction of the magnetic moment at the site  $i$ . These couplings are typically in the range of few meV. The spin moments  $S_i$  could be the same as  $S_j$  for systems with only one sort of magnetic lattice. In addition the product  $\mathbf{S}_i \cdot \mathbf{S}_j$  can be more simplified with collinear magnetic orders (spins are parallel), i. e. it is reduced to  $S_i \cdot S_j$  or simply to  $S^2$  for systems with one kind of magnetic sites. Note here that the model in Eq. (3.60) is just the classical version of the most general quantum Heisenberg model with a difference that  $\mathbf{S}_i$  is taken as the operator  $\hat{\mathbf{S}}_i$  instead.

For an accurate description of strongly correlated electrons, it might be necessary in some cases to extend Eq. (3.60) to take into account more complicated terms, e. g. single-ion anisotropy, anisotropic exchange interactions ( $\mathbf{S}_i \nparallel \mathbf{S}_j$  and  $J_{ij}$  are tensors), higher-order couplings such as the ring exchanges. For the sake of simplicity, these terms are neglected throughout the thesis.

The Heisenberg model parameters  $J_{ij}$  are unknown and have to be determined. Their experimental determination is made using magnetic exchange force spectroscopy [142–144], Infrared and Raman optical absorption, inelastic neutron scattering or x-ray magnetic circular dichroism [145]. The theoretical determination is based on first-principles calculations and will be demonstrated in the following within the framework of pseudopotential total energy calculations and the Korringa-Kohn-Rostoker method.

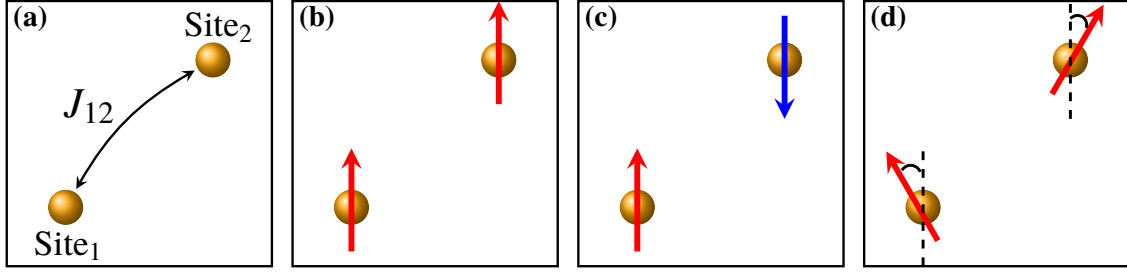


FIGURE 3.8: The two used methods to calculate the exchange interaction  $J_{12}$ , as shown in (a), for a simple system. (b) and (c) show the two needed magnetic configurations for the total energy mapping method, one ferromagnetic (b) and an antiferromagnetic configuration (c). On the other hand the idea of using the magnetic force theorem method is illustrated in (d), where the magnetic spin directions are rotated by an opposed angle of  $\theta/2$ .

### 3.4.1 Total energy differences

The method consists of mapping the total energy of different spin configurations [146–148] onto the Heisenberg Hamiltonian in Eq. (3.60). Consider a simple system of two magnetic sites called site<sub>1</sub> and site<sub>2</sub>. They interact through the exchange coupling  $J_{12}$ . Thus two magnetic configurations are needed to determine  $J_{12}$ . One with ferromagnetic coupling between the two sites, called *I* and a second called *II* with an antiferromagnetic coupling between the sites, see Fig. 3.8. The total energies can be written as

$$E_I = E_0 + J_{12}S^2, \quad (3.61)$$

$$E_{II} = E_0 - J_{12}S^2. \quad (3.62)$$

As a consequence,  $J_{12}$  is simply equal to  $(E_I - E_{II})/2S^2$ . The energy  $E_0$  is thereby a reference energy, which could be here the non-magnetic total energy. The same method applies to realistic systems where more than one unique exchange interaction occur. Each of the couplings is uniquely defined by the distance separating the pair of magnetic sites. Note here that the system symmetry plays an important role for a correct enumeration of the symmetrically equivalent exchange couplings. This allows to write the total energy of any magnetic configuration as

$$E_{\text{mag}} = E_0 + \frac{S^2}{2} \left[ \sum_{i \neq j} \sum_n N_n \sigma_i \sigma_j J_{ij} \right], \quad (3.63)$$

where  $n$  runs over the number of exchange interactions taken into account with Eq. (3.60) and belongs to the considered supercell.  $N$  is the multiplicity of each  $J_{ij}$  within the considered supercell. According to Heisenberg's assumption, just few interactions are needed. the occupation numbers  $\sigma_i$  define the spin orientation at the site  $i$ . It could be whether +1 for a spin-up or -1 for spin-down alignments. Taking only one exchange interaction, i. e.  $n = 1$  in a system with two atoms gives back the Eq. (3.61) or Eq. (3.62). This scheme results generally in a linear system of independent equations of exchange interactions. The solutions can be found using a linear least-square fit if the problem is over-determined. Therefore the more equations are used, the more accurate values of exchange couplings are obtained. It is worth mentioning here that the exchange correlation treatment plays a crucial role in the determination of the magnetic couplings.

### 3.4.2 Magnetic force theorem

Another approach to calculate the magnetic exchange interactions was developed by Liechtenstein *et al.* [31] and is based on the local force theorem [149]. It is mostly suitable with KKR-Green's-function formalism. The basic idea behind calculating the exchange coupling constants  $J_{ij}$  is as follows: consider a small rotation of the magnetic moment direction at the site  $i$  by an angle  $\theta/2$  and similarly at the site  $j$  but with the opposite angle  $-\theta/2$ , see Fig. 3.8(c and d). The energy deviation from that of a ground state is quantified as:

$$\delta E = J_{ij}(1 - \cos\theta) \approx \frac{1}{2}J_{ij}\theta^2. \quad (3.64)$$

However, none of the total energy nor its variation  $\delta E$  needs to be calculated if the local force theorem is applied. Accordingly, the energy variation is expressed via Lloyd's formula [150], which is in turn given by the scattering path operator  $\tau^{ij}$ . Thus,  $J_{ij}$  is calculated via:

$$J_{ij} = \frac{1}{4\pi} \int^{E_f} dE \Im \text{Tr} \left[ (t_{i,\uparrow}^{-1} - t_{i,\downarrow}^{-1}) \tau_{\uparrow}^{ij} (t_{j,\uparrow}^{-1} - t_{j,\downarrow}^{-1}) \tau_{\downarrow}^{ij} \right], \quad (3.65)$$

here the  $t$ -matrices are directly accessible with the KKR-GF method and  $\Im \text{Tr}$  is the imaginary part of the matrix trace. Therefore only one magnetic configuration is needed to obtain the exchange coupling. This holds also true for alloy systems by employing the CPA method [31]. This establishes one of the prominent KKR-GF advantages compared to the energy mapping method. In this latter, a large supercell is foremost needed for the disorder simulation, which might be as well not large enough to describe a certain exchange interaction.

Once the exchange couplings are obtained, the mechanism behind the stability of a certain magnetic order is determined. This order can obviously occur only below a defined temperature  $T_m$  known as Curie temperature  $T_C$  for ferromagnetic and Néel temperature  $T_N$  for antiferromagnetic systems. However, DFT itself is a ground state theory and all the shown equations are strictly valid only for  $T = 0$  K. Thus the temperature dependence should be added as a complement to the so far obtained first-principles results. The method of choice here is the Monte Carlo (MC) simulation.

## 3.5 Monte Carlo simulations

MC simulations offer a great opportunity to start from the classical Heisenberg model and to estimate as well all thermodynamic related quantities such as the magnetic susceptibility, heat capacity and the magnetic phase transition temperature  $T_m$  [151]. Besides, the method does not depend on the DFT implementation for calculating the exchange interactions  $J_{ij}$ . Generally, the Monte Carlo method is used to determine any physical observable,  $A$ , in a  $NVT$  canonical ensemble (the number of particles  $N$ , the system's volume and the temperature  $T$  are fixed at each MC step):

$$\langle A \rangle = \sum_{\sigma} A_{\sigma} e^{-\beta E_{\sigma}}, \quad (3.66)$$



where the sum runs over all taken  $\sigma$  configurations (MC steps),  $E_\sigma$  is the energy of the system in the configuration  $\sigma$  and  $\beta = 1/k_B T$ ,  $k_B$  is the Boltzmann constant. A configuration here means a different distribution of the spin moment directions  $\mathbf{S}_i$ , which is swept with every MC step.

Since the method is statistical, a large number of configurations is needed to obtain an accurate average. This would not be an easy computational task with Eq. (3.66). But, by employing the *importance sampling* [151] method within the Markov processes, the problem can be handled. The method discards from the summation in Eq. (3.66) those configurations with high energies and only configurations with high probabilities (low energies) enter Eq. (3.66). Accordingly each new configuration  $v$  has to be constructed from its predecessor  $\sigma$  with a time-independent transition probability, which depends only on the two configurations properties ( $\sigma, v$ ) and not earlier states. Consequently, a chain of Markov processes ( $\sigma \rightarrow v \rightarrow \zeta \rightarrow \dots$ ) is generated. Additionally each configuration from the Markov chain should be attainable from any of its predecessors to ensure a transition probability defined by the Boltzmann distribution. This condition is known as the *ergodicity* condition. Another condition, which has to be fulfilled is the *detailed balance* [151]. It states that the Boltzmann distribution is only reached after the achievement of a thermal equilibrium in the system.

One of the most widely used MC algorithms was introduced by Metropolis *et al.* [152]. The algorithm makes use of the Markov processes and gives the same transition probability for all possible states  $v$  from  $\sigma$ . It follows that the detailed balance condition reads:

$$\frac{W(\sigma \rightarrow v)}{W(v \rightarrow \sigma)} = e^{-\beta(E_v - E_\sigma)}. \quad (3.67)$$

Such condition can be satisfied by defining an acceptance ratio for the trial transition from  $\sigma \rightarrow v$  to be 1 (fully accepted), if the new state energy  $E_v$  is lower than  $E_\sigma$  or accepted but with probability  $e^{-\beta(E_v - E_\sigma)}$  otherwise. Thus an ensemble of configurations is formed at each temperature and the measurement of any observable can be made. However the number of used configurations highly depends on the studied system and has to be checked carefully. The number of sites  $i$  which is defined by the MC supercell has to be checked as well. A good convergence criteria could be of course the resulting magnetic transition temperature. This latter can be easily determined from the heat capacity, the susceptibility or also from the Binder cumulant [153].

The importance of Monte Carlo simulations for an accurate determination of the magnetic transition temperature is illustrated in Fig. 3.9. The diluted antiferromagnetic system of  $\text{Ni}_c\text{Mg}_{1-c}\text{O}$  is taken as an example where the experimental data is taken from the elastic magnetic neutron scattering and SQUID measurements [154]. The disorder in these solid solutions is simulated with the CPA method in the framework of the KKR-GF. The LDA+U method ( $U = 3$  eV) is used to take into account the exchange-correlation effects. The cell parameters in the CPA calculations were fixed to those from the experiment [155]. As clearly seen in Fig. 3.9, the MC calculated Néel temperature ( $T_N$ ) of NiO ties very well with its experimental counterpart. This result is superior to the MC results of Fischer *et al.* [156], where an underestimation of  $T_N$  by about 70 K was reported. Note that Fischer *et al.* [156] used the local self-interaction correction approach to treat the exchange-correlation effects in NiO. The good agreement with experiment was not only found for the undoped NiO but even for NiO doped with magnesium. The MC transition temperatures follow the same trend of the measured values [154]. This shows the accuracy of MC simulations in the determination of transition temperature of material oxides.



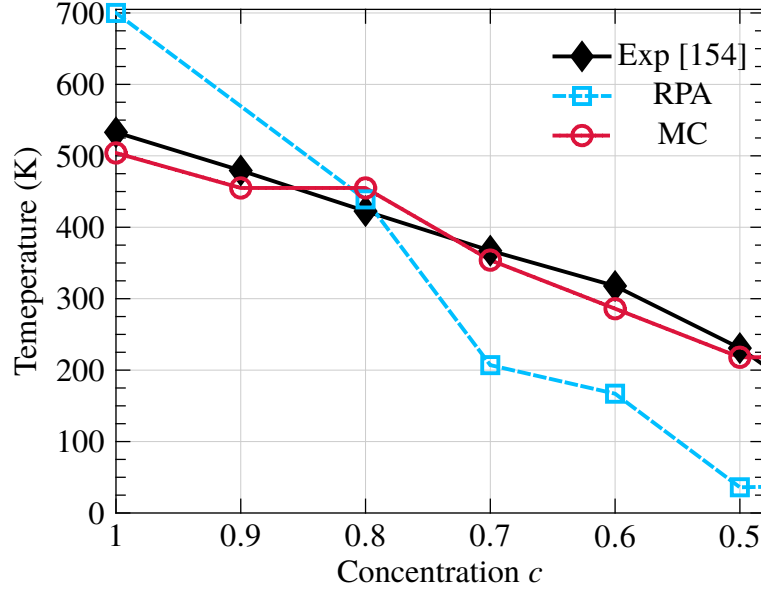


FIGURE 3.9: A comparison between the calculated and experimental magnetic transition temperatures of the solid solutions of  $\text{Ni}_c\text{Mg}_{1-c}\text{O}$ . The coherent potential approximation in the framework of the KKR-GF was used to calculate the exchange interactions. The derived temperatures from the random phase approximation are plotted with the blue line, while the results of Monte Carlo are plotted with the red line. The experimental temperatures are taken from the elastic magnetic neutron scattering and SQUID measurements [154].

### 3.6 Defect formation energies

Thermodynamic considerations are not only needed for magnetic phase transitions. Actually, a direct comparison between first-principles and experimental results is not always correct and one has to check the experimental conditions because DFT results, as already mentioned, are only meaningful for ground state properties. Especially, the presence of defects and impurities and their effect on the electronic structure of the host materials should be related to the growth conditions which made the stabilization of such imperfections possible. The central theoretical quantity which quantifies the aforementioned conditions is the defect formation energy [157–159]:

$$E_{\text{form}}(D, q) = \Delta E_{\text{tot}} - \sum_i n_i \mu_i + q\mu_e + E_{\text{corr}}, \quad (3.68)$$

here  $\Delta E_{\text{tot}}$  is the difference between total energies of the defective system  $D$  and the host material. The growth conditions for a crystal are here incorporated through the consideration of a chemical potential  $\mu_i$  of the elemental species  $i$ . The number of added or removed atoms from the pristine system are defined with  $n_i$ . A positive (negative) number of  $n_i$  expresses an addition (removal) of one atom from the pristine system. Charged defects can be as well treated with Eq. (3.68), where  $q$  is the charge of the supercell and has not to be confused with the charge of atom  $i$ .  $\mu_e$  is the chemical potential of involved electrons in charging the defect. This term can be taken as free parameter with a reference to the valence band maximum of the host material  $E_v$ . For semiconductors and insulators,  $\mu_e$  can vary between 0 and the band gap value. The last term  $E_{\text{corr}}$  in Eq. (3.68) accounts for all additional corrections, which have to be added into the formation energy

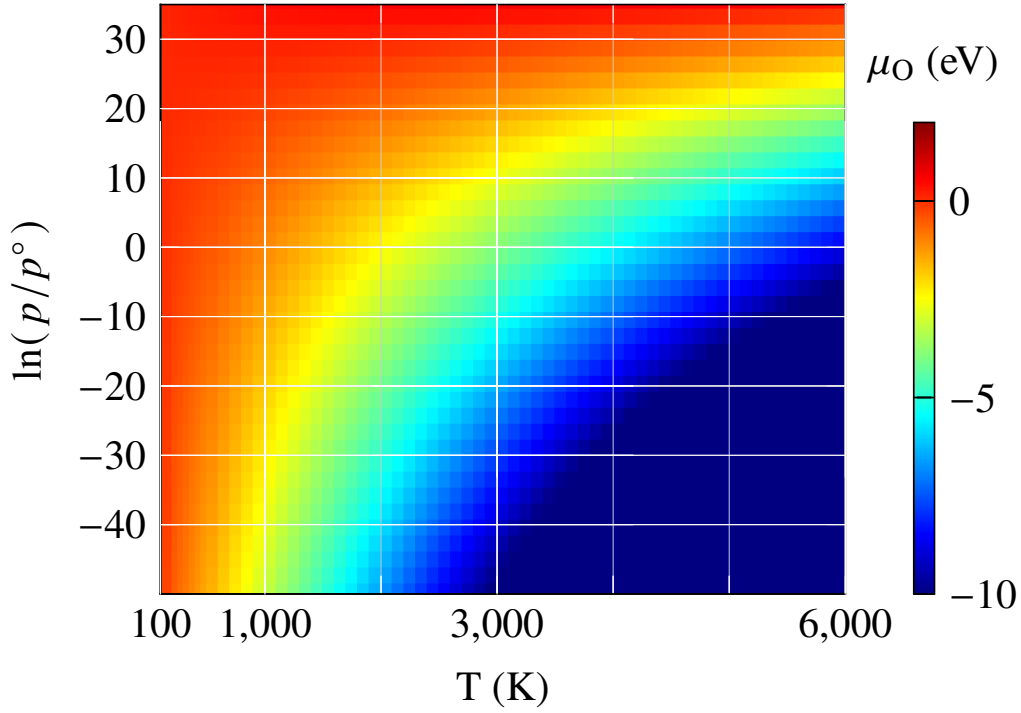


FIGURE 3.10: Illustration of the two dimensional function of the chemical potential  $\mu_{\text{O}}(T, p)$ . Its exact value can be determined for any experimental growth condition of oxide materials by extracting it from the corresponding temperature and oxygen partial pressure as demonstrated in Eq. (3.72). The values of  $\mu_{\text{O}}(T, p^\circ)$  at the standard atmospheric pressure are taken from the thermochemical tables in NIST-JANAF database [160].

and are not expressed so far in other terms. It includes the effects of finite  $k$ -points sampling for shallow defects and elastic or electrostatic interactions between periodic supercells of the charged defect. More detailed information are given in the review paper of Freysoldt *et al.* [157].

Though chemical potentials of adding or removing one atom according to the experimental growth conditions are in general unknown, formation energies can be at least calculated at their extreme boundaries. For instance, DFT total energies of bulk or even molecular species serve as a great source to obtain the chemical potentials. It is enough to calculate the total energy of the most stable compound in nature, which has the element  $i$  and relate it to  $\mu_i$  through the chemical reaction. In oxides, it is practical to express the chemical potential of any element  $i$  with that of oxygen. As example, to determine  $\mu_{\text{Ti}}$  one needs to calculate the total energy of bulk  $\text{TiO}_2$  and uses:

$$\mu_{\text{Ti}} = E_{\text{tot}}(\text{TiO}_2) - 2\mu_{\text{O}}. \quad (3.69)$$

To ease the handling of Eq. (3.68), the O chemical potential  $\mu_{\text{O}}$  is treated as a variable defined between its two extreme conditions. The upper limit corresponds to the solid oxygen (the O gas phase condensed in the sample) realized by the DFT total energy i. e. :

$$\mu_{\text{O}}^{\text{max}} = 1/2 E_{\text{tot}}(\text{O}_2). \quad (3.70)$$

where  $E_{\text{tot}}(\text{O}_2)$  is the total energy of a an isolated  $\text{O}_2$  molecule in the triplet state at  $T = 0$  K. It is often called oxygen-rich condition [161]. On the other hand, the lower limit, oxygen-poor condition, is defined by the reduction of  $\mu_{\text{O}}$ , which occurs when all oxygen leave the sample, and it is written as:

$$\mu_{\text{O}}^{\text{min}} = 1/2 [E_{\text{tot}}(\text{TiO}_2) - E_{\text{tot}}(\text{Ti})] . \quad (3.71)$$

Hence, the two boundaries are defined and any value in between could be assigned to a special experimental growth condition like temperature and oxygen partial pressure  $p$ . They are related to the oxygen chemical potential through [161]:

$$\mu_{\text{O}}(T, p) = \mu_{\text{O}}(T, p^\circ) + \frac{1}{2} k_{\text{B}} T \ln \left( \frac{p}{p^\circ} \right) . \quad (3.72)$$

where  $p^\circ$  is the standard atmospheric pressure (1.01325 bar). At this pressure, the values of  $\mu_{\text{O}}(T, p^\circ)$  at each temperature are already known and stored in thermodynamical tables [160]. Hence the experimental temperature and pressure determine together the value of  $\mu_{\text{O}}$  as shown in Fig. 3.10. Once the temperature and the pressure are fixed, the resulting chemical potential  $\mu_{\text{O}}(T, p)$  enters Eq. (3.69) and solves at the end Eq. (3.68) to obtain the formation energy of adding/removing one Ti atom.

The defect formation energies will be calculated in the following chapters, whenever the defect is considered as a structural modification for the oxide material. As well, all the other presented methods in this chapter will be applied in the following for the determination of structural, electronic and magnetic properties of the studied oxides.



## 4 Defect induced magnetism: $\text{TiO}_2$ as an example

Titanium dioxide ( $\text{TiO}_2$ ) is by far one of the most important semiconductors of the last decade. Indeed, it has fostered an increasing interest for its broad range of applications by virtue of its rich features. For instance,  $\text{TiO}_2$  is regarded as a valuable semiconductor for applications in photocatalysis [12], dye-sensitized solar cells [162], gas sensors [163], pigments [164] and batteries [165]. Such large spectrum of applications is acquired due to the high stability, non-toxicity, low cost, and the large band gap of  $\text{TiO}_2$ .

The extend of success to achieve the best outcome for the aforementioned features highly depends on the electronic, optical and thermodynamical properties of  $\text{TiO}_2$ . These properties depend in turn on the structural phase of  $\text{TiO}_2$ . Three common phases are mostly investigated, which are the rutile, the anatase and the brookite forms. Especially, the two first phases (rutile, anatase) were extensively investigated by experimental and theoretical studies. It is mainly due to the high stability of the rutile structure compared to the other structures, which explains the focus on the rutile structure. In fact the anatase is the most considered structure because of its advantages over the rutile structure for many fundamental properties like the larger band gap, the smaller electron effective mass which significantly enhances the quality of devices based on  $\text{TiO}_2$ . This explains our choice of picking the anatase structure to discuss the properties of  $\text{TiO}_2$  in this thesis.

Magnetism on the other hand is a rich phenomenon with a lot of applications which makes any magnetic material more than favorable. However  $\text{TiO}_2$  is not magnetic in nature because of the absence of unpaired  $d$  or  $f$  electrons. The reason is that Ti ion has an electron configuration of  $\text{Ti}^{4+}$ , i. e.  $[\text{Ar}] 3d^0 4s^0$ . Such configuration contradicts the necessary condition of Heisenberg [141] that a magnetic order can be only triggered if the involved ions have a principal quantum number  $n$  satisfying  $n \gtrsim 3$ . Thus a magnetic order in crystals with only  $s$  and  $p$  electronic bands is ruled out.

The Heisenberg condition was to some extent disproved by the emergence of ferromagnetism in carbon-based materials and also in transition metal oxides caused by defects without any magnetic atom. The intrinsic nature of this phenomenon is called nowadays "Defect Induced Magnetism" (DIM) or the  $p$ -magnetism [166]. This phenomenon is related to the so-called "Diluted Magnetic Semiconductors" (DMS). It refers to semiconducting materials where a magnetic order occurs after doping with a relatively low amount of magnetic ions. The only difference between the two phenomena is the requirement of doping with magnetic atoms in DMS whereas the magnetic moments in DIM are created by the defects. Different reasons for the appearance of DIM were discussed and the subject remains an open question for theoreticians and experimentalists [167–172]. Defect induced magnetism was also found experimentally in anatase  $\text{TiO}_2$ . Its

microscopic origin caused long debates in literature [173–182, H2] with quite controversial results over the responsible kind of defect in the appearance of experimentally observed magnetic order.

Defects are reported to be experimentally created by low-energy ion irradiation [183]. The same condition was taken by Robinson *et al.* [184] in their molecular dynamics simulations in order to determine theoretically the most probable formation of native defects in TiO<sub>2</sub>. A Buckingham pair potential [185] was used to identify the possible defects in the anatase structure of TiO<sub>2</sub>. In this respect the defect formation probability of each defect, whether isolated or complex, is quantified as a function of the so-called primary knock-on atom energy. The probability is therefore determined after the defect cluster analysis. Interestingly the highest probability was not reported for an isolated defect which were broadly investigated in the literature. It was that of the di-Frenkel pair formation, where a Frenkel pair (FP) corresponds to the occurrence of one titanium vacancy ( $V_{\text{Ti}}$ ) and one titanium interstitial ( $I_{\text{Ti}}$ ) and di-FP corresponds to the occurrence of two Ti vacancies and two Ti interstitial occur at the same time. The second high probable defect to form was found for oxygen interstitial ( $I_{\text{O}}$ ) followed by an oxygen vacancy ( $V_{\text{O}}$ ). Then the combination of a single Frenkel pair and an  $V_{\text{O}}$  follows. Thereafter the same probability was found for the formation of an  $I_{\text{Ti}}$  and the combination of a  $V_{\text{O}}$  and a  $V_{\text{Ti}}$ . We note here that only structural degree of freedom is considered and the most important one in our actual study, i. e. spin, was not examined in [184].

Among the series of possible defects, a special focus in literature to explain the origin of magnetism in undoped TiO<sub>2</sub> was given to just few native defects. A ferromagnetic order was observed experimentally and was attributed to the presence of  $V_{\text{O}}$  with a Curie temperature higher than 400 K [173] in TiO<sub>2</sub> films deposited on (100) LaAlO<sub>3</sub> substrates. Using the same substrate, a higher magnetic transition temperature of 800 K was reported [174]. This result is backed by density functional theory calculations [174], where a high competition between ferromagnetic and ferrimagnetic couplings is predicted. The FM coupling between Ti cations is mediated by an oxygen anion whereas the ferrimagnetic coupling occurs between Ti cations via an oxygen vacancy. A completely different and robust magnetic order, AFM, was also determined by GGA+U pseudopotential calculations [175] with the AFM energy lower by almost 500 meV than the FM one. Each of the two coupled Ti cations has a local magnetic moment of  $1\mu_{\text{B}}$ . The same method GGA+U but with the more accurate full-potential linearized augmented plane wave basis [176] does not detect any sort of magnetism up to which the authors considered as reasonable value of  $U$  for the  $3d$  electrons, i. e. 4 eV. A result that agrees well with another GGA calculation [177].

Cation vacancy  $V_{\text{Ti}}$  was also attributed to the ferromagnetic order in TiO<sub>2</sub> using LSDA calculations [178] and GGA+U for both Ti  $d$  and O  $p$  orbitals [179]. A single  $V_{\text{Ti}}$  is reported to induce a local magnetic moment of  $3.5\mu_{\text{B}}$  whereas an isolated divacancy ( $2V_{\text{Ti}}$ ) gives only a total magnetic moment of  $2\mu_{\text{B}}$ . The decrease of the total magnetic moment is assigned to a hole compensation mechanism [178].

The defect complex ( $V_{\text{O}} + I_{\text{Ti}}$ ) was as well demonstrated using a combination of x-ray diffraction, Raman scattering and electron-spin resonance spectroscopy [180] to be the origin of the observed ferromagnetism. This conclusion is supported by an extensive experimental analysis of TiO<sub>2</sub> nanoparticles [181]. An excess of  $I_{\text{Ti}}$  and  $V_{\text{O}}$  was easily obtained through rapid cooling process. In this mechanism, the  $V_{\text{O}}$  polarizes the neighboring Ti which couple ferromagnetically to

the  $I_{Ti}$ . For higher concentrations of this defect complex the  $I_{Ti}$  couple between each other antiferromagnetically. However a theoretical understanding of this kind of defect complex is still missing.

The di-Frenkel pair (di-FP) defect complex on the other hand was mentioned in recent experimental studies not only to be responsible for the enhanced ferromagnetism but also for a strong observed perpendicular anisotropy in  $TiO_2$  films deposited on  $SrTiO_3$  [182] or  $LaAlO_3$  [H2]. Nevertheless this kind of defect is described as a non stable defect as stated also in the molecular dynamics simulations study [184]. The total magnetic moment of di-FP is found to decrease from  $2\mu_B$  after the first low-energy ion irradiation to  $1.3\mu_B$  after the second irradiation. GGA+U calculations were performed as well and a good agreement with experimental finding was reported [H2]. The calculated magnetic moment on each Frenkel pair was found to be  $0.7\mu_B$  which gives a total di-FP moments of  $1.4\mu_B$  where the total magnetic moment of the used supercell is  $2\mu_B$ .

As previously discussed, a plethora of possible origins of magnetic order in  $TiO_2$  was reported with different methods. Experimental results showed that ferromagnetism, ferrimagnetism and antiferromagnetism can appear whether exclusively or combined. Theoretical results on the other hand are strongly dependent on the electronic exchange correlation approximations. A consistent (same exchange correlation approach) and extensive (taking into account all possible defects predicted by Robinson *et al.* [184]) investigation to explain the experimental results is still unavailable. Moreover a direct comparison of the stability of different defects, which are calculated with different approximations, is not straightforward. Besides, most of the theoretical investigations focused only on the oxygen rich condition which is far from the real growth conditions. Thus we aim in this chapter to benchmark our results with the available literature and extend it to cover all possible native defects predicted by molecular dynamics simulations and also at different thermodynamical conditions, i. e. oxygen rich and poor conditions and also the experimental growth condition of anatase  $TiO_2$ .

## 4.1 Theoretical background

The modelling of oxides systems with DFT calculations is a tricky task and special care has to be taken for an accurate description of the electronic and magnetic properties [H1]. Electronic correlations can be treated with the accurate but numerically expensive methods of GW approximation or hybrid functionals [H3]. Such methods are widely applied to study small systems with few atoms per unit cell but become extremely demanding and mostly unfeasible for large systems. A situation is always encountered when dealing with defects with supercell calculations. On one hand, DFT+U method has shown a great success in the description of oxides compared to the more expensive methods. Only the U parameter has to be checked and its best value should lead to the best agreement with available experimental data. On the other hand, many defect configurations are not studied in detail and their electronic structures are not yet reported by experimental works, i. e. the lack of experimental reference to decide the best U value. An *ab initio* method was also proposed to calculate U without requiring any reference [186]. Nevertheless a global and unique U value for a specific transition metal ion does not exist because of the local chemical environment dependence of the transition metal ion [187]. This turns out to be more obvious in different defect

configurations which might lead as well to completely different  $U$  values. Thus a direct comparison of total energies and consequently defect formation energies is not possible. Therefore a single  $U$  value,  $U = 4$  eV, is used throughout all the following discussions. This choice was based on the best compromise between the numerical reported values for defective and pristine system of TiO<sub>2</sub> [188].

As previously mentioned, there is a large discrepancy in literature between the reported reasons of magnetic order in defective TiO<sub>2</sub>. This was also found by using exactly the same theoretical approach to study the same kind of defect which raises here the question about the basic reasons for such disagreement. Actually, the defect induced magnetism, discussed here, is mainly driven by the chemical environment surrounding the defect atom. Such environment is affected by structural relaxations of the internal coordinates within the considered supercell which are obtained after energy minimization. In fact a small deviation from the global energy minimum during relaxation is more expected with tiny local magnetic moments which is the case in most native defects of TiO<sub>2</sub>. To overcome this problem, the fixed spin moment method [189] is used where only the total magnetic moment of the supercell is fixed to integer numbers but the local ones are allowed to relax. Afterwards only the structure which gives the lowest total energy is considered for further analysis. Hence the magnetic orders of the defect configuration can be categorized after applying this method into two major classes. The first class encloses the ferromagnetic and ferrimagnetic orders where the total magnetic moment is non zero and a second class characterized by a zero net magnetic moment which takes into account the antiferromagnetic and also the non magnetic solutions.

## 4.2 Vacancies

### 4.2.1 Anion vacancies V<sub>O</sub>

The existence of magnetic order in oxygen deficient anatase TiO<sub>2</sub> has activated a lot of discussions and disagreement in theoretical investigations. Some studies have reported the non existence of magnetic order [176, 177] while other studies claimed the stability of antiferromagnetic [175], ferromagnetic or even ferrimagnetic orders [174].

Actually the concentration of oxygen vacancies may matter in the comparison of the reported results. Therefore a very low concentration is considered in this study by taking out one oxygen ion from a supercell constituting of  $3 \times 3 \times 1$  repetitions of the unit cell. Hence, the removal of one single oxygen ion gives rise to a defect concentration of 1.38 % which is typical for experimental conditions [H4]. It is worth mentioning here that a removal of one oxygen atom from the supercell induces an excess of two electrons in the system giving rise to a charged supercell. The neutrality is restored by addition of a compensating and homogeneous background charge [190]. Note, this addition does not explicitly affect the electronic density and the total energy of the system.

Technically, without imposing any magnetic constraints onto the supercell, the most stable magnetic or non magnetic configuration was hard to detect since most of the configurations have similar energies and restarting the structural relaxation of the supercell from one precise magnetic order may converge to a completely different order. Only by fixing the total spin moment of the supercell to integers values between 0 to  $4\mu_B$ , structural relaxations were guided towards the predefined magnetic orders. The structure with zero net magnetic moment was found to have the lowest total



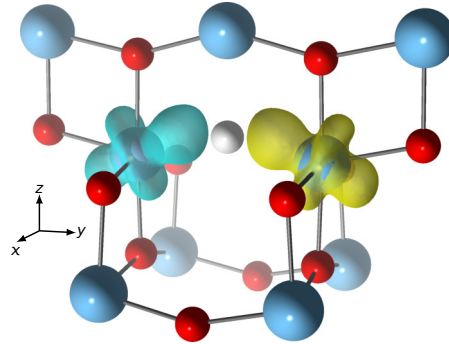


FIGURE 4.1: The spin density of  $\text{TiO}_2$  with one oxygen vacancy is shown for the vacancy and its surrounding environment. The position of the oxygen vacancy is highlighted with the small white ball. Ti (O) atoms are presented by the large blue (small red) balls. The Ti ions around the vacancy are antiferromagnetically coupled. The isosurfaces of the spin density around the vacancy are plotted at the isovalue of  $\pm 0.005 \text{ \AA}^3$  with positive density (spin-up) in yellow and negative density (spin-down) in light blue color.

energy which is 20 meV lower than that of  $2\mu_B$ . The two Ti first neighbors of the oxygen vacancy in the  $(xy)$ -plane were found to be polarized with a local magnetic moment of  $\pm 0.35\mu_B$  which agrees with the measurements of Stevin *et al.* [191] and Moser *et al.* [192]. The two Ti ions couple to each other antiferromagnetically as shown in Fig. 4.1. This indicates that the two additional electrons, induced by removing one oxygen atom, are localized directly on the two Ti ions which are first neighbors of the vacancy. Such localization transforms the two neighboring  $\text{Ti}^{4+}$  into  $\text{Ti}^{3+}$ . Based on the total energy differences between the FM ( $2\mu_B$ ) and the AFM and the localized spins in a Heisenberg Hamiltonian as mentioned in Sec. 3.4, one can assign a magnetic exchange interaction,  $J$ , with a strength of  $-10$  meV between the two  $\text{Ti}^{3+}$  sites.

The stability of the antiferromagnetic order in the defective system is accompanied by the reduction of the distance between the two magnetic ions from  $3.78 \text{ \AA}$  in the pristine system to  $3.75 \text{ \AA}$ . Also the bond angle which makes each of the two Ti ions with the vacancy and the next oxygen ion is reduced by  $3^\circ$ . In other words the two Ti ions are pulled to the vacancy center ( $y$ -direction) and moved upward along  $z$  direction. Such kind of relaxation is mainly responsible for the appearance of polarized  $d_{yz}$  states contrarily to the pristine system as shown by the densities of states (DOS) of the pristine system and defective system in Fig. 4.1 (a) and (b), respectively. The obtained DOS revealed that the defect states are localized in the middle of the band gap region. The valence band maximum is as well pulled down by almost 1 meV but still purely dominated by oxygen  $p$ -states. A similar reduction is also found for the conduction band minimum where two narrow bands, mainly from the  $d_{xy}$  states contribution, are formed.

In fact, the obtained antiferromagnetic order in oxygen deficient  $\text{TiO}_2$  is not the only reported magnetic state for this system. As already mentioned, ferromagnetic and ferrimagnetic order can occur in oxygen deficient  $\text{TiO}_2$  as well. Such structures are not obtained so far with the low defect concentration of  $\approx 1\%$ . To check the possible stability of other reported magnetic orders, the concentration of oxygen vacancies is increased up to  $2.77\%$  by removing two oxygen atoms from the supercell. To consider the two defects as isolated in the supercell, their interaction has to be carefully checked. Therefore, the distance between the two vacancies is varied from first nearest neighbors separation to the eighth neighbor separation which corresponds to a distance of about

#### 4 Defect induced magnetism: TiO<sub>2</sub> as an example

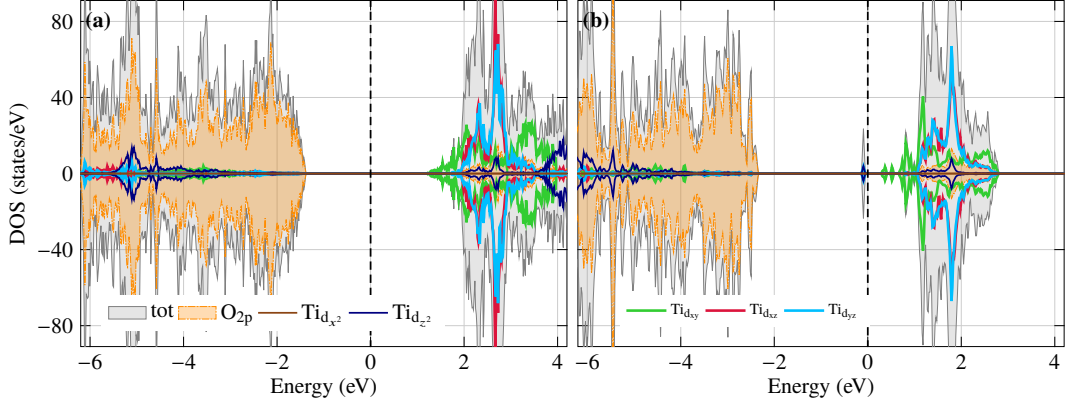


FIGURE 4.2: The density of states of pristine TiO<sub>2</sub> (a), of defective TiO<sub>2</sub> with 1.38 % oxygen vacancies (b). The total density of states is shaded in gray. The partial density of states (PDOS) of oxygen 2*p* is shown by the filled orange areas. The decomposed PDOS of Ti 3*d* is presented by the colored solid lines, green for *d<sub>xy</sub>*, red for *d<sub>xz</sub>*, light blue for *d<sub>yz</sub>*, dark blue for *d<sub>z<sup>2</sup></sub>*, and brown for *d<sub>x<sup>2</sup>-y<sup>2</sup></sub>*. The black dashed lines indicate the zero energy levels of the considered systems.

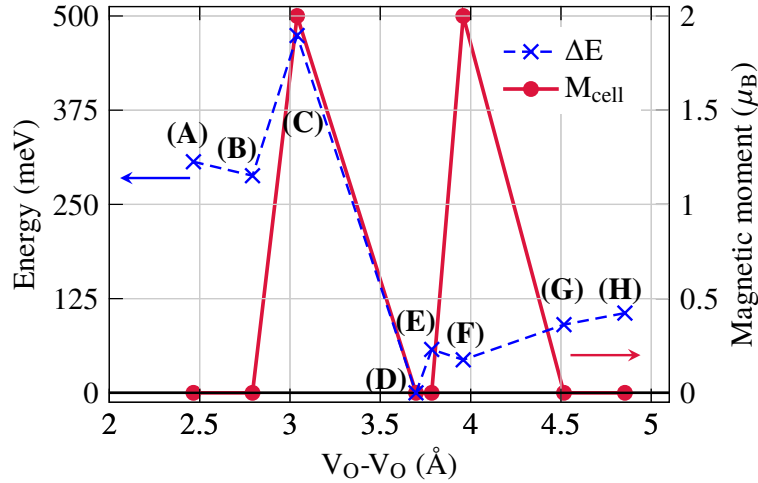


FIGURE 4.3: The stability of the defective TiO<sub>2</sub> with 2.77 % oxygen vacancies, simulated with two V<sub>O</sub> in a supercell of TiO<sub>2</sub>, is shown by the variation of the total energy (blue dashed line). The distance separating two V<sub>O</sub>, V<sub>O</sub>-V<sub>O</sub>, is varied from the shortest possible one in the supercell,  $\approx 2.5$  Å, to a distance of  $\approx 5$  Å, i. e. corresponds to the eighth nearest neighbor. The total magnetic moment of the supercell is presented by the solid red color. A ferromagnetic order corresponds to non zero total magnetic moment whereas the antiferromagnetic order is defined by the zero total magnetic moment.

5 Å. The fixed spin moment method is here used as well by taking into account total magnetic moments between 0 and  $4\mu_B$  for each of the structures. The one which gives the lowest energy for each divacancy configuration is kept for further analysis. Among the considered supercell magnetic moments only two of them are found to be stable from the eight configurations. This corresponds to the antiferromagnetic one and the ferromagnetic one with a total magnetic moment of  $2\mu_B$  as shown in Fig. 4.4. The number of polarized Ti ions is found also to change and highly depends on the defect configuration.

Having the two vacancies as first nearest neighbors stabilizes the antiferromagnetic order like the single vacancy case but at the cost of a high total energy compared to other configurations, i. e. about 300 meV as shown in Fig. 4.3. The coupling of Ti ions close to the vacancies in this configuration is antiferromagnetic within the  $(xy)$ -plane and ferromagnetic along the  $z$ -direction as depicted in Fig. 4.4 (A). However the polarization of the out of plane ions disappears when the two vacancies share one common in-plane Ti ion as shown in Fig. 4.4 (B). This gives rise to only three magnetic sites by removing an oxygen ion which corresponds to the second nearest neighbor of the first vacancy. The energy in this second configuration is lowered but still high. Though such decrease of energy is not preserved for the third shell divacancy as presented in Fig. 4.3. In this configuration, the two oxygen ions are removed from the same Ti ion which relax to a ferromagnetic coupling to the second in-plane Ti ion, see Fig. 4.4 (C). This coupling confirms the experimental results of Hong *et al.* [173], where a room-temperature ferromagnetism was observed although the obtained energy is high.

On the other hand, the energy of the defective  $\text{TiO}_2$  is lowered to its lowest obtained value in all studied configurations at  $V_{\text{O}}-V_{\text{O}} \approx 3.69 \text{ \AA}$ . The magnetic coupling in D does not differ much from that of the configuration A. The only exception here is that the two oxygen ions are removed from the  $(xz)$  plane instead of the  $(yz)$  in the first one. Thus the Ti ions relax towards the vacancies centers on the  $(xz)$  plane which reduces consequently the distances between the polarized in-plane and out of plane Ti ions by almost  $0.1 \text{ \AA}$  compared to the first configuration.

In addition, a metastable configuration was also obtained by having the two oxygen vacancies along  $z$  as shown in Fig. 4.4 (F). It corresponds to a mixing between ferromagnetic and ferrimagnetic coupling between the polarized Ti ions. The total magnetic moment of this structure was found to be  $2\mu_{\text{B}}$ , see Fig. 4.3. Interestingly, its total energy, see Fig. 4.3, is only 40 meV higher than the most stable configuration D. This competition between ferro- and ferrimagnetism was also experimentally reported by Yoon *et al.* [174] for  $\text{TiO}_{2-\delta}$  grown on (100)  $\text{LaAlO}_3$  [174]. Increasing further the distance between the two vacancies did not stabilize the total energy but did sustain the antiferromagnetic order in the remaining configurations as shown in Fig. 4.3.

The total and partial density of states for the two most stable configurations of double oxygen vacancy are presented in Fig. 4.5. In both configurations the defects states appear in the middle of the band gap region but their origin is different. The peak in the configuration F is from the  $d_{z^2}$  orbitals of Ti whereas two peaks, originated from the mixing between  $d_{z^2}$  and  $d_{yz}$  orbitals contributions, exist in the antiferromagnetic configuration. In this structure, the density of states is nearly similar to that of a single oxygen defect except the number of peaks at the band gap. This could be the result of the crystal field splitting due to the defect environment. The position of the valence band maximum, the contribution's nature of the conduction band minimum and also the conduction band width are exactly the same as those of single oxygen vacancy. On the other hand, the conduction band minimum and also the width of the conduction band of the structure F is more similar to those of pristine system.

#### 4.2.2 Cation vacancy $V_{\text{Ti}}$

Contrarily to  $V_{\text{O}}$ , the inclusion of  $V_{\text{Ti}}$  yields to a deficiency of four electrons in the system. Therefore it is the aim of this study to check the way the system follows to stabilize its energy and also its effect on the electronic distribution due to the electron deficiency (or excess of holes). Will this

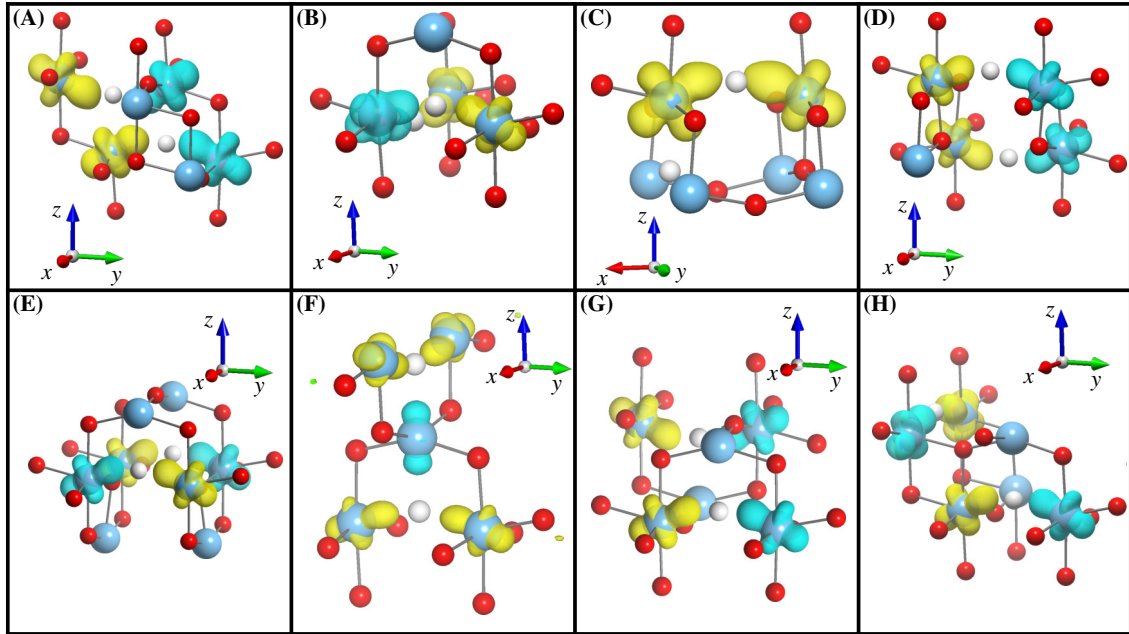


FIGURE 4.4: The spin densities for different configurations of TiO<sub>2</sub> with two oxygen vacancies are shown. The realization of different magnetic order is possible by varying the distance between the two oxygen vacancies: a competition between ferromagnetic and antiferromagnetic coupling in (A,B,D,E,G,H), between ferromagnetic and ferrimagnetic (F) and a ferromagnetic order in (C). Ti (O) atoms are presented by the large blue (small red) balls. The lowest total energy was found for the configuration D. The position of the two oxygen vacancies are highlighted with the small white balls. The isosurfaces of the spin densities around the vacancies are plotted at the isovalue of  $\pm 0.008 \text{ \AA}^3$  with positive density (spin-up) in yellow and negative density (spin-down) in light blue color.

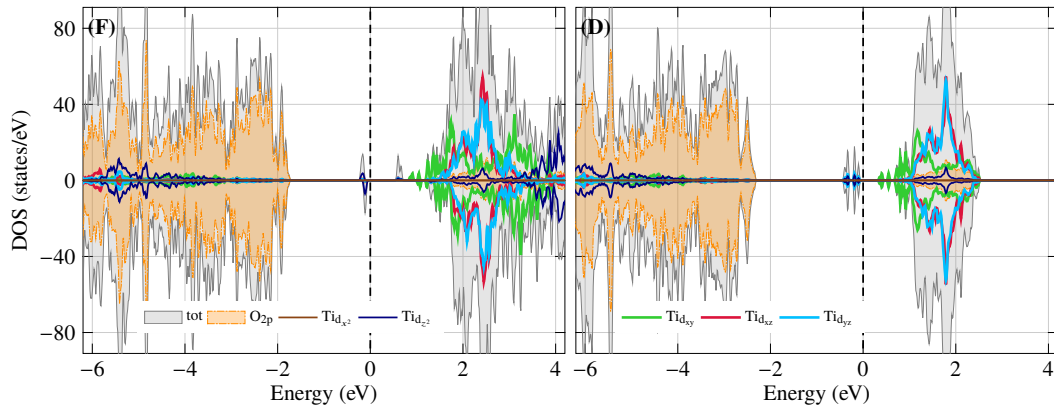


FIGURE 4.5: The density of states of the two most stable configurations of double oxygen vacancy, D and F, which were shown in Fig. 4.4. F is the metastable configuration whereas D is the most stable configuration ( see Fig. 4.4). The total density of states is shaded in gray. The partial density of states (PDOS) of oxygen 2p is shown by the filled orange areas. The decomposed PDOS of Ti 3d is presented by the colored solid lines, green for  $d_{xy}$ , red for  $d_{xz}$ , light blue for  $d_{yz}$ , dark blue for  $d_{z^2}$ , and brown for  $d_{x^2-y^2}$ . The black dashed lines indicate the zero energy levels of the considered systems.

TABLE 4.1: Comparison of the calculated total energies for different Ti divacancy configurations in the supercell of anatase  $\text{TiO}_2$ .  $V_{\text{Ti}}-V_{\text{Ti}}$  is the distance separating the two Ti vacancies, E is the total energy with reference to the lowest one and M is the total magnetic moment of the supercell.

$V_{\text{Ti}}-V_{\text{Ti}}$ ( $\text{\AA}$ )	3.04	3.78	4.85	5.35	5.46	6.15	7.23	7.64
E (eV)	0.00	4.45	4.77	4.94	4.64	2.01	5.05	4.95
M ( $\mu_{\text{B}}$ )	2.0	8.0	8.0	8.0	8.0	4.0	8.0	8.0

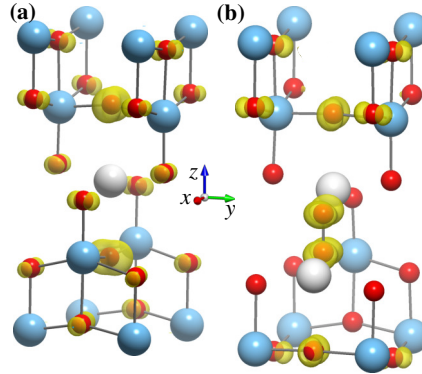


FIGURE 4.6: The spin densities of  $\text{TiO}_2$  with (a) one single  $V_{\text{Ti}}$  and (b) for two  $V_{\text{Ti}}$  are shown. Ti (O) atoms are presented by the large blue (small red) balls. The position of the titanium vacancies are highlighted with the large white balls. The isosurfaces of the spin densities around the vacancies are plotted in yellow color at the isovalue of  $0.008 \text{ \AA}^3$ .

excess be localized on Ti ions as electrons did in oxygen deficient system or on the surrounding oxygen ions of the Ti vacancy? To model this defect system one Ti atom is removed from the considered supercell which gives access to a defect concentration of 2.77 %.

The calculated structure with a single Ti vacancy was found to relax towards a ferromagnetic orientation of the oxygen spins. That means none of the Ti ions are polarized but the magnetic order is coming purely from the oxygen  $p$ -states. The total magnetic moment was found to be  $4 \mu_{\text{B}}$  which is a little larger than the reported value of  $3.5 \mu_{\text{B}}$  by Peng *et al.* [178]. The calculated local magnetic moments of each of the apical oxygen ( $\text{O}_a$ ), O atoms on top or below  $V_{\text{Ti}}$  along  $z$ -direction, is only  $0.46 \mu_{\text{B}}$  while almost  $3 \mu_{\text{B}}$  are homogeneously distributed over all oxygen ions within the same unit cell of  $V_{\text{Ti}}$  as shown in Fig. 4.6 (a). The total energy of the most stable configuration, FM, is found to be 85 meV lower than the antiferromagnetic one. The stability of FM order is induced by the large relaxation of the two apical oxygen ions away from  $V_{\text{Ti}}$ . This is manifested by the large elongation of  $d_{V_{\text{Ti}}-\text{O}_a}$  distance of  $2.47 \text{ \AA}$  compared to its initial value,  $d_{\text{Ti}-\text{O}_a}$ , of  $1.97 \text{ \AA}$  in the pristine system. Such elongation polarizes the oxygen ions mostly along the  $y$  direction as shown in the partial density of states in Fig. 4.7 (a). In addition, from the DOS in Fig. 4.7 (a), the defect states,  $p_y$  here, appear on the valence band maximum edge instead of the middle of the band gap region as already demonstrated in the case of single and double oxygen vacancies.

Increasing the concentration of  $V_{\text{Ti}}$  to 5.55 % is as well checked by taking out two Ti atoms from the supercell. Again, the position of the second  $V_{\text{Ti}}$  is varied from the first nearest neighbor of  $V_{\text{Ti}}$  to its eighth neighbor. For each of the configurations, a series of fixed total magnetic moment of

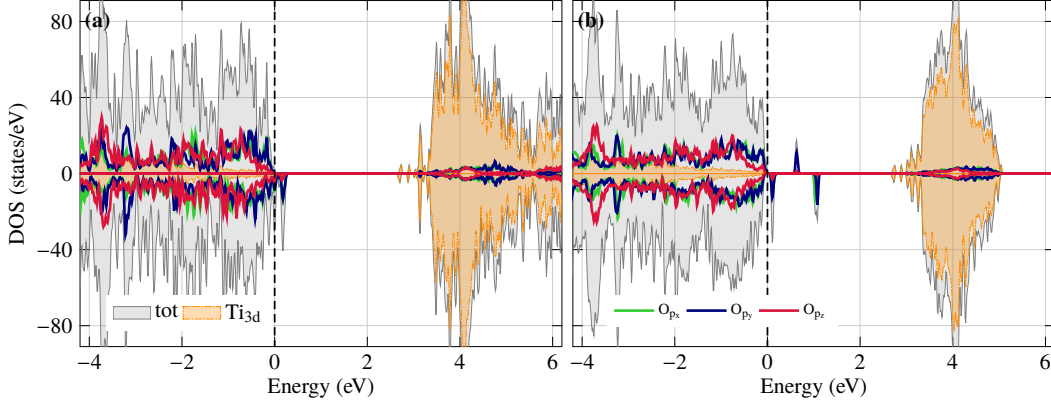


FIGURE 4.7: The density of states of TiO<sub>2</sub> in the presence of (a) single Ti vacancy and (b) two Ti vacancies in its most stable configuration. The total density of states is shaded in gray. The partial density of states (PDOS) of titanium 3d is shown by the filled orange areas. The decomposed PDOS of O 2p is presented by the colored solid lines, green for  $p_x$ , dark blue for  $p_y$  and red for  $p_z$ . The black dashed lines indicate the zero energy levels of the considered systems.

the supercell were taken from 0  $\mu_B$  to 8  $\mu_B$ . All configurations converged to a FM order but with different total magnetic moments. The lowest energy was obtained for the configuration with Ti vacancies as nearest neighbors which is surprisingly very much lower than other configurations by at least 2 eV (see Tab. 4.1). Interestingly, this configuration has only a total magnetic moment of 2  $\mu_B$  while most of the other configurations have a moment of 8  $\mu_B$ . This result agrees well with the findings of Peng *et al.* [178] where neighbors are considered only up to the third shell.

To understand the reason behind the stability of this configuration, its magnetization density is plotted in Fig. 4.6 (b). Only one from the two apical oxygen ions for each  $V_{Ti}$  is polarized whereas two of them were polarized in the single  $V_{Ti}$  configuration. Because of the symmetry of anatase, the two  $V_{Ti}O_6$  octahedra share the same edge. After introducing the double vacancies, the pair of oxygen ions which establishes this edge are released and consequently form an O<sub>2</sub> dimer-like complex between the vacancies. This agrees well with the reported results of Peng *et al.* [178]. The length of this dimer-like complex is about 1.2 Å which is very close to the bond length of 1.22 Å in an isolated O<sub>2</sub> molecule calculated here with PBEsol method for comparison. In fact a huge relaxation along the  $x$  direction of one of the oxygen ions was observed and could be assigned as the responsible mechanism for the appearance of such dimer. Note, that the same bond has a length of about 2.46 Å in the pristine system. In fact it is not the only structural modification caused by the double Ti vacancy. Also the second apical oxygen ion for each  $V_{Ti}$  is pushed away from the  $V_{Ti}$ . This is manifested, as shown in Fig. 4.6 (b), by the transformation of the bond angle Ti-O<sub>a</sub>-Ti from 156° in the pristine system to 176° in the defective system.

The local magnetic moment of each of the oxygen ions constituting the O<sub>2</sub> dimer-like complex is found to be 0.42  $\mu_B$  out of 2  $\mu_B$  for the entire supercell. This shows more localization of holes in the case of Ti divacancy compared to single  $V_{Ti}$ . The density of states of this configuration is plotted in Fig. 4.7 (b) and compared to that of a single  $V_{Ti}$ . The conduction band is almost similar in both systems which is also valid for the valence band width. The same  $p_y$  state appears also on the edge of the valence band maximum. In addition, two new peaks appear in the middle of the



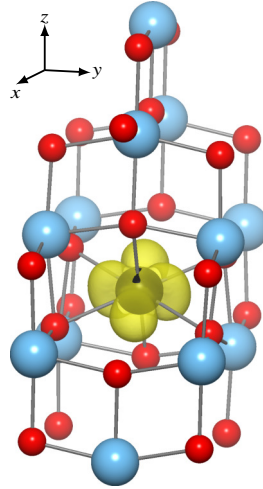


FIGURE 4.8: The spin density of  $\text{TiO}_2$  in the presence of titanium interstitial,  $I_{\text{Ti}}$ , is shown for the interstitial environment. Ti (O) atoms are presented by the large blue (small red) balls. The Ti interstitial is highlighted with the large black ball. The isosurfaces of the spin density are plotted at the isovalue of  $\pm 0.008 \text{ \AA}^3$  with positive density (spin-up) in yellow color. The surrounding Ti ions of  $I_{\text{Ti}}$  are antiferromagnetically coupled to  $I_{\text{Ti}}$  but with tiny local magnetic moments, i. e. their contributions to the spin density can not be seen with the actual isovalue.

band gap in the case of  $2V_{\text{Ti}}$ . These peaks are coming mainly from the mixed states of  $p_x$  and  $p_y$ . Moreover a new peak originated from  $p_x$  shows up at the energy level of 6.4 eV below the Fermi energy which were not previously observed in the single  $V_{\text{Ti}}$  DOS.

### 4.3 Interstitials

The occurrence of native interstitial ions in  $\text{TiO}_2$  is also examined in this study. The stability of both cation and anion interstitials are checked here by taking only one defect configuration which has an inserted Ti or O ion in the  $\text{TiO}_2$  supercell at the void between Ti atoms, as can be seen in Fig. 4.8. In order to scan the possible magnetic orders of  $\text{TiO}_2$  in the presence of  $I_{\text{Ti}}$ , the supercell spin moments is varied from 0 to  $4\mu_B$ . The lowest energy was found for the one which has a fixed moment of  $0\mu_B$ . But it does not correspond to a robust antiferromagnetic order because only the interstitial ion has a finite local magnetic moment of  $0.85\mu_B$  as illustrated in Fig. 4.8. The compensation of this moment is found to distribute over most of the neighboring Ti ions which have tiny negative moments. Increasing more the total spin value did not lower the energy but localized more the extra moment on the interstitial ion with small proportions on its nearest neighbors.

The Ti interstitial was found to form an octahedron with its neighboring oxygen ions in agreement with Na-Phattalung *et al.* results [193]. The in-plane and out of plane bond lengths of  $I_{\text{Ti}}\text{O}_6$  are found to be 2.13 Å and 1.99 Å, respectively.

The same procedure was applied to the oxygen interstitial,  $I_{\text{O}}$ , by taking the same interstitial position as  $I_{\text{Ti}}$ . Contrarily to  $I_{\text{Ti}}$ , The structural relaxation of  $\text{TiO}_2$  with  $I_{\text{O}}$  lead to a non magnetic system with an energy lower by at least 1.3 eV than other considered ferromagnetic configurations. The  $I_{\text{O}}$  did not prefer to stay in the void between the Ti ions as observed for  $I_{\text{Ti}}$  but relax outward to bond simultaneously with two in-plane Ti ions and the oxygen ion in between. This latter is pushed

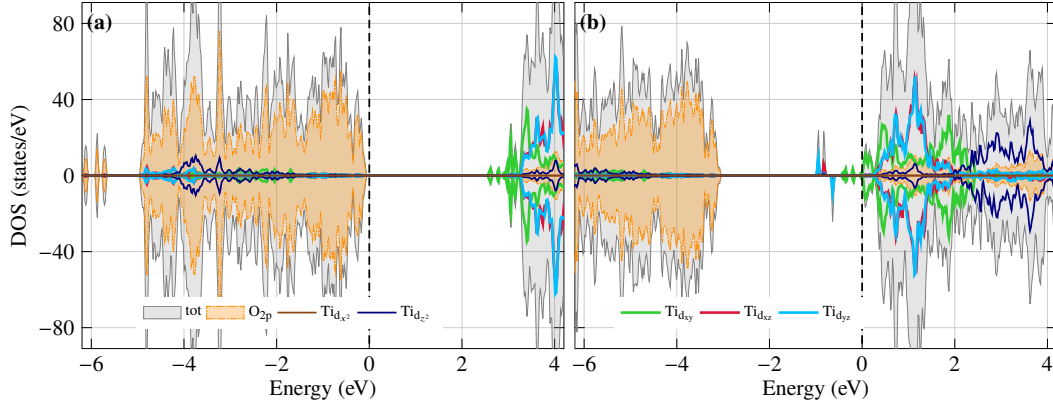


FIGURE 4.9: The density of states of TiO<sub>2</sub> in the presence of (a) oxygen interstitial and (b) Ti interstitial. The total density of states is shaded in gray. The partial density of states (PDOS) of oxygen 2p is shown by the filled orange areas. The decomposed PDOS of Ti 3d is presented by the colored solid lines, green for  $d_{xy}$ , red for  $d_{xz}$ , light blue for  $d_{yz}$ , dark blue for  $d_{z^2}$ , and brown for  $d_{x^2-y^2}$ . The black dashed lines indicate the zero energy levels of the considered systems.

away from its optimal position along  $x$ -direction which induced a structural distortion around I<sub>O</sub>. This becomes more obvious by looking at the bond angle Ti-I<sub>O</sub>-Ti or Ti-O-Ti (with O here as the displaced O ion) which is found to be 132° instead of 156° for other O ions.

In the interest of checking the difference between electronic properties of I<sub>Ti</sub> and I<sub>O</sub> related systems, the densities of states of the two defects are plotted and compared in Fig. 4.9. It can be seen in Fig. 4.9 (a), that no spin polarization for the defective system with I<sub>O</sub> is detected and the overall DOS does not show much difference compared to the pristine system in Fig. 4.2 (a). On the other hand, the DOS of the system with I<sub>Ti</sub> shown in Fig. 4.9 (b) exhibits different defect states at the edge of the conduction bands minimum. Those states emerged strictly from all the three  $t_{2g}$  ones.

## 4.4 Defects complexes

### 4.4.1 V<sub>O</sub>+I<sub>Ti</sub>

The defect complex V<sub>O</sub> + I<sub>Ti</sub> has been earlier identified as the origin of ferromagnetism in defective TiO<sub>2</sub> single crystals by Zhou *et al.* [180] by using a combination of x-ray diffraction, Raman scattering, and electron-spin resonance spectroscopy measurements as the origin of ferromagnetism in defective TiO<sub>2</sub> single crystals. This was recently confirmed by Dhakshinamoorthy *et al.*, [181] for TiO<sub>2</sub> nanoparticles. However, both single defects, V<sub>O</sub> and I<sub>Ti</sub>, were shown here to have an antiferromagnetic order instead. Will the combination of the two defects alter the magnetic order of the system?

The position of V<sub>O</sub> was fixed as the same used above for the single vacancy but the I<sub>Ti</sub> position was varied to check the stability of the defect total energy. Thus multiple starting configurations ranging from having I<sub>Ti</sub> exactly at the same position of V<sub>O</sub>, corresponding to a distance between the defects from 1 Å up to 4 Å were investigated. Also a fixed total spin moment from 0 to 4μ<sub>B</sub> is taken for each defect complex configuration. Interestingly, two classes of magnetic orders were obtained by



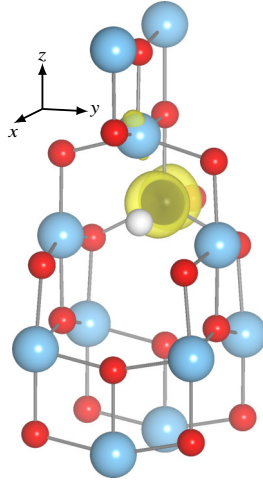


FIGURE 4.10: The spin density of  $\text{TiO}_2$  in the presence of the defect complex, oxygen vacancy and titanium interstitial ( $\text{V}_\text{O}+\text{I}_\text{Ti}$ ), is shown. Ti (O) atoms are presented by the large blue (small red) balls. The Ti interstitial is highlighted with the large black ball and oxygen vacancy with the small white balls. The isosurfaces of the spin density are plotted at the isovalue of  $\pm 0.02 \text{ \AA}^3$  with positive density (spin-up) in yellow color.

varying the distance  $\text{V}_\text{O}-\text{I}_\text{Ti}$ . The first one is the ferromagnetic order with a net magnetic moment of  $2\mu_\text{B}$  which was found as ground state for the smallest distance of  $1 \text{ \AA}$ . Actually the  $\text{I}_\text{Ti}$  has the freedom to relax and this distance will not necessarily be the same after relaxation which was the case for the two configurations. Putting the  $\text{I}_\text{Ti}$  on the position of  $\text{V}_\text{O}$  gives a higher total energy hence the interstitial did not maintain its initial position after relaxation and moved far away from the vacancy making a distance of  $1.71 \text{ \AA}$  between them. Indeed the second configuration has by far the lowest total energy among all the considered ones and corresponds to a distance of  $1.83 \text{ \AA}$  between the single defects. The second obtained class is the antiferromagnetic order for initial distance larger than  $2 \text{ \AA}$  which in turn relaxed to even larger distances than  $3 \text{ \AA}$ . This indicates that beyond a certain distance, which is here in the range of the usual  $\text{TiO}_6$  octahedral bond lengths, the two defects become isolated and did not interact. Therefore their antiferromagnetic nature is restored by having the single defects far apart. Such magnetic order is almost  $80 \text{ meV}$  higher than the FM one.

The interstitial Ti ion was found to hold a relatively large local magnetic moment of  $1.2\mu_\text{B}$  as illustrated in Fig. 4.10. Since  $\text{V}_\text{O}$ , as previously shown, prefers to polarize the in-plane nearest neighbor Ti ions,  $\text{I}_\text{Ti}$  was pulled upward to be on the same  $x$ -direction as  $\text{V}_\text{O}$ . The short distance of  $1.83 \text{ \AA}$  and the absence of a second Ti ion on the same  $(xz)$ -plane of the  $\text{V}_\text{O}$  (see Fig. 4.10) might be the reason of such large local magnetic moment which is not detected for all previous studied kind of defects.

The densities of states of isolated defects and the defect complex are compared in Fig. 4.11. The defects states  $d_{xz}$  are slightly pulled down by almost  $0.5 \text{ eV}$  towards the middle of the band gap region in Fig. 4.11 (c) compared to the isolated  $\text{I}_\text{Ti}$  DOS in Fig. 4.11 (b) and have more discontinuities like in  $\text{V}_\text{O}$  in Fig. 4.11 (a). Furthermore, the contribution of  $d_{yz}$  (Fig. 4.11 (b)) into the defect states are not anymore detected for the defect complex. Besides the intensity of  $d_{xz}$  is enhanced which confirms that the  $d_{xz}$  orbitals as origin of the observed FM order in  $\text{V}_\text{O}+\text{I}_\text{Ti}$  defective system.

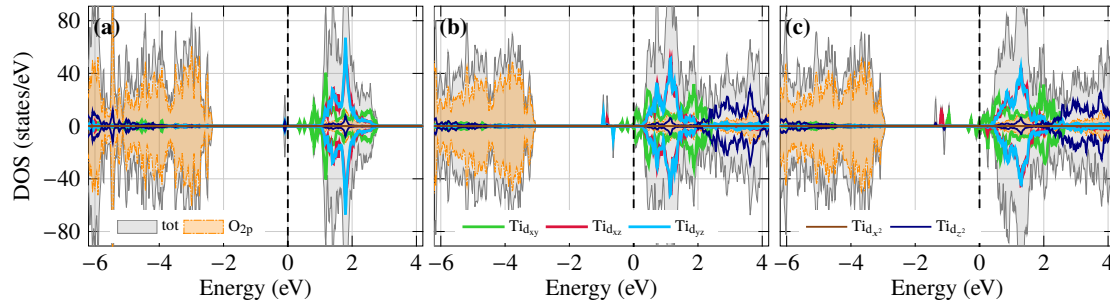


FIGURE 4.11: The density of states of TiO<sub>2</sub> in the presence of (a) oxygen vacancy , (b) Ti interstitial , and (c) the combination of an oxygen vacancy and Ti interstitial for the most stable configuration . The total density of states is shaded in gray. The partial density of states (PDOS) of oxygen 2*p* is shown by the filled orange areas. The decomposed PDOS of Ti 3*d* is presented by the colored solid lines, green for *d<sub>xy</sub>*, red for *d<sub>xz</sub>*, light blue for *d<sub>yz</sub>*, dark blue for *d<sub>z<sup>2</sup></sub>* , and brown for *d<sub>x<sup>2</sup>-y<sup>2</sup></sub>* . The black dashed lines indicate the zero energy levels of the considered systems.

#### 4.4.2 Frenkel pairs

Another defect complex which attracted recently much attention is the Frenkel pair in anatase TiO<sub>2</sub> [182, H2, 184, 194, 195]. The number of atoms within this kind of defect is preserved and only one (for FP) or two Ti atoms (for di-FP) are moved from their ideal anatase positions. Despite the high probability of the di-Frenkel pair formation as reported by Robinson *et al.* [184], the single Frenkel pair was found to be unstable and its formation probability is very low. The reason is the recombination of the interstitial and the vacancy. This result was recently confirmed with DFT calculations in [H2] where part of these investigations have been published. However the single Frenkel pair when combined with oxygen vacancy becomes stable and has the fourth highest defect formation probability according to Robinson *et al.* [184]. Thus the three defects will be discussed in the following and their electronic and magnetic properties will be compared.

This study is based on the previous theoretical investigations which were published in [H2]. After a thorough lookup for the most stable and magnetic di-Frenkel pairs in anatase TiO<sub>2</sub> among many considered configurations (more than 100 configurations), only the two most stable were carefully discussed [H2]. Here only the magnetic configuration with the lowest total energy will be considered for the di-Frenkel pair. Since the single Frenkel pair is unstable and prefers to recombine, configurations with close isolated defects will be ignored and only one pair from the di-Frenkel pair is considered. The same Frenkel pair is also combined with an oxygen vacancy. The magnetic moments of the three defects are as well checked with the fixed spin moment method.

Figure. 4.12 (a) presents the density of states of FP. As can be clearly seen no spin polarization is detected and the defect was found to be non magnetic. Due to the defect distortion, large distance between interstitial and its initial position (5.98 Å), the top of the valence band maximum is slightly changed with reference to the pristine system in Fig. 4.2 (a). However defect states which are mainly

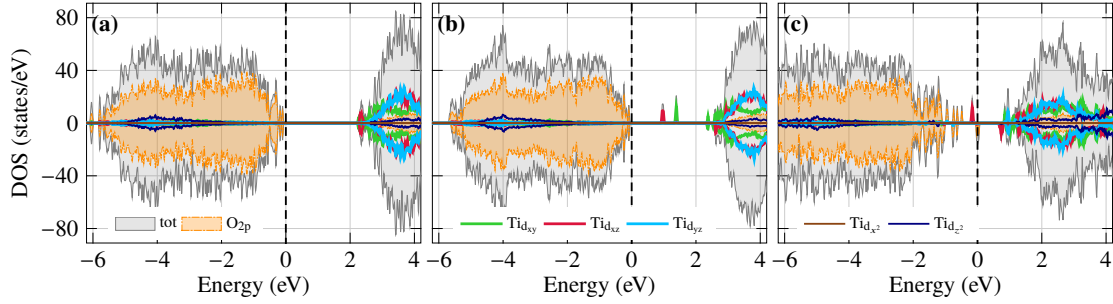


FIGURE 4.12: The density of states of  $\text{TiO}_2$  in the presence of (a) Frenkel pair, (b) Frenkel pair and oxygen vacancy, and (c) di-Frenkel pairs. The total density of states is shaded in gray. The partial density of states (PDOS) of oxygen  $2p$  is shown by the filled orange areas. The decomposed PDOS of Ti  $3d$  is presented by the colored solid lines, green for  $d_{xy}$ , red for  $d_{xz}$ , light blue for  $d_{yz}$ , dark blue for  $d_{z^2}$ , and brown for  $d_{x^2}$ . The black dashed lines indicate the zero energy levels of the considered systems.

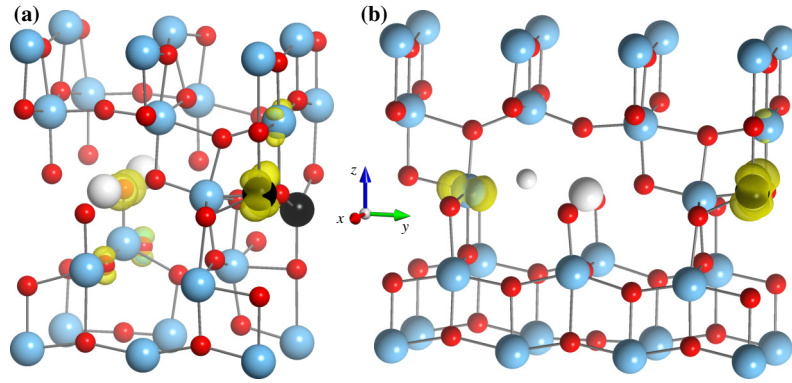


FIGURE 4.13: The spin densities for defective  $\text{TiO}_2$  with (a) di-Frenkel pair defect shown here in  $1 \times 2 \times 1$  supercell and (b) a Frenkel pair defect together with an oxygen vacancy shown here in  $1 \times 3 \times 1$  supercell. Ti (O) atoms are presented by the large blue (small red) balls. The Ti interstitial atoms are shown by the large black balls whereas the vacancies are presented by the white balls, small for oxygen vacancy and large for Ti vacancy. The isosurfaces of the spin densities are plotted at the isovalue of  $\pm 0.008 \text{ \AA}^3$  with positive density (spin-up) in yellow and negative density (spin-down) in blue color.

from Ti  $d_{xz}$  contribution were obtained on the conduction band minimum edge. In contrast to most investigated defects here, except O interstitial, the material shows a band gap of about 2.3 eV.

On the other hand, adding O vacancy to FP defect system pulled down the Ti  $d_{xz}$  states in the density of states to the middle of the band gap region as shown in Fig. 4.12 (b). These states together with Ti  $d_{xy}$  indicate a ferromagnetic response. This corresponds to a total magnetic moment of the supercell of  $2\mu_B$  with only two polarized Ti ions. The interstitial one has been found to have a local magnetic moment of  $0.7\mu_B$  whereas one of the Ti neighbors of the O vacancy relaxed to a moment of  $0.8\mu_B$  like the case of  $V_O + I_{Ti}$ .

The magnetic moments of di-FP defect is recalculated here and compared to the previous reported results [H2] where a total moment of  $2\mu_B$  was obtained. Surprisingly, by comparing the total

TABLE 4.2: Formation energies of the magnetic native defects in TiO<sub>2</sub> under the O-rich condition. Only neutral defects are considered here.

Defect	V <sub>O</sub>	2V <sub>O</sub>	V <sub>Ti</sub>	2V <sub>Ti</sub>	I <sub>Ti</sub>	V <sub>O</sub> +I <sub>Ti</sub>	FP+V <sub>O</sub>	di-FP
E <sub>form</sub> (eV)	5.29	10.47	6.75	8.30	10.05	14.84	10.08	15.53

energies of the defect supercells with fixed moments from 0 to  $4\mu_B$ , the lowest energy was obtained for  $1\mu_B$  instead of  $2\mu_B$  with a difference of 433 meV. Accordingly the local magnetic moments were found to be  $0.35\mu_B$  for I<sub>Ti</sub> and  $0.28\mu_B$  on the O ion between the two vacancies as illustrated in Fig. 4.13 (a). As obtained also for FP and FP+V<sub>O</sub>, the main defect states in di-FP are those from Ti  $d_{xz}$  states. In addition, some O  $p$ -states were also detected on the valence band maximum edge as shown in Fig. 4.12 (c).

## 4.5 Formation energies

In order to characterize the thermodynamical stability of defects, the defect formation energies have to be calculated as explained in Sec. 3.6. Only those defects which lead to a spin polarization will be considered in the following. Accordingly the formation energies are obtained using:

$$E_{\text{form}}(D, q) = \Delta E_{\text{tot}} - \sum_i n_i \mu_i + q\mu_e + E_{\text{corr}} \quad (4.1)$$

Only neutral defects are considered here, hence the last two terms in Eq. (4.1) which involve the supercell charge  $q$  are neglected in the following. Each of the chemical potentials in Eq. (4.1) is rewritten in terms of  $\mu_O$  to simplify the equation and keep only its dependence on  $\mu_O$ . Therefore the experimental conditions, whether pressure or temperature can be easily inserted by means of Eq. (3.72). In fact, DFT total energies define also a DFT condition which is most known as the oxygen rich limit. In this condition only the DFT total energies enter Eq. (4.1) which includes also the  $\mu_O$ . This latter is simply half of the DFT total energy of the free isolated molecule of O<sub>2</sub> in the triplet state. Afterwards, the chemical potential  $\mu_O$  at this condition will serve as a common reference for any other chemical potential [161], i. e.  $\Delta\mu_O = \mu_O(T, p^\circ) - \mu_O^{\text{max}}$ .

Table. 4.2 shows the calculated formation energies under the O-rich condition. Among the considered defects, V<sub>O</sub> is found to have the lowest formation energy of 5.29 eV. A close value of 4.95 eV was obtained by Li *et al.* using screened exchange functional [196]. The second and third lowest formation energies were obtained for V<sub>Ti</sub> and 2V<sub>Ti</sub>, respectively. Whereas the highest one was obtained for di-Frenkel pair defect. This high energy is simply the difference between the total energies for the supercells of di-Frenkel pairs and the pristine system because of the same number and nature of added and removed atoms. It follows that this kind of defect is unstable under the O-rich and any other condition. Note here that the discussion concerns only the magnetic di-FP which in turn has a higher total energy than the most stable and non magnetic di-Frenkel pairs. The non magnetic di-Frenkel pairs defect is only 262 meV higher than the pristine energy. The di-Frenkel pairs defect will be dropped from the further analysis because of its independence on the chemical potentials.

The so far obtained formation energies stem only from DFT energies under a condition characterized by solid state of  $O_2$ . In order to implement realistic conditions in the calculation of formation energies certain factors have to be taken into account. For instance polycrystalline and epitaxial films of  $TiO_2$  were obtained after a postgrowth annealing at 1,000 K [H2, 197]. This temperature is then inserted in Eq. (3.72) to obtain the appropriate oxygen chemical potential. The procedure requires also taking the experimental thermodynamical data from the thermochemical tables in NIST-JANAF database [160].

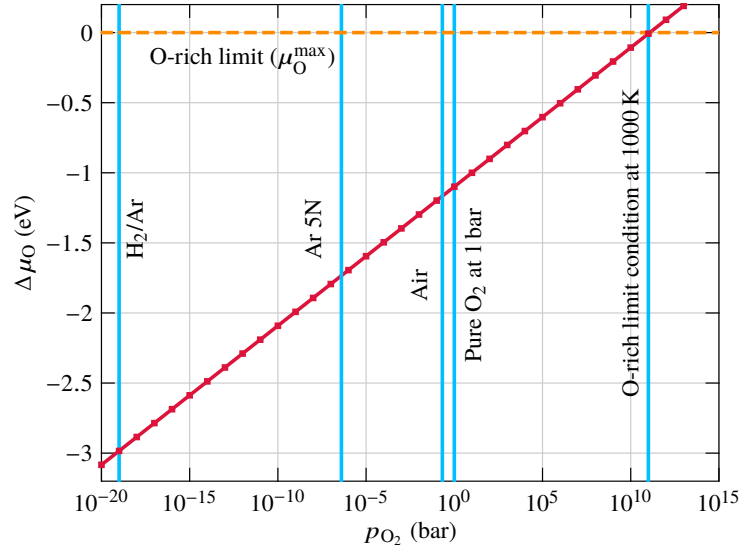


FIGURE 4.14: The relationship between oxygen partial pressures  $p_{O_2}$  and the relative chemical potential of oxygen  $\Delta\mu_O$  at a defined temperature of 1,000 K. The chemical potential under the O-rich condition  $\Delta\mu_O^{\max}$  is taken as reference. The dependence of the chemical potential on temperature and pressure is considered by applying Eq. (3.72). The values of the experimental pressures are taken from [H5].

The variation of the relative chemical potential of oxygen with respect to its partial pressure at 1,000 K is shown in Fig. 4.14. The intersection of the pressure-dependent chemical potential, presented in red color, with each of the experimental pressures of  $O_2$ , plotted by blue lines, determine the relative chemical potential at the chosen experimental pressure. It follows from Fig. 4.14 that the gas mixture condition of  $H_2/Ar$  corresponds to  $\Delta\mu_O = -2.98$  eV. As well the Ar 5N condition corresponds to  $\Delta\mu_O = -1.72$  eV whereas the air and the pure oxygen at 1 bar are equivalent to  $\Delta\mu_O$  of  $-1.17$  eV and  $-1.08$  eV, respectively. By the same way the corresponding  $p_{O_2}$  of the DFT condition (O-rich limit) is determined from the intersection of  $\Delta\mu_O^{\max}$  and pressure-dependent chemical potential, see Fig. 4.14. It is found to be equivalent here to 0.1 Tbar.

Once the relative chemical potentials  $\Delta\mu_O$  at the chosen experimental conditions are calculated, the formation energies for the different defects in  $TiO_2$  at those conditions can be determined. Fig. 4.15 shows the variation of defect formation energies with the experimental pressure condition at 1,000 K. The high formation energies obtained at O-rich limit as shown in Tab. 4.2 of both Ti vacancy and Ti divacancy are found to further increase with lowering  $\Delta\mu_O$  and consequently decreasing of  $p_{O_2}$ . However all the remaining defects lowered their formation energies by reducing  $p_{O_2}$ . The

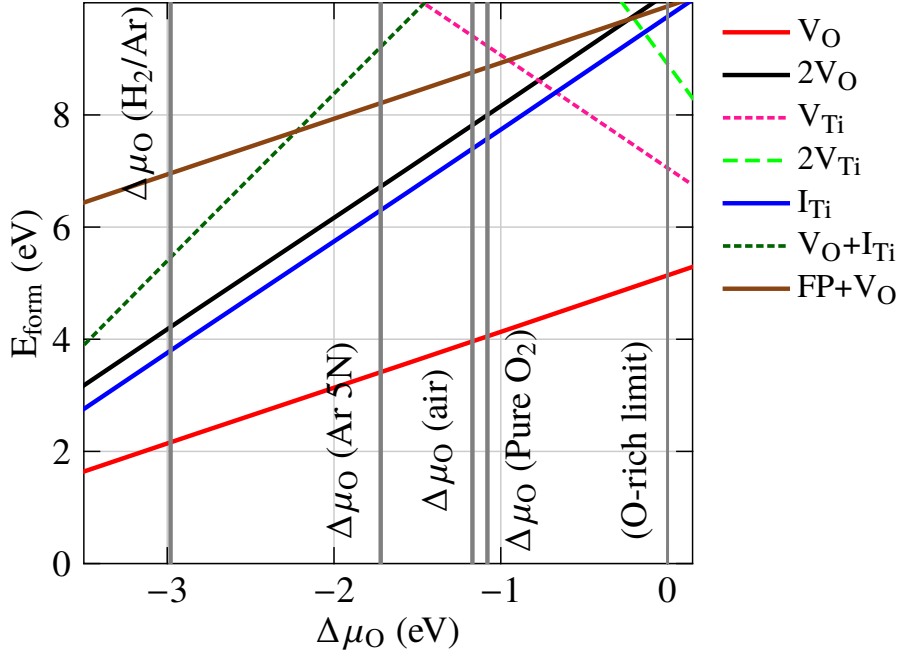


FIGURE 4.15: Formation energies for the selected magnetic defects in TiO<sub>2</sub> in dependence of the relative oxygen chemical potential  $\Delta\mu_{\text{O}}$  at  $T = 1,000$  K.

formation of  $V_{\text{O}}$  retained the lowest energy among all the considered defects, independently of  $p_{\text{O}_2}$  but decreased its value with the decrease of  $p_{\text{O}_2}$ . At air condition,  $I_{\text{Ti}}$  established the second obtained lowest formation energy after  $V_{\text{O}}$  which is almost half of its initial value at O-rich limit condition. However the combination  $V_{\text{O}}+I_{\text{Ti}}$  lead to high formation energy at the air condition. Such high value is nevertheless drastically reduced at the low pressure conditions. In addition the defect complex  $\text{FP}+V_{\text{O}}$  is found to reduce its formation energies by reducing  $p_{\text{O}_2}$ . It is worth mentioning here that including compensating charges to the supercell, in addition to the already used homogeneous background charge, might extremely affect the formation energies of the studied defects and also diminish the so far obtained differences between them [179, 193]. As example, the insertion of Ti atom and the removal of two oxygen atoms leads to the same charge number, i. e. +4 electrons. This is clearly reflected in Fig. 4.15 by their very close formation energies.

The inclusion of temperature dependence in the formation energy is also possible at a fixed pressure with Eq. (3.72). For instance the relation between the relative chemical potential  $\Delta\mu_{\text{O}}$  and the temperature at (Ar, 5N) condition can be deduced from Fig. 3.10, as demonstrated previously with the fixed temperature of 1,000 K and varied oxygen partial pressure. Four arbitrary temperatures are chosen here to demonstrate the effect of temperature on the defect formation energies in TiO<sub>2</sub>. The room temperature, 300 K, corresponds to  $\Delta\mu_{\text{O}} = -0.46$  eV. The higher temperatures of 500 K and 750 K correspond to a  $\Delta\mu_{\text{O}}$  of  $-0.81$  eV and  $-1.26$  eV respectively. The resulting formation energy of  $V_{\text{O}}$  was found to have the lowest formation energy. Its value decreased from 4.81 eV at 300 K to 3.56 eV at 1,000 K. In fact this decrease of the formation energy with increasing the temperature is not only achieved for  $V_{\text{O}}$  but for all considered defects except  $V_{\text{Ti}}$  and  $2V_{\text{Ti}}$ .

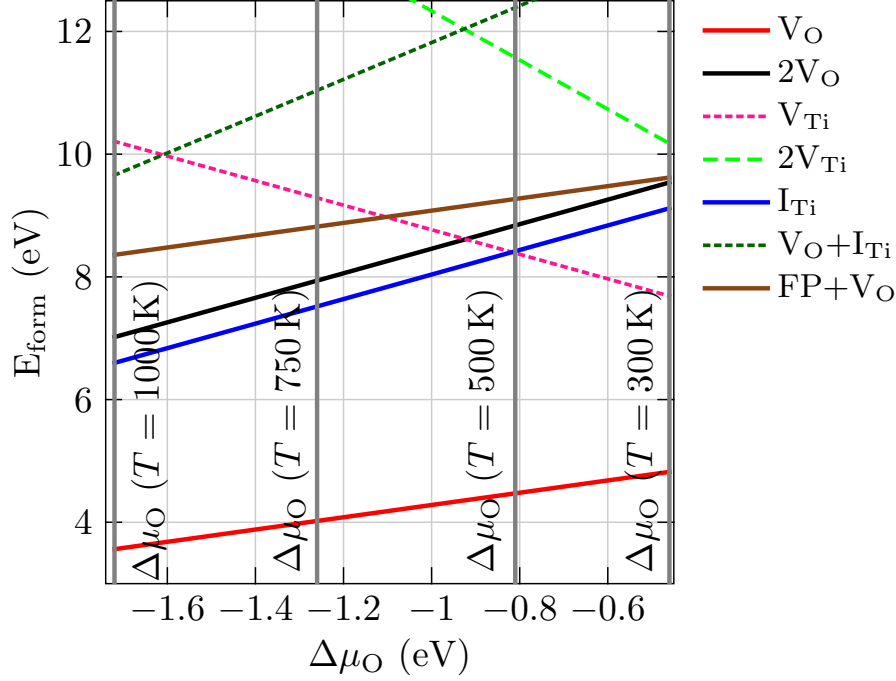


FIGURE 4.16: Formation energies for the selected magnetic defects in  $\text{TiO}_2$  in dependence of the temperature at the (Ar,5N) condition.

TABLE 4.3: The calculated magnetocrystalline anisotropy energies of defective  $\text{TiO}_2$ , which are obtained from total energy differences between configurations with spins oriented along  $x$ ,  $y$  and  $z$  crystallographic axes.

	Defect	$V_{\text{O}}$	$2V_{\text{O}}$	$I_{\text{Ti}}$	$V_{\text{O}}+I_{\text{Ti}}$	$\text{FP}+V_{\text{O}}$	di-FP
$\Delta E_{\text{tot}}$ (meV)	$x$	0.0	0.0	0.005	0.0	0.003	0.014
	$y$	0.008	0.013	0.0	0.0	0.0006	0.014
	$z$	0.005	0.007	0.003	0.0	0.0	0.0

## 4.6 Magnetocrystalline anisotropy

In all previous calculations, spin-orbit coupling is neglected. It was assumed to have a negligible effect on the structural relaxations of the different defect structures in  $\text{TiO}_2$ . However, strong spin-orbit contribution might induce a strong coupling between the magnetization and the crystallographic lattice. This results in an orbital contribution to the magnetization. Such contribution can reach or even exceed in some systems  $0.1\mu_{\text{B}}$  per atom [198]. This value is even comparable to the so far demonstrated spin contributions to the magnetization in the studied defect structures. Thus, the magnetocrystalline energy is calculated in the following for most of the magnetic defect structures. Owing mainly to the high formation energies of Ti vacancies ( $V_{\text{Ti}}$ ,  $2V_{\text{Ti}}$ ), whether by fixing the temperature to 1,000 K or the pressure to (Ar, 5N) conditions and also their oxygen originated magnetization, Ti vacancies will be dropped out from the following analysis.



Table 4.3 shows the obtained total energies for the different defects by varying only the spin moment directions. Only the three crystallographic directions are taken here for sake of simplicity. The energetically favorable direction is taken as reference energy in Tab. 4.3. Thus only the cost of aligning the spin moments along the other two directions is given. An easy axis along  $x$ -direction was found for defects involving only oxygen vacancies. On the other hand, Ti interstitial defect was found to adapt the  $y$ -direction instead as easy axis. Nevertheless, the combination of oxygen vacancy and Ti interstitial resulted in an isotropic magnetization along the three crystallographic axes. It is the only obtained defect which has equivalent total energies when changing the spin moment directions. It might be attributed to the anisotropy compensation of its forming isolated defects. The  $z$ -direction is prevailed as well as the easy axis of the magnetization for defects involving the Frenkel pair defects whether a single pair with an oxygen vacancy or di-Frenkel pairs. This latter gives the largest calculated magnetocrystalline anisotropy among the considered defects, i. e. 0.014 meV in agreement with the x-ray magnetic circular dichroism measurements [H2].

## Conclusion

The origin of the experimentally observed magnetism in TiO<sub>2</sub> is discussed with results of calculations based on the density functional theory. Various magnetic orders in the defective TiO<sub>2</sub> were obtained ranging from ferromagnetic, antiferromagnetic to ferrimagnetic. For instance, the presence of V<sub>O</sub> induces the polarization of the two neighboring Ti ions. These two Ti ions are antiferromagnetically coupled with a local magnetic moment of  $0.35\mu_B$  on each of them. This magnetic polarization is accompanied by the appearance of Ti  $d_{xy}$  states as defect states in the presence of one V<sub>O</sub>. Increasing the concentration of oxygen vacancies to have 2V<sub>O</sub> in the supercell was found to stabilize as well the AFM order with a difference of total energies of only 40 meV per supercell to another meta stable ferrimagnetic configuration. In this latter, the in-plane Ti ions, close to V<sub>O</sub>, are ferromagnetically coupled to each other but antiferromagnetically coupled to the same out-of-plane Ti ion. This leads to a total magnetic moment of  $2\mu_B$ . The density of states analysis of these two configurations of double V<sub>O</sub> showed that the defect states are mainly from the Ti  $d_{yz}$  and  $d_{z^2}$  states in the most stable configuration (AFM) while they are only from the Ti  $d_{z^2}$  in the metastable configuration. The effect of cation vacancies is as well checked. The inclusion of V<sub>Ti</sub> yields the polarization of all neighboring oxygen ions which gives a total magnetic moment of  $4\mu_B$ . Such magnetic moment reduces to  $2\mu_B$  in the presence of Ti vacancies as nearest neighbors due to the formation of O<sub>2</sub> dimer-like complex in the defect supercell. Only the O  $p_y$  states appear as defect states in the case of a single V<sub>Ti</sub> while both O  $p_x$  and  $p_y$  states show up as defect states in the density of states of double V<sub>Ti</sub>. The incorporation of Ti interstitials on the other hand is demonstrated to stabilize an AFM characterized by a large local magnetic moment of  $0.85\mu_B$  on I<sub>Ti</sub> compensated with tiny local moments of the surrounding oxygen ions. The formation of this defect was found to be accompanied by the onset of all three  $t_{2g}$  states as defect states. The situation is different with the incorporation of oxygen I<sub>O</sub> where the defect was stabilized to a non magnetic solution.

The combination of I<sub>Ti</sub> and V<sub>O</sub> as defect complex is likewise investigated. A FM ground state was obtained with a total magnetic moment of  $2\mu_B$ , most of it is localized on Ti interstitial, with a moment of  $1.2\mu_B$ . The local magnetic moment of the I<sub>Ti</sub> is by far the largest among all the studied defects in this chapter. Again, the defect states were checked from the density of states and it was concluded that they are primarily from the Ti  $d_{xz}$  states. The same states were found also as defect states for the defect complexes FP+V<sub>O</sub> and di-FP where  $p_x$  states appear as well on the valence



band minimum edge in the di-FP density of states. While the FP is non magnetic, the addition of  $V_O$  to FP or taking two FP as di-FP in the supercell have been shown to stabilize a FM order with a net magnetic moments of  $2\mu_B$  for FP+ $V_O$  and  $1\mu_B$  for di-FP.

Afterwards, the defect formation energies were calculated for only the obtained magnetic defects. It was found that  $V_O$  has the lowest defect formation energy which is followed by  $I_{Ti}$  and 2  $V_O$ , consecutively. Hence, these defects are more probable to form in anatase structure of  $TiO_2$ . Finally, magnetocrystalline anisotropy energies were examined and the largest anisotropic energy was obtained for the di-Frenkel pairs which supports the measured strong out-of-plane magnetic anisotropy [182, H2].



## 5 Strain and doping induced structural stability in BaTiO<sub>3</sub>

Barium titanate (BaTiO<sub>3</sub>) is one of the most interesting materials among the perovskite oxides. It is essentially considered as a prototype of ferroelectricity in material systems. Apart the ferroelectric characteristic, BaTiO<sub>3</sub> was also identified as a material with wide range of technical applications [199]. Apart its broad applicability, BaTiO<sub>3</sub> has been as well the focus of many theoretical and experimental investigations by virtue of its various structural phase transitions [200–204].

Starting from the simple cubic structure, structural transitions of BaTiO<sub>3</sub> can follow two distinct schemes. The first one is the so-called 3C modification: the cubic structure, which is stable for temperatures larger than 453 K [205] transforms into the tetragonal structure at 398 K. The tetragonal structure remains stable by cooling down up to 278 K. Below that, BaTiO<sub>3</sub> undergoes a transition towards the orthorhombic structure. At  $T = 183$  K, the rhombohedral structure becomes the most favorable structure. On the other hand, the second scheme to stabilize other structural phases of BaTiO<sub>3</sub> is indeed the 6H modification. It starts as well from the cubic structure. By heating up to 1,700 K, the hexagonal phase is stabilized. By extremely fast cooling down up to  $T = 222$  K, the orthorhombic phase is stabilized and remains the ground state structure till  $T = 70$  K where the monoclinic phase becomes most favored [206].

The 3C modification is extensively studied in literature with theoretical and experimental methods [207–210]. The choice is based on the occurrence of the ferroelectric tetragonal structure in this path. Although, the 6H modification is still not fully explored and only few studies were conducted on the structures of this modification. In particular, the hexagonal phase of BaTiO<sub>3</sub> has a fascinating structure with corner and face sharing octahedra. Such geometry leads to two different B sites, here Ti ions, with two different environments. Therefore much more flexibility can be accessed to control the system properties. Moreover, hexagonal perovskite structures were shown recently to accommodate ion conductivity [211] which is of great importance in energy-related applications. These two reasons make the hexagonal phase of BaTiO<sub>3</sub> a good candidate for new functionalities. The only drawback here is that BaTiO<sub>3</sub> is only stable at high temperatures, 1,700 K which is not far from the melting temperature of 1,898 K for BaTiO<sub>3</sub>.

Actually, the stabilization of the hexagonal phase of BaTiO<sub>3</sub> was shown to take place at lower temperatures but with external stimulus. It manifests on one hand with cooling the sample in strongly reducing atmosphere [212, 213]. Therewith, the hexagonal structure becomes stable at  $T \approx 1,473$  K. Doping with  $3d$  transition metal elements was shown on the other hand to stabilize BaTiO<sub>3</sub> at room temperature [214–219]. Interestingly, a simultaneous coexistence of room-temperature ferromagnetism and ferroelectricity was detected in Fe-doped BaTiO<sub>3</sub> [219].

TABLE 5.1: The theoretical atomic positions of the hexagonal phase of BaTiO<sub>3</sub> obtained with the cell parameters  $a = 5.805 \text{ \AA}$  and  $c = 14.077 \text{ \AA}$  [222]. The Wyckoff site of each atom is indicated by W.S.

Atoms	W.S	Coordinates		
		$x$	$y$	$z$
Ba(1)	$2b$	0.0	0.0	$1/4$
Ba(2)	$4f$	$1/3$	$2/3$	0.0967
Ti(1)	$2a$	0.0	0.0	0.0
Ti(2)	$4f$	$1/3$	$2/3$	0.8463
O(1)	$6h$	0.5185	0.0370	$1/4$
O(2)	$12k$	0.8349	0.3302	0.0802

In this direction, a theoretical investigation of Fe-doped BaTiO<sub>3</sub> is made here to demonstrate the exact position of Fe in the structure of BaTiO<sub>3</sub>. The stability of whether single defects or defects complexes incorporating oxygen vacancies will be discussed in terms of defect formation energies (Sec. 3.6). The results will be as well compared to the angle-dependent single crystal electron paramagnetic resonance (EPR) results [16]. Such method allows retrieving a detailed information on the charge state and defect geometry of the impurity which permits a direct comparison with the actual calculations. Later, the hexagonal phase will be shown to be stable even without doping with transition metal elements. Only a biaxial strain along the  $ab$ -plane will be shown as enough to have a stable hexagonal BaTiO<sub>3</sub> phase. The results will be discussed with phonon calculations of the IR and Raman spectra and compared to available experimental data.

## 5.1 Crystal structure

Hexagonal BaTiO<sub>3</sub> adapts the space group  $P6_3/mmc$  (No. 194). The primitive cell consists of six functional units of BaTiO<sub>3</sub> with 30 atoms in total. The crystal structure can also be considered as stacked layers of BaO<sub>3</sub> and TiO<sub>2</sub> along the  $c$  axis as shown in Fig. 5.1 which is not the same as the cubic phase. The stacking sequence is (ABC)(ABC) in the cubic whereas it is (ABA)(CBC) in the hexagonal phase [H6]. The corner-sharing octahedra are formed by Ti(1) and O(2). This kind of octahedra is present in cubic and hexagonal structures. The face-sharing octahedra occur only in the hexagonal phase and are formed by Ti(2) and O(1). The calculated atomic positions in BaTiO<sub>3</sub> are summarized in Tab. 5.1 which are in agreement with the reported experimental structures [220, 221].

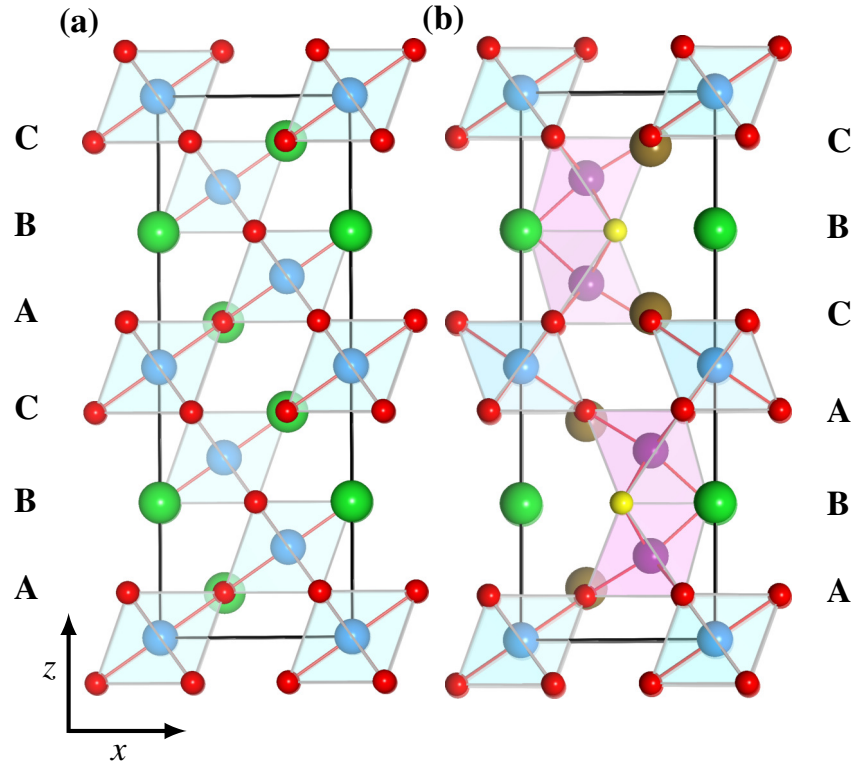


FIGURE 5.1: Crystal structure of (a) the cubic phase shown here along (111) direction (b) the hexagonal phase of  $\text{BaTiO}_3$ . The two different Ba atoms in the hexagonal phase are distinguished with colors: green balls for Ba(1) and brown balls for Ba(2). The same applies for Ti atoms where Ti(1) (Ti(2)) are presented with the light blue (violet) balls. Oxygen atoms are also distinguished with yellow balls for O(1) and red balls for O(2). The same colors will be adapted for all the following figures in this chapter. The corner-sharing oxygen octahedra of Ti(1) (light blue) and the face-sharing oxygen octahedra of Ti(2) (violet) are as well highlighted with octahedral colors. The stacking of different  $\text{BaO}_3$  and  $\text{TiO}_2$  layers is indicated for each of the two phases with the corresponding stacking sequence.

## 5.2 Structural stability with Fe-doping

### 5.2.1 Isolated defect $\text{Fe}_{\text{Ti}}$

In order to model the defective Fe-doped  $\text{BaTiO}_3$  system, a large supercell of  $3 \times 3 \times 1$  is considered, which gives in total 270 atoms. The substitution of one Ti by Fe corresponds to defect concentration of 1.85 % which is in the order of the experimentally reported value of 2 % [16]. Note here that, two different Ti atoms exist in the unit cell, therefore the Fe substitution is checked on both sites, Ti(1) and Ti(2). In addition, the charge state of the Fe impurity is varied by imposing a supercell charge  $q = (-2, -1, 0, 1)$ . The Fe ion in the neutral state  $q = 0$  is assumed to have the same oxidation state of Ti, i. e.  $\text{Fe}^{4+}$ . Hence, an oxidation state of +2 and +3 can be assigned for the charged supercells with  $q = -2$  and  $-1$ , respectively. Similarly, the oxidation state like Fe in the charged supercell of  $q = 1$  is assumed to be 5+.

TABLE 5.2: The dependence on the Ti site of the calculated magnetic moments and formation energies of Fe-doped BaTiO<sub>3</sub>. Only charge state which gives the lowest formation energy ( $E_{\text{form}}$ ) at each site are presented. Formation energies are calculated at the air condition and  $T = 1,673$  K [H5].  $m_{\text{Fe}}$  is the local magnetic moment of Fe atom and  $M$  is the supercell magnetic moment.

Site	$q$	Fe state	$m_{\text{Fe}} (\mu_{\text{B}})$	$M (\mu_{\text{B}})$	$E_{\text{form}} (\text{eV})$
Ti(1)	1	Fe <sup>5+</sup>	4.21	5.00	0.739
Ti(2)	1	Fe <sup>5+</sup>	3.34	3.00	0.226

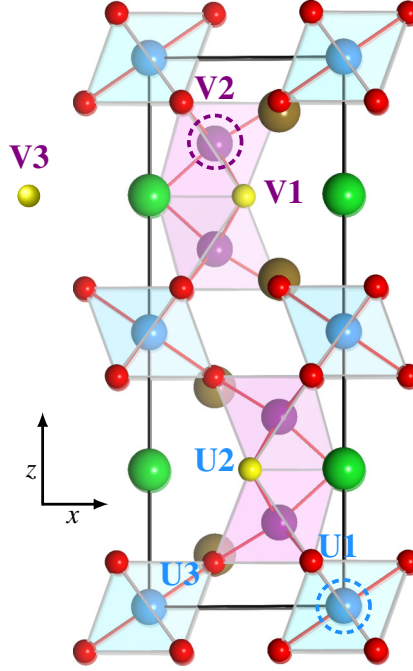


FIGURE 5.2: The oxygen vacancy positions in the hexagonal phase of BaTiO<sub>3</sub> adapted here to model the defect complex  $\text{Fe}_{\text{Ti}}+\text{V}_{\text{O}}$ . The  $U_i$  are related to the substitution of Ti(1) with Fe (highlighted with dashed light blue circle) while the  $V_i$  are related to the substitution of Ti(2) with Fe (highlighted with dashed violet circle). Note that V3 is the image of V1 in the neighboring unit cell. Distances between  $U_i$  ( $V_i$ ) and the corresponding Ti are given in Tab. 5.3.

Substituting Ti(2) with Fe was found to be more stable than inserting Fe at Ti(1) position (lower formation energy, see Tab. 5.2). Moreover despite having the same supercell charge, the two defects lead to different magnetic moments with a deviation of  $2\mu_{\text{B}}$ . Such moments were as well cross checked with the spin fixed moments method as explained in Sec. 4.1. In the case of Ti(2), the local magnetic moment of Fe is larger than that of the supercell which hints to small negative polarization of the surrounding oxygen atoms.

### 5.2.2 Defect complex $\text{Fe}_{\text{Ti}}+\text{V}_{\text{O}}$

Apart the excess electron compensation mechanism, Böttcher *et al.* [16] proposed a charge-compensation through oxygen vacancies. Hence, two excess electrons are induced. As the isolated defect  $\text{Fe}_{\text{Ti}}$  favors a charge of  $q = +1$ , the addition of one electron is again checked for the complex

TABLE 5.3: Comparison of the calculated properties for the  $\text{Fe}_{\text{Ti}}\text{-V}_{\text{O}}$  complexes for various lattice positions of  $\text{V}_{\text{O}}$ . The different  $\text{V}_{\text{O}}$  sites are indicated in Fig. 5.2.  $d_{\text{Fe-V}_{\text{O}}}$  is the distance between Fe impurity and O vacancy and  $E_{\text{form}}$  is the formation energy of the defect complex calculated using  $\Delta\mu_{\text{O}}$  (air). Data are presented in ascending order of formation energies.

site	Defect configuration			$E_{\text{form}}$ (eV)	
	$\text{V}_{\text{O}}$	$d_{\text{Fe-V}_{\text{O}}} (\text{\AA})$	shell	$(\text{Fe}^{2+}\text{-V}_{\text{O}})$	$(\text{Fe}^{3+}\text{-V}_{\text{O}})$
Ti(1)	U2	4.57	2	-0.18	-1.67
	U1	2.01	1	0.28	-0.99
	U3	4.59	2	0.56	-0.97
Ti(2)	V2	2.01	1	-0.11	-1.63
	V3	4.77	2	-0.05	-1.48
	V1	1.98	1	0.35	-0.90

defect. Thus, the two possible Ti types are reconsidered here, Ti(1) and Ti(2), to host the Fe ion. The oxygen vacancy position is then taken up to the second shell around the corresponding  $\text{Fe}_{\text{Ti}}$ , as illustrated in Fig. 5.2. Following the previous assumption that Fe has the charge state of +4 (that of Ti) in a neutral isolated defect, the charge state is +2 in the presence of oxygen vacancy. Hence the supercell charges of 0 and +1 will be attributed to the presence of Fe as  $\text{Fe}^{2+}$  and  $\text{Fe}^{2+}$ , respectively.

Table 5.3 shows the calculated formation energies for different defect configurations at air condition. The lowest formation energy is found for the U2 configuration where Fe is introduced in Ti(1) position and the oxygen vacancy is formed on the second shell, see Fig. 5.2. Note that, the isolated defect was shown previously to stabilize onto Ti(2) instead. However, the second lowest formation energy corresponds to V2 which is characterized by substituting Ti(2) with Fe and putting an oxygen vacancy on the first shell of Fe. Interestingly, adding one electron into the system ( $\text{Fe}^{2+}\text{-V}_{\text{O}}$ ) was found to largely decrease the formation energies by almost 1.5 eV for all defect configurations without altering their order, see Tab. 5.3. This agrees very well with the EPR measurements where only  $\text{Fe}^{3+}$  were detected [16].

### 5.3 Structural stability with biaxial strain

It is obvious here to start by investigating the microscopic origin of the structural instability of the hexagonal phase of  $\text{BaTiO}_3$ . Hence, the driving reason of instability can be checked with an applied uniaxial strain. In this direction, the vibrational properties of the system are computed using:

$$\det\left(\frac{1}{\sqrt{M_s M_{s'}}} \frac{\partial^2 E(\mathbf{R})}{\partial \mathbf{u}_{s,\alpha}(\mathbf{k}) \partial \mathbf{u}_{s',\alpha'}(\mathbf{k})} - \omega_{i,\mathbf{k}}^2\right) = 0, \quad (5.1)$$

TABLE 5.4: The decomposed irreducible representation of the hexagonal point group D<sub>6h</sub>(6/mmm). The optical Infrared active modes are  $6A_{2u} \oplus 8E_{1u}$  while the optical Raman active modes are:  $5A_{1g} \oplus 8E_{2g} \oplus 6E_{1g}$ . Data is taken from [227].

Atom	Site	IR active modes	Raman active modes
Ti(1)	2a	$A_{2u} \oplus E_{1u}$	—
Ba(1)	2b	$A_{2u} \oplus E_{1u}$	$E_{2g}$
Ba(2), Ti(2)	4f	$A_{2u} \oplus E_{1u}$	$A_{1g} \oplus E_{2g} \oplus E_{1g}$
O(1)	6h	$A_{2u} \oplus 2 E_{1u}$	$A_{1g} \oplus 2 E_{2g} \oplus E_{1g}$
O(2)	12k	$2 A_{2u} \oplus 3 E_{1u}$	$2 A_{1g} \oplus 3 E_{2g} \oplus 3 E_{1g}$

where  $s$  runs over the number of atoms ( $1 \cdots S$ ),  $M_s$  is atomic mass of  $s$ .  $E$  is the total energy of the system and  $R$  is real space vector. The cartesian components are denoted by  $\alpha$ .  $\mathbf{u}_{s,\alpha}$  is the displacement of atom  $s$  along  $\alpha$ .  $\omega$  is the vibration frequency at  $\mathbf{k}$  of the mode  $i$ . There are in total  $3S$  modes, three of them are acoustic while the remaining are optic modes.

The phonon frequencies in Eq. (5.1) can be computed with the change of total energy  $E$  under a finite atomic displacement with the framework of the so-called frozen phonon technique [223]. However, this method requires sometimes a very large supercell to cover a  $q$  vector of interest beyond the  $\Gamma$  zone-center. This requirement is avoided by using the density functional perturbation theory (DFPT) [224–226] which is restricted to the unit cell at the cost of a moderate additional computational effort. Nevertheless, it allows a direct calculation of the vibrational properties at any given  $q$  using only the unit cell. Therefore, the method will be applied in the following.

Within the harmonic approximation, if  $\omega_{i,\mathbf{k}}$  in Eq. (5.1) is real, the mode  $i$  is stable while an imaginary value of  $\omega_{i,\mathbf{k}}$  signifies the presence of an unstable mode, referred to as soft mode, and consequently the instability of crystal structure. Such instabilities are commonly ascribed to either ferroelectricity or ferroelasticity in perovskite oxides. Ferroelectric instability occurs on the Brillouin zone center  $\Gamma$  whereas the ferroelastic one shows up at the boundary of the Brillouin zone ( $\mathbf{q} \neq \Gamma$ ). This kind of instability will be on the focus of the following investigations using mainly the IR active modes. Based on the space group symmetries of the hexagonal phase of BaTiO<sub>3</sub>, the 87 optic modes (30 atoms give rise to 90 modes, three of them are acoustic) can be decomposed into individual irreducible representations as shown in Tab. 5.4.

### 5.3.1 Unstrained structure

From experiment, two soft modes were reported, both of them are zone-centered [228–231]. The first mode,  $E_{2u}$  is associated to the structural phase transition at 222 K. The second mode,  $A_{2u}$ , is in turn associated to the structural transition at 74 K. This latter is ferroelectric and responsible for the giant LO-TO splitting in hexagonal BaTiO<sub>3</sub> as reported by Inoue [232].



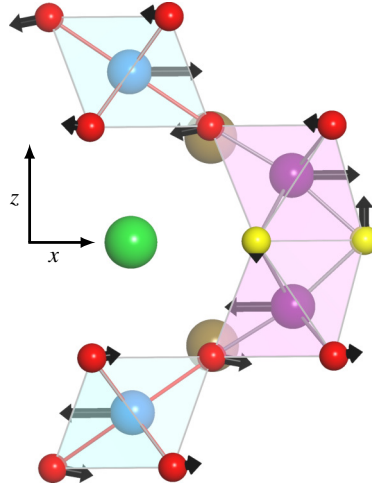


FIGURE 5.3: Eigenvectors of the soft acoustic mode  $E_{2u}$  ( $\omega = 99.4i \text{ cm}^{-1}$ ) in the hexagonal phase of  $\text{BaTiO}_3$ . The vibration directions are highlighted with the black arrows on each vibrating atom.

In agreement with experiment, the two soft modes were found in density functional perturbation theory calculations where the first one,  $E_{2u}$ , is acoustic and neither IR nor Raman active as already demonstrated in the irreducible representation of the hexagonal  $\text{BaTiO}_3$ , see Tab. 5.4. This mode is found to be double degenerate with a frequency  $\omega$  of  $99.4i \text{ cm}^{-1}$ . Such degeneracy is checked by breaking the hexagonal symmetries along different directions. In all used directions, the  $E_{2u}$  mode remains double degenerate. A result was earlier proposed in the experimental work of Yamaguchi *et al.* [233] where the  $E_{2u}$  was believed to split into two undamped Raman active modes only below 222 K. The two resulting modes harden on further cooling and exhibit non classical temperature behavior.

Figure. 5.3 shows the eigenvectors of the acoustic mode  $E_{2u}$ . Therein, the Ti ions on each layer move in the opposite direction of those in the adjacent layers. Each Ti displacement is compensated by its surrounding O ions forming  $\text{TiO}_6$ . The O ions move along the same  $x$  or  $y$  direction as Ti ions but with opposite sign, except O(1) ions. The vibration of O(1) is rather different from O(2) in the direction and does not follow in addition a collective displacement as for O(2), see Fig. 5.3. The O(1) ions move actually in the out-of-plane  $z$  direction but with an antiparallel vibration to each other.

The  $A_{2u}$  mode is on the other hand IR active and its calculated frequency is very close to the experimental one as shown in Tab. 5.5. Such agreement is not only obtained for the soft mode but for all  $A_{2u}$  modes. An analogy with the modes of cubic phase is also possible and is made in Tab. 5.5 following Inoue *et al.* [232]. The hexagonal  $A_{2u}$  mode is harder than its cubic counterpart in calculated and measured frequencies. In addition, the soft TO mode  $A_{2u}$  in both  $\text{BaTiO}_3$  phases (Fig. 5.4) are associated with the hard modes at  $\omega = 92.03 \text{ cm}^{-1}$  for the hexagonal phase and  $\omega = 178.46 \text{ cm}^{-1}$  for the cubic phase. This finding goes in line with the observed splitting by Inoue *et al.* [232] which was referred to as giant LO-TO splitting. Hence, the obtained results confirm that such large splitting is a common characteristic of  $\text{TiO}_6$  octahedra and is independent of the octahedral stacking sequence.

TABLE 5.5: Optical phonon  $A_{2u}$  mode frequencies in the hexagonal phase of BaTiO<sub>3</sub> with their corresponding modes in the cubic phase of BaTiO<sub>3</sub>. A comparison between the calculated frequencies using density functional perturbation theory and those obtained from experimental IR measurements of Inoue *et al.* [232], values in parentheses correspond to measured frequencies with hyper-Raman spectroscopy. Frequencies are given in (cm<sup>-1</sup>).

mode	Hexagonal BaTiO <sub>3</sub>		Cubic BaTiO <sub>3</sub>		
	Calculation	experiment [232]	Calculation	experiment [232]	
TO	1	94.76i	78i (80i)	112.53i	87i
	2	93.30	109 (110)		
	3	129.13	141	181.90	182
	4	329.29	397		
	5	451.13	466 (480)	481.65	482
	6	660.16	698(715)		
LO	1	92.03	105	178.46	178
	2	128.85	139		
	3	328.78	381	455.74	460
	4	434.16	452		
	5	614.58	646	682.87	710
	6	695.66	742 (754)		

In order to check the origin of the  $A_{2u}$  instability, its eigenvectors are shown in Fig. 5.4 in both cubic and hexagonal phases of BaTiO<sub>3</sub>. In overall, the vibrations in both structures are quite similar. Only the Ti and O ions are moving while the Ba ions are frozen with almost zero contribution. The Ti ions (Ti(1) and Ti(2)) are moving in the opposite direction of the surrounding O ions (O(1) and O(2)) with a minor distortion of TiO<sub>6</sub> octahedra. This confirms the ferroelectric nature of the  $A_{2u}$  mode in cubic and hexagonal phases. Such ferroelectricity is the direct result of a delicate balance between long-range Coulomb interactions and short-range forces [234].

The effect of Coulomb interactions on the crystal can be determined with the dynamical Born effective charges which are directly connected to LO-TO splitting through the dynamical matrix [235]. Here, the Born effective charge tensors  $Z_s^*$ , Tab. 5.6, are computed by two methods: from the induced polarization along the  $\alpha$  direction when a small displacement of atom  $s$  in  $\beta$  direction or from the induced force on  $s$  after applying an electric field, following the idea of Umari and Pasquarello [236]. Both methods are implemented in Quantum espresso code [24] and the Born effective charges are cross checked with these methods.

Table. 5.6 summarizes the non zero components of  $Z_s^*$  tensors for each ion. As clearly seen in Tab. 5.6, most of the effective charges are larger in magnitude than their nominal charges. In particular, the Born effective charge of Ti(1) was found to be  $\approx 3e$  larger than its nominal value. A similar value was also obtained for the cubic phase of BaTiO<sub>3</sub>. Such large Born charges were always seen as feature of perovskite ABO<sub>3</sub> [234]. Again, this study shows that large Born effective

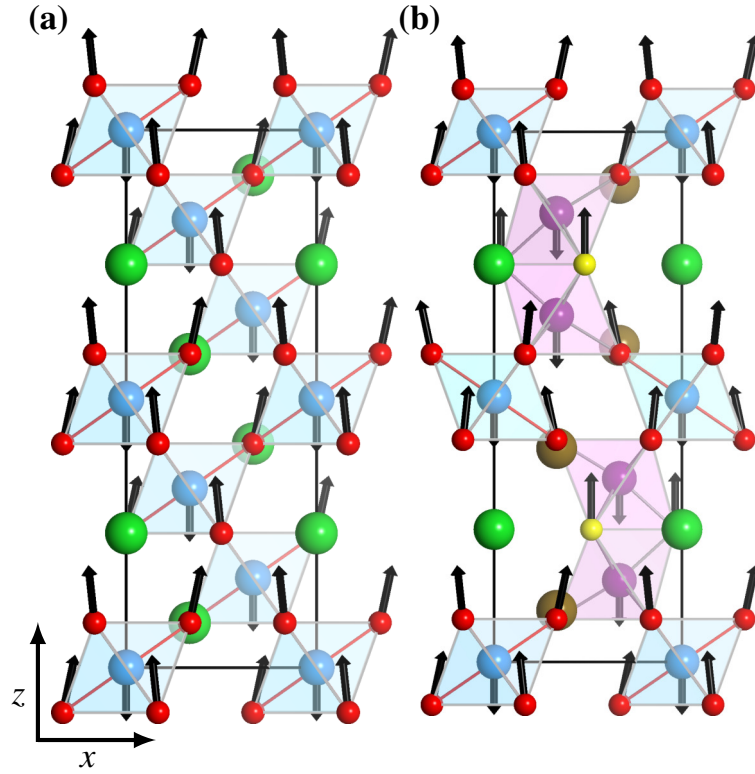


FIGURE 5.4: Eigenvectors of the optical vibrational modes  $A_{2u}$  (TO) (a) in the cubic phase along  $(111)$  direction (b) in the hexagonal phase of  $\text{BaTiO}_3$ . The vibration directions are highlighted with the black arrows on each vibrating atom within the  $A_{2u}$  mode. Only Ti and O ions are vibrating within this mode whereas the Ba ions are frozen in their positions. The corresponding frequencies are given in Tab. 5.5.

TABLE 5.6: The Born effective charge  $Z^*$  tensors in Cartesian coordinates for the hexagonal phase of  $\text{BaTiO}_3$ .  $Z$  are the nominal ionic charges in  $\text{BaTiO}_3$ . The atoms O(1) and O(2) have more than a unique tensor, most of them differ only by the component signs (the sign  $\pm$  is added to the respective component). Zero components are not written here for sake of readability. Units are in  $e$ .

Atom	$Z$	$Z^*_{xx}$	$Z^*_{yy}$	$Z^*_{zz}$	$Z^*_{xy}$	$Z^*_{yx}$	$Z^*_{xz}$	$Z^*_{zx}$	$Z^*_{yz}$	$Z^*_{zy}$
Ba(1)	2	2.79	2.79	2.66						
Ba(2)	2	2.97	2.97	2.72						
Ti(1)	4	7.46	7.46	7.13						
Ti(2)	4	5.42	5.42	7.02						
O(1)	-2	-1.97	-2.95	-3.45						
O(1)	-2	-2.71	-2.21	-3.45	$\pm 0.42$	$\pm 0.42$				
O(2)	-2	-1.95	-4.60	-3.15					$\pm 1.66$	$\pm 1.83$
O(2)	-2	-3.93	-2.61	-3.15	-1.14	-1.14	$\pm 1.44$	$\pm 1.58$	$\pm 0.83$	$\pm 0.91$
O(2)	-2	-3.93	-2.61	-3.15	1.14	1.14	$\pm 1.44$	$\pm 1.58$	$\mp 0.83$	$\mp 0.91$

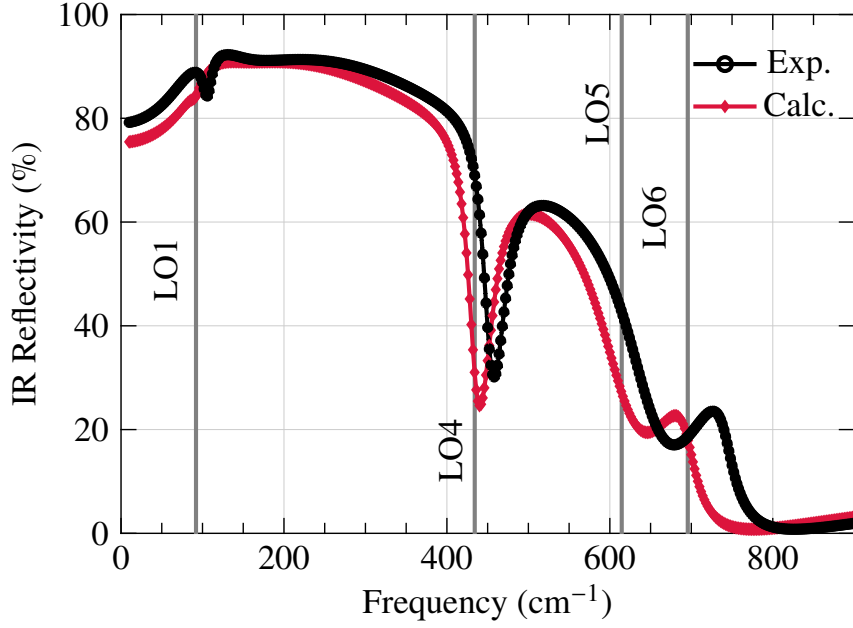


FIGURE 5.5: A comparison between the experimental and theoretical infrared reflection spectrum obtained with  $A_{2u}$  modes in the hexagonal phase of BaTiO<sub>3</sub>. The experimental data is adapted from [232]. The vertical lines show the strongest changes in the IR reflectivity which correspond to the longitudinal  $A_{2u}$  modes (LO1, LO4, LO5 and LO6) as given in Tab. 5.5.

charges like the giant LO-TO splitting are not exclusive features of perovskite structures but of TiO<sub>6</sub> octahedra. Interestingly, Ti(2) has lower effective charge than Ti(1) especially in the  $xy$  in-plane components,  $5.42 e$  compared to  $7.46 e$  for Ti(1). That means, Ti(1) ion carry more charge than Ti(2) when a small atomic displacement is applied on both ions. Moreover, a strong anisotropy was obtained for oxygen Born effective charges which is more pronounced at O(2). Knowing that O(2) are bound to Ti(1), the reduction of  $Z_{\text{Ti}(1)}^*$  and the anisotropy of  $Z_{\text{O}(2)}^*$  can be ascribed mainly to the resulting strong hybridization between Ti(1) and O(2) states, much stronger than that between Ti(2) and O(1).

The Born effective charges are not easily accessible from experiment. But their effect, namely the LO-TO splitting can be directly measured. In order to quantify rigorously the deviation of the calculated splitting from the experiment, Tab. 5.5, one needs to gather all the mode splittings in one quantity which can be directly accessed from experiment. The infrared reflectivity  $R$  presents the ideal quantity to deal with, especially for polar modes like  $A_{2u}$  modes (an electric field parallel to  $z$  direction couples with the polarization of  $A_{2u}$  [237]). The determination of  $R$  is made with the complex dielectric function  $\varepsilon(\omega)$ . In turn,  $\varepsilon(\omega)$  can be obtained by fitting a four parameters model [238]: frequency of longitudinal (transversal) modes  $j$ ,  $\omega_j(\text{LO})$  ( $\omega_j(\text{TO})$ ), the damping constants of  $j$ -th LO (TO) modes,  $\gamma_j(\text{LO})$  ( $\gamma_j(\text{TO})$ ):

$$\varepsilon(\omega) = \varepsilon_\infty \prod_j \frac{\omega_j^2(\text{LO}) - \omega^2 + i\omega\gamma_j(\text{LO})}{\omega_j^2(\text{TO}) - \omega^2 + i\omega\gamma_j(\text{TO})}, \quad (5.2)$$

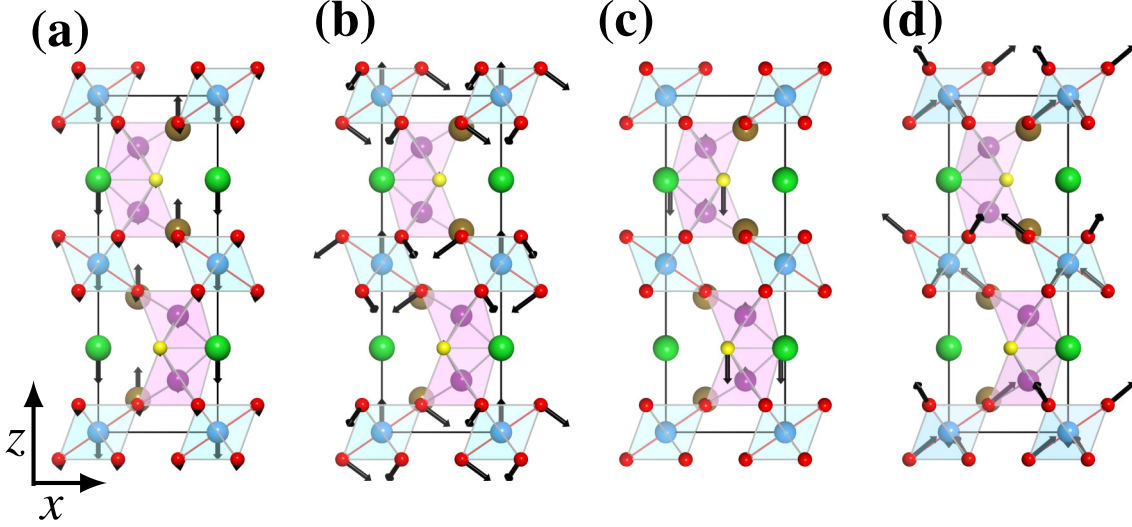


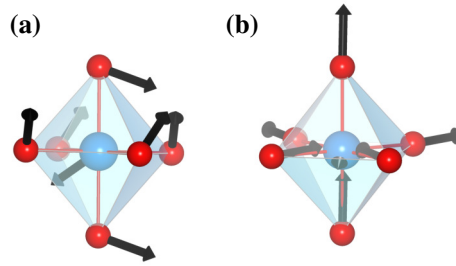
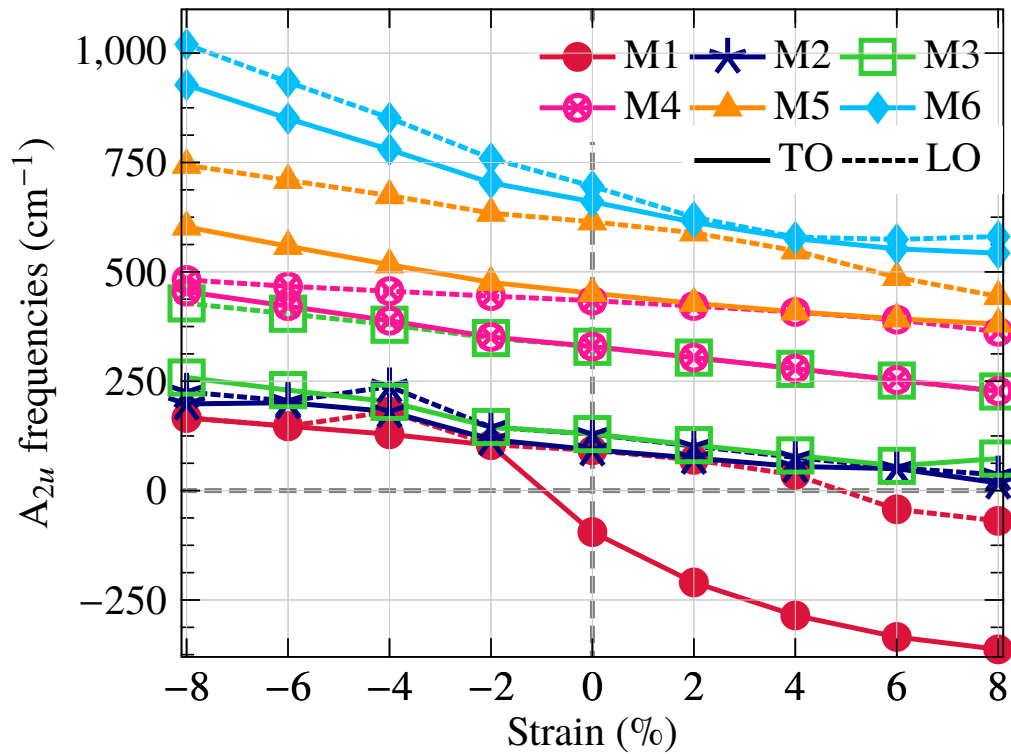
FIGURE 5.6: The eigenvectors of the four longitudinal  $A_{2u}$  modes, which are highlighted in Fig. 5.5. (a) LO1, (b) LO4, (c) LO5, and (d) LO6 mode. The corresponding frequencies are given in Tab. 5.5.

where  $\varepsilon_\infty$  is the dielectric constant. Once the complex dielectric function is determined, it can be used in the calculation of the IR reflectivity:

$$R(\omega) = \left| \frac{\sqrt{\varepsilon(\omega - 1)}}{\sqrt{\varepsilon(\omega + 1)}} \right|^2. \quad (5.3)$$

Figure. 5.5 shows the fitted IR reflectivity from the  $A_{2u}$  phonon frequencies  $\omega$  in Tab. 5.5. Since the damping constants are not available from the DFPT calculations, the reported values of Inoue [232] were taken for both experimental and theoretical models. A good agreement between theoretical and experimental IR reflectivity was obtained as illustrated in Fig. 5.5. Therein, all the experimental features are well reproduced with the theoretical values. Only a slight backward shift at high frequencies is observed which is inherited from the underestimation by using the LDA approximation of the exchange correlations. This underestimation was also reported for the high frequency of the simple cubic BaTiO<sub>3</sub> [239], see also Tab. 5.5. Among the 12  $A_{2u}$  adapted frequencies (LO and TO), 4 of them show noticeable changes in the reflectivity. They correspond to the LO modes at  $\omega = 92.03 \text{ cm}^{-1}$ ,  $434.16 \text{ cm}^{-1}$ ,  $614.58 \text{ cm}^{-1}$  and  $695.66 \text{ cm}^{-1}$ . In order to understand their microscopic origin, their corresponding eigenvectors are shown in Fig. 5.6.

With the LO1 mode, Fig. 5.6 (a), Ba(2) move in the opposite direction of both Ti(1) and Ba(1) whereas O ions are frozen within this mode. All moving atoms are displaced along the  $z$  direction meaning that this mode is a pure LO mode. Contrarily in LO4 (Fig. 5.6 (b)), only Ti(a) are moving along  $z$  but O(2) ions displace in the  $xz$  plane making in some way a rotation around the cubic  $z$  direction as illustrated in Fig. 5.7 (a). This signifies that LO4 is an oblique LO mode which might be the result of LO4 coupling with an active IR LO  $E_{1u}$  mode at  $\omega = 436.78 \text{ cm}^{-1}$  (obtained from DFPT calculations). On the other hand, LO5 mode is characterized by the exclusive vibrations of O(1) ions along  $z$  direction. The last mode, LO6, is also defined by the only vibrations of O(2) but with the  $xz$  plane, see also Fig. 5.7 (b). Such deviation from a pure  $A_{2u}$  LO mode could be as well caused by a coupling with a calculated  $E_{1u}$  LO mode at  $\omega = 672.25 \text{ cm}^{-1}$ .

FIGURE 5.7: The eigenvectors of the  $A_{2u}$  modes (a) LO4 (b) LO6 shown for an  $\text{TiO}_6$  octahedra.FIGURE 5.8: The effect of an applied biaxial strain on the optical  $A_{2u}$  modes frequencies and their corresponding LO-TO splitting. TO mode frequencies are plotted with solid lines while LO mode frequencies are plotted with dashed lines.

### 5.3.2 Strained structure

The effect of biaxial strain in the  $xy$  plane is investigated here. The in-plane cell parameters  $a$  were stretched and compressed up to  $\pm 8\%$  while the ratio  $c/a$  is kept fixed as the experimental value of the unstrained crystal. The internal coordinates were relaxed within each strain percentage. Afterwards, phonon calculations were done for each of the strained structures.

Firstly, the two unstable zone-center phonons,  $E_{2u}$  and  $A_{2u}$ , at  $0\%$  are checked against the applied strain. By a tensile strain, both modes were found to further soften, their frequencies exceed  $300i \text{ cm}^{-1}$  for strains larger than  $4\%$ . However, applying only a compressive strain of about  $-1\%$

lead to the stabilization of the IR active  $A_{2u}$  mode. By the same way, a compressive strain of  $-2\%$  caused the stability of the  $E_{2u}$  mode. The hardening of  $E_{2u}$  mode continues with the applied compressive strain and reaches a value of about  $100\text{ cm}^{-1}$  at  $-1\%$ . Unlike its split with cooling down below  $222\text{ K}$  [233], the  $E_{2u}$  mode remains double degenerate through all the applied strains.

The variation of the LO-TO splitting of all 6  $A_{2u}$  modes is presented in Fig. 5.8. The largest splitting,  $\approx 321\text{ cm}^{-1}$  was found for the soft mode at  $0\%$ , M1, at the tensile strain of  $4\%$ . Note that for tensile strain larger than  $6\%$ , Both LO and TO of M1 are soft. Compared to whether unstrained or tensile strained  $\text{BaTiO}_3$ , the LO-TO splitting with compressive strain was found to be slightly reduced, particularly for M1 and M2. However, all frequencies were found to be positive, meaning the stability of these 12 modes. Therefore, the hexagonal structure of  $\text{BaTiO}_3$  become stable.

## Conclusion

Since the hexagonal phase of  $\text{BaTiO}_3$  is unstable under ambient conditions and also at  $0\text{ K}$ , two schemes were proposed in this chapter to stabilize it. The first one constitutes of doping with transition metal ions as already proposed in experiment. It was found that doping with  $1.85\%$  of Fe is enough to induce a stable ferromagnetism in  $\text{BaTiO}_3$ . The Fe ion was found to favor the Ti(2) site position. However, adding one oxygen vacancy was demonstrated to further lower the formation energy of the defect complex which is characterized by an Fe ion sitting on the Ti(1) site with an oxygen vacancy from its second nearest neighbor. On the other hand, structural stability of hexagonal  $\text{BaTiO}_3$  was discussed in terms of phonon modes in the second part. the LO-TO splitting of the optical  $A_{2u}$  mode was investigated and the calculated frequencies were benchmarked against the measured ones through the infrared reflection spectrum. For this purpose, a four parameters model was used for the dielectric function. The calculated spectrum was demonstrated to be very similar to its experimental counterpart. Moreover, the two soft phonon modes obtained for hexagonal  $\text{BaTiO}_3$  were carefully examined. The optical phonon mode  $A_{2u}$  was determined to be dominated by the opposite movements of Ti and O ions. The acoustic mode  $E_{2u}$  on the other hand was attributed to opposite movement of Ti on each layer and different relaxations of O(1) and O(2). Thereafter, the robustness of these two modes and all  $A_{2u}$  modes was checked by applying an in-plane biaxial strain. Interestingly, the application of a moderate compressive strain, in the range of  $-2\%$ , was shown to harden the two soft phonon modes in hexagonal  $\text{BaTiO}_3$  and hence the stability of the structure. This scheme is still not discussed in experiment and reported experimental details are still scarce. Thus this finding could pave the ways for more experimental and theoretical investigations of the interesting hexagonal phase of  $\text{BaTiO}_3$ .





## 6 Doping induced magnetic phase transitions in $\text{GdMnO}_3$

Rare earth manganites  $RMnO_3$  series ( $R$  = rare earth element) have attracted a lot of interest in recent years due to their intriguing properties. They exhibit rich phase diagrams with spin, charge and orbital orders. Consequently, the  $RMnO_3$  systems show a strong interplay between structural, electronic and magnetic properties, which give rise to the colossal magneto-resistance (CMR) effect in manganites [18, 19].

$\text{GdMnO}_3$  constitutes one of the prominent members of the  $RMnO_3$  series owing to its special features. Foremost  $\text{GdMnO}_3$  lies on the borderline between a simple A-type antiferromagnetic state (A-AFM) and the more complicated ferroelectric states in the  $RMnO_3$  phase diagram [240–243], see Fig. 6.1. In addition,  $\text{GdMnO}_3$  shows a strong magneto-dielectric coupling even with a low applied magnetic fields of 1 T [240, 244–246]. As a consequence of the large coupling, different fundamental spin excitations such as electromagnons and spin waves are observed [246–248]. Such features make  $\text{GdMnO}_3$  a promising material for modern electrically or magnetically switchable devices.

Moreover, structural changes of  $\text{GdMnO}_3$  may lead to the stabilization of new ground states, as already demonstrated for other  $RMnO_3$  members [251–255]. Note, that the CMR effect was not detected in the pure state of  $RMnO_3$  but in its doping state, where the rare earth element is substituted by an alkaline earth ( $A$ ) element. This substitution does not affect indeed the perovskite structure which most of the  $RMnO_3$  adopt. Hence a full miscibility between the  $R$  and  $A$  elements is obtained in the solid solutions of  $R_{1-x}A_x\text{MnO}_3$ , where  $x$  is the concentration of elements  $A$ . In fact each of the two elements,  $R$  and  $A$ , has a different valence state, i. e. a 3+ for  $R$  element and 2+ for the  $A$  element. By substituting  $R$  with  $A$ , this latter gains one electron from the neighboring Mn ions, which were initially in the pure  $RMnO_3$  as  $\text{Mn}^{3+}$ . Thus, two types of manganese emerge in the cell, namely,  $\text{Mn}^{3+}$  and  $\text{Mn}^{4+}$ . The resulting materials are hence called mixed valence manganites [251, 253, 254].

Recently, the magnetic phase diagram of the  $\text{GdMnO}_3$  doped with calcium (GCMO) is obtained by Beiranvand *et al.* [17], see Fig. 6.2. Based on magnetoresistive measurements, a rich and complicated magnetic phase diagram was reported. The A-AFM magnetic ground state of  $\text{GdMnO}_3$  was found to destabilize towards the ferromagnetic (FM) state with very low concentrations of calcium. Such FM state remained the ground state for all concentrations  $0.1 \leq x \leq 0.5$ . At the half doping,  $x = 0$ , GCMO showed again a stable AFM ground state which was proven also for concentrations  $0.5 < x \leq 0.8$ . This AFM is accompanied by charge ordering (CO) state only between the concentrations of 0.5 and 0.7. An even high CO transition temperature of about 270 K was affirmed at  $x = 0.5$ . Moreover, an evidence of the magnetoresistivity properties (CMR)

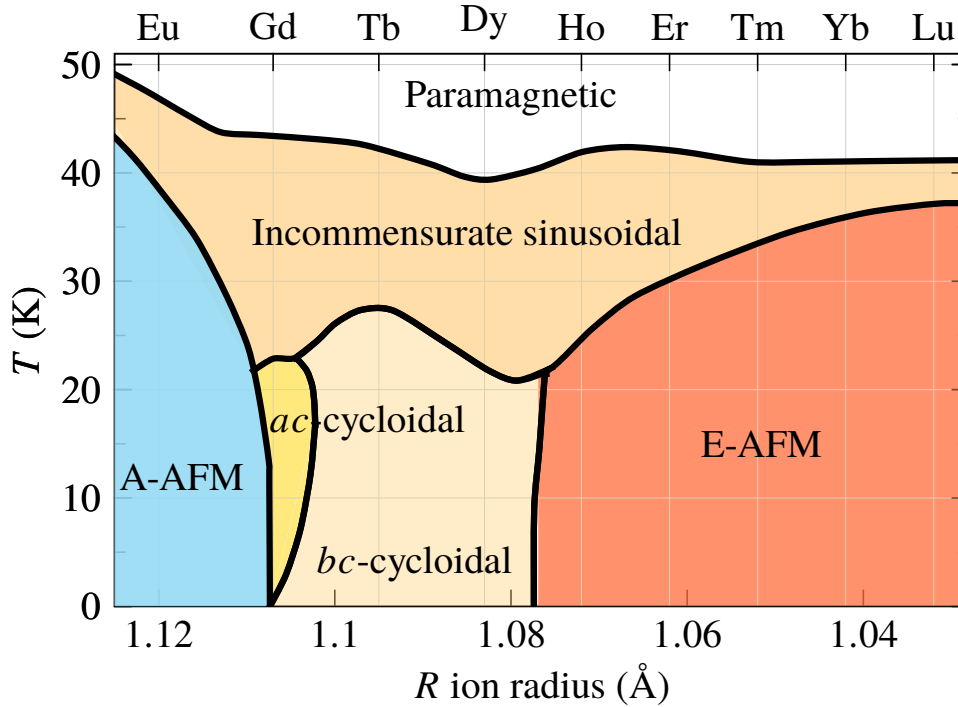


FIGURE 6.1: Experimental phase diagram of bulk orthorhombic  $RMnO_3$  (adapted from [243, 249]). The coordination number of  $R$  in  $RMnO_3$  is assumed here to be 9. The corresponding ionic radius are then taken from [250]. The transition temperatures and the borders between different magnetic regions are determined by magnetic and dielectric measurements. A-AFM (E-AFM) stands for the A (E)-type of antiferromagnetic order. The magnetic states  $ac$  and  $bc$  cycloidal correspond to the noncollinear cycloidal spin orders in the  $ac$  and  $bc$ -plane, respectively.

were demonstrated at the concentrations  $x$  between 0.8 and 0.9. Beyond that, a cluster glass semiconductor state was shown with increasing the magnetic field up to 9 T. This rules out any metal-insulator transition like in other doped manganites. However Taguchi *et al.* [256] showed that GCMO exhibit a metal-insulator transition for  $x$  between 0.6 and 0.9. On the other hand, most of the GCMO investigations [257–265] concentrated on  $x = 1/3$  because of the maximum double exchange mechanism at this concentration [266].

Although, a comprehensive study on the magnetic properties of GdMnO<sub>3</sub> doped with calcium for the full range of concentrations is still missing due to the fact that Gd has the strongest neutron-absorbent among all natural elements [267]. Hence an experimental magnetic measurement with the most accurate method of neutron diffraction can not be easily done. Furthermore, the underlying microscopic mechanisms behind the multiple phase transitions shown by Beiranvand *et al.* [17] are not yet fully understood. Thus, a theoretical study by means of DFT calculations combined with a Heisenberg model and post-processed with Monte Carlo simulations will allow to identify the responsible cause of magnetic phase transitions. The magnetic properties are discussed then in terms of magnetic exchange interactions between the Mn sites. They are next used in a classical Heisenberg model in order to determine the critical magnetic transition temperatures. Also, the type of AFM ground states, which could not be accessed directly from the magnetoresistance

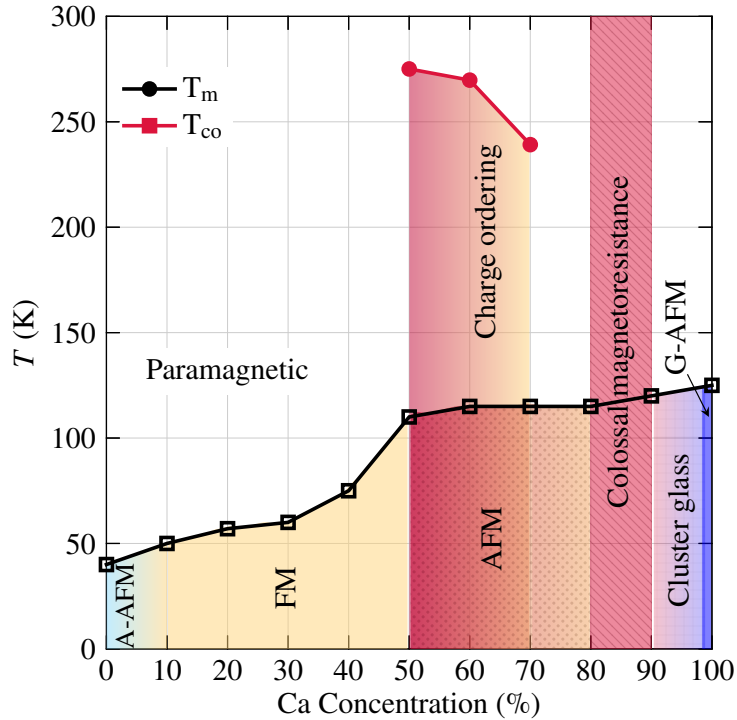


FIGURE 6.2: Experimental magnetic phase diagram of  $Gd_{1-x}Ca_xMnO_3$  (adapted from [17]). AFM denotes an antiferromagnetic order where its nature is still experimentally undetermined. A-AFM (G-AFM) stands for A-type (G-type) AFM state, FM denotes the ferromagnetic order. The charge ordering region is indicated by CO. The region where the colossal magneto-resistance is detected is denoted by CMR while CG stands for the cluster spin-glass phase. Magnetic transition temperatures are plotted with black lines and the maximal CO transition temperatures are plotted with red lines.

experiments in [17], can be determined by comparing the total energies of different AFM states of GCMO series.

## 6.1 Structural, electronic and magnetic properties

$GdMnO_3$  crystallizes in the orthorhombic structure with the  $Pbnm$  symmetry of the space group 62 including 20 sites (see Fig. 6.3). The Gd atoms occupy the  $4c$  Wyckoff position while the Mn atoms are at the  $4b$  Wyckoff position. The oxygen atoms are located at the two different sites of  $4c$  and  $8d$ . Those at  $4c$  sites bind with the Mn atom in  $z$  direction while O atoms at the  $8d$  are bonded to Mn ions in the  $(xy)$  plane (see Fig. 6.3). The same crystal structure was also obtained for the whole series of Ca doped  $GdMnO_3$  where only Ca atoms substitute Gd atoms. However the study of the magnetic properties of the GCMO series, needs a careful consideration of the parent compound,  $GdMnO_3$ , and also a validation of the structural, electronic and magnetic properties against the previous theoretical and experimental results. In this direction, DFT calculations were carried out with the projector augmented-wave method [92, 268] (Sec. 3.1.2) as implemented in the Vienna *ab*

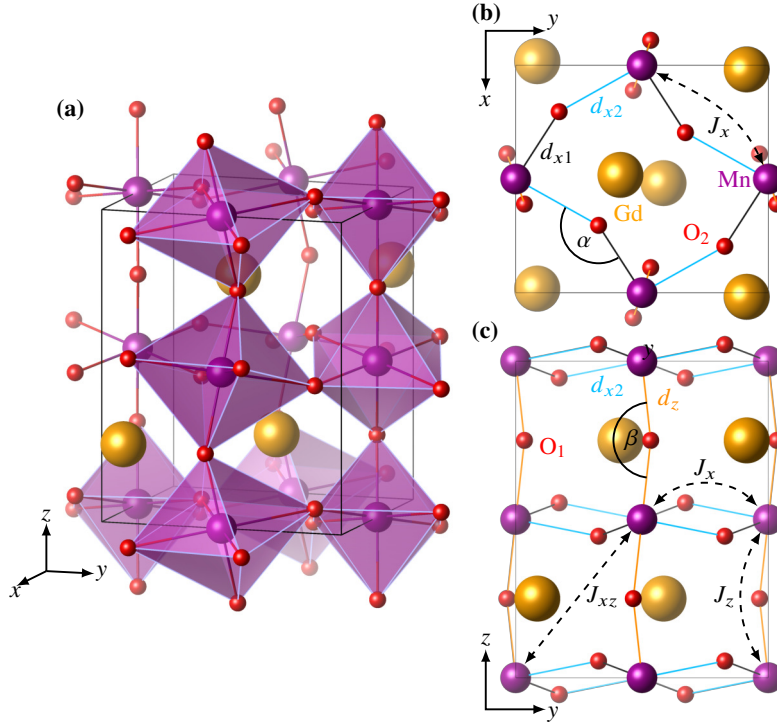


FIGURE 6.3: Structural representation of the Pbnm unit cell of GdMnO<sub>3</sub>. (a) 3-dimensional representation of unit cell including the distorted oxygen octahedra. (b) the top view ( $xy$  plane) of the unit cell. (c) the side view of the unit cell ( $yz$  plane). The Gd ions atoms are depicted with the balls in golden color whereas the Mn and O are showed with the balls in violet and red color, respectively. The structural notation is also indicated for bond length Mn–O and the bond angle enclosed in the Mn–O–Mn bond ( $\alpha$  and  $\beta$ ). The three different bond length are noted as (Mn–O) <sub>$z$</sub>  (orange,  $d_z$ ), (Mn–O) <sub>$x_1$</sub>  (black,  $d_{x_1}$ ), and (Mn–O) <sub>$x_2$</sub>  (blue,  $d_{x_2}$ ). The direction of the three magnetic exchange interactions between the Mn sites, as will be explained latter, is pictured as well with dashed arrows.

*initio* simulation package (VASP) [22, 23] and using only the experimental structure of GdMnO<sub>3</sub> [269].

The results of four common exchange correlation functionals are compared. These functionals are those of Perdew-Burke-Ernzerhof (PBE) [59], its revised version for solids (PBEsol) [59], Perdew-Wang (PW91) [56], and Perdew-Zunger (PZ) [54]. The effect of strong electronic correlations is as well studied by adding an isotropic screened on-site Coulomb interaction [67].

The effect of the Hubbard  $U$  correction is then checked by varying its value from 0 eV to 8 eV with each of the aforementioned functionals. The choice of  $U$  was made based on the best compromise between the three most important properties: the electronic band gap, the magnetic moment, and primarily the stability of the magnetic order. This latter is checked by calculating the total energies of the different magnetic configurations shown in Fig. 6.4. Afterwards, only energies of the simple structures ( first row in Fig. 6.4) are mapped in to the Heisenberg Hamiltonian in Eq. (3.60). They are A-AFM (A), C-AFM (C), G-AFM (G) and FM (F) orders. The ferrimagnetic structure FI (with net moment but smaller than the FM) is taken as energy reference as explained in [270]. The

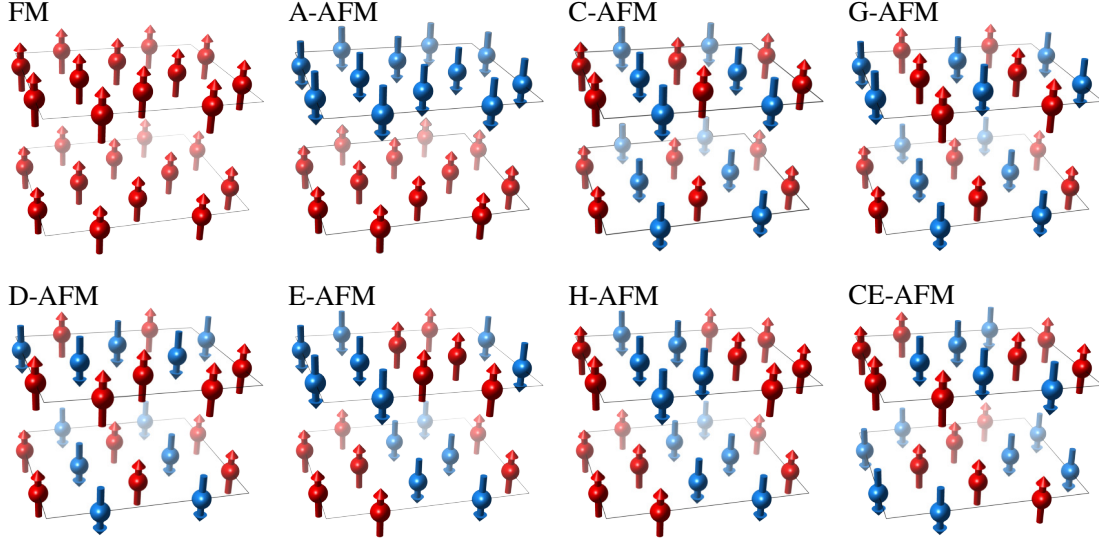


FIGURE 6.4: Sketch of the considered antiferromagnetic structures, which were suggested by Wollan *et al.* [253]. Only the magnetic Mn atoms are shown here ((balls with arrows, red (blue) for spin up (spin down))). All configurations are represented in a supercell of  $2 \times 2 \times 1$  times the orthorhombic unit cell with the  $Pbnm$  symmetry.

resulting system of equations can be expressed as a matrix problem by writing the total energies as a vector:

$$\mathbf{E} = (E_A, E_C, E_G, E_F)^T. \quad (6.1)$$

The vector of magnetic exchange interactions is defined as

$$\mathbf{J} = (J_z, J_x, J_{xz})^T. \quad (6.2)$$

Then, the matrix form of the system of equations to calculate all  $J_{ij}$  in the model is given by

$$\mathbf{E} = -\frac{S^2}{2}(4\mathbf{T})\mathbf{J}, \quad (6.3)$$

where the matrix  $\mathbf{T}$  contains the essential number of interacting Mn atoms and reads (right column only for overview):

$$\mathbf{T} = \begin{pmatrix} -2 & 4 & -8 \\ 2 & -4 & -8 \\ -2 & -4 & 8 \\ 2 & 4 & 8 \end{pmatrix} \begin{array}{l} \text{A} \\ \text{C} \\ \text{G} \\ \text{FM} \end{array}$$

Hence, a linear least-squares fitting can be used to obtain the three exchange interactions.

Figure 6.5 illustrates the dependence of the electronic band gap, the local magnetic moment of Mn and the exchange interactions in  $\text{GdMnO}_3$  on the chosen  $U$  value with the appropriate exchange correlation functional. It was found for small  $U$  values, i. e.  $U < 2 \text{ eV}$ , that the electronic band gap

is too small compared to experimental value of 2.0 eV [271]. The same underestimation applies for the local magnetic moments of Mn ions. In addition the magnetic ground state was wrongly determined to be the G-AFM state instead of the A-AFM, demonstrated by the negative three exchange interactions. Only with  $U = 2$  eV, the A-AFM order become more robust, i. e. positive (negative) in-plane  $J_x$  (out of plane  $J_z$ ) interaction. As well the local magnetic moment at  $U = 2$  eV become more close the obtained moment with hybrid functional [270]. Although higher  $U$  value leads to closer band gap value to experiment, it results in a FM ground state. On the other, minor difference between the results from PBE and PBEsol are found for the three compared properties. Therefore, the best choice of  $U$  was decided for  $U_{\text{Mn}} = 2$  eV and an exchange correlation treatment with PBE functional. Note here, that the Gd  $f$ -electrons are treated as frozen in the core region in all calculations.

As the theoretical consideration of the exchange correlation effects is decided, purely first principles calculations can be made. That means no dependence on the experimental structure anymore and a full relaxation of the cell can be done. This will help to benchmark the results for the Ca doped GdMnO<sub>3</sub> where experimental structures are still missing. Thus the cell parameters of GdMnO<sub>3</sub> are relaxed together with the internal coordinates. Tab. 6.1 summarizes the obtained structural properties of GdMnO<sub>3</sub> with a comparison to other theoretical and experimental results. In order to obtain the theoretical equilibrium structure, different cell volumes ranging between  $\pm 5\%$  of the experimental one [269] were taken and the cell parameters and the internal coordinates within each volume were optimized. The A-AFM magnetic ground state order was imposed in all structural relaxations. By means of this, the optimal three cell parameters for each of the chosen volumes were obtained. Consequently, the resulting total energy of the different volumes were then fitted to  $E(V)$  with the Murnaghan equation of state. The volume of the lowest energy from the fitting is again relaxed to obtain its best cell parameters and atomic positions, which converge the interatomic forces below a threshold value of  $5 \text{ meV } \text{\AA}^{-1}$ . The obtained equilibrium cell parameters and their corresponding bulk modulus  $B_0$  are given in Tab. 6.1 and compared to other theoretical and experimental works.

The relaxed volume is by 2% smaller than the experimental values [269, 272]. This underestimation of the theoretical equilibrium volume agrees with the observation of Fedorova *et al.* [249], although the present results are closer to the experimental reference. The calculated bulk modulus and its derivative were found also very close to the experimental values. The other equilibrium properties, namely the bulk modulus and its derivative, are close to the experimental values. Besides, the resulting internal parameters are also compared to the available theoretical and experimental results in Tab. 6.1. The bond length  $d_{x_2}$  was found to be the longest among the three Mn–O bond lengths which was also reported in the other theoretical and experimental structure. Also the calculated out of plane bond angle  $\beta$  was larger than its in-plane counterpart in the three structures. In overall, a better agreement was obtained between the actual calculated structural properties and the experimental ones than the reported theoretical results [249].

Since the substitution of Gd atoms by Ca will be taken up to 100% of Ca in the following, the electronic and magnetic properties of the second parent compound, CaMnO<sub>3</sub> are also very important to validate with the available experimental data. Hence, the same previous examination of electronic correlation effects in GdMnO<sub>3</sub> with  $U$  correction are reconsidered for CaMnO<sub>3</sub>. This latter has the G-AFM order as the experimental magnetic ground state. It was found by applying a larger  $U$  value than 5 eV the magnetic ground state turns to be the FM order [H7]. However with the chosen value

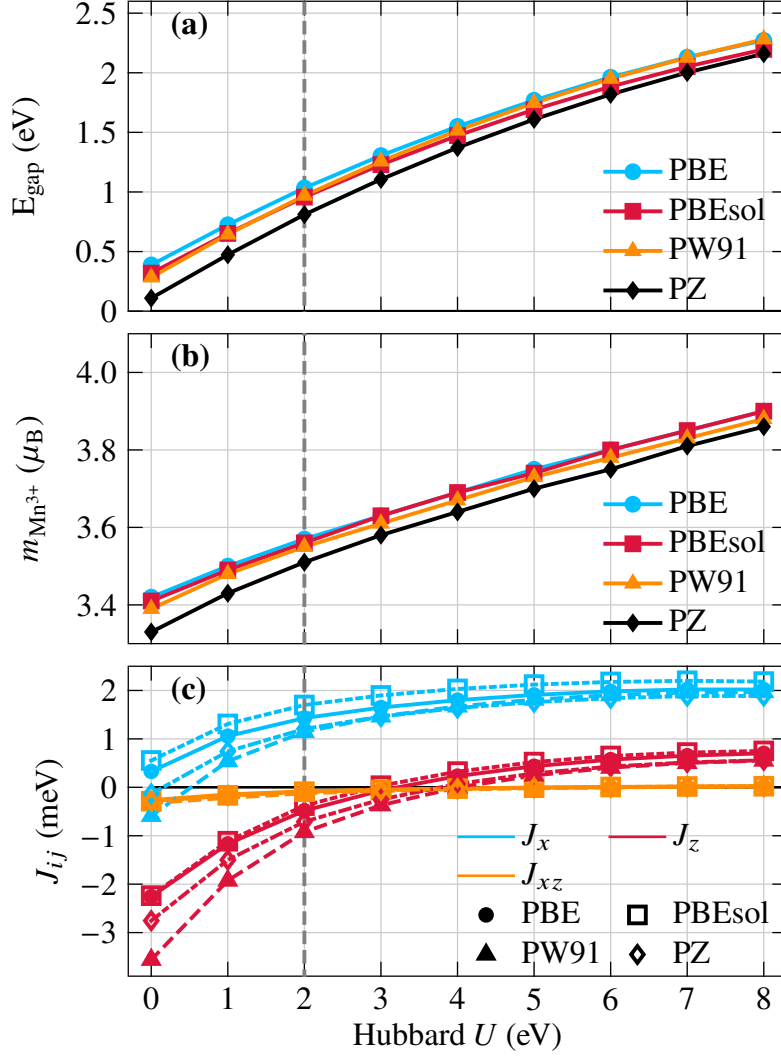


FIGURE 6.5: The dependence on the Hubbard  $U$  correction and the exchange correlation potential of the (a) magnetic moments of  $\text{Mn}^{3+}$  (b) the magnetic exchange interactions in  $\text{GdMnO}_3$  depicted in Fig. 6.3, which are obtained by mapping the total energies of the different magnetic configurations in Fig. 6.4 into a Heisenberg Hamiltonian as already explained in Sec. 3.4. The gray dashed line indicates the choice of  $U = 2$  eV.

of 2 eV for  $\text{GdMnO}_3$ , the local magnetic moment was  $2.66\mu_B$  which is in line with experimental measurements of Wollan and Koehler [253] and theoretical calculations of Pickett and Singh [274]. The band gap was also checked with  $U$  values and a value of 0.92 eV was found for  $U = 2$  eV which is still lower than the measured one of 1.55 eV by Loshkareva *et al.* [275]. But higher  $U$  values as already mentioned will destabilize the magnetic structure towards the FM order. Therefore a  $U$  value of 2 eV can be considered as safe choice for  $\text{CaMnO}_3$  as well. Such thorough investigation of the electronic and magnetic properties of the parent compounds permits to establish a solid theoretical framework and will serve as a basis for the following substitutional alloy discussions.



TABLE 6.1: The obtained equilibrium structure of the orthorhombic GdMnO<sub>3</sub> with  $U_{\text{Mn}} = 2$  meV compared to the theoretical results of Fedorova *et al.* [249] and experimental results of Mori *et al.* [269]. The parameters  $a$ ,  $b$ , and  $c$  are the lattice constants.  $B_0$  and  $B'_0$  are the bulk modulus and its derivative. The Mn–O bond lengths ( $d_{x_1}$ ,  $d_{x_2}$  and  $d_z$ ) and Mn–O–Mn bond angles ( $\alpha, \beta$ ) are those presented in Fig. 6.3. The experimental bulk modulus and its derivative values are taken from [273]. More details on the structure are given in [H7, H8].

	This work	Theory [249]	Experiment [269]
$a$	5.280	5.261	5.318
$b$	5.831	5.807	5.866
$c$	7.364	7.367	7.431
$V_0$	226.72	225.07	231.81
$B_0$	165.964	-	$170 \pm 1$
$B'_0$	4.47	-	$3.72 \pm 0.07$
$d_{x_1}$	1.913	1.916	1.910
$d_{x_2}$	2.203	2.182	2.228
$d_z$	1.937	1.934	1.944
$\alpha$	143.66	144.37	145.30
$\beta$	145.55	145.80	147.76

## 6.2 Solid solutions with Ca doping

The disorder at the (Gd,Ca) sub-lattice in the solid solution of Gd<sub>1-x</sub>Ca<sub>x</sub>MnO<sub>3</sub> was simulated with the special quasi-random structure (SQS) method [29] (Sec. 3.3.2). The best candidates to represent the disordered states at the different concentrations  $x$  are obtained using Monte Carlo simulated annealing loops as implemented in the MCSQS program [30, 276]. Therein, pair, triplet and quadruplet clusters are taken into account. The pair clusters are included up to a distance of 7 Å which corresponds to the ninth shell. This translates into a maximum figure of  $f = (2, 9)$  in the cluster expansion terminology (Sec. 3.3.2), see Tab. 6.2. Whereas triplet and quadruplet clusters are considered only up to the fifth nearest neighbor. Note that most of the reported SQS cells in literature were limited to pair clusters for mimicking the correlation functions of the completely random alloy. Table. 6.2 shows the differences between the SQS candidates of Gd<sub>1-x</sub>Ca<sub>x</sub>MnO<sub>3</sub>, which will be used in the following, and their target disordered states. In fact, the lowest possible concentration  $x$  to model with SQS is restricted by the choice of the supercell size and can not be continuously chosen between 0 to 1. Therefore the smallest concentration step which corresponds to supercell of  $2 \times 2 \times 2$  can be  $1/2^3 = 1/8$ . Hence calculations were performed for the concentrations  $x = 0, 1/8, 1/4, \dots, 7/8, 1$ .

As shown in Tab. 6.2, the objective function at  $x = 1/2$  tends towards  $\infty$  and the two system correlation functions are equal, which means a perfect matching between the SQS candidate and its target disordered state. Furthermore, the correlations functions at  $(1 - x)$  were found to be the



TABLE 6.2: The difference between the correlation functions of the SQS candidates for  $\text{Gd}_{1-x}\text{Ca}_x\text{MnO}_3$  and the target disordered state for concentrations  $x$  between  $1/8$  and  $1/2$ . Note, that the correlation functions at  $1 - x$  are the same as those for  $x$ . The different numbers of interaction partners (pair-, three- or four interactions) are presented by  $n$ , and different corresponding distances ( $r$ ). The optimal SQS has the same correlation functions as the targeted disordered state, i.e., the difference is zero. The last row shows the objective function  $\mathcal{Q}$  value which was given by Eq. (3.59).

Figure ( $f = (k, m)$ )		Concentration ( $x$ )			
$k$	$m$	$1/8$	$1/4$	$3/8$	$1/2$
2	1	$1/16$	0	$1/16$	0
2	2	$1/16$	0	$1/16$	0
2	3	$1/16$	0	$1/16$	0
2	4	$1/16$	0	$1/16$	0
2	5	$1/16$	0	$1/16$	0
2	6	$1/16$	0	$1/16$	0
2	7	$1/16$	0	$1/16$	0
2	8	$1/16$	0	$1/16$	0
2	9	$1/16$	0	$1/16$	0
3	4	$3/64$	$1/8$	$1/64$	0
3	5	$3/64$	$1/8$	$1/64$	0
4	5	$15/256$	$1/16$	$1/256$	0
$\mathcal{Q}$		-2.93	-5.19	-2.95	$-\infty$

same as those at  $x$  which is expected because of the non chemical but geometrical nature of the SQS generation. As example, 50% of element Gd is equivalent to 50% of Ca. However, despite the equivalence between the correlation and the objective functions at  $x$  and  $(1 - x)$ , their obtained SQS are not necessarily a simple alteration of Gd and Ca as illustrated in Fig. 6.6. The atomic distributions at  $(1/8, 7/8)$ ,  $(1/4, 3/4)$  and  $(3/8, 5/8)$  do not correspond to a just switching between Gd and Ca atoms. This reflects the statistical way with which these structures were obtained, i. e. two different atomic distributions with the same supercell can have the same probability. It is worth mentioning here that an optimal SQS structure candidate may not have necessarily an orthogonal supercell as shown in Fig. 6.6. It is actually a constraint which was introduced in this work for the purpose of keeping the same definition of the exchange interactions (see Fig. 6.3).

In fact, by assuming a disordered states of  $\text{Gd}_{1-x}\text{Ca}_x\text{MnO}_3$ , the charge and orbital ordering of the Mn ions are implicitly excluded. These two ordering states are experimentally observed in the electron doped region, i. e.  $0.5 < x < 1$ . The reason is that the random distribution of Gd and Ca affects consequently the  $\text{Mn}^{3+}/\text{Mn}^{4+}$  distribution. In none of the obtained SQS structures, as

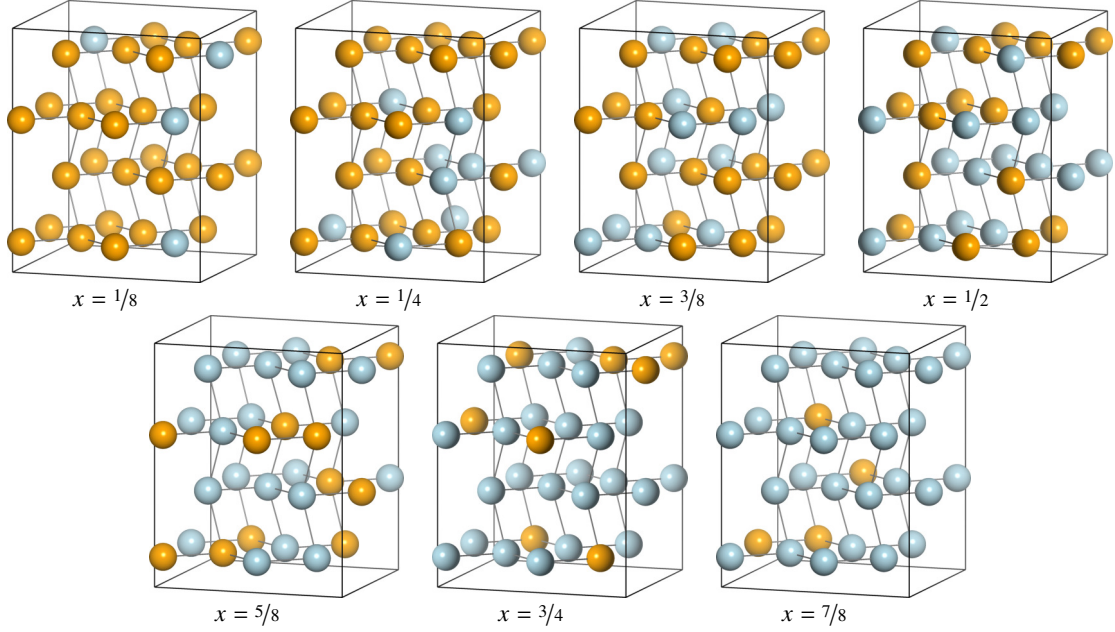


FIGURE 6.6: The SQS structures of  $\text{Gd}_{1-x}\text{Ca}_x\text{MnO}_3$  with a supercell of 32 f.u. at the different considered concentrations  $x$ . The difference between the correlation functions of these structures and their random counterparts are presented in Tab. 6.2. The Golden (gray) balls represent the Gd (Ca) atoms. The Mn and O atoms are omitted here for the sake of clarity.

shown in Fig. 6.6, the Gd and Ca atoms follow a defined pattern which can be also followed by the  $\text{Mn}^{3+}$  and  $\text{Mn}^{4+}$  ions. Hence the results at  $0.5 < x < 1$  may deviate from the measured ones [17].

Owing to the large size of the considered supercells and the complexity of relaxing at the same time the cell parameters and the internal coordinates, only those latter are relaxed. The cell parameters are then fixed to the experimental values for  $0 < x < 1$  [17]. Also, from the magnetoresistive measurements [17], only a FM or AFM order can be assigned but the nature of the AFM is not conclusive. Therefore, all SQS cells were relaxed in the FM configuration of the Mn spin moments.

### 6.3 Hole doping region

The doping region of  $\text{Gd}_{1-x}\text{Ca}_x\text{MnO}_3$ , where  $x < 1/2$ , is called hole doping region because of the insertion of Ca into  $\text{GdMnO}_3$ . In the parent compound at  $x = 0$ , Gd exists as  $\text{Gd}^{3+}$  ion whereas Ca ion exists in the state of  $\text{Ca}^{2+}$  at  $x = 1$ . Thus the substitution of Gd by Ca induces a hole in the Gd states. But such a hole is attracted by the Mn ion instead, which was initially in the state of  $\text{Mn}^{3+}$  in  $\text{GdMnO}_3$ , and transforms into  $\text{Mn}^{4+}$  where Gd restores its  $\text{Gd}^{3+}$  state. This process was shown by Beiranvand *et al.* [17], to cause a transition of the ground state from the A-AFM order at  $x = 0$  to the FM state in the concentration range  $0 < x < 0.5$ . The same FM phase transition is also obtained here in DFT calculation with the SQS structure at  $x = 1/8$ . The FM state, which has an energy about 4 eV higher than that of A-AFM at  $x = 0$ , lowers abruptly its energy at  $x = 1/8$  to be even lower than the A-AFM one by 29 eV. To elucidate the origin of this

transition, the Heisenberg Hamiltonian defined in Eq. (3.60) was used. The total energies of the different magnetic configurations in Fig. 6.4 are then mapped into Eq. (3.60) and the three exchange parameters, which are shown in Fig. 6.3, are determined. However, with doping the spin moments in Eq. (3.60) are not anymore equal to 2 ( $\text{Mn}^{3+}$ ) as they were in  $\text{GdMnO}_3$  or  $3/2$  ( $\text{Mn}^{4+}$ ) in the case of  $\text{CaMnO}_3$ . It was indeed taken as doping dependent and equal to the mean value of the spin moments at the two limits :

$$S_x = (1 - x)S_{\text{Mn}^{3+}} + xS_{\text{Mn}^{4+}} \quad (6.4)$$

It was found that the FM transition is induced by a strong sign reversal of the out of-plane exchange parameter  $J_z$  from  $-0.8$  meV to  $2$  meV at  $x = 1/8$ . Moreover, the in-plane coupling  $J_x$  was found also to strengthen its value to reach  $3.6$  meV. Therefore the FM is stabilized because in an A-AFM state the effective out of plane  $J_{\text{eff}}$  should be negative to compensate the positive  $J_x$  which is not fulfilled at  $x = 1/8$ .

A structural analysis was as well made for the supercell to figure out which of the structural properties has a more pronounced change. Therefore, the distortion of the Mn octahedra are tracked for the whole concentration range between 0 and 1. The bond angles and bond lengths, shown in Fig. 6.3 and Tab. 6.1 for  $\text{GdMnO}_3$ , are determined as mean values of all present bond lengths and angles inside the relaxed SQS cells. In other words, the distortions inside the relaxed SQS cells are folded back inside the primitive cell to facilitate the comparison with the parent compounds properties. Figure. 6.8 summarizes the obtained variation of the bond lengths and bond angles with varying the concentration  $x$  in  $\text{Gd}_{1-x}\text{Ca}_x\text{MnO}_3$ . By looking at the difference of the bond angles and bond lengths between  $x = 0$  and  $x = 1/8$ ,  $d_{x_1}$  ( $d_{x_2}$ ) was found to increase (decrease) its value at  $x = 1/8$  whereas the out of plane bond length  $d_z$  was slightly changed. Also both of the two angles were increased by the introduction of Ca at  $x = 1/8$  compared to their initial values.

At the close concentration of  $x = 0.1$ , the temperature dependent SQUID measurements [17] showed, in addition to the FM orientation of the Mn spin moments, a negative magnetization which was attributed to the ordering of the Gd spins which prefer to align in the opposite direction of Mn spins at  $T < 20$  K. Such ferrimagnetic coupling between Gd and Mn spins was actually earlier proposed for  $x = 0.3$  [257] and thereafter generalized for  $x < 1/2$  [17, 258] of  $\text{Gd}_{1-x}\text{Ca}_x\text{MnO}_3$ . But studying this coupling with pseudopotential method is still rather complicated because of the difficulty of  $f$ -states treatment in this method. Thus only the ordering of Mn spin moments was checked here and for other considered concentrations.

Increasing more the Ca concentration up to  $x = 1/4$  was shown to drastically shrink the in-plane Mn–O bond length  $d_{x_2}$  while similar value was obtained for the other two bond lengths. Although the bond angles continued to increase with  $x = 1/4$  to reach a value of  $151.7^\circ$  for  $\alpha$  and  $147^\circ$  for  $\beta$  where their average is practically close to the measured value of  $149.7^\circ$  by Peřkařa and Drozd [277]. These structural changes raised further the stability of the FM state at  $x = 1/4$ , i. e. the difference of the FM to the A-AFM energy was found to be almost  $50$  meV. Interestingly, this difference is the largest among all the considered concentrations. At  $x = 3/8$ , the difference is only  $40$  meV. In fact, this concentration is the closet possible one to  $x = 1/3$  which can be covered with the present supercell calculations which was believed by Snyder *et al.* [257] to maximize the double exchange effects. The calculated in-plane exchange interaction  $J_x$  was also maximized at  $x = 3/8$ , see Fig. 6.7. Such large value of  $J_x$  is accompanied by an increase of the two bond angles to attain the same

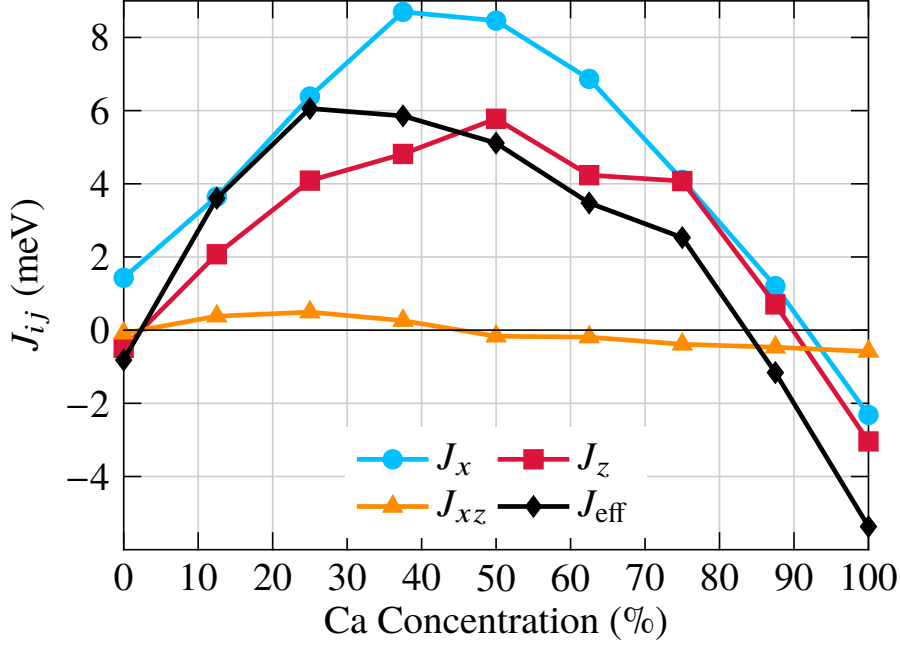


FIGURE 6.7: The calculated Heisenberg exchange interactions in  $\text{Gd}_{1-x}\text{Ca}_x\text{MnO}_3$  following Eqs. (3.60) and (6.4). The couplings  $J_x$ ,  $J_z$  and  $J_{xz}$  are depicted in Fig. 6.3 whereas the effective out of plane  $J_{\text{eff}} = J_z + 4J_{xz}$ .

value of  $151^\circ$ . Hence, the octahedral distortion is reduced in favor of the Jahn-Teller distortion as stated for Sr doped  $\text{LaMnO}_3$  by Millis *et al.* [266].

## 6.4 Half doping region

The mid-doping concentration of  $x = 1/2$  asserted the first magnetic phase transition from the FM state to the AFM state in the experimental phase diagram [17]. A transition was not detected actually by the present DFT calculations but the AFM structures were found to further lower their energies at this concentration, see Tab. 6.3. As well all the three exchange interactions start to decrease at this concentration with a clear transition of the second nearest out of plane coupling  $J_{xz}$  from the FM to the AFM. It is the first time that one of the exchange interactions becomes negative after the inclusion of Ca, see Fig. 6.7. However the experimental phase diagram revealed in addition a stabilization of a charge ordering state at  $x = 1/2$ . It concerns an ordering of the Mn ions of  $\text{Mn}^{3+}$  and  $\text{Mn}^{4+}$ . In this state, both ions are distributed over the cell with a special pattern, similar to the spin patterns shown earlier in Fig. 6.4. This ordering might play an important role in the stabilization of the AFM state as already demonstrated by Schiffer *et al.* [278] for  $\text{La}_{0.5}\text{Ca}_{0.5}\text{MnO}_3$ . In this compound, the FM was shown to be suppressed by the occurrence of charge ordering which stabilizes the AFM state. Furthermore orbital order can also occur which is very common in manganese-oxide perovskites [279] where the  $3d e_g$  orbitals make also a special

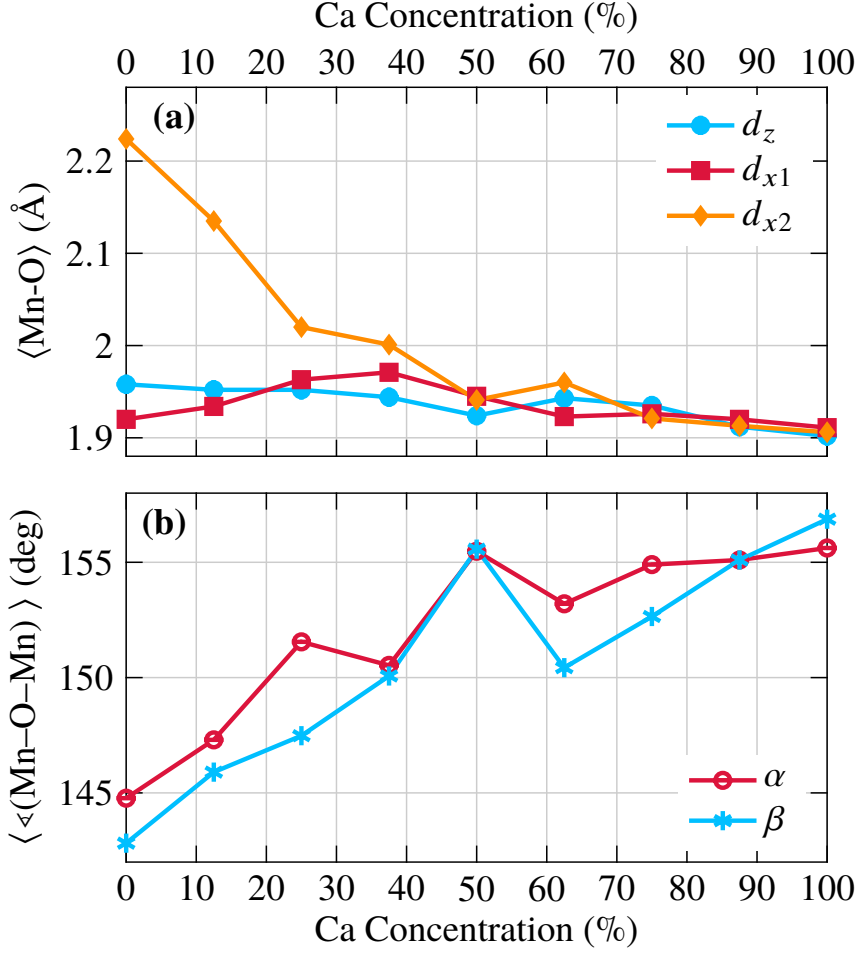


FIGURE 6.8: The variation of (a) the three Mn–O bond lengths and (b) the Mn–O–Mn bond angles averaged over the SQS bond lengths and angles, respectively, with respect to the Ca concentration in  $\text{Gd}_{1-x}\text{Ca}_x\text{MnO}_3$ . See Fig. 6.3 for the visualization of both structural properties.

decoration. Although the disorder in Gd/Ca distribution prevents the setup of charge or orbital patterns. Thus these phenomena are ignored in this study.

Another potential mechanism to stabilize the AFM order was proposed for  $\text{Pr}_{1-x}\text{Ca}_x\text{MnO}_3$  (PCMO). The magnetic order of PCMO at  $x = 0.5$  is rather maintained by the presence of the so called Zener polarons, because a stabilization of an AFM (CE-type) order by means of the charge ordering could be excluded based on single-crystal neutron diffraction measurements [255, 280]. This phenomenon results from trapped electrons between the two Mn sites causing a valence of  $3.5+$  in the neighboring Mn ions instead of the natural valence of  $3+$  or  $4+$ , respectively. An analogous argument was given by García *et al.* [281] using a ferromagnetic Kondo lattice model. Therewith, they demonstrate that the formation of magnetic polarons is an important ingredient in the description of systems with correlated spin-charge degrees of freedom. This correlation is induced from the strong competition between double exchange and superexchange mechanisms in these systems.

TABLE 6.3: The total energies per f.u. for Gd<sub>1-x</sub>Ca<sub>x</sub>MnO<sub>3</sub> calculated for all the magnetic structures presented in Fig. 6.4 with reference to the lowest energy at each concentration. The distribution of Gd and Ca ions for each concentration are given in Fig. 6.6. The FI structure stands for the ferrimagnetic state which was taken as reference energy in Eq. (3.60). Units are in meV.

	0	0.125	0.25	0.375	0.5	0.625	0.75	0.875	1
A-AFM	0.00	29.01	49.090	42.85	37.91	24.55	16.57	0.00	11.77
C-AFM	29.3	96.56	147.25	179.55	185.4	79.07	35.31	11.87	4.624
G-AFM	30.9	99.68	198.16	360.88	211.7	126.74	74.75	28.69	0.00
FM	4.09	0.00	0.00	0.00	0.00	0.00	0.00	2.08	32.10
D-AFM	19.9	78.75	124.98	138.51	118.4	143.41	38.33	18.57	8.618
E-AFM	9.27	66.66	116.44	185.25	113.9	173.03	63.62	28.40	8.315
H-AFM	8.17	52.73	85.540	98.14	85.00	71.47	45.64	20.14	14.66
CE-AFM	12.8	145.0	120.88	122.30	94.10	69.75	44.23	15.31	5.146
FI	14.0	57.24	158.74	133.70	81.65	71.46	20.21	4.84	11.56

## 6.5 Electron doping region

The last doping regime represents essentially CaMnO<sub>3</sub> doped with Gd ions, which adds excess electrons from Gd<sup>3+</sup> to the system and consequently Mn<sup>3+</sup> to coexist with Mn<sup>4+</sup>. For concentrations  $x \geq 5/8$ , a split between the Mn–O–Mn bond angles was obtained again. But both two calculated angles showed a decrease of about 5° compared to  $x \geq 1/2$ . This might be inherited from the taken experimental lattice parameters. These latter were reported also to show a sort of cell expansion at this concentration range, especially the  $c$  parameter which the more affected angle  $\beta$  is related. By increasing more the concentration of Ca, an increase of the value of  $\beta$  and also  $\alpha$  was obtained. In addition, the total energies of the AFM configurations were reduced with increasing  $x$ . For instance, The A-AFM energy is the second lowest obtained energy after the FM which still persists as the lowest energy which contradicts the experimental measurement. Such stabilization of the FM order might be favored by the adaption of FM order in the structural relaxation of the SQS cells in addition to the already discussed and neglected charge and orbital ordering and formation of Zener polarons. These three phenomena are known to appear in the charge ordering phase which was reported to develop in the range of 50 % to 70 % of Ca [17]. It was even detected at  $x = 0.85$  by another experimental measurement of Khan *et al.* [282]. The authors [282] reported a very robust charge ordering which coexist simultaneously with an orbital ordering at  $x = 0.85$ . The application of a magnetic field up to 15 T between 5 K to 300 K did not annihilate this charge ordering.

Only at  $x = 7/8$ , the A-AFM overcomes the ferromagnetic order (see Tab. 6.3 and Fig. 6.9 (a) ) and becomes the most stable structure. It follows that the effective out of plane coupling  $J_{\text{eff}}$  becomes negative (AFM) for the first time after starting the doping. It has the same magnitude as the positive (FM) coupling  $J_x$ . Other AFM and also the FI states reduce as well their energies to be lower than 20 meV, see Fig. 6.9 (a). In particular the C-type AFM order lowers its energy to 11 meV. This AFM order was assumed by Beiranvand *et al.* [17] to be the magnetic ground state at  $x = 0.8$ . On

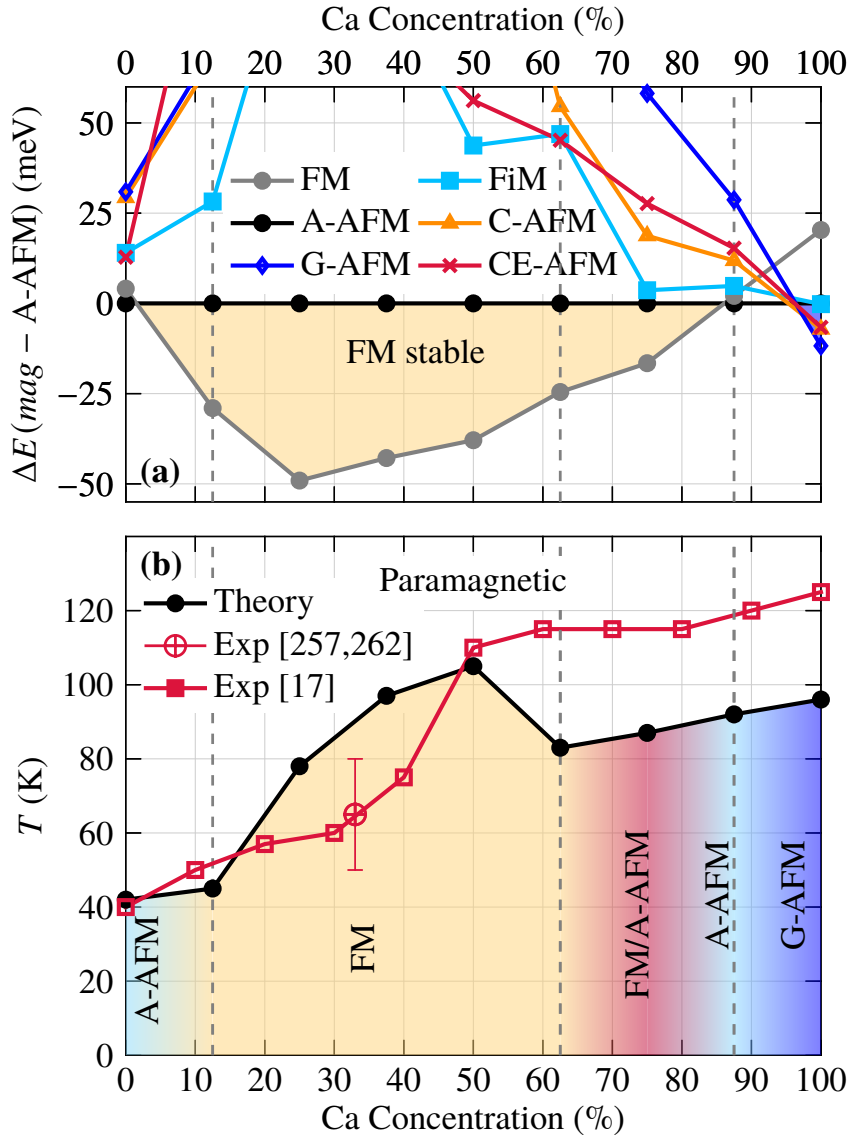


FIGURE 6.9: (a) The concentration dependent total energy landscape of the most relevant magnetic ground state structures (*mag*) depicted in Fig. 6.4. The energy differences  $\Delta E(\text{mag} - \text{A-AFM})$  are calculated with respect to the A-AFM state. The most stable magnetic state (*mag*) corresponds to the one which has, the lowest  $\Delta E$ . (b) The theoretical magnetic phase diagram of  $\text{Gd}_{1-x}\text{Ca}_x\text{MnO}_3$ . The critical temperatures (red circles) were determined via the Monte Carlo simulations, while the magnetic phases were identified from the minimal total energy. The measured critical temperatures from Ref. [17] (blue squares) and for  $x = 1/3$  from Ref. [257, 262] (red  $\oplus$  with error bars) are shown for comparison. higher temperatures than the magnetic ordering temperature corresponds to the paramagnetic state. The region marked with FM/A-AFM identifies the concentration range, where the total energy difference of the FM and A-AFM magnetic phase is below 25 meV. Dashed lines mark qualitative changes of the magnetic ordering.



the other hand the G-AFM which is the magnetic order of CaMnO<sub>3</sub> ( $x = 1$ ) is still high in energy at  $x = 7/8$ ,  $\approx 28$  meV. In the experimental magnetic phase diagram [17], the considered concentration of  $x = 7/8$  lies in the region where the colossal magneto resistance of Gd<sub>1-x</sub>Ca<sub>x</sub>MnO<sub>3</sub> was detected, i. e.  $0.8 < x < 0.9$ . Beyond that a cluster-glass (CG) state was observed [17]. These two complicate phenomena are far from being obtained by a simple model taking only collinear magnetic orders. Therefore a more sophisticated theoretical consideration has to be taken into account in order to describe properly the magnetic properties for the region 80 % to  $\sim 95$  % of Ca in GdMnO<sub>3</sub>.

The G-AFM ground state order is recovered at  $x = 1$  where its energy is about 32 meV lower than the FM. The closest energies among the considered magnetic structure are those of C-AFM and CE-AFM with only a difference of 4 meV and 5 meV, respectively. The structural distortion is as well reduced at  $x = 1$  with angles approaching more and more the limit of 180° for undistorted structures. The exchange interactions are negative and lower than -2 meV at  $x = 1$  which explains the robust G-AFM order of CaMnO<sub>3</sub>.

## 6.6 Transition temperatures of GCMO series

To assess the magnetic phase transition temperatures (whether Néel temperature  $T_N$  for AFM ground states or Curie Temperature  $T_C$  for FM ground states), Monte Carlo simulations were performed [H1]. An initial direction of the spin moments was taken along  $z$ -direction and the coupling between the different Mn sites are taken from the so far obtained ones with the Heisenberg Hamiltonian in Eq. (3.60) and presented in Fig. 6.7. A large Monte Carlo simulation cell of  $16 \times 16 \times 16$  repetitions of the primitive  $Pbnm$  unit cell which leads to a box with a volume about  $100 \text{ \AA}^3$ . The thermal equilibrium was firstly assumed to be reached after 60,000 MC steps. Thereafter, another 60,000 MC steps are used in the thermal averaging. Starting from 1,000 K and cooling down the samples in steps of 3 K, the transition temperature corresponding to each concentration of Gd<sub>1-x</sub>Ca<sub>x</sub>MnO<sub>3</sub> is determined, see Fig. 6.9 (b). Such magnetic transition temperatures are extracted from the temperature dependence of three quantities namely the magnetic susceptibility, the saturated magnetization, and the heat capacity.

An ordering temperature of 42 K was obtained for GdMnO<sub>3</sub>,  $x = 0$ , in agreement with the experimental value of 40 K [283, 284]. on the other hand, the stabilization of the FM order and also the increase of the exchange interactions magnitude affected also the Curie temperature in the hole doped region. It was found that  $T_C$  monotonically increases until  $x = 1/2$  to reach a maximum value of 110 K at  $x = 1/2$  as shown in Fig. 6.9 (b). This agrees very well with the reported temperature of Beiranvand *et al.* [17] and also the measured value at  $x = 1/3$  by Peña *et al.* [262]. The calculated Curie temperature followed as well the character of the hump-like showed in the Mn–O–Mn bond angle  $\beta$  at  $x = 5/8$  ( Fig. 6.8) and the exchange interaction  $J_z$ . This results in an underestimation of  $T_C$  by about 30 K from  $x = 5/8$  to  $x = 7/8$ . The same order of magnitude was also found for CaMnO<sub>3</sub> ( $x = 1$ ) where a value of 96 K was obtained by the MC calculations whereas the experimentally observed one equal to 125 K [285]. The disagreement between the measured and calculated transition temperatures in Fig. 6.9 (b) could have several explanations. Lattice imperfections, e. g. vacancies, at the oxygen sub-lattice might cause significant changes in



the magnetic properties as observed for other oxides like  $\text{SrCoO}_3$  [286] or  $\text{Sr}_2\text{FeMoO}_6$  [287]. In addition, the difference between experimental and theoretical results may be connected to the fact that an ideal periodic crystal is assumed in the simulation while the samples are polycrystalline in experiment. Furthermore, a more complicated magnetic structure might occur like the already detected canted antiferromagnetic order or the cluster glass state which can not be simulated with just three exchange interactions and involving only collinear magnetic structures.

## Conclusion

The effect of substituting the Gd ions by Ca ions on the magnetic properties of  $\text{GdMnO}_3$  is investigated. In overall, a good agreement with experiment was obtained in the calculated magnetic phase diagram of Ca doped  $\text{GdMnO}_3$ ,  $\text{Gd}_{1-x}\text{Ca}_x\text{MnO}_3$ . In that respect many concentrations are considered and their solid solutions were modeled by constructing special quasi-random structures to mimic as much as possible the disorder in such materials. A simple Heisenberg model (Eq. (3.60)) with only three exchange interactions is then used with the energy difference method explained in Sec. 3.4.1 and taking the magnetic configurations in Fig. 6.4. The AFM order in  $\text{GdMnO}_3$  transforms into a FM order when the concentration of Ca is less than  $1/2$  which agrees very well with the experimental data [17] in terms of energies and also transition temperatures. Such transition is mainly due to the conversion of the out-of-plane magnetic coupling nature from AFM to FM. Thus, the FM becomes more robust by doping with Ca. An analysis of the structural distortions of the  $\text{MnO}_6$  octahedra permitted to conclude that the stability of the FM state in the GCMO series is induced by the lowering of distortion, which is manifested in the simultaneous large reduction of the in-plane bond length  $d_{x_2}$  and the increase of two Mn–O–Mn bond angles. Increasing more the Ca concentration beyond  $x=1/2$ , leads to a systematic difference compared to experiment for  $x \geq 5/8$ . This might be connected with many factors, neglect of charge/orbital ordering or the formation of polarons in this region. Only for  $x > 7/8$ , the experimental AFM state is recovered with the considered model with slight underestimation of the Néel temperatures. In summary, a qualitative agreement between the numerical calculations and the measured magnetic phase diagram of  $\text{Gd}_{1-x}\text{Ca}_x\text{MnO}_3$  was obtained. Nevertheless several questions still open in this subject: Do the magnetic structures in  $\text{Gd}_{1-x}\text{Ca}_x\text{MnO}_3$  favor a non-collinear magnetism? If so which kind of magnetic order? What is the effect of Gd spins on the spin orientations of Mn particularly at low temperatures? Which combination of spin, charge and orbital ordering is likely to occur in  $\text{Gd}_{1-x}\text{Ca}_x\text{MnO}_3$ ? What is the effect of strain or lattice imperfections on the magnetic phase diagram of  $\text{Gd}_{1-x}\text{Ca}_x\text{MnO}_3$ ? On account on that, the present chapter could serve as a basis for further experimental and theoretical investigations of  $\text{GdMnO}_3$  related compounds.



## 7 Strain induced magnetic phase transitions in $\text{GdMnO}_3$

Another route to control the magnetic ground state of oxides, particularly  $\text{GdMnO}_3$  is the physical pressure. Such method includes all related mechanisms without involving any new chemical substance. This includes a hydrostatic pressure where the three cell axis are homogeneously compressed. An experimental realization can be obtained by using the diamond anvil cell technique [288] or the recent nanocrystalline anvils, which can make up to 770 GPa [289]. Compressing or elongating any material oxide along only one (two) cell axis is also possible with uni(bi)-axial strain. On one hand uniaxial strain can be induced by clamping the sample between two anvils [290], using bending devices [291] or by attaching the sample to piezoelectric stacks [292]. The biaxial strain on the other hand might be obtained by an epitaxial growth of the sample on crystalline substrates [14, 293], where the strain is induced by the lattice mismatch between the sample and the substrate. Another alternative is to insert an ultra-thin interface layer without requiring single crystal substrates [294]. Most of these schemes were examined in literature for  $\text{GdMnO}_3$  [15, 249, 295–299] and lead to the stabilization of essentially two magnetic orders, namely the ferromagnetic or E-type antiferromagnetic orders.

For instance, the application of a hydrostatic pressure of about 10 GPa using a diamond anvil cell leads to the stabilization of the E-type AFM [295]. The same magnetic order was reported as the ground state of the epitaxial  $\text{GdMnO}_3$  films deposited on the (010)-oriented orthorhombic  $\text{YAlO}_3$  by means of neutron-diffraction and resonant soft x-ray scattering measurements [15] and also by density functional calculations [249, 296].

As well the FM order was found to be stable in the  $\text{GdMnO}_3$  thin films, prepared by a chemical solution method on oriented Pt substrates [297]. Even a high Curie temperature of 70 K was reported. A similar finding was also experimentally revealed for the  $\text{GdMnO}_3$  thin films grown on (001)  $\text{SrTiO}_3$  substrate [298], where the films develop a ferromagnetic order with a Curie temperature of 105 K. Such order was not only confirmed by density functional calculations for the (001) substrate orientation but also predicted for the (110) direction [299].

Actually, structural modifications through epitaxial strain are anisotropic along the three axis [15, 300] and a straightforward understanding of the mechanisms behind the magnetic phase transitions might be a little bit tricky. To this end, the strain in this study will be restricted to either uniaxial, where just one cell parameter is changed but the two remaining cell parameters were fixed to the equilibrium ones, or an isotropic biaxial strain on the (ab)-plane with a relaxation of the out-of-plane cell parameter. The results of the last mentioned strain could serve as a guide for choosing the right substrate to produce a sought magnetic order for  $\text{GdMnO}_3$ . That means, a certain magnetic order, if obtained by the actual biaxial strain calculations, could be tuned by just looking for a substrate which has a lattice mismatch value corresponding to the strain percentage.

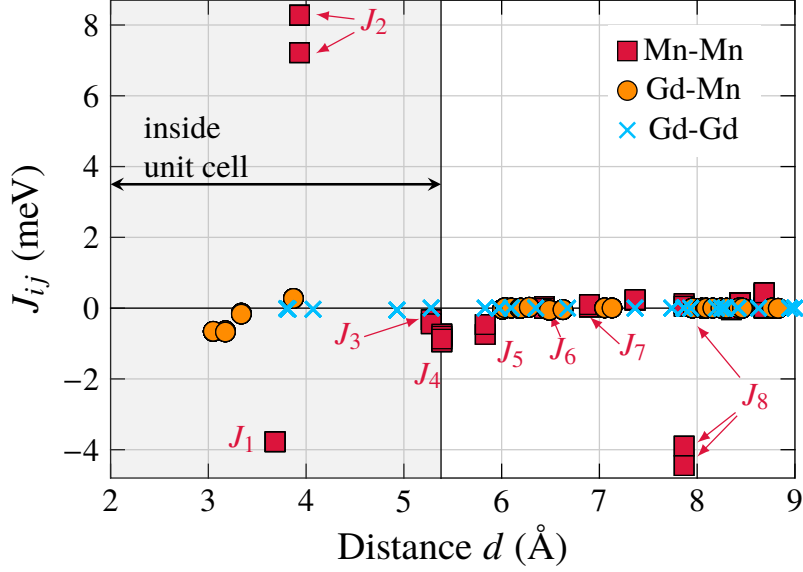


FIGURE 7.1: Magnetic exchange interactions of GdMnO<sub>3</sub>, calculated with the GF method, in dependence of the distances.  $J_{ij}$  inside one unit cell are underlaid with gray color. Labels  $J_1, \dots, J_8$  represent the respective  $J_{ij}$  used in the energy difference method.  $J_1$  corresponds to the  $J_z$  previous definitions while  $J_2$  and  $J_4$  correspond to  $J_x$  and  $J_{xz}$ , respectively. The Mn-Mn interaction with  $d \sim 7.36$  Å was neglected (not marked). Note that few values are different for the same distance (see text).

Furthermore, it was shown earlier that the lattice distortions of GdMnO<sub>3</sub> (see Fig. 6.3) were the origin of the observed magnetic phase transitions [301], mainly due to the strong competition between the different magnetic interactions. In this direction, the magnetic properties of GdMnO<sub>3</sub> are revised in the absence of strain and further extended in the presence of strain.

## 7.1 Extend of magnetic exchange interactions

In the previous chapter, experimental cell parameters were used in the determination of the magnetic phase diagram of Ca doped GdMnO<sub>3</sub> where a good agreement with experimental measurements was found. The results were obtained by means of a Heisenberg model with only three exchange interactions determined from four magnetic configurations. However, for strain calculations, a reference structure with the lowest possible internal forces is needed in order to compare the relative changes from a tensile or a compressive strain. This is not absolutely the case with the experimental structure. Thus, the fully relaxed structure of GdMnO<sub>3</sub> is adapted in the following discussions. Based on the previous Heisenberg model, minor changes were found for the calculated exchange interactions but an overestimation of the Néel temperature was found, 65 K compared to experimental value of 41 K.

To understand the reason behind this large obtained transition temperature, a thorough analysis of the intervened properties is made and the reliability of the three parameters model is reexamined. In this direction, the magnetic force theorem, see Sec. 3.4.2, is used with Korringa-Kohn-Rostoker method

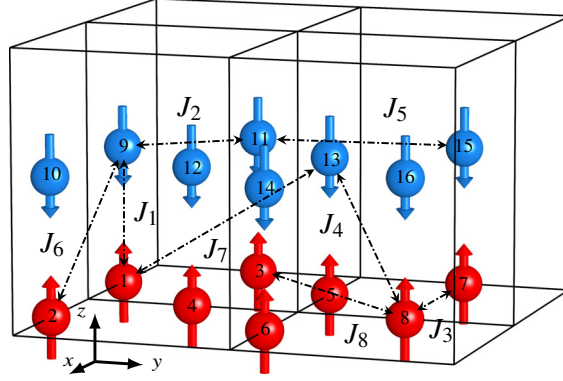


FIGURE 7.2: Sketch of the eight exchange interactions between Mn atoms in a supercell of  $2 \times 2 \times 1$  of  $\text{GdMnO}_3$  used in the Heisenberg Hamiltonian in Eq. (3.60) [H8]. For the sake of simplicity only nonequivalent Mn ions are presented. The ground state A-AFM is shown here with red (blue) balls with arrows for spin up (spin down).

as implemented in HUTSEPOT [H1]. In this scheme, not only Mn-Mn exchange interactions in  $\text{GdMnO}_3$  can be directly accessed but also Gd-Mn and Gd-Gd interactions.

Figure. 7.1 illustrates the calculated exchange interactions between the magnetic sites in  $\text{GdMnO}_3$ . Only Mn-Mn interactions are enumerated with their distances to test the reliability of the previous used method of total energies mapping (Chap. 6) [H7]). In this latter, interactions beyond the highlighted gray region in Fig. 7.1 were neglected. Although not all of them can be neglected as seen in Fig. 7.1, as some interactions beyond the unit cell have the same order of magnitude as those inside. In addition, contrarily to the energy difference method, the KKR based method leads to more than a single value for the same exchange interactions, e. g.  $J_8$  (Fig. 7.1). This stems from small structural variations of the orthorhombic symmetry, which can be only reflected in the results of the Green's function method. In the latter, the magnetic coupling parameters are determined for each pair of atoms and different angles and distances to oxygen or Gd sites can increase or lower the coupling strengths even with the same distances between the considered atoms.

The smallest obtained values of magnetic exchange interactions were found for Gd-Gd, i. e.  $4f-4f$ , magnetic interactions:  $|J_{ij}| \leq 0.1$  meV (see Fig. 7.1). Their negative signs approve an antiferromagnetic coupling between Gd sites in agreement with the experiment [284]. Those values explain also the small experimentally obtained magnetic transition temperature of the Gd sublattice, of about 7 K. This low temperature is in fact not an exception for Gd but holds true for all rare earth elements in manganites. Therefore, this coupling can be safely neglected in further model Hamiltonians aiming to study the magnetic properties of  $\text{RMnO}_3$ .

The more interesting interactions are those between Mn-Mn. The coupling constants reach a value of about 8 meV for the second nearest neighbor exchange  $J_2$  (Fig. 7.1). Beyond that, the coupling constants become much smaller. Only  $J_8$  at  $d \sim 7.86$  Å is an exception. It has four different values at this distance, two of them are strongly AFM ( $\approx -4$  meV). Therefore, this distance is also included in the new energy difference model.

The Gd ions on the other hand couple weak-antiferromagnetically to the Mn spins, in agreement with the experimental findings of Hemberger *et al.* [284]. The first two Gd-Mn exchange interactions were found to be negative and small ( $\sim -0.7$  meV) and interaction constants with larger distances become even smaller (see Fig. 7.1). Therefore, these interactions are neglected below.

By virtue of the observed strengths of the Mn-Mn exchange interactions beyond a single unit cell, the previous model in Chap. 6 is extended here by taking into account magnetic interactions up to 7.86 Å in the energy difference method. Such consideration results in a model with 8 exchange interactions as demonstrated in Fig. 7.2. Hence more than the 8 magnetic configurations, shown in Fig. 6.4, are needed for the total energy calculations. To this end, 5 additional antiferromagnetic configurations are added, see Fig. 7.3, which gives a total of 13 magnetic structures. The system of equations in Eq. (6.3) is then rewritten to cover all the considered magnetic structures:

$$\mathbf{E} = (E_A, E_C, \dots, E_T, E_X)^T. \quad (7.1)$$

The vector of magnetic exchange interactions is defined now as

$$\mathbf{J} = (J_1, \dots, J_8)^T. \quad (7.2)$$

which gives the matrix form of the system of equations:

$$\mathbf{E} = -\frac{S^2}{2}(16\mathbf{T})\mathbf{J}, \quad (7.3)$$

where the matrix  $\mathbf{T}$  contains now the essential number of interacting Mn atoms and reads:

$$\mathbf{T} = \begin{pmatrix} -2 & 4 & 2 & -8 & 2 & -4 & -4 & 4 \\ 2 & -4 & 2 & -8 & 2 & 4 & 4 & 4 \\ -2 & -4 & 2 & 8 & 2 & -4 & -4 & 4 \\ 2 & 4 & 2 & 8 & 2 & 4 & 4 & 4 \\ -2 & 0 & 2 & 0 & -2 & -4 & 4 & -4 \\ 2 & 0 & 2 & 0 & -2 & 4 & -4 & -4 \\ 0 & 0 & 2 & 0 & -2 & 0 & 0 & -4 \\ 0 & -2 & 0 & 0 & 2 & 0 & 0 & 0 \\ -2 & 0 & 0 & 0 & -2 & 0 & 4 & 0 \\ 0 & 0 & 2 & 0 & 0 & 0 & -4 & 0 \\ 0 & 0 & 2 & 0 & 0 & 0 & -4 & 0 \\ 0 & 0 & 2 & -4 & 0 & 0 & 0 & 0 \\ -2 & 0 & 2 & 0 & 0 & -4 & 0 & 0 \end{pmatrix} \begin{array}{l} \text{A} \\ \text{C} \\ \text{G} \\ \text{FM} \\ \text{E} \\ \text{E}^* \\ \text{H} \\ \text{D} \\ \text{CE} \\ \text{J} \\ \text{P} \\ \text{T} \\ \text{X} \end{array}$$

The right column here is only introduced for an easy reading of the dependence of each the magnetic configurations total energy on the 8 exchange interactions.

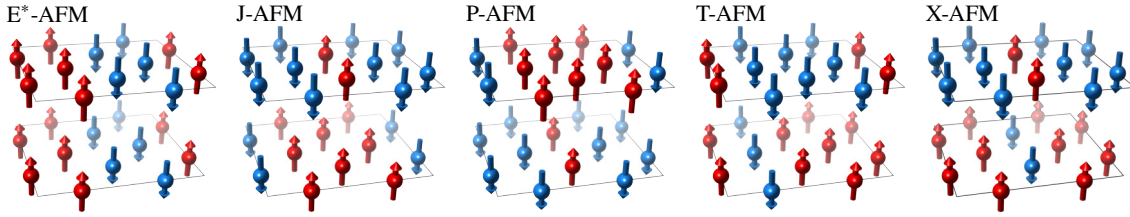


FIGURE 7.3: The additional magnetic configurations to those presented in Fig. 6.4 which were adapted here to calculate the exchange interactions of  $\text{GdMnO}_3$  in Eq. (3.60) and Eq. (7.3).

## 7.2 Lattice distortions effect on the magnetic interactions

Kimura *et al.* [283] attributed the destabilization of the A-AFM structure as ground state for  $\text{RMnO}_3$  in favor of the E-AFM order to the tilting of the  $\text{MnO}_6$  octahedra, known as  $\text{GdFeO}_3$ -type distortion, which is very pronounced in  $\text{GdMnO}_3$ . Nevertheless, a microscopic understanding of this destabilization based on first principles calculations is still unavailable. Thus, the cell distortions in  $\text{GdMnO}_3$  were decomposed in this study by starting from a purely cubic structure where the cell parameter for its primitive cell was taken as  $a/\sqrt{2}$  and  $a$  is the lattice constant of the relaxed orthorhombic cell along  $x$  direction. After that, the tetragonal structure is taken by keeping the in-plane cell parameter of the primitive cell as before and stretching the out-of plane cell parameter  $c$  to match that of the orthorhombic cell. In both structures, cubic and tetragonal, all atoms remain at their internal high symmetry positions.

Afterwards, the distortion of the  $\text{MnO}_6$  cage was gradually introduced using cell parameters from the orthorhombic structure in three steps: Jahn-Teller distortion Q2 corresponds to two long and four short Mn-O bonds. In the second Jahn-Teller distortion Q3, the  $\text{MnO}_6$  octahedron has two long, two medium, and two short Mn-O bonds. The final step before the orthorhombic structure is the cooperative rotations of the  $\text{MnO}_6$  polyhedra called  $\text{GdFeO}_3$ -type (GFO) distortion. The Gd ions were kept at the high symmetry points in all gradually distorted structures.

The same cell size and number of atoms are used for all structures in the total energy calculations with the magnetic structures shown in both Fig. 6.4 and Fig. 7.3. The results are given in Fig. 7.4. For the cubic structure, the FM order is the most favorable magnetic order followed by the E\*-AFM order. Stretching the  $c$  parameter in the tetragonal structure slightly reduces the difference between the FM and A-AFM energies. but the E\*-AFM order gets the second lowest energy. Most of the remaining structures have higher energies than that of the A-AFM state (Fig. 7.4).

Only introducing distortions in the  $\text{MnO}_6$  octahedra reduces further the total energy difference between the FM and A-AFM states until the A-AFM becomes the ground state for JT(Q3). This continues to be the case with the inclusion of the octahedra rotations in the GFO structure. Interestingly, most antiferromagnetic energies are lowered with this kind of distortion and become in the range of 10 meV to the A-AFM energy ( see Fig. 7.4). Taking into account all kinds of distortions with the fully relaxed structure of  $\text{GdMnO}_3$  does not affect much the sequence and the energy differences of the magnetic orders. Only slight changes were found compared to the GFO structure, which confirms the earlier hypothesis of Kimura *et al.* [283].

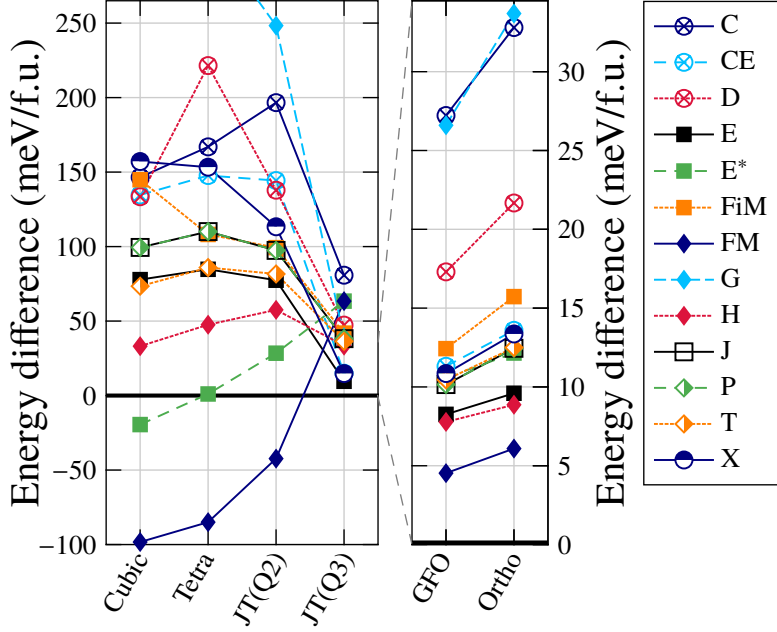


FIGURE 7.4: Total energy difference with respect to the final magnetic ground state A-AFM for different magnetic configurations and distortions of the GdMnO<sub>3</sub> lattice. Note that the energy differences for GFO distortion and orthorhombic structure are much smaller than the other distortions (gray dashed lines indicate the different scales).

Further validation of the latter results can be made with the exchange interactions ( Tab. 7.1). Due to the cubic symmetry, the two coupling parameters  $J_1$  and  $J_2$ , the three parameters  $J_3$ ,  $J_4$ , and  $J_5$ , as well as  $J_6$  and  $J_7$  are assumed to be equivalent in the fitting procedure of Eq. (7.3). The resulting magnetic ground state is clearly ferromagnetic, due to the strong FM coupling for nearest neighbor Mn sites and almost negligible second nearest neighbor interaction ( $J_3$ ). Although,  $J_8$  has AFM character (negative) it cannot overcome the large positive value of  $J_1$  ( $\sim 16$  meV). This fact can be also observed in the very high magnetic transition temperature of more than 900 K, calculated from the magnetic exchange parameters with Monte Carlo simulations (see bottom line in Tab. 7.1).

The introduction of the tetragonal distortion breaks the symmetry of  $J_1$  and  $J_2$ , although they stay FM (positive). Despite the large AFM coupling  $J_8$ , the magnetic ground state still remains FM with a high  $T_m = 714$  K because more magnetic exchange parameters have positive contributions resulting from the straight Mn–O–Mn bonds in this structural setting.

Including also internal structural variations through the Jahn-Teller mode Q2 does not alter the magnetic ground state, which remains FM, but reduces most of the coupling parameters. Only with Q3 distortion and beyond, the ground state starts to be the A-AFM order. This is clearly manifested by the large negative value of  $J_1$ . This fact changes again when the collective rotations of octahedra along  $c$ -axis are introduced (GFO distortion). The in-plane bond angle between Mn–O–Mn just changes by  $8^\circ$ , whereas out-of plane angle is strongly reduced by about  $40^\circ$ . Hence, the  $J_1$  interaction strength is significantly affected and the A-AFM state is destabilized.



TABLE 7.1: The calculated exchange interactions in  $\text{GdMnO}_3$  using the total energy difference method with gradual distortions from the perfect cubic to the orthorhombic structure (see text).  $J_{ij}$  are given in meV and magnetic transition temperatures in K. The three distortions on the left hand side show FM behavior, whereas the other show AFM behavior in the Monte Carlo simulations.

$J_{ij}$	Cub	Tet	JT(Q2)	JT(Q3)	GFO	Ortho
$J_1$	15.83	9.21	6.54	-7.23	-0.71	-1.04
$J_2$	15.83	18.55	15.23	1.77	1.54	1.89
$J_3$	-0.06	5.24	4.28	0.44	0.24	0.46
$J_4$	-0.06	-0.88	-0.14	-0.35	-0.07	-0.11
$J_5$	-0.06	5.24	5.59	0.42	0.32	0.40
$J_6$	0.26	1.61	-0.28	0.34	0.22	0.39
$J_7$	0.26	1.61	0.43	-0.04	-0.05	-0.05
$J_8$	-2.97	-5.71	-5.60	-0.86	-0.52	-0.70
$T_m$	926	714	504.4	63.9	40.3	41.0
	FM	FM	FM	AFM	AFM	AFM

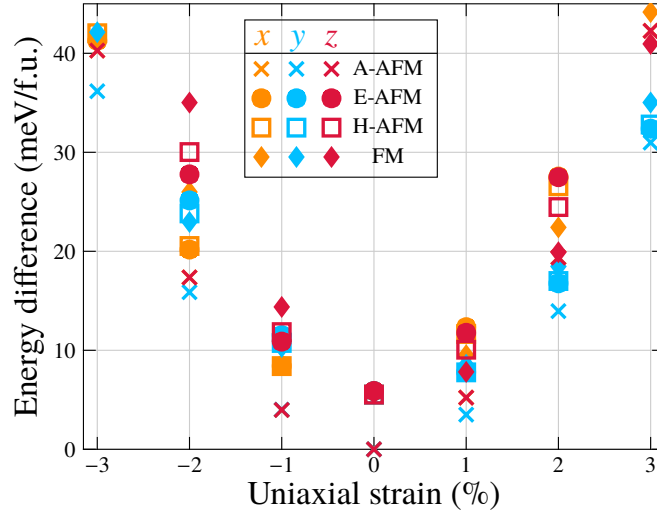


FIGURE 7.5: Total energy for the different magnetic configurations for the uniaxial strains along  $x$  (orange color), along  $y$  (light blue color) and along  $z$  direction (red color). At 0 % strain, the theoretical lattice structure in Tab. 6.1 is used.

The calculated magnetic transition temperatures show as well the importance of the GFO distortion (Tab. 7.1). The obtained  $T_m$  of 40.3 K is very close to that of the orthorhombic symmetry (last column in Tab. 7.1). This latter agrees very well with the measurement of Kimura *et al.* [283] and much better than the previous one, obtained by three exchange interactions. Only the Monte Carlo transition temperature of the Q3 structure and the real orthorhombic structure are still close to the experimental value among the other considered symmetries of  $\text{GdMnO}_3$ . The remaining structures lead to high  $T_m$  due to the large obtained exchange interactions.

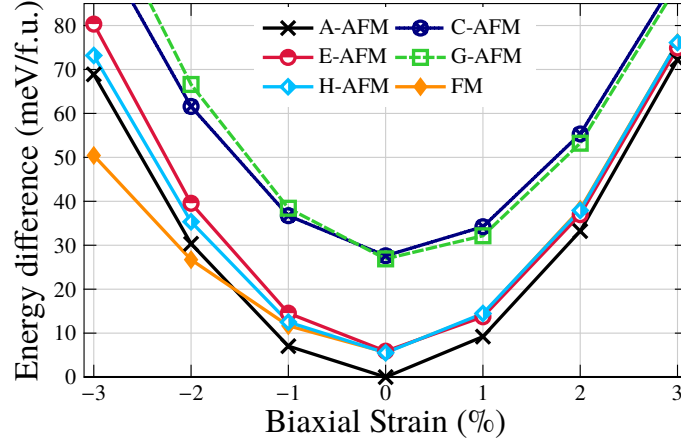


FIGURE 7.6: Total energy for the different magnetic configurations for biaxial strains in the  $xy$  plane. At 0% strain, the theoretical lattice structure in Tab. 6.1 is used.

### 7.3 Uniaxial strain

As already discussed in Sec. 7.2, the exchange couplings  $J_{ij}$  in GdMnO<sub>3</sub> show different FM and AFM behaviors with comparable strengths. These couplings were also demonstrated to be strongly affected by the internal structural distortions. This motivates the application of strain as tool to tune the magnetic properties of GdMnO<sub>3</sub>. Hence, the effect of uniaxial strain along the three different crystallographic axes on the stability of the magnetic order in GdMnO<sub>3</sub> is checked.

Owing to the orthorhombic structure of GdMnO<sub>3</sub> and consequently the challenging numerical task to control the convergence of two cell parameters if the third one is adjusted, those along the perpendicular directions of the applied uniaxial strain are fixed to their equilibrium values. Therefore the cell volume is adjusted by the same amount of the applied uniaxial strain and the stability of the magnetic orders are checked within the strained volumes.

Being A-AFM for the unstrained system, the magnetic order does not show any transition whether with compressive or tensile strain along the  $x$  direction up to 3% (see Fig. 7.5). Nevertheless, the energy difference to the E-AFM and H-AFM structures are reduced with compressive strain. The situation reverses with tensile strain where the total energies of the two previous AFM orders increase, while the FM energy becomes only few meV higher than the A-AFM. The total energies of the C-AFM and G-AFM configurations remain barely unaffected here and are higher than 50 meV. For uniaxial strain along the  $y$  direction, the order of the total energies of the magnetic structures does not change noteworthy (see Fig. 7.5). On the other hand, the situation becomes more interesting for uniaxial strain along the  $z$  direction (see Fig. 7.5). There, a tensile strain of 3% changes the order of the total energies and the FM order is found to stabilize as ground state. This amount of strain was insufficient along the other two uniaxial strain directions. In other words, only a tensile strain in  $z$  direction may affect the magnetic ground state of GdMnO<sub>3</sub>. This transition is mainly driven by the drastic change of the calculated value of  $J_1$ . It goes from an AFM coupling of  $-1.04$  meV in the unstrained system to a weak FM coupling of  $0.12$  meV. Most of other exchange coupling were slightly affected, except the FM  $J_2$  and the AFM  $J_3$  which were strengthened by  $0.35$  meV or weakened by  $0.1$  meV, respectively.

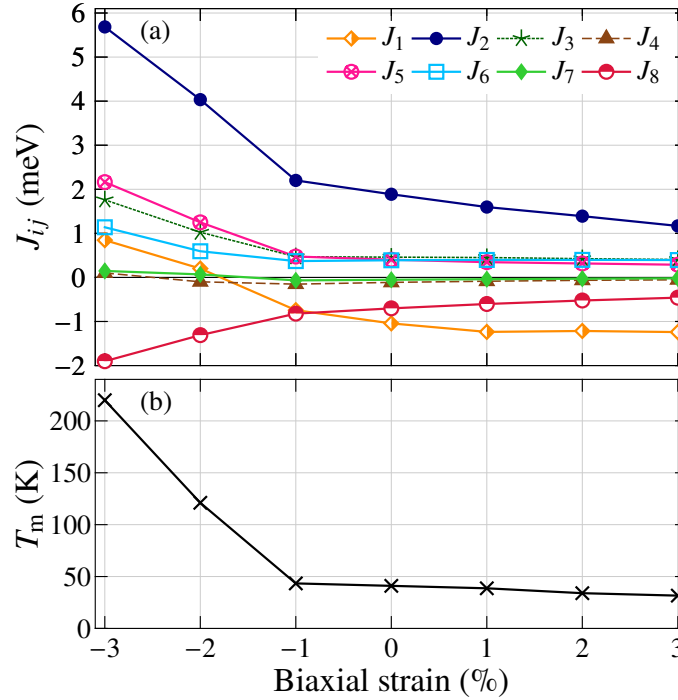


FIGURE 7.7: Variation of (a) the exchange interactions and (b) the magnetic transition temperature  $T_m$  in orthorhombic  $\text{GdMnO}_3$  with the applied biaxial strain within the  $xy$  plane.

## 7.4 Biaxial strain

The biaxial strain is defined here as the application of an uniform strain in one chosen plane – here the  $xy$  plane. That means that the  $a$  and  $b$  cell parameters were equally compressed or stretched and kept fixed in the DFT calculations according to the given strain percentage, while the  $c$  parameter was relaxed in order to minimize the total energy (Fig. 7.6).

The application of 1% tensile strain was found to lower the difference between the A-AFM, which remains the ground state, see Fig. 7.6. The same holds true for the H-AFM state, which becomes just  $\sim 0.8$  meV higher than that of the E-AFM state. Increasing further the tensile strain lowers only the energy differences but the A-AFM state remains the magnetic ground state. Similar observations can be made from the magnetic exchange interactions for tensile strain region (Fig. 7.7a). The variations in  $J_{ij}$  are moderate, which is in line with the small differences in the energy landscape. Nevertheless, the in-plane magnetic coupling parameters are affected. In particular,  $J_2$  decreases its value by almost  $\sim 1$  meV. The same thing was also found for  $J_5$  and  $J_8$  with smaller change than  $J_2$ , almost 1 meV,  $J_8$  from  $\sim -0.7$  meV to  $-0.46$  meV, and  $J_5$  from  $\sim 0.4$  meV to  $0.29$  meV. This results in an energetic preference towards the E-AFM order, which is essentially similar to the AFM order in out-of-plane direction but has AFM contributions in the  $xy$  plane.

On the other hand, compressing the in-plane lattice constants of  $\text{GdMnO}_3$  shows an amplification of the  $J_2$  value (Fig. 7.7a). By the same way, the other FM couplings in the unstrained structure ( $J_3$ ,  $J_5$ , and  $J_6$ ) increase their strength with compressive strain. In contrast, the AFM couplings in the unstrained structure, except  $J_8$ , ( $J_1$ ,  $J_4$ , and  $J_7$ ) gradually develop a FM behavior which

TABLE 7.2: Structural distortion parameters for biaxial strain. The 3 different Mn-O bond lengths are short ( $d_{x_1}$ ), medium ( $d_z$ ), and long ( $d_{x_2}$ ) and given in Å. The in-plane and out-of-plane Mn-O-Mn bond angles are  $\alpha$  and  $\beta$ , respectively [H7]. A graphical representation of the 5 structural properties are given in Fig. 6.3.

Strain	$d_{x_1}$	$d_z$	$d_{x_2}$	$\alpha$	$\beta$
-3 %	1.92	1.98	2.06	145.40	148.67
-2 %	1.91	1.96	2.12	145.42	146.77
-1 %	1.90	1.94	2.16	145.42	145.17
0 %	1.91	1.94	2.21	145.50	143.66
1 %	1.91	1.92	2.23	145.53	142.14
2 %	1.92	1.92	2.27	145.39	140.89
3 %	1.91	1.92	2.31	145.31	139.85

starts at 2 % for both  $J_1$  and  $J_7$  and later at 3 % strain for  $J_4$ , too. This goes in line with the total energy difference for compressive strain (Fig. 7.6). At a strain of -2 %, the FM order becomes more favorable with 3.6 meV lower than the A-AFM state.

These magnetic variations are driven essentially by the internal distortions of the MnO<sub>6</sub> octahedra (as shown in Sec. 7.2). The changes in the MnO<sub>6</sub> are briefly discussed in the following in terms of the Mn-O bond lengths and the Mn-O-Mn bonding angles (Tab. 7.2). The shortest bond length  $d_{x_1}$  in the MnO<sub>6</sub> octahedron does not change significantly, but the medium bond length  $d_z$  (1.94 Å at zero strain) decreases by 0.2 Å for tensile strains and becomes almost similar to  $d_{x_1}$ . The latter can hint to a structural transition from JT(Q3) to JT(Q2), which could indicate a FM ground state (Tab. 7.1). Surprisingly,  $d_z$  increases up to 1.98 Å for compressive strains. Only the longest bond length  $d_{x_2}$  – in-plane and initially 2.21 Å – follows a linear increase from the highest compressive strain of -3 % to the highest studied tensile strain of 3 %. Besides the bond lengths, the Mn-O-Mn bond angles indicate as well internal distortions (Tab. 7.2). Only the out-of-plane bond angle  $\beta$  is affected by the biaxial strain and decreases linearly from 148.67° to 139.85° from compressive to tensile strain. It becomes smaller or larger than  $\alpha$  for compressive or tensile strain, respectively. This indicates again that two different kinds of structural distortions occur for compressive and tensile strain.

By decreasing the value of  $\beta$  with tensile strain, the GFO structural distortions increase (Tab. 7.2) where the E-AFM magnetic order should be consequently stabilized for large GFO distortions in RMnO<sub>3</sub> [283]. Thus, it is believed here also that larger tensile strain might stabilize as well the E-AFM order in GdMnO<sub>3</sub> (Tab. 7.2).

Finally, the obtained exchange interactions for each biaxial strain value were used in a Monte Carlo calculation (see Fig. 7.7b). On one hand an abrupt increase of the Curie temperature with compressive strain was obtained. On the other hand, only a minimal decrease of the Néel temperature was observed with tensile strain. The same trend was also reported in the magnetic phase diagram of RMnO<sub>3</sub> [283] where the transition temperature decreases linearly from compounds with A-AFM order to those with E-AFM order. This confirms again a possible magnetic phase transition of GdMnO<sub>3</sub> towards the E-AFM magnetic order with a rather large tensile strain.

## Conclusion

The stability of different magnetic configurations is extensively discussed for  $\text{GdMnO}_3$ . The A-type antiferromagnetic structure is identified as the magnetic ground state of the system using a Heisenberg Hamiltonian which takes not only three nearest neighbor Mn-Mn exchange interactions but values up to a distance of  $\sim 7.86 \text{ \AA}$ . This distance goes beyond the unit cell of  $\text{GdMnO}_3$  and covers also the in-plane interaction  $J_8$ , which was rather large and AFM. It explains the observed close relationship of  $\text{GdMnO}_3$  with the H-AFM and E-AFM magnetic orders and the experimental observation of E-AFM under some conditions.

These results were confirmed by magnetic exchange interactions obtained with the magnetic force theorem. Note here, that a comparison of the calculated exchange interactions with experimental results is not directly possible because the latter may include contributions from the magnetism of the rare earth ion, which are ignored in the considered model Hamiltonian.

As main results, the internal structural distortions were shown to be a main ingredient for magnetic stability in  $\text{GdMnO}_3$ . All possible lattice distortions of the  $\text{MnO}_6$  octahedra had to be taken into account in order to reproduce the experimentally measured magnetic transition temperature. Starting instead from the fully relaxed structure, uniaxial and biaxial strain were applied to  $\text{GdMnO}_3$ . Uniaxial strain did alter the magnetic order only when the cell is compressed along the  $z$  direction. However, biaxial strain results in two different behaviors when applied. A compression of the  $ab$ -plane was able to destroy the AFM coupling in  $\text{GdMnO}_3$  and promote a robust FM order, besides tensile strain might be able to trigger a phase transition towards the E-AFM. One possible realization of these transitions can be acquired in thin films, where the variation of the substrate can cause epitaxial strain. The obtained results demonstrate that tailoring the magnetic properties of  $\text{GdMnO}_3$  is possible by small structural distortions, being internally or externally via uniaxial or biaxial strain.



## 8 Summary

The main goal of this thesis was the investigation of different functional oxide materials under an applied constraint by means of *ab initio* methods. The effect of three structural-modification factors, namely defects, doping and strain, on the oxide functionalities was carefully checked.

A diverse spectrum of theoretical methods were therefore used. They are based on two schemes of dealing with the density functional theory formulations. The plane-wave pseudopotential method on one hand was proven to perform very well with all kinds of structural modifications. Structural, electronic and magnetic properties of the targeted oxides were demonstrated to be broadly consistent with experimental results. On the other hand, the Green's function Korringa-Kohn-Rostoker method, which is very promising and versatile method to deal with disordered states, was shown to compare well with pseudopotential results and reproduce the magnetic properties of oxides. Unfortunately, the large needed computational effort of the KKR method hindered a greater gain from it in this thesis. But nevertheless the Green's function Korringa-Kohn-Rostoker method was successfully used to understand and confirm the pseudopotential results for some selected oxides.

The first main contribution, proposed in this thesis, to tune oxide functionalities concerns the magnetic order in  $\text{TiO}_2$ . The induced magnetism was demonstrated to stabilize  $\text{TiO}_2$  without any intermediate magnetic element. Only with point defects, isolated or complex, ferromagnetic, ferrimagnetic and antiferromagnetic orders were obtained. This finding would settle the debate in literature over the responsible defect in  $\text{TiO}_2$  for the appearance of the different experimentally reported magnetic orders. For instance, antiferromagnetism was established to arise in the presence of an isolated oxygen vacancy. However, two isolated oxygen vacancies, with a certain configuration, were shown to stabilize a ferrimagnetic state. The ferromagnetic order on the other hand was obtained with different defects, like the titanium vacancies, the combination of one Frenkel pair and an oxygen vacancy or the di-Frenkel pair. This latter was even demonstrated to induce the largest magnetic crystalline anisotropy energy. Such new anisotropic functionality has many practical advantages.

The second contribution was the structural stability of the hexagonal phase of  $\text{BaTiO}_3$  where two routes were proposed. Stability with the transition metal, iron, defect was largely discussed in experiment but no conclusive information was given which site the iron ion from the two distinct titanium sites prefers. In this work, and based on thermodynamical analysis with the defect formation energy method, the iron ion was found to favor the special Ti site, characteristic of the hexagonal phase of  $\text{BaTiO}_3$ . This site does not have an equivalent in the simple cubic structure of  $\text{BaTiO}_3$ . Though the obtained formation energy value is still high. The inclusion of oxygen vacancy in combination with an iron substitution of titanium whether from the cubic or hexagonal Ti sites was as well checked. The results indicated that putting an oxygen vacancy on the second shell of an iron placed at the cubic Ti site is more favorable. This may be considered as a validation of the recent electron paramagnetic resonance measurements. Another route to stabilize the hexagonal phase was

also argued in this thesis. Therein, the stability was discussed from another perspective, phonon infrared active modes. Importantly, the application of a moderate biaxial strain was demonstrated to harden all soft modes of the unstrained structure. This scheme provides a new potential mechanism to stabilize the hexagonal phase of  $\text{BaTiO}_3$ .

The third main contribution involves the magnetic phase stability, instead of the structural stability in the previous point. The target oxide  $\text{GdMnO}_3$  was chosen for this purpose owing to its interesting features. The control of the ground state magnetostructure of  $\text{GdMnO}_3$  was made with two different ways: chemical pressure through doping with the alkaline earth metal calcium ions along with the physical pressure manifested in different applied strains. In order to simulate the solid solutions of  $\text{GdMnO}_3$  doped with calcium, special quasi-random structures were constructed and used. In addition, the magnetic properties were discussed with a three-parameters Heisenberg model. The resulting structural, electronic and magnetic properties were substantially found to be in a good agreement with experiment for the hole doped region. By doping with low concentrations, about 10 %, the weak antiferromagnetic couplings in  $\text{GdMnO}_3$  was completely destroyed and a strong ferromagnetic started to develop from 10 % to reach its maximum at 50 %. Beyond that and up to a concentration of about 85 %, the experimental ground-state magnetic orders were not detected and also the calculated transition temperatures were underestimated. The reason of these limitations are the neglect of charge and orbital ordering within this concentration range. For the electron doped region, the stability of the antiferromagnetic order was recovered but the Néel temperatures remained lower than those from experiment. The driving force of all of these magnetic transitions was assigned to the diminution of octahedral distortions with doping. Overall, the considered methods were successfully applied to understand and reproduce theoretically, at some extent, the rich and complicated magnetic phase diagram of GCMO series.

In the last part, the previously adapted Heisenberg model was extended to take into account long-range interactions. Such interactions were shown by means of total energy and Green's function calculations to play an important role in the stability of antiferromagnetic order in  $\text{GdMnO}_3$ . An additional confirmation was demonstrated for importance of structural distortions in the determination of the magnetic ground state. Extensive calculations were carried out for a decomposed distortion from the perfect cubic perovskite structure to the experimental orthorhombic structure. The results provided a great evidence to the importance of collective octahedral rotations in  $\text{GdMnO}_3$  for an appropriate theoretical description of magnetic properties. The study was extended to check the effect of on applied strain on the magnetic ground state. Uniaxial strain on one hand was found to alter the magnetic order only by compressing the cell along the  $z$  direction. The application of biaxial strain, on the other hand, showed the possible stability of two new magnetic states in dependence of the applied strain character. A compressive strain promoted a robust ferromagnetic order. Whereas a tensile strain was apparently able to trigger a phase transition towards the E-type antiferromagnetic order, which favors in turn the appearance of ferroelectricity in manganites. In future work, it would be important to look for new functionalities by calculating the properties of constructed heterostructures from the studied oxides in this thesis.



## Bibliography

1. Ohzuku, T. & Ueda, A. Why transition metal (di) oxides are the most attractive materials for batteries. *Solid State Ionics* **69**, 201. doi:10.1016/0167-2738(94)90410-3 (1994).
2. Thackeray, M. M. Manganese oxides for lithium batteries. *Prog. Solid State Chem.* **25**, 1. doi:10.1016/S0079-6786(97)81003-5 (1997).
3. Poizot, P., Laruelle, S., Grugeon, S., Dupont, L. & Tarascon, J.-M. Nano-sized transition-metal oxides as negative-electrode materials for lithium-ion batteries. *Nature* **407**, 496. doi:10.1038/35035045 (2000).
4. Fergus, J. W. Oxide materials for high temperature thermoelectric energy conversion. *J. Eur. Ceram. Soc.* **32**, 525. doi:10.1016/j.jeurceramsoc.2011.10.007 (2012).
5. Koumoto, K., Wang, Y., Zhang, R., Kosuga, A. & Funahashi, R. Oxide Thermoelectric Materials: A Nanostructuring Approach. *Annu. Rev. Mater. Res.* **40**, 363. doi:10.1146/annurev-matsci-070909-104521 (2010).
6. Koumoto, K., Terasaki, I. & Funahashi, R. Complex Oxide Materials for Potential Thermoelectric Applications. *MRS Bull.* **31**, 206. doi:10.1557/mrs2006.46 (2006).
7. Eranna, G., Joshi, B. C., Runthala, D. P. & Gupta, R. P. Oxide Materials for Development of Integrated Gas Sensors—A Comprehensive Review. *Crit. Rev. Solid State Mater. Sci.* **29**, 111. doi:10.1080/10408430490888977 (2004).
8. Barsan, N. & Weimar, U. Conduction Model of Metal Oxide Gas Sensors. *J. Electroceram.* **7**, 143. doi:10.1023/A:1014405811371 (2001).
9. Wang, C., Yin, L., Zhang, L., Xiang, D. & Gao, R. Metal Oxide Gas Sensors: Sensitivity and Influencing Factors. *Sensors* **10**, 2088. doi:10.3390/s100302088 (2010).
10. Dunbar, T. D. *Method for making electronic devices using metal oxide nanoparticles* US Patent 7,507,618. 2009.
11. Spaldin, N. A. & Ramesh, R. Advances in magnetoelectric multiferroics. *Nat. Mater.* **18**, 203. doi:10.1038/s41563-018-0275-2 (2019).
12. Akira, F. & Honda, K. Electrochemical Photolysis of Water at a Semiconductor Electrode. *Nature* **238**, 37. doi:10.1038/238037a0 (1972).
13. Functionality of Oxide Interfaces. *Phys. Status Solidi B* **257**, 2000270. doi:10.1002/pssb.202000270 (2020).
14. Biswas, A. & Jeong, Y. H. *Epitaxy* (ed Zhong, M.) chapter 1 (IntechOpen, Rijeka, 2018). doi:10.5772/intechopen.70125.
15. Mukherjee, S. *et al.* Multiferroic phase diagram of *E*-type  $RMnO_3$  films studied by neutron and x-ray diffraction. *Phys. Rev. B* **98**, 174416. doi:10.1103/PhysRevB.98.174416 (2018).

16. Böttcher, R., Langhammer, H. T., Kücker, S., Eisenschmidt, C. & Ebbinghaus, S. G. On the incorporation of iron into hexagonal barium titanate: I. electron paramagnetic resonance (EPR) study. *J. Phys.: Condens. Matter* **30**, 425701. doi:10.1088/1361-648x/aadea8 (2018).
17. Beiranvand, A., Tikkanen, J., Huhtinen, H. & Paturi, P. Electronic and magnetic phase diagram of polycrystalline  $\text{Gd}_{1-x}\text{Ca}_x\text{MnO}_3$  manganites. *J. Alloys Compd.* **720**, 126. doi:10.1016/j.jallcom.2017.05.231 (2017).
18. Von Helmolt, R., Wecker, J., Holzäpfel, B., Schultz, L. & Samwer, K. Giant negative magnetoresistance in perovskitelike  $\text{La}_{2/3}\text{Ba}_{1/3}\text{MnO}_x$  ferromagnetic films. *Phys. Rev. Lett.* **71**, 2331. doi:10.1103/PhysRevLett.71.2331 (1993).
19. Salamon, M. B. & Jaime, M. The physics of manganites: Structure and transport. *Rev. Mod. Phys.* **73**, 583. doi:10.1103/RevModPhys.73.583 (2001).
20. Nickel, J. & Zhang, S. *Colossal magnetoresistance sensor* US Patent 5,835,003. 1998.
21. Haghiri-Gosnet, A.-M. & Renard, J.-P. CMR manganites: physics, thin films and devices. *J. Phys. D: Appl. Phys.* **36**, R127. doi:10.1088/0022-3727/36/8/201 (2003).
22. Kresse, G. & Furthmüller, J. Efficiency of ab-initio total energy calculations for metals and semiconductors using a plane-wave basis set. *Comput. Mater. Sci.* **6**, 15. doi:10.1016/0927-0256(96)00008-0 (1996).
23. Kresse, G. & Furthmüller, J. Efficient iterative schemes for ab initio total-energy calculations using a plane-wave basis set. *Phys. Rev. B* **54**, 11169. doi:10.1103/PhysRevB.54.11169 (1996).
24. Giannozzi, P. *et al.* Advanced capabilities for materials modelling with Quantum ESPRESSO. *J. Phys.: Condens. Matter* **29**, 465901. doi:10.1088/1361-648x/aa8f79 (2017).
25. Korringa, J. On the calculation of the energy of a Bloch wave in a metal. *Physica* **13**, 392. doi:10.1016/0031-8914(47)90013-X (1947).
26. Kohn, W. & Rostoker, N. Solution of the Schrödinger Equation in Periodic Lattices with an Application to Metallic Lithium. *Phys. Rev.* **94**, 1111. doi:10.1103/PhysRev.94.1111 (1954).
27. Soven, P. Coherent-Potential Model of Substitutional Disordered Alloys. *Phys. Rev.* **156**, 809. doi:10.1103/PhysRev.156.809 (1967).
28. Taylor, D. W. Vibrational Properties of Imperfect Crystals with Large Defect Concentrations. *Phys. Rev.* **156**, 1017. doi:10.1103/PhysRev.156.1017 (1967).
29. Zunger, A., Wei, S.-H., Ferreira, L. G. & Bernard, J. E. Special quasirandom structures. *Phys. Rev. Lett.* **65**, 353. doi:10.1103/PhysRevLett.65.353 (1990).
30. De Walle, A. V., Tiwary, P., de Jong, M., Olmsted, D., Asta, M., Dick, A., Shin, D., Wang, Y., Chen, L.-Q. & Liu, Z.-K. Efficient stochastic generation of special quasirandom structures. *Calphad* **42**, 13. doi:10.1016/j.calphad.2013.06.006 (2013).
31. Liechtenstein, A., Katsnelson, M., Antropov, V. & Gubanov, V. Local spin density functional approach to the theory of exchange interactions in ferromagnetic metals and alloys. *J. Magn. Magn. Mater.* **67**, 65. doi:10.1016/0304-8853(87)90721-9 (1987).
32. Born, M. & Oppenheimer, R. Zur Quantentheorie der Molekeln. *Ann. Phys.* **389**, 457. doi:10.1002/andp.19273892002 (1927).
33. Aronowitz, S. Adiabatic approximation and the Jahn-Teller theorem. *Phys. Rev. A* **14**, 1319. doi:10.1103/PhysRevA.14.1319 (1976).

34. Pisana, S., Lazzeri, M., Casiraghi, C., Novoselov, K. S., Geim, A. K., Ferrari, A. C. & Mauri, F. Breakdown of the adiabatic Born-Oppenheimer approximation in graphene. *Nat. Mater.* **6**, 198. doi:10.1038/nmat1846 (2007).
35. Hartree, D. R. The Wave Mechanics of an Atom with a Non-Coulomb Central Field. Part I. Theory and Methods. *Math. Proc. Cambridge Philos. Soc.* **24**, 89. doi:10.1017/S0305004100011919 (1928).
36. Fock, V. Näherungsmethode zur Lösung des quantenmechanischen Mehrkörperproblems. *Z. Phys.* **61**, 126. doi:10.1007/BF01340294 (1930).
37. Slater, J. C. The Self Consistent Field and the Structure of Atoms. *Phys. Rev.* **32**, 339. doi:10.1103/PhysRev.32.339 (1928).
38. Condon, E. U. The Theory of Complex Spectra. *Phys. Rev.* **36**, 1121. doi:10.1103/PhysRev.36.1121 (1930).
39. Thomas, L. H. The calculation of atomic fields. *Math. Proc. Cambridge Philos. Soc.* **23**, 542. doi:10.1017/S0305004100011683 (1927).
40. Fermi, E. Eine statistische Methode zur Bestimmung einiger Eigenschaften des Atoms und ihre Anwendung auf die Theorie des periodischen Systems der Elemente. *Z. Phys.* **48**, 73. doi:10.1007/BF01351576 (1928).
41. Zink, J. W. Shell Structure and the Thomas-Fermi Equation of State. *Phys. Rev.* **176**, 279. doi:10.1103/PhysRev.176.279 (1968).
42. Teller, E. On the Stability of Molecules in the Thomas-Fermi Theory. *Rev. Mod. Phys.* **34**, 627. doi:10.1103/RevModPhys.34.627 (1962).
43. Weizsäcker, C. F. v. Zur Theorie der Kernmassen. *Z. Phys.* **96**, 431. doi:10.1007/BF01337700 (1935).
44. Dirac, P. A. M. Note on Exchange Phenomena in the Thomas Atom. *Math. Proc. Cambridge Philos. Soc.* **26**, 376. doi:10.1017/S0305004100016108 (1930).
45. Hohenberg, P. & Kohn, W. Inhomogeneous Electron Gas. *Phys. Rev.* **136**, B864. doi:10.1103/PhysRev.136.B864 (1964).
46. Levy, M. Universal variational functionals of electron densities, first-order density matrices, and natural spin-orbitals and solution of the  $v$ -representability problem. *Proc. Natl. Acad. Sci. U. S. A.* **76**, 6062. doi:10.1073/pnas.76.12.6062 (1979).
47. Lieb, E. H. Density functionals for coulomb systems. *Int. J. Quantum Chem.* **24**, 243. doi:10.1002/qua.560240302 (1983).
48. Coulson, C. A. & Neilson, A. H. Electron Correlation in the Ground State of Helium. *Proc. Phys. Soc.* **78**, 831. doi:10.1088/0370-1328/78/5/328 (1961).
49. Puzder, A., Chou, M. Y. & Hood, R. Q. Exchange and correlation in the Si atom: A quantum Monte Carlo study. *Phys. Rev. A* **64**, 022501. doi:10.1103/PhysRevA.64.022501 (2001).
50. Kohn, W. & Sham, L. J. Self-Consistent Equations Including Exchange and Correlation Effects. *Phys. Rev.* **140**, A1133. doi:10.1103/PhysRev.140.A1133 (1965).
51. Kohn, W. Nobel Lecture: Electronic structure of matter—wave functions and density functionals. *Rev. Mod. Phys.* **71**, 1253. doi:10.1103/RevModPhys.71.1253 (1999).

52. Slater, J. C. A Simplification of the Hartree-Fock Method. *Phys. Rev.* **81**, 385. doi:[10.1103/PhysRev.81.385](https://doi.org/10.1103/PhysRev.81.385) (1951).
53. Ceperley, D. M. & Alder, B. J. Ground State of the Electron Gas by a Stochastic Method. *Phys. Rev. Lett.* **45**, 566. doi:[10.1103/PhysRevLett.45.566](https://doi.org/10.1103/PhysRevLett.45.566) (1980).
54. Perdew, J. P. & Zunger, A. Self-interaction correction to density-functional approximations for many-electron systems. *Phys. Rev. B* **23**, 5048. doi:[10.1103/PhysRevB.23.5048](https://doi.org/10.1103/PhysRevB.23.5048) (1981).
55. Vosko, S. H., Wilk, L. & Nusair, M. Accurate spin-dependent electron liquid correlation energies for local spin density calculations: a critical analysis. *Can. J. Phys.* **58**, 1200. doi:[10.1139/p80-159](https://doi.org/10.1139/p80-159) (1980).
56. Perdew, J. P. & Wang, Y. Accurate and simple analytic representation of the electron-gas correlation energy. *Phys. Rev. B* **45**, 13244. doi:[10.1103/PhysRevB.45.13244](https://doi.org/10.1103/PhysRevB.45.13244) (1992).
57. Martin, R. M. *Electronic Structure: Basic Theory and Practical Methods* doi:[10.1017/CB09780511805769](https://doi.org/10.1017/CB09780511805769) (Cambridge University Press, 2004).
58. Perdew, J. P. Density-functional approximation for the correlation energy of the inhomogeneous electron gas. *Phys. Rev. B* **33**, 8822. doi:[10.1103/PhysRevB.33.8822](https://doi.org/10.1103/PhysRevB.33.8822) (1986).
59. Perdew, J. P., Burke, K. & Ernzerhof, M. Generalized Gradient Approximation Made Simple. *Phys. Rev. Lett.* **77**, 3865. doi:[10.1103/PhysRevLett.77.3865](https://doi.org/10.1103/PhysRevLett.77.3865) (1996).
60. Csonka, G. I., Perdew, J. P., Ruzsinszky, A., Philippen, P. H. T., Lebègue, S., Paier, J., Vydrov, O. A. & Ángyán, J. G. Assessing the performance of recent density functionals for bulk solids. *Phys. Rev. B* **79**, 155107. doi:[10.1103/PhysRevB.79.155107](https://doi.org/10.1103/PhysRevB.79.155107) (2009).
61. Lehtola, S., Steigemann, C., Oliveira, M. J. & Marques, M. A. Recent developments in libxc — A comprehensive library of functionals for density functional theory. *SoftwareX* **7**, 1. doi:<https://doi.org/10.1016/j.softx.2017.11.002> (2018).
62. Perdew, J. P., Parr, R. G., Levy, M. & Balduz, J. L. Density-Functional Theory for Fractional Particle Number: Derivative Discontinuities of the Energy. *Phys. Rev. Lett.* **49**, 1691. doi:[10.1103/PhysRevLett.49.1691](https://doi.org/10.1103/PhysRevLett.49.1691) (1982).
63. Perdew, J. P. & Levy, M. Physical Content of the Exact Kohn-Sham Orbital Energies: Band Gaps and Derivative Discontinuities. *Phys. Rev. Lett.* **51**, 1884. doi:[10.1103/PhysRevLett.51.1884](https://doi.org/10.1103/PhysRevLett.51.1884) (1983).
64. Lüders, M., Ernst, A., Däne, M., Szotek, Z., Svane, A., Ködderitzsch, D., Hergert, W., Györffy, B. L. & Temmerman, W. M. Self-interaction correction in multiple scattering theory. *Phys. Rev. B* **71**, 205109. doi:[10.1103/PhysRevB.71.205109](https://doi.org/10.1103/PhysRevB.71.205109) (2005).
65. Liechtenstein, A. I., Anisimov, V. I. & Zaanen, J. Density-functional theory and strong interactions: Orbital ordering in Mott-Hubbard insulators. *Phys. Rev. B* **52**, R5467. doi:[10.1103/PhysRevB.52.R5467](https://doi.org/10.1103/PhysRevB.52.R5467) (1995).
66. Hubbard, J. & Flowers, B. H. Electron correlations in narrow energy bands. *Proc. R. Soc. A* **276**, 238. doi:[10.1098/rspa.1963.0204](https://doi.org/10.1098/rspa.1963.0204) (1963).
67. Dudarev, S. L., Botton, G. A., Savrasov, S. Y., Humphreys, C. J. & Sutton, A. P. Electron-energy-loss spectra and the structural stability of nickel oxide: An LSDA+U study. *Phys. Rev. B* **57**, 1505. doi:[10.1103/PhysRevB.57.1505](https://doi.org/10.1103/PhysRevB.57.1505) (1998).

68. Krukau, A. V., Vydrov, O. A., Izmaylov, A. F. & Scuseria, G. E. Influence of the exchange screening parameter on the performance of screened hybrid functionals. *J. Chem. Phys.* **125**, 224106. doi:10.1063/1.2404663 (2006).
69. Hedin, L. New Method for Calculating the One-Particle Green's Function with Application to the Electron-Gas Problem. *Phys. Rev.* **139**, A796. doi:10.1103/PhysRev.139.A796 (1965).
70. Shishkin, M. & Kresse, G. Implementation and performance of the frequency-dependent *GW* method within the PAW framework. *Phys. Rev. B* **74**, 035101. doi:10.1103/PhysRevB.74.035101 (2006).
71. Özgür, Ü., Alivov, Y. I., Liu, C., Teke, A., Reshchikov, M. A., Doğan, S., Avrutin, V., Cho, S.-J. & Morkoç, H. A comprehensive review of ZnO materials and devices. *J. Appl. Phys.* **98**, 041301. doi:10.1063/1.1992666 (2005).
72. Dietrich, C. P., Lange, M., Klüpfel, F. J., von Wenckstern, H., Schmidt-Grund, R. & Grundmann, M. Strain distribution in bent ZnO microwires. *Appl. Phys. Lett.* **98**, 031105. doi:10.1063/1.3544939 (2011).
73. Preston, A. R. H., Ruck, B. J., Piper, L. F. J., DeMasi, A., Smith, K. E., Schleife, A., Fuchs, F., Bechstedt, F., Chai, J. & Durbin, S. M. Band structure of ZnO from resonant x-ray emission spectroscopy. *Phys. Rev. B* **78**, 155114. doi:10.1103/PhysRevB.78.155114 (2008).
74. Powell, R. A., Spicer, W. E. & McMenamin, J. C. Location of the Zn 3d States in ZnO. *Phys. Rev. Lett.* **27**, 97. doi:10.1103/PhysRevLett.27.97 (1971).
75. Vesely, C. J., Hengehold, R. L. & Langer, D. W. uv Photoemission Measurements of the Upper *d* Levels in the IIB-VIA Compounds. *Phys. Rev. B* **5**, 2296. doi:10.1103/PhysRevB.5.2296 (1972).
76. Ma, X., Wu, Y., Lv, Y. & Zhu, Y. Correlation Effects on Lattice Relaxation and Electronic Structure of ZnO within the GGA+U Formalism. *J. Phys. Chem. C* **117**, 26029. doi:10.1021/jp407281x (2013).
77. Adeagbo, W. A., Thomas, S., Nayak, S. K., Ernst, A. & Hergert, W. First-principles study of uniaxial strained and bent ZnO wires. *Phys. Rev. B* **89**, 195135. doi:10.1103/PhysRevB.89.195135 (2014).
78. Hergert, W. & Geilhufe, R. M. *Front Matter* doi:10.1002/9783527695799 (John Wiley & Sons, Ltd, 2018).
79. Monkhorst, H. J. & Pack, J. D. Special points for Brillouin-zone integrations. *Phys. Rev. B* **13**, 5188. doi:10.1103/PhysRevB.13.5188 (1976).
80. Baldereschi, A. Mean-Value Point in the Brillouin Zone. *Phys. Rev. B* **7**, 5212. doi:10.1103/PhysRevB.7.5212 (1973).
81. Chadi, D. J. & Cohen, M. L. Special Points in the Brillouin Zone. *Phys. Rev. B* **8**, 5747. doi:10.1103/PhysRevB.8.5747 (1973).
82. Jepsen, O. & Anderson, O. The electronic structure of h.c.p. Ytterbium. *Solid State Commun.* **9**, 1763. doi:10.1016/0038-1098(71)90313-9 (1971).
83. Lehmann, G. & Taut, M. On the Numerical Calculation of the Density of States and Related Properties. *Phys. Status Solidi B* **54**, 469. doi:10.1002/pssb.2220540211 (1972).
84. Blöchl, P. E., Jepsen, O. & Andersen, O. K. Improved tetrahedron method for Brillouin-zone integrations. *Phys. Rev. B* **49**, 16223. doi:10.1103/PhysRevB.49.16223 (1994).

85. Phillips, J. C. & Kleinman, L. New Method for Calculating Wave Functions in Crystals and Molecules. *Phys. Rev.* **116**, 287. doi:10.1103/PhysRev.116.287 (1959).
86. Herring, C. A New Method for Calculating Wave Functions in Crystals. *Phys. Rev.* **57**, 1169. doi:10.1103/PhysRev.57.1169 (1940).
87. Hamann, D. R., Schlüter, M. & Chiang, C. Norm-Conserving Pseudopotentials. *Phys. Rev. Lett.* **43**, 1494. doi:10.1103/PhysRevLett.43.1494 (1979).
88. Bachelet, G. B., Hamann, D. R. & Schlüter, M. Pseudopotentials that work: From H to Pu. *Phys. Rev. B* **26**, 4199. doi:10.1103/PhysRevB.26.4199 (1982).
89. Kerker, G. P. Non-singular atomic pseudopotentials for solid state applications. *J. Phys. C: Solid State Phys.* **13**, L189. doi:10.1088/0022-3719/13/9/004 (1980).
90. Troullier, N. & Martins, J. L. Efficient pseudopotentials for plane-wave calculations. *Phys. Rev. B* **43**, 1993. doi:10.1103/PhysRevB.43.1993 (1991).
91. Hamann, D. R. Optimized norm-conserving Vanderbilt pseudopotentials. *Phys. Rev. B* **88**, 085117. doi:10.1103/PhysRevB.88.085117 (2013).
92. Blöchl, P. E. Projector augmented-wave method. *Phys. Rev. B* **50**, 17953. doi:10.1103/PhysRevB.50.17953 (1994).
93. Lejaeghere, K. *et al.* Reproducibility in density functional theory calculations of solids. *Science* **351**. doi:10.1126/science.aad3000 (2016).
94. *The Fleur code* <http://www.flapw.de/>.
95. Blaha, P., Schwarz, K., Tran, F., Laskowski, R., Madsen, G. K. H. & Marks, L. D. WIEN2k: An APW+lo program for calculating the properties of solids. *J. Chem. Phys.* **152**, 074101. doi:10.1063/1.5143061 (2020).
96. *The Elk Code* <http://elk.sourceforge.net/>.
97. Gulans, A., Kontur, S., Meisenbichler, C., Nabok, D., Pavone, P., Rigamonti, S., Sagmeister, S., Werner, U. & Draxl, C. exciting: a full-potential all-electron package implementing density-functional theory and many-body perturbation theory. *J. Phys.: Condens. Matter* **26**, 363202. doi:10.1088/0953-8984/26/36/363202 (2014).
98. Ham, F. S. & Segall, B. Energy Bands in Periodic Lattices—Green’s Function Method. *Phys. Rev.* **124**, 1786. doi:10.1103/PhysRev.124.1786 (1961).
99. Faulkner, J. S., Davis, H. L. & Joy, H. W. Calculation of Constant-Energy Surfaces for Copper by the Korringa-Kohn-Rostoker Method. *Phys. Rev.* **161**, 656. doi:10.1103/PhysRev.161.656 (1967).
100. Johnson, K. H. Multiple-Scattering Model for Polyatomic Molecules. *J. Chem. Phys.* **45**, 3085. doi:10.1063/1.1728065 (1966).
101. Treusch, J. & Sandrock, R. Energy Band Structures of Selenium and Tellurium (Kohn-Rostoker Method). *Phys. Status Solidi B* **16**, 487. doi:10.1002/pssb.19660160214 (1966).
102. Green, G. *An essay on the application of mathematical analysis to the theories of electricity and magnetism* (Wezäta-Melins Aktiebolag, 1828).
103. Green, G. *An Essay on the Application of mathematical Analysis to the theories of Electricity and Magnetism* 2008.



104. Hirose, K., Ono, T., Fujimoto, Y. & Tsukamoto, S. *First-Principles Calculations in Real-Space Formalism* doi:10.1142/p370 (Imperial College Press and Distributed by World Scientific Publishing CO.SHING Co., 2005).
105. Dyson, F. J. The  $S$  Matrix in Quantum Electrodynamics. *Phys. Rev.* **75**, 1736. doi:10.1103/PhysRev.75.1736 (1949).
106. Lippmann, B. A. & Schwinger, J. Variational Principles for Scattering Processes. I. *Phys. Rev.* **79**, 469. doi:10.1103/PhysRev.79.469 (1950).
107. Slater, J. C. Wave Functions in a Periodic Potential. *Phys. Rev.* **51**, 846. doi:10.1103/PhysRev.51.846 (1937).
108. Andersen, O. K. Linear methods in band theory. *Phys. Rev. B* **12**, 3060. doi:10.1103/PhysRevB.12.3060 (1975).
109. *Computational Nanoscience: Do It Yourself!; NIC Winter School, 2006, Forschungszentrum Jülich, Germany - Lecture Notes* (eds Grotendorst, J., Blügel, S. & Marx, D.) (FZJ, John von Neumann Institute for Computing, Jülich, 2006).
110. Ebert, H., Ködderitzsch, D. & Minár, J. Calculating condensed matter properties using the KKR-Green's function method—recent developments and applications. *Rep. Prog. Phys.* **74**, 096501. doi:10.1088/0034-4885/74/9/096501 (2011).
111. Hölzer, M. *Lattice dynamics from first principles* PhD thesis (Martin-Luther-Universität Halle-Wittenberg, 2015). doi:10.25673/1840.
112. Schweflinghaus, B. J. *First-principles investigation of inelastic magnetic excitations in nanostructures deposited on surfaces* Dissertation (RWTH Aachen, 2016).
113. Zeller, R. Multiple-scattering solution of Schrodinger's equation for potentials of general shape. *J. Phys. C: Solid State Phys.* **20**, 2347. doi:10.1088/0022-3719/20/16/010 (1987).
114. Gonis, A. *Theoretical Materials Science: Tracing the Electronic Origins of Materials Behavior* (Materials Research Society, 2000).
115. Bauer, D. S. G. *Development of a relativistic full-potential first-principles multiple scattering Green function method applied to complex magnetic textures of nano structures at surfaces* Dissertation (RWTH Aachen, 2013).
116. Beeby, J. L. & Edwards, S. F. The density of electrons in a perfect or imperfect lattice. *Proc. R. Soc. A* **302**, 113. doi:10.1098/rspa.1967.0230 (1967).
117. Ernst, A. *Multiple-Scattering Theory: New Developments and Applications* Kumulative Habilitationsschrift (Martin-Luther-Universität Halle-Wittenberg, 2007), 65.
118. Fabian, D. & Watson, L. *Band structure spectroscopy of metals and alloys* (Academic Press, 1973).
119. Stefanou, N., Akai, H. & Zeller, R. An efficient numerical method to calculate shape truncation functions for Wigner-Seitz atomic polyhedra. *Comput. Phys. Commun.* **60**, 231. doi:10.1016/0010-4655(90)90009-P (1990).
120. King, P. D. C., Veal, T. D., Schleife, A., Zúñiga-Pérez, J., Martel, B., Jefferson, P. H., Fuchs, F., Muñoz-Sanjosé, V., Bechstedt, F. & McConville, C. F. Valence-band electronic structure of CdO, ZnO, and MgO from x-ray photoemission spectroscopy and quasi-particle-corrected density-functional theory calculations. *Phys. Rev. B* **79**, 205205. doi:10.1103/PhysRevB.79.205205 (2009).

121. Nordheim, L. Zur Elektronentheorie der Metalle. I. *Ann. Phys.* **401**, 607. doi:10.1002/andp.19314010507 (1931).
122. Bellaiche, L. & Vanderbilt, D. Virtual crystal approximation revisited: Application to dielectric and piezoelectric properties of perovskites. *Phys. Rev. B* **61**, 7877. doi:10.1103/PhysRevB.61.7877 (2000).
123. Elliott, R. J., Taylor, D. W. & Peierls, R. E. Vibrations of random dilute alloys. *Proc. R. Soc. A* **296**, 161. doi:10.1098/rspa.1967.0012 (1967).
124. Elliott, R. J., Krumhansl, J. A. & Leath, P. L. The theory and properties of randomly disordered crystals and related physical systems. *Rev. Mod. Phys.* **46**, 465. doi:10.1103/RevModPhys.46.465 (1974).
125. Lifshic, M. Some problems of the dynamic theory of non-ideal crystal lattices. *Nuovo Cim* **3**, 716. doi:10.1007/BF02746071 (1956).
126. Koster, G. F. & Slater, J. C. Wave Functions for Impurity Levels. *Phys. Rev.* **95**, 1167. doi:10.1103/PhysRev.95.1167 (1954).
127. Callaway, J. Theory of Scattering in Solids. *J. Math. Phys.* **5**, 783. doi:10.1063/1.1704180 (1964).
128. Faulkner, J. The modern theory of alloys. *Prog. Mater Sci.* **27**, 1. doi:10.1016/0079-6425(82)90005-6 (1982).
129. Zabloudil, J., Hammerling, R., Szunyogh, L. & Weinberger, P. *Electron Scattering in Solid Matter: a theoretical and computational treatise* doi:10.1007/b138290 (Springer Science & Business Media, 2006).
130. Weinberger, P. *Electron Scattering Theory for Ordered and Disordered Matter* (Clarendon Press, 1990).
131. Kikuchi, R. A Theory of Cooperative Phenomena. *Phys. Rev.* **81**, 988. doi:10.1103/PhysRev.81.988 (1951).
132. Sanchez, J., Ducastelle, F. & Gratias, D. Generalized cluster description of multicomponent systems. *Physica A* **128**, 334. doi:10.1016/0378-4371(84)90096-7 (1984).
133. Binder, K. Ordering of the Face-Centered-Cubic Lattice with Nearest-Neighbor Interaction. *Phys. Rev. Lett.* **45**, 811. doi:10.1103/PhysRevLett.45.811 (1980).
134. Wei, S.-H., Ferreira, L. G., Bernard, J. E. & Zunger, A. Electronic properties of random alloys: Special quasirandom structures. *Phys. Rev. B* **42**, 9622. doi:10.1103/PhysRevB.42.9622 (1990).
135. Hart, G. L. W. & Forcade, R. W. Algorithm for generating derivative structures. *Phys. Rev. B* **77**, 224115. doi:10.1103/PhysRevB.77.224115 (2008).
136. Maznichenko, I. V., Ernst, A., Bouhassoune, M., Henk, J., Däne, M., Lüders, M., Bruno, P., Hergert, W., Mertig, I., Szotek, Z. & Temmerman, W. M. Structural phase transitions and fundamental band gaps of  $\text{Mg}_x\text{Zn}_{1-x}\text{O}$  alloys from first principles. *Phys. Rev. B* **80**, 144101. doi:10.1103/PhysRevB.80.144101 (2009).
137. Langevin, P. Sur la théorie du magnétisme. *J. Phys. Theor. Appl.* **4**, 678. doi:10.1051/jphysap:019050040067800 (1905).
138. Weiss, Pierre. L'hypothèse du champ moléculaire et la propriété ferromagnétique. *J. Phys. Theor. Appl.* **6**, 661. doi:10.1051/jphysap:019070060066100 (1907).



139. Moriya, T. *Spin Fluctuations in Itinerant Electron Magnetism* 109 (Springer Berlin Heidelberg, Berlin, Heidelberg, 1985). doi:10.1007/978-3-642-82499-9\_6.
140. Dirac, P. A. M. & Fowler, R. H. The quantum theory of the electron. *Proc. R. Soc. A* **117**, 610. doi:10.1098/rspa.1928.0023 (1928).
141. Heisenberg, W. Zur Theorie des Ferromagnetismus. *Z. Phys.* **49**, 619. doi:10.1007/BF01328601 (1928).
142. Schmidt, R., Lazo, C., Kaiser, U., Schwarz, A., Heinze, S. & Wiesendanger, R. Quantitative Measurement of the Magnetic Exchange Interaction across a Vacuum Gap. *Phys. Rev. Lett.* **106**, 257202. doi:10.1103/PhysRevLett.106.257202 (2011).
143. Kaiser, U., Schwarz, A. & Wiesendanger, R. Magnetic exchange force microscopy with atomic resolution. *Nature* **446**, 522. doi:10.1038/nature05617 (2007).
144. Schmidt, R., Lazo, C., Hölscher, H., Pi, U. H., Caciuc, V., Schwarz, A., Wiesendanger, R. & Heinze, S. Probing the Magnetic Exchange Forces of Iron on the Atomic Scale. *Nano Lett.* **9**, 200. doi:10.1021/nl802770x (2009).
145. Sapozhnik, A. A., Luo, C., Ryll, H., Radu, F., Jourdan, M., Zabel, H. & Elmers, H.-J. Experimental determination of exchange constants in antiferromagnetic  $\text{Mn}_2\text{Au}$ . *Phys. Rev. B* **97**, 184416. doi:10.1103/PhysRevB.97.184416 (2018).
146. Noodleman, L. Valence bond description of antiferromagnetic coupling in transition metal dimers. *J. Chem. Phys.* **74**, 5737. doi:10.1063/1.440939 (1981).
147. Xiang, H. J., Kan, E. J., Wei, S.-H., Whangbo, M.-H. & Gong, X. G. Predicting the spin-lattice order of frustrated systems from first principles. *Phys. Rev. B* **84**, 224429. doi:10.1103/PhysRevB.84.224429 (2011).
148. Rivero, P., de Pr Moreira, I. & Illas, F. Spin Hamiltonian effective parameters from periodic electronic structure calculations. *J. Phys. Conf. Ser.* **117**, 012025. doi:10.1088/1742-6596/117/1/012025 (2008).
149. Methfessel, M. & Kubler, J. Bond analysis of heats of formation: application to some group VIII and IB hydrides. *J. Phys. F: Met. Phys.* **12**, 141. doi:10.1088/0305-4608/12/1/013 (1982).
150. Lloyd, P. & Smith, P. Multiple scattering theory in condensed materials. *Adv. Phys.* **21**, 69. doi:10.1080/00018737200101268 (1972).
151. Landau, D. P. & Binder, K. *A Guide to Monte Carlo Simulations in Statistical Physics* 4th edition. doi:10.1017/CB09781139696463 (Cambridge University Press, 2014).
152. Metropolis, N., Rosenbluth, A. W., Rosenbluth, M. N., Teller, A. H. & Teller, E. Equation of State Calculations by Fast Computing Machines. *J. Chem. Phys.* **21**, 1087. doi:10.1063/1.1699114 (1953).
153. Binder, K. & W. Heermann, D. *Monte Carlo Simulation in Statistical Physics, An introduction* doi:10.1007/978-3-642-03163-2 (Springer, Berlin, Heidelberg, 2010).
154. Cazzanelli, E., Kuzmin, A., Mariotto, G. & Mironova-Ulmane, N. Study of vibrational and magnetic excitations in  $\text{Ni}_c\text{Mg}_{1-c}\text{O}$  solid solutions by Raman spectroscopy. *J. Phys.: Condens. Matter* **15**, 2045. doi:10.1088/0953-8984/15/12/321 (2003).

155. Kuzmin, A. & Mironova, N. Composition dependence of the lattice parameter in  $\text{Ni}_c\text{Mg}_{1-c}\text{O}$  solid solutions. *J. Phys.: Condens. Matter* **10**, 7937. doi:10.1088/0953-8984/10/36/004 (1998).
156. Fischer, G., Däne, M., Ernst, A., Bruno, P., Lüders, M., Szotek, Z., Temmerman, W. & Hergert, W. Exchange coupling in transition metal monoxides: Electronic structure calculations. *Phys. Rev. B* **80**, 014408. doi:10.1103/PhysRevB.80.014408 (2009).
157. Freysoldt, C., Grabowski, B., Hickel, T., Neugebauer, J., Kresse, G., Janotti, A. & Van de Walle, C. G. First-principles calculations for point defects in solids. *Rev. Mod. Phys.* **86**, 253. doi:10.1103/RevModPhys.86.253 (2014).
158. Zhang, S. B. & Northrup, J. E. Chemical potential dependence of defect formation energies in GaAs: Application to Ga self-diffusion. *Phys. Rev. Lett.* **67**, 2339. doi:10.1103/PhysRevLett.67.2339 (1991).
159. Van de Walle, C. G. & Neugebauer, J. First-principles calculations for defects and impurities: Applications to III-nitrides. *J. Appl. Phys.* **95**, 3851. doi:10.1063/1.1682673 (2004).
160. Chase, M. W. NIST-JANAF thermochemical tables for the bromine oxides. *J. Phys. Chem. Ref. Data* **25**, 1069 (1996).
161. Reuter, K. & Scheffler, M. Composition, structure, and stability of  $\text{RuO}_2(110)$  as a function of oxygen pressure. *Phys. Rev. B* **65**, 035406. doi:10.1103/PhysRevB.65.035406 (2001).
162. O'Regan, B. & Grätzel, M. A low-cost, high-efficiency solar cell based on dye-sensitized colloidal  $\text{TiO}_2$  films. *Nature* **353**, 737. doi:10.1038/353737a0 (1991).
163. Seo, M.-H., Yuasa, M., Kida, T., Huh, J.-S., Shimanoe, K. & Yamazoe, N. Gas sensing characteristics and porosity control of nanostructured films composed of  $\text{TiO}_2$  nanotubes. *Sens. Actuators, B* **137**, 513. doi:10.1016/j.snb.2009.01.057 (2009).
164. Braun, J. H., Baidins, A. & Marganski, R. E.  $\text{TiO}_2$  pigment technology: a review. *Prog. Org. Coat.* **20**, 105. doi:10.1016/0033-0655(92)80001-D (1992).
165. Aricò, A. S., Bruce, P., Scrosati, B., Tarascon, J.-M. & van Schalkwijk, W. Nanostructured materials for advanced energy conversion and storage devices. *Nat. Mater.* **4**, 366. doi:10.1038/nmat1368 (2005).
166. Venkatesan, M., Fitzgerald, C. B. & Coey, J. M. D. Unexpected magnetism in a dielectric oxide. *Nature* **430**, 630. doi:10.1038/430630a (2004).
167. Coey, J. M. D. Magnetism in  $d^0$  oxides. *Nat. Mater.* **18**, 652. doi:10.1038/s41563-019-0365-9 (2019).
168. Zunger, A., Lany, S. & Raebiger, H. Trend: the quest for dilute ferromagnetism in semiconductors: guides and misguides by theory. *Physics* **3**, 53 (2010).
169. Coey, J.  $d^0$  ferromagnetism. *Solid State Sci.* **7**, 660. doi:10.1016/j.solidstatesciences.2004.11.012 (2005).
170. Volnianska, O. & Boguslawski, P. Magnetism of solids resulting from spin polarization of p orbitals. *J. Phys.: Condens. Matter* **22**, 073202. doi:10.1088/0953-8984/22/7/073202 (2010).
171. Ogale, S. B. Dilute Doping, Defects, and Ferromagnetism in Metal Oxide Systems. *Adv. Mater.* **22**, 3125. doi:10.1002/adma.200903891 (2010).
172. Stoneham, M. The strange magnetism of oxides and carbons. *J. Phys.: Condens. Matter* **22**, 074211. doi:10.1088/0953-8984/22/7/074211 (2010).

173. Hong, N. H., Sakai, J., Poirot, N. & Brizé, V. Room-temperature ferromagnetism observed in undoped semiconducting and insulating oxide thin films. *Phys. Rev. B* **73**, 132404. doi:10.1103/PhysRevB.73.132404 (2006).
174. Yoon, S. D., Chen, Y., Yang, A., Goodrich, T. L., Zuo, X., Ziemer, K., Vittoria, C. & Harris, V. G. Magnetic semiconducting anatase  $\text{TiO}_{2-\delta}$  grown on (100)  $\text{LaAlO}_3$  having magnetic order up to 880K. *J. Magn. Magn. Mater.* **309**, 171. doi:10.1016/j.jmmm.2006.05.014 (2007).
175. Yang, K., Dai, Y., Huang, B. & Feng, Y. P. Density-functional characterization of antiferromagnetism in oxygen-deficient anatase and rutile  $\text{TiO}_2$ . *Phys. Rev. B* **81**, 033202. doi:10.1103/PhysRevB.81.033202 (2010).
176. Pandey, S. K. & Choudhary, R. J. Effect of non-magnetic impurities on the magnetic states of anatase  $\text{TiO}_2$ . *J. Phys.: Condens. Matter* **23**, 276005. doi:10.1088/0953-8984/23/27/276005 (2011).
177. Kim, D., Hong, J., Park, Y. R. & Kim, K. J. The origin of oxygen vacancy induced ferromagnetism in undoped  $\text{TiO}_2$ . *J. Phys.: Condens. Matter* **21**, 195405. doi:10.1088/0953-8984/21/19/195405 (2009).
178. Peng, H., Li, J., Li, S.-S. & Xia, J.-B. Possible origin of ferromagnetism in undoped anatase  $\text{TiO}_2$ . *Phys. Rev. B* **79**, 092411. doi:10.1103/PhysRevB.79.092411 (2009).
179. Morgan, B. J. & Watson, G. W. Polaronic trapping of electrons and holes by native defects in anatase  $\text{TiO}_2$ . *Phys. Rev. B* **80**, 233102. doi:10.1103/PhysRevB.80.233102 (2009).
180. Zhou, S., Čižmár, E., Potzger, K., Krause, M., Talut, G., Helm, M., Fassbender, J., Zvyagin, S. A., Wosnitza, J. & Schmidt, H. Origin of magnetic moments in defective  $\text{TiO}_2$  single crystals. *Phys. Rev. B* **79**, 113201. doi:10.1103/PhysRevB.79.113201 (2009).
181. Dhakshinamoorthy, J., Prasad, A. K., Dhara, S. & Pullithadathil, B. Anomalous Effects of Lattice Strain and  $\text{Ti}^{3+}$  Interstitials on Room-Temperature Magnetic Ordering in Defect-Engineered Nano- $\text{TiO}_2$ . *J. Phys. Chem. C* **122**, 27782. doi:10.1021/acs.jpcc.8b09851 (2018).
182. Stiller, M., Barzola-Quiquia, J., Esquinazi, P., Spemann, D., Meijer, J., Lorenz, M. & Grundmann, M. Strong out-of-plane magnetic anisotropy in ion irradiated anatase  $\text{TiO}_2$  thin films. *AIP Adv.* **6**, 125009. doi:10.1063/1.4971794 (2016).
183. Gnaser, H. & Gnaser, H. *Low-energy ion irradiation of solid surfaces* (Springer, 1999).
184. Robinson, M., Marks, N. & Lumpkin, G. Structural dependence of threshold displacement energies in rutile, anatase and brookite  $\text{TiO}_2$ . *Mater. Chem. Phys.* **147**, 311. doi:10.1016/j.matchemphys.2014.05.006 (2014).
185. Matsui, M. & Akaogi, M. Molecular Dynamics Simulation of the Structural and Physical Properties of the Four Polymorphs of  $\text{TiO}_2$ . *Mol. Simul.* **6**, 239. doi:10.1080/08927029108022432 (1991).
186. Cococcioni, M. & de Gironcoli, S. Linear response approach to the calculation of the effective interaction parameters in the LDA + U method. *Phys. Rev. B* **71**, 035105. doi:10.1103/PhysRevB.71.035105 (2005).
187. Ricca, C., Timrov, I., Cococcioni, M., Marzari, N. & Aschauer, U. Self-consistent site-dependent DFT+U study of stoichiometric and defective  $\text{SrMnO}_3$ . *Phys. Rev. B* **99**, 094102. doi:10.1103/PhysRevB.99.094102 (2019).

188. Hu, Z. & Metiu, H. Choice of U for DFT+U Calculations for Titanium Oxides. *J. Phys. Chem. C* **115**, 5841. doi:10.1021/jp111350u (2011).
189. Moruzzi, V. L., Marcus, P. M., Schwarz, K. & Mohn, P. Ferromagnetic phases of bcc and fcc Fe, Co, and Ni. *Phys. Rev. B* **34**, 1784. doi:10.1103/PhysRevB.34.1784 (1986).
190. Makov, G. & Payne, M. C. Periodic boundary conditions in ab initio calculations. *Phys. Rev. B* **51**, 4014. doi:10.1103/PhysRevB.51.4014 (1995).
191. Setvin, M., Franchini, C., Hao, X., Schmid, M., Janotti, A., Kaltak, M., Van de Walle, C. G., Kresse, G. & Diebold, U. Direct View at Excess Electrons in TiO<sub>2</sub> Rutile and Anatase. *Phys. Rev. Lett.* **113**, 086402. doi:10.1103/PhysRevLett.113.086402 (2014).
192. Moser, S. *et al.* Tunable Polaronic Conduction in Anatase TiO<sub>2</sub>. *Phys. Rev. Lett.* **110**, 196403. doi:10.1103/PhysRevLett.110.196403 (2013).
193. Na-Phattalung, S., Smith, M. F., Kim, K., Du, M.-H., Wei, S.-H., Zhang, S. B. & Limpijum-nong, S. First-principles study of native defects in anatase TiO<sub>2</sub>. *Phys. Rev. B* **73**, 125205. doi:10.1103/PhysRevB.73.125205 (2006).
194. Cowen, B. J. & El-Genk, M. S. Characterization of radiation damage in TiO<sub>2</sub> using molecular dynamics simulations. *Modell. Simul. Mater. Sci. Eng.* **26**, 085005. doi:10.1088/1361-651x/aae21b (2018).
195. Bahmanrokh, G., Cazorla, C., Mofarah, S. S., Shahmiri, R., Yao, Y., Ismail, I., Chen, W.-F., Koshy, P. & Sorrell, C. C. Band gap engineering of Ce-doped anatase TiO<sub>2</sub> through solid solubility mechanisms and new defect equilibria formalism. *Nanoscale* **12**, 4916. doi:10.1039/C9NR08604H (2020).
196. Li, H., Guo, Y. & Robertson, J. Calculation of TiO<sub>2</sub> Surface and Subsurface Oxygen Vacancy by the Screened Exchange Functional. *J. Phys. Chem. C* **119**, 18160. doi:10.1021/acs.jpcc.5b02430 (2015).
197. Bundesmann, C., Lautenschläger, T., Spemann, D., Finzel, A., Thelander, E., Mensing, M. & Frost, F. Systematic investigation of the properties of TiO<sub>2</sub> films grown by reactive ion beam sputter deposition. *Appl. Surf. Sci.* **421**, 331. doi:10.1016/j.apsusc.2016.08.056 (2017).
198. Bruno, P. Tight-binding approach to the orbital magnetic moment and magnetocrystalline anisotropy of transition-metal monolayers. *Phys. Rev. B* **39**, 865. doi:10.1103/PhysRevB.39.865 (1989).
199. Acosta, M., Novak, N., Rojas, V., Patel, S., Vaish, R., Koruza, J., Rossetti, G. A. & Rödel, J. BaTiO<sub>3</sub>-based piezoelectrics: Fundamentals, current status, and perspectives. *Appl. Phys. Rev.* **4**, 041305. doi:10.1063/1.4990046 (2017).
200. Kay, H. & Vousden, P. XCV. Symmetry changes in barium titanate at low temperatures and their relation to its ferroelectric properties. *London, Edinburgh Dublin Philos. Mag. J. Sci.* **40**, 1019. doi:10.1080/14786444908561371 (1949).
201. Merz, W. J. The Electric and Optical Behavior of BaTiO<sub>3</sub> Single-Domain Crystals. *Phys. Rev.* **76**, 1221. doi:10.1103/PhysRev.76.1221 (1949).
202. Park, S.-E., Wada, S., Cross, L. E. & Shrout, T. R. Crystallographically engineered BaTiO<sub>3</sub> single crystals for high-performance piezoelectrics. *J. Appl. Phys.* **86**, 2746. doi:10.1063/1.371120 (1999).

203. Zhang, H. A theory for structural phase transitions in BaTiO<sub>3</sub> single crystal and PbZrO<sub>3</sub>-xPbTiO<sub>3</sub> solid solution. *AIP Adv.* **3**, 042118. doi:10.1063/1.4802874 (2013).
204. Ma, Z., Xi, L., Liu, H., Zheng, F., Gao, H., Chen, Z. & Chen, H. Ferroelectric phase transition of BaTiO<sub>3</sub> single crystal based on a tenth order Landau-Devonshire potential. *Comput. Mater. Sci.* **135**, 109. doi:10.1016/j.commatsci.2017.04.011 (2017).
205. Itoh, K., Zeng, L. Z., Nakamura, E. & Mishima, N. Crystal structure of BaTiO<sub>3</sub> in the cubic phase. *Ferroelectrics* **63**, 29. doi:10.1080/00150198508221381 (1985).
206. Sawaguchi, E., Akishige, Y., Yamamoto, T. & Nakahara, J. Phase transition in hexagonal type BaTiO<sub>3</sub>. *Ferroelectrics* **95**, 29. doi:10.1080/00150198908245174 (1989).
207. Kornev, I. A., Bellaiche, L., Bouvier, P., Janolin, P.-E., Dkhil, B. & Kreisel, J. Ferroelectricity of Perovskites under Pressure. *Phys. Rev. Lett.* **95**, 196804. doi:10.1103/PhysRevLett.95.196804 (2005).
208. Seo, Y.-S. & Ahn, J. S. Pressure dependence of the phonon spectrum in BaTiO<sub>3</sub> polytypes studied by ab initio calculations. *Phys. Rev. B* **88**, 014114. doi:10.1103/PhysRevB.88.014114 (2013).
209. Evarestov, R. A. & Bandura, A. V. First-principles calculations on the four phases of BaTiO<sub>3</sub>. *J. Comput. Chem.* **33**, 1123. doi:10.1002/jcc.22942 (2012).
210. Venkateswaran, U. D., Naik, V. M. & Naik, R. High-pressure Raman studies of polycrystalline BaTiO<sub>3</sub>. *Phys. Rev. B* **58**, 14256. doi:10.1103/PhysRevB.58.14256 (1998).
211. Fop, S., McCombie, K. S., Wildman, E. J., Skakle, J. M. S. & McLaughlin, A. C. Hexagonal perovskite derivatives: a new direction in the design of oxide ion conducting materials. *Chem. Commun.* **55**, 2127. doi:10.1039/C8CC09534E (2019).
212. Glaister, R. M. & Kay, H. F. An Investigation of the Cubic-Hexagonal Transition in Barium Titanate. *Proc. Phys. Soc.* **76**, 763. doi:10.1088/0370-1328/76/5/317 (1960).
213. Kolar, D., Kunaver, U. & Rečnik, A. Exaggerated Anisotropic Grain Growth in Hexagonal Barium Titanate Ceramics. *Phys. Status Solidi A* **166**, 219. doi:10.1002/(SICI)1521-396X(199803)166:1<219::AID-PSSA219>3.0.CO;2-R (1998).
214. Dickson, J. G., Katz, L. & Ward, R. Compounds with the Hexagonal Barium Titanate Structure 1,2. *J. Am. Chem. Soc.* **83**, 3026. doi:10.1021/ja01475a012 (1961).
215. Ren, F., Ishida, S. & Mineta, S. Effect of Manganese Addition on Phase Stability of Hexagonal BaTiO<sub>3</sub>. *J. Ceram. Soc. Jpn.* **102**, 105. doi:10.2109/jcersj.102.105 (1994).
216. Keith, G. M., Rampling, M. J., Sarma, K., Alford, N. M. & Sinclair, D. Synthesis and characterisation of doped 6H-BaTiO<sub>3</sub> ceramics. *J. Eur. Ceram. Soc.* **24**. Electroceramics VIII, 1721. doi:10.1016/S0955-2219(03)00495-3 (2004).
217. Langhammer, H. T., Müller, T., Felgner, K.-H. & Abicht, H.-P. Crystal Structure and Related Properties of Manganese-Doped Barium Titanate Ceramics. *J. Am. Ceram. Soc.* **83**, 605. doi:10.1111/j.1151-2916.2000.tb01239.x (2000).
218. Langhammer, H. T., Müller, T., Böttcher, R. & Abicht, H.-P. Structural and optical properties of chromium-doped hexagonal barium titanate ceramics. *J. Phys.: Condens. Matter* **20**, 085206. doi:10.1088/0953-8984/20/8/085206 (2008).



219. Pal, P., Rudrapal, K., Mahana, S., Yadav, S., Paramanik, T., Mishra, S., Singh, K., Sheet, G., Topwal, D., Chaudhuri, A. R. & Choudhury, D. Origin and tuning of room-temperature multiferroicity in Fe-doped BaTiO<sub>3</sub>. *Phys. Rev. B* **101**, 064409. doi:10.1103/PhysRevB.101.064409 (2020).
220. Burbank, R. D. & Evans, H. T. The crystal structure of hexagonal barium titanate. *Acta Crystallogr.* **1**, 330. doi:10.1107/S0365110X48000867 (1948).
221. Yashima, M., Hoshina, T., Ishimura, D., Kobayashi, S., Nakamura, W., Tsurumi, T. & Wada, S. Size effect on the crystal structure of barium titanate nanoparticles. *J. Appl. Phys.* **98**, 014313. doi:10.1063/1.1935132 (2005).
222. Nayak, S. K., Langhammer, H. T., Adeagbo, W. A., Hergert, W., Müller, T. & Böttcher, R. Chromium point defects in hexagonal BaTiO<sub>3</sub>: A comparative study of first-principles calculations and experiments. *Phys. Rev. B* **91**, 155105. doi:10.1103/PhysRevB.91.155105 (2015).
223. Chadi, D. & Martin, R. Calculation of lattice dynamical properties from electronic energies: Application to C, Si and Ge. *Solid State Commun.* **19**, 643. doi:10.1016/0038-1098(76)91094-2 (1976).
224. Baroni, S., Giannozzi, P. & Testa, A. Green's-function approach to linear response in solids. *Phys. Rev. Lett.* **58**, 1861. doi:10.1103/PhysRevLett.58.1861 (1987).
225. Gonze, X. Adiabatic density-functional perturbation theory. *Phys. Rev. A* **52**, 1096. doi:10.1103/PhysRevA.52.1096 (1995).
226. Baroni, S., de Gironcoli, S., Dal Corso, A. & Giannozzi, P. Phonons and related crystal properties from density-functional perturbation theory. *Rev. Mod. Phys.* **73**, 515. doi:10.1103/RevModPhys.73.515 (2001).
227. Kroumova, E., Aroyo, M., Perez-Mato, J., Kirov, A., Capillas, C., Ivantchev, S. & Wondratschek, H. Bilbao Crystallographic Server : Useful Databases and Tools for Phase-Transition Studies. *Phase Transitions* **76**, 155. doi:10.1080/0141159031000076110 (2003).
228. Yamaguchi, M., Watanabe, M., Inoue, K., Akishige, Y. & Yagi, T. Light Scattering Study of the Coupled Soft-Optic and Acoustic Mode in Hexagonal Barium Titanate. *Phys. Rev. Lett.* **75**, 1399. doi:10.1103/PhysRevLett.75.1399 (1995).
229. Inoue, K., Hasegawa, A., Watanabe, K., Yamaguchi, H., Uwe, H. & Sakudo, T. Silent soft mode in hexagonal barium titanate observed by hyper-Raman scattering. *Phys. Rev. B* **38**, 6352. doi:10.1103/PhysRevB.38.6352 (1988).
230. Akishige, Y., Yokozeki, N., Kobayashi, M. & Sawaguchi, E. Optical properties of hexagonal BaTiO<sub>3</sub> around the 222 K structural phase transition. *Solid State Commun.* **60**, 445. doi:10.1016/0038-1098(86)90077-3 (1986).
231. Yamaguchi, M., Inoue, K., Yagi, T. & Akishige, Y. Soft Acoustic Mode in the Ferroelectric Phase Transition of Hexagonal Barium Titanate. *Phys. Rev. Lett.* **74**, 2126. doi:10.1103/PhysRevLett.74.2126 (1995).
232. Inoue, K., Wada, M. & Yamanaka, A. Experimental Study of TO-LO Splitting in Hexagonal Barium Titanate. *J. Korean Phys. Soc.* **29**, S721 (1996).
233. Yamaguchi, H., Uwe, H., Sakudo, T. & Sawaguchi, E. Raman-Scattering Study of the Soft Phonon Modes in Hexagonal Barium Titanate. *J. Phys. Soc. Jpn.* **56**, 589. doi:10.1143/JPSJ.56.589 (1987).

234. Zhong, W., King-Smith, R. D. & Vanderbilt, D. Giant LO-TO splittings in perovskite ferroelectrics. *Phys. Rev. Lett.* **72**, 3618. doi:10.1103/PhysRevLett.72.3618 (1994).
235. Pick, R. M., Cohen, M. H. & Martin, R. M. Microscopic Theory of Force Constants in the Adiabatic Approximation. *Phys. Rev. B* **1**, 910. doi:10.1103/PhysRevB.1.910 (1970).
236. Umari, P. & Pasquarello, A. Ab initio Molecular Dynamics in a Finite Homogeneous Electric Field. *Phys. Rev. Lett.* **89**, 157602. doi:10.1103/PhysRevLett.89.157602 (2002).
237. Perry, C. H., Khanna, B. N. & Rupprecht, G. Infrared Studies of Perovskite Titanates. *Phys. Rev.* **135**, A408. doi:10.1103/PhysRev.135.A408 (1964).
238. Berreman, D. W. & Unterwald, F. C. Adjusting Poles and Zeros of Dielectric Dispersion to Fit Reststrahlen of  $\text{PrCl}_3$  and  $\text{LaCl}_3$ . *Phys. Rev.* **174**, 791. doi:10.1103/PhysRev.174.791 (1968).
239. Ghosez, P. H., Gonze, X. & Michenaud, J. P. Ab initio phonon dispersion curves and interatomic force constants of barium titanate. *Ferroelectrics* **206**, 205. doi:10.1080/00150199808009159 (1998).
240. Kimura, T., Lawes, G., Goto, T., Tokura, Y. & Ramirez, A. P. Magnetoelectric phase diagrams of orthorhombic  $\text{RMnO}_3$  ( $R = \text{Gd, Tb, and Dy}$ ). *Phys. Rev. B* **71**, 224425. doi:10.1103/PhysRevB.71.224425 (2005).
241. Yamasaki, Y., Sagayama, H., Abe, N., Arima, T., Sasai, K., Matsuura, M., Hirota, K., Okuyama, D., Noda, Y. & Tokura, Y. Cycloidal Spin Order in the  $a$ -Axis Polarized Ferroelectric Phase of Orthorhombic Perovskite Manganite. *Phys. Rev. Lett.* **101**, 097204. doi:10.1103/PhysRevLett.101.097204 (2008).
242. Fontcuberta, J. *Multiferroic  $\text{RMnO}_3$  thin films* 2015. doi:10.1016/j.crhy.2015.01.012.
243. Ishiwata, S., Kaneko, Y., Tokunaga, Y., Taguchi, Y., Arima, T.-h. & Tokura, Y. Perovskite manganites hosting versatile multiferroic phases with symmetric and antisymmetric exchange strictions. *Phys. Rev. B* **81**, 100411. doi:10.1103/PhysRevB.81.100411 (2010).
244. Kadomtseva, A. M., Popov, Y. F., Vorob'ev, G. P., Kamilov, K. I., Pyatakov, A. P., Ivanov, V. Y., Mukhin, A. A. & Balbashov, A. M. Specificity of magnetoelectric effects in a new  $\text{GdMnO}_3$  magnetic ferroelectric. *J. Exp. Theor. Phys.* **81**, 19. doi:10.1134/1.1881729 (2005).
245. Lin, L., Li, L., Yan, Z. B., Tao, Y. M., Dong, S. & Liu, J.-M. Ferroelectricity of polycrystalline  $\text{GdMnO}_3$  and multifold magnetoelectric responses. *Appl. Phys. A* **112**, 947. doi:10.1007/s00339-012-7453-x (2013).
246. Pimenov, A., Mukhin, A. A., Ivanov, V. Y., Travkin, V. D., Balbashov, A. M. & Loidl, A. Possible evidence for electromagnons in multiferroic manganites. *Nat. Phys.* **2**, 97. doi:10.1038/nphys212 (2006).
247. Pimenov, A., Rudolf, T., Mayr, F., Loidl, A., Mukhin, A. A. & Balbashov, A. M. Coupling of phonons and electromagnons in  $\text{GdMnO}_3$ . *Phys. Rev. B* **74**, 100403. doi:10.1103/PhysRevB.74.100403 (2006).
248. Shuvaev, A. M., Mayr, F., Loidl, A., Mukhin, A. A. & Pimenov, A. High-frequency electromagnon in  $\text{GdMnO}_3$ . *Eur. Phys. J. B* **80**, 351. doi:10.1140/epjb/e2011-10691-3 (2011).
249. Fedorova, N. S. *et al.* Relationship between crystal structure and multiferroic orders in orthorhombic perovskite manganites. *Phys. Rev. Materials* **2**, 104414. doi:10.1103/PhysRevMaterials.2.104414 (2018).

250. Shannon, R. D. Revised effective ionic radii and systematic studies of interatomic distances in halides and chalcogenides. *Acta Crystallogr. A* **32**, 751. doi:10.1107/S0567739476001551 (1976).
251. Dagotto, E. *Nanoscale Phase Separation and Colossal Magnetoresistance* doi:10.1007/978-3-662-05244-0 (Springer Berlin Heidelberg, 2003).
252. Mufti, N., Nugroho, A. A., Blake, G. R. & Palstra, T. T. M. Relaxor ferroelectric behavior in Ca-doped TbMnO<sub>3</sub>. *Phys. Rev. B* **78**, 024109. doi:10.1103/PhysRevB.78.024109 (2008).
253. Wollan, E. O. & Koehler, W. C. Neutron Diffraction Study of the Magnetic Properties of the Series of Perovskite-Type Compounds [(1 - x)La, x Ca] MnO<sub>3</sub>. *Phys. Rev.* **100**, 545. doi:10.1103/PhysRev.100.545 (1955).
254. Goodenough, J. B. Theory of the Role of Covalence in the Perovskite-Type Manganites [La, M(II)]MnO<sub>3</sub>. *Phys. Rev.* **100**, 564. doi:10.1103/PhysRev.100.564 (1955).
255. Langner, M. C. *et al.* Ultrafast x-ray and optical signatures of phase competition and separation underlying the photoinduced metallic phase in Pr<sub>1-x</sub>Ca<sub>x</sub>MnO<sub>3</sub>. *Phys. Rev. B* **92**, 155148. doi:10.1103/PhysRevB.92.155148 (2015).
256. Taguchi, H., Nagao, M. & Shimada, M. Metal-insulator transition in the system (Gd<sub>1-x</sub>Ca<sub>x</sub>)MnO<sub>2.98</sub>. *J. Solid State Chem.* **82**, 8. doi:10.1016/0022-4596(89)90215-6 (1989).
257. Snyder, G. J., Booth, C. H., Bridges, F., Hiskes, R., DiCarolis, S., Beasley, M. R. & Geballe, T. H. Local structure, transport, and rare-earth magnetism in the ferrimagnetic perovskite Gd<sub>0.67</sub>Ca<sub>0.33</sub>MnO<sub>3</sub>. *Phys. Rev. B* **55**, 6453. doi:10.1103/PhysRevB.55.6453 (1997).
258. Peña, O., Bahout, M., Ghanimi, K., Duran, P., Gutierrez, D. & Moure, C. Spin reversal and ferrimagnetism in (Gd,Ca)MnO<sub>3</sub>. *J. Mater. Chem.* **12**, 2480. doi:10.1039/B202079N (2002).
259. Ma, Y., Guilloux-Viry, M., Barahona, P., Peña, O. & Moure, C. Observation of magnetization reversal in epitaxial Gd<sub>0.67</sub>Ca<sub>0.33</sub>MnO<sub>3</sub> thin films. *Appl. Phys. Lett.* **86**, 062506. doi:10.1063/1.1862787 (2005).
260. Biswas, S., Khan, M. H., Pal, S. & Bose, E. The Effects of Mn Substitution on Magnetization Reversal Properties in Gd<sub>0.7</sub>Ca<sub>0.3</sub>MnO<sub>3</sub>. *J. Supercond. Novel Magn.* **27**, 463. doi:10.1007/s10948-013-2284-3 (2014).
261. Kim, J., Haberkorn, N., Civale, L., Nazaretski, E., Dowden, P., Saxena, A., Thompson, J. D. & Movshovich, R. Direct observation of magnetic phase coexistence and magnetization reversal in a Gd<sub>0.67</sub>Ca<sub>0.33</sub>MnO<sub>3</sub> thin film. *Appl. Phys. Lett.* **100**, 022407. doi:10.1063/1.3676045 (2012).
262. Peña, O., Ma, Y., Guilloux-Viry, M. & Moure, C. Magnetization reversal in Gd<sub>0.67</sub>Ca<sub>0.33</sub>MnO<sub>3</sub>: Comparison between epitaxial thin films and bulk. *Appl. Surf. Sci.* **254**, 339. doi:10.1016/j.apsusc.2007.07.061 (2007).
263. Haberkorn, N., Larrégola, S., Franco, D. & Nieva, G. Inhomogeneous ferrimagnetic-like behavior in Gd<sub>2/3</sub>Ca<sub>1/3</sub>MnO<sub>3</sub> single crystals. *J. Magn. Magn. Mater.* **321**, 1133. doi:10.1016/j.jmmm.2008.10.027 (2009).
264. Correa, V. F., Haberkorn, N., Nieva, G., García, D. J. & Alascio, B. Unusual large magnetostriction in the ferrimagnet Gd<sub>2/3</sub>Ca<sub>1/3</sub>MnO<sub>3</sub>. *EPL (Europhysics Letters)* **98**, 37003. doi:10.1209/0295-5075/98/37003 (2012).



265. Correa, V. F., Sänger, N., G.Jorge, G.Nieva & Haberkorn, N. Giant magnetostructural coupling in  $\text{Gd}_{2/3}\text{Ca}_{1/3}\text{MnO}_3$ . *J. Phys. Conf. Ser.* **167**, 012010. doi:10.1088/1742-6596/167/1/012010 (2009).
266. Millis, A. J., Shraiman, B. I. & Mueller, R. Dynamic Jahn-Teller Effect and Colossal Magnetoresistance in  $\text{La}_{1-x}\text{Sr}_x\text{MnO}_3$ . *Phys. Rev. Lett.* **77**, 175. doi:10.1103/PhysRevLett.77.175 (1996).
267. Cadogan, J. M., Ryan, D. H., Napoletano, M., Riani, P. & Cranswick, L. M. D. Neutron powder diffraction determination of the magnetic structure of  $\text{Gd}_3\text{Ag}_4\text{Sn}_4$ . *J. Phys.: Condens. Matter* **21**, 124201. doi:10.1088/0953-8984/21/12/124201 (2009).
268. Kresse, G. & Joubert, D. From ultrasoft pseudopotentials to the projector augmented-wave method. *Phys. Rev. B* **59**, 1758. doi:10.1103/PhysRevB.59.1758 (1999).
269. Mori, T., Kamegashira, N., Aoki, K., Shishido, T. & Fukuda, T. Crystal growth and crystal structures of the  $\text{LnMnO}_3$  perovskites:  $\text{Ln}=\text{Nd, Sm, Eu}$  and  $\text{Gd}$ . *Mater. Lett.* **54**, 238. doi:10.1016/S0167-577X(01)00569-9 (2002).
270. Kováčik, R., Murthy, S. S., Quiroga, C. E., Ederer, C. & Franchini, C. Combined first-principles and model Hamiltonian study of the perovskite series  $\text{RMnO}_3$  ( $R = \text{La, Pr, Nd, Sm, Eu, and Gd}$ ). *Phys. Rev. B* **93**, 075139. doi:10.1103/PhysRevB.93.075139 (2016).
271. Wang, X. L., Li, D., Cui, T. Y., Kharel, P., Liu, W. & Zhang, Z. D. Magnetic and optical properties of multiferroic  $\text{GdMnO}_3$  nanoparticles. *J. Appl. Phys.* **107**, 09B510. doi:10.1063/1.3358007 (2010).
272. Muthu, D. V. S., Midgley, A. E., Scott, P. R., Kruger, M. B., Sahu, J. R., Sood, A. K. & Rao, C. N. R. High-pressure synchrotron x-ray diffraction study of  $\text{RMnO}_3$  ( $R = \text{Eu, Gd, Tb}$  and  $\text{Dy}$ ) upto 50 GPa. *J. Phys. Conf. Ser.* **377**, 012025. doi:10.1088/1742-6596/377/1/012025 (2012).
273. Mota, D. A., Almeida, A., Rodrigues, V. H., Costa, M. M. R., Tavares, P., Bouvier, P., Guennou, M., Kreisel, J. & Moreira, J. A. Dynamic and structural properties of orthorhombic rare-earth manganites under high pressure. *Phys. Rev. B* **90**, 054104. doi:10.1103/PhysRevB.90.054104 (2014).
274. Pickett, W. E. & Singh, D. J. Electronic structure and half-metallic transport in the  $\text{La}_{1-x}\text{Ca}_x\text{MnO}_3$  system. *Phys. Rev. B* **53**, 1146. doi:10.1103/PhysRevB.53.1146 (1996).
275. Loshkareva, N. N., Nomerovannaya, L. V., Mostovshchikova, E. V., Makhnev, A. A., Sukhorukov, Y. P., Solin, N. I., Arbuzova, T. I., Naumov, S. V., Kostromitina, N. V., Balbashov, A. M. & Rybina, L. N. Electronic structure and polarons in  $\text{CaMnO}_{3-\delta}$  single crystals: Optical data. *Phys. Rev. B* **70**, 224406. doi:10.1103/PhysRevB.70.224406 (2004).
276. van de Walle, A. Multicomponent multisublattice alloys, nonconfigurational entropy and other additions to the Alloy Theoretic Automated Toolkit. *Calphad* **33**. Tools for Computational Thermodynamics, 266. doi:https://doi.org/10.1016/j.calphad.2008.12.005 (2009).
277. Peęala, M. & Drozd, V. Magneto-transport study of manganites ( $\text{La}_{0.75-x}\text{Gd}_x$ ) $\text{Ca}_{0.25}\text{MnO}_3$ . *J. Alloys Compd.* **437**, 12. doi:10.1016/j.jallcom.2006.07.086 (2007).
278. Schiffer, P., Ramirez, A. P., Bao, W. & Cheong, S.-W. Low Temperature Magnetoresistance and the Magnetic Phase Diagram of  $\text{La}_{1-x}\text{Ca}_x\text{MnO}_3$ . *Phys. Rev. Lett.* **75**, 3336. doi:10.1103/PhysRevLett.75.3336 (1995).

279. Tomioka, Y., Okuda, T., Okimoto, Y., Asamitsu, A., Kuwahara, H. & Tokura, Y. Charge/orbital ordering in perovskite manganites. *J. Alloys Compd.* **326**, 27. doi:10.1016/S0925-8388(01)01222-1 (2001).
280. Daoud-Aladine, A., Rodríguez-Carvajal, J., Pinsard-Gaudart, L., Fernández-Díaz, M. T. & Revcolevschi, A. Zener Polaron Ordering in Half-Doped Manganites. *Phys. Rev. Lett.* **89**, 097205. doi:10.1103/PhysRevLett.89.097205 (2002).
281. García, D. J., Hallberg, K., Batista, C. D., Avignon, M. & Alascio, B. New Type of Charge and Magnetic Order in the Ferromagnetic Kondo Lattice. *Phys. Rev. Lett.* **85**, 3720. doi:10.1103/PhysRevLett.85.3720 (2000).
282. Khan, M. H. & Pal, S. Nature of electrical hopping conduction and magnetotransport studies in the electron doped manganite  $\text{Ca}_{0.85}\text{Gd}_{0.15}\text{MnO}_3$ . *Phys. Lett. A* **379**, 401. doi:10.1016/j.physleta.2014.11.017 (2015).
283. Kimura, T., Ishihara, S., Shintani, H., Arima, T., Takahashi, K. T., Ishizaka, K. & Tokura, Y. Distorted perovskite with  $e_g^1$  configuration as a frustrated spin system. *Phys. Rev. B* **68**, 060403. doi:10.1103/PhysRevB.68.060403 (2003).
284. Hemberger, J., Lobina, S., Krug von Nidda, H.-A., Tristan, N., Ivanov, V. Y., Mukhin, A. A., Balbashov, A. M. & Loidl, A. Complex interplay of  $3d$  and  $4f$  magnetism in  $\text{La}_{1-x}\text{Gd}_x\text{MnO}_3$ . *Phys. Rev. B* **70**, 024414. doi:10.1103/PhysRevB.70.024414 (2004).
285. Zeng, Z., Greenblatt, M. & Croft, M. Large magnetoresistance in antiferromagnetic  $\text{CaMnO}_{3-\delta}$ . *Phys. Rev. B* **59**, 8784. doi:10.1103/PhysRevB.59.8784 (1999).
286. Hoffmann, M., Borisov, V. S., Ostanin, S., Mertig, I., Hergert, W. & Ernst, A. Magnetic properties of defect-free and oxygen-deficient cubic  $\text{SrCoO}_{3-\delta}$ . *Phys. Rev. B* **92**, 094427. doi:10.1103/PhysRevB.92.094427 (2015).
287. Hoffmann, M., Antonov, V. N., Bekenov, L. V., Kokko, K., Hergert, W. & Ernst, A. Variation of magnetic properties of  $\text{Sr}_2\text{FeMoO}_6$  due to oxygen vacancies. *J. Phys.: Condens. Matter* **30**, 305801. doi:10.1088/1361-648x/aacb8d (2018).
288. Dubrovinsky, L., Dubrovinskaia, N., Prakapenka, V. B. & Abakumov, A. M. Implementation of micro-ball nanodiamond anvils for high-pressure studies above 6 Mbar. *Nat. Commun.* **3**, 1163. doi:10.1038/ncomms2160 (2012).
289. Dubrovinsky, L. *et al.* The most incompressible metal osmium at static pressures above 750 gigapascals. *Nature* **525**, 226. doi:10.1038/nature14681 (2015).
290. Hicks, C. W., Barber, M. E., Edkins, S. D., Brodsky, D. O. & Mackenzie, A. P. Piezoelectric-based apparatus for strain tuning. *Rev. Sci. Instrum.* **85**, 065003. doi:10.1063/1.4881611 (2014).
291. Cao, J., Ertekin, E., Srinivasan, V., Fan, W., Huang, S., Zheng, H., Yim, J. W. L., Khanal, D. R., Ogletree, D. F., Grossman, J. C. & Wu, J. Strain engineering and one-dimensional organization of metal-insulator domains in single-crystal vanadium dioxide beams. *Nat. Nanotechnol.* **4**, 732. doi:10.1038/nnano.2009.266 (2009).
292. Shayegan, M., Karrai, K., Shkolnikov, Y. P., Vakili, K., De Poortere, E. P. & Manus, S. Low-temperature, in situ tunable, uniaxial stress measurements in semiconductors using a piezoelectric actuator. *Appl. Phys. Lett.* **83**, 5235. doi:10.1063/1.1635963 (2003).

- 
293. Schlom, D. G., Chen, L.-Q., Fennie, C. J., Gopalan, V., Muller, D. A., Pan, X., Ramesh, R. & Uecker, R. Elastic strain engineering of ferroic oxides. *MRS Bull.* **39**, 118. doi:10.1557/mrs.2014.1 (2014).
294. Deng, X., Chen, C., Chen, D., Cai, X., Xu, C., Yin, X., Tian, G., Fan, Z., Hou, Z., Qin, M., *et al.* Strain engineering of epitaxial oxide heterostructures beyond substrate limitations. *arXiv preprint arXiv:1905.01070* (2019).
295. Aoyama, T., Iyama, A., Shimizu, K. & Kimura, T. Multiferroicity in orthorhombic  $RMnO_3$  ( $R = Dy, Tb, \text{ and } Gd$ ) under high pressure. *Phys. Rev. B* **91**, 081107. doi:10.1103/PhysRevB.91.081107 (2015).
296. Zhang, J. T., Ji, C., Wang, J. L., Xia, W. S., Lu, X. M. & Zhu, J. S. Stabilization of  $E$ -type magnetic order caused by epitaxial strain in perovskite manganites. *Phys. Rev. B* **97**, 085124. doi:10.1103/PhysRevB.97.085124 (2018).
297. Romaguera-Barcelay, Y., Moreira, J. A., Almeida, A., Araújo, J. & de la Cruz, J. P. Dimensional effects on the structure and magnetic properties of  $GdMnO_3$  thin films. *Mater. Lett.* **70**, 167. doi:10.1016/j.matlet.2011.12.018 (2012).
298. Li, X., Lu, C., Dai, J., Dong, S., Chen, Y., Hu, N., Wu, G., Liu, M., Yan, Z. & Liu, J.-M. Novel multiferroicity in  $GdMnO_3$  thin films with self-assembled nano-twinned domains. *Sci. Rep.* **4**, 7019. doi:10.1038/srep07019 (2014).
299. Zhang, J., Ji, C., Shangguan, Y., Guo, B., Wang, J., Huang, F., Lu, X. & Zhu, J. Strain-driven magnetic phase transitions from an antiferromagnetic to a ferromagnetic state in perovskite  $RMnO_3$  films. *Phys. Rev. B* **98**, 195133. doi:10.1103/PhysRevB.98.195133 (2018).
300. Lin, C., Zhang, Y., Liu, J., Li, X., Li, Y., Tang, L. & Xiong, L. Pressure-induced structural change in orthorhombic perovskite  $GdMnO_3$ . *J. Phys.: Condens. Matter* **24**, 115402. doi:10.1088/0953-8984/24/11/115402 (2012).
301. Mochizuki, M. & Furukawa, N. Microscopic model and phase diagrams of the multiferroic perovskite manganites. *Phys. Rev. B* **80**, 134416. doi:10.1103/PhysRevB.80.134416 (2009).



## List of Publications

- H1. Hoffmann, M., Ernst, A., Hergert, W., Antonov, V. N., Adeagbo, W. A., Geilhufe, R. M. & Ben Hamed, H. Magnetic and Electronic Properties of Complex Oxides from First-Principles. *physica status solidi (b)* **257**, 1900671. doi:10.1002/pssb.201900671 (2020).
- H2. Stiller, M. *et al.* Titanium 3d ferromagnetism with perpendicular anisotropy in defective anatase. *Phys. Rev. B* **101**, 014412. doi:10.1103/PhysRevB.101.014412 (2020).
- H3. Ben Hamed, H., Qteish, A., Meskini, N. & Alouani, M. Calculated hybrid and semilocal functionals and *GW* electronic structure of the metal trifluorides  $MF_3$  ( $M = \text{Sc, Y, Al}$ ). *Phys. Rev. B* **92**, 165202. doi:10.1103/PhysRevB.92.165202 (2015).
- H4. Esquinazi, P. D., Hergert, W., Stiller, M., Botsch, L., Ohldag, H., Spemann, D., Hoffmann, M., Adeagbo, W. A., Chassé, A., Nayak, S. K. & Ben Hamed, H. Defect-Induced Magnetism in Nonmagnetic Oxides: Basic Principles, Experimental Evidence, and Possible Devices with ZnO and TiO<sub>2</sub>. *physica status solidi (b)* **257**, 1900623. doi:10.1002/pssb.201900623 (2020).
- H5. Adeagbo, W. A., Ben Hamed, H., Nayak, S. K., Böttcher, R., Langhammer, H. T. & Hergert, W. Theoretical investigation of iron incorporation in hexagonal barium titanate. *Phys. Rev. B* **100**, 184108. doi:10.1103/PhysRevB.100.184108 (2019).
- H6. Adeagbo, W. A., Maznichenko, I. V., Ben Hamed, H., Mertig, I., Ernst, A. & Hergert, W. Electronic and Magnetic Properties of BaFeO<sub>3</sub> on the Pt(111) Surface in a Quasicrystalline Approximant Structure. *physica status solidi (b)* **257**, 1900649. doi:10.1002/pssb.201900649 (2020).
- H7. Ben Hamed, H., Hoffmann, M., Adeagbo, W. A., Ernst, A., Hergert, W., Hynninen, T., Kokko, K. & Paturi, P. First-principles investigations of the magnetic phase diagram of Gd<sub>1-x</sub>Ca<sub>x</sub>MnO<sub>3</sub>. *Phys. Rev. B* **99**, 144428. doi:10.1103/PhysRevB.99.144428 (2019).
- H8. Ben Hamed, H., Hoffmann, M., Adeagbo, W. A., Ernst, A. & Hergert, W. Magnetic Structure of Bulk GdMnO<sub>3</sub>: Influence of Strain. *physica status solidi (b)* **257**, 1900632. doi:10.1002/pssb.201900632 (2020).



## Acknowledgments

It is a great pleasure, when I sum up what is supposed to be a great achievement, to feel how grateful I am to a lot of people. This thesis is indeed no exception. There are many people to thank for their support and encouragement.

First and foremost, I would like to thank Prof. Dr. Wolfram Hergert, for providing me the opportunity to work in his group, for sharing his knowledge with me and for his continuous guidance. I am especially grateful for his support, valuable advice and encouragement for scientific discussions with other collaborators.

I would also like to express my gratitude to Univ.-Prof. Dr. Arthur Ernst, for his help and the many fruitful discussions we had, especially about the KKR results. I would like to thank him for providing me the HUTSEPOT code.

Furthermore, I would like to thank Dr. Martin Hoffmann, for his help, for the countless discussions we had and for reading my thesis and offering helpful comments and advice. Moreover, I would like to acknowledge the support of Dr. Waheed Adeagbo, with him I shared the office for three years. I would like to thank him for his help in several scientific and computational problems.

In addition, I would like to take the opportunity to thank my colleagues from the Leipzig university. I really appreciate the collaboration with Prof. Dr. Pablo Esquinazi and Markus Stiller on the project of defect induced magnetism in nonmagnetic oxides. I also would like to thank Prof. Kalevi Kokko from the Turku university, for his hospitality and his support to apply for computational resources from the Finnish IT center for science. I am also grateful for the collaboration with him and also with Prof. Petriina Paturi on the electronic structure and magnetic phase transitions in low bandwidth manganite films and bulks.

Finally, I would like to express my heartiest gratitude to my family, particularly my wife who had been very patient with me in the stressful times. I would like to thank her for the continuous and unconditional support. My deepest gratitude goes to my lovely little kids, Anas and Lyn, to whom I dedicate this thesis.





# Lebenslauf

Name: Hichem Ben Hamed  
Staatsangehörigkeit: Tunesisch  
Geburtsdatum: 2. September 1985  
Geburtsort: Zarzis (Tunesien)

## STUDIUM

---

seit 10/2016	Promotionsstudium Martin-Luther-Universität Halle-Wittenberg
11/2009 – 11/2011	Masterarbeit: “Electronic Structure of Defects in Silicon using DFT Theory and GW Approximation.” Tunis El Manar Universität, Tunesien.
10/2005 – 06/2009	Studium Diplom Physik Carthage Universität, Tunesien.

## SCHULE

---

1998 – 2005	Allgemeine Hochschulreife Zarzis Gymnasium, (Tunesien)
1992 – 1997	Grundschule Khaoui-Elghadir, Zarzis (Tunesien)



# Eidesstattliche Erklärung

Hiermit erkläre ich gemäß §5 der Promotionsordnung der Naturwissenschaftlichen Fakultäten I, II, III und des Zentrums für Ingenieurwissenschaften der Martin-Luther-Universität Halle-Wittenberg vom 13. Juni 2012, in der Fassung vom 26. Februar 2013, dass ich die vorliegende Dissertation

## **Computational tailoring of multifunctional oxide materials**

selbständig und ohne fremde Hilfe verfasst habe, keine anderen als die von mir angegebenen Quellen und Hilfsmittel benutzt habe und die den benutzten Werken wörtlich oder inhaltlich entnommenen Stellen als solche kenntlich gemacht habe.

Weiter erkläre ich, dass ich bisher keine vergeblichen Promotionsversuche unternommen habe und dass diese Dissertation weder in der gegenwärtigen, noch in einer anderen Fassung, einer anderen Fakultät vorgelegen hat.

Halle (Saale), 30.07.2020

---

Hichem Ben Hamed